THE EFFECT OF POST WELD HEAT TREATMENT ON HIGH STRENGTH FERROUS WELD METALS

BY

JOHN ROBERT BARCLAY M.Eng.Sc., B.E.(Met).

A thesis submitted for the degree
of Doctor of Philosophy
The University of Aston in Birmingham

October 1976

SUMMARY:

It has been observed that post weld heat treatments designed to reduce or remove residual welding stresses, may cause weld metal embrittlement. In this investigation, the effects of post weld heat treatment on three high strength submerged arc weld metals were examined in terms of changes in mechanical properties, principally fracture toughness. Metallographic work was carried out to determine the cause of embrittlement. Post weld heat treatment was performed in the 450 to 650°C temperature range for times up to 50 hours and embrittlement was measured in terms of Charpy, COD and J contour integral tests. It was found that each weld metal could be embrittled and that two distinct forms of embrittlement occurred. The first was due to alloy carbide precipitation which promoted trans-granular cleavage. Vanadium at 0.12% could cause severe embrittlement while molybdenum at up to 0.6% did not. The second form of embrittlement was classical temper embrittlement which caused low energy decohesion along prior austenite grain boundaries. This was caused by the migration of phosphorus to these boundaries during heat treatment and bulk phosphorus concentrations of 0.011% could cause severe embrittlement. Embrittlement occurred in the 450 to 550°C temperature range and increased with time and decreasing cooling rate. Martensitic microstructures were more susceptible than acicular ferrite. Defect tolerance calculations based on COD and J determinations showed that defect tolerance could increase after heat treatment despite embrittlement although the final defect tolerance was strongly dependent on residual stress levels remaining after heat treatment. Heat treatment procedures for the three weld metals examined were suggested, along with general guidelines for the post weld heat treatment of other high strength weld metals.

Dedicated to my mother and father.

CONTENTS

CHAPTER 1 - INTRODUCTION

There is a considerable economic incentive for design engineers to use steels with a higher yield strength because they reduce the amount of material required for a given structure. In static structures, such as bridges, the weight saving reduces material costs, while in transportation applications,weight saved by lowering structural weight can be used to increase payloads. This economic advantage has fostered the development of higher strength steels over the last few decades, but full benefit can only be achieved if they are readily weldable. Experience has shown that welding problems tend to increase with increasing yield strengths and considerable research effort has been devoted to overcoming problems such as heat affected zone (HAZ) cracking, weld metal cracking and low HAZ and weld metal toughness. Development has now reached a stage where quenched and tempered steels with yield strengths up to 900 MN/m^2 (130,000 psi) can be readily welded, the weld metals exhibiting matching strength and adequate toughness. Thus,welded quenched and tempered plate has been successfully used in bridges, storage tanks, penstocks, pressure vessels, earth moving equipment and naval applications such as surface ships and submarine hulls.

A current limitation on the use of these materials is that post weld heat treatment may cause a reduction in properties in the welded joint, principally in terms of weld metal embrittlement and reheat cracking in the parent plate heat affected zone. It is for these reasons that these weldments are often put into service in the as welded condition (1). Post weld heat treatment has traditionally been employed to improve fracture resistance of welded mild and carbon manganese steel structures. The possibility of embrittlement has meant that the advantages of heat treatment cannot be applied to quenched and tempered steel weldments without some uncertainty about the final fracture resistance of the structure.

The aims of a post weld heat treatment operation can be listed as follows:

1. The removal or reduction of residual stresses.
2. The removal of residual hydrogen to reduce the risk of HAZ and weld metal cold cracking.
3. The elimination of strain ageing.
4. The tempering of hardened microstructures in the HAZ.

Post weld heat treatment is principally applied to pressure vessels and structures containing thick weldments likely to be operating at high design stresses where failure could cause catastrophic damage to people or property. The principal requirement in this context is the removal of residual stresses since these are considered to be of yield point magnitude and therefore increase the risk of fracture from weld defects when working stresses are sumperimposed on the residual stress field. During post weld heat treatment, these stresses are relaxed by plastic flow in the highly stressed areas.

The benefit of removing residual stresses on the defect tolerance of a structure, and hence the benefit of heat treatment, can be illustrated by considering the Welding Institute crack opening displacement (COD) design equation (2). This equation is used to predict the maximum crack size that will not propogate at a given stress level when the fracture toughness parameter of a material is known. For cracks in an as deposited main seam, the critical crack size is given by:

$$\bar{a} = \frac{\delta_c E}{2\pi(\sigma_w + 0.75\,\sigma_y)}$$

$\bar{a}$ - critical crack dominant dimension

δ_c - COD at fracture

E - Young's modulus

σ_y - weld metal yield stress

σ_w - working stress. $0.5\sigma_y < \sigma_w < \sigma_y$

This equation assumes that residual stresses of yield point magnitude are present. If the seam is free from residual stresses, the equation reduces to:

$$\bar{a} = \frac{\delta_c E}{2\pi(\sigma_w - 0.25\sigma_y)}$$

If a working stress of $0.75\sigma_y$ is assumed, and the weld metal is not embrittled i.e. δ_c remains constant, the critical crack size in the residual stress free seam is three times greater than in the as deposited seam and the benefit of post weld heat treatment is apparent.

There are numerous codes of practice, principally applicable to pressure vessels, which specify post weld heat treatment (3, 4, 5). The exact requirements vary depending on the service conditions and the material used. For carbon manganese steels, BS1515 Part 1 specifies a treatment temperature in the range 580 - 620°C to be held for 1 hour per 25mm. of thickness, while for a $1\frac{1}{4}$Cr - $\frac{1}{2}$Mo steel, the temperature range is 620 - 660°C for a minimum of 2 hours. The higher strength steels now being used for pressure vessels are usually supplied in a normalized and tempered, or quenched and tempered condition and the maximum treatment temperature is specified such that the plate tempering temperature is not exceeded.

When high strength steel weldments are heat treated, problems such as HAZ cracking, HAZ embrittlement and weld metal embrittlement have been encountered. The possibility of weld metal embrittlement is extremely serious because the attainment of high as deposited toughness has been a major consideration in the development of weld metals suitable for quenched and tempered steels. Work at the Welding Institute has indicated that post weld heat treatment can embrittle mild steel weld metals and it is considered that the problem could equally apply to low alloy high strength weld metals, particularly in view of the possibility of temper embrittlement occurring, and the need for further research in this area has been highlighted. (6, 45).

A survey of the literature on weld metal embrittlement indicates that precipitation of alloy carbides is thought responsible, particularly those of vanadium, molybdenum and niobium. While temper embrittlement is admitted as a possibility, there appears to be only one specific identification of this form of embrittlement during a stress relieving post weld heat treatment operation. Examination of the literature also shows that the toughness after post weld heat treatment is related to the as deposited microstructure, and that embrittling tendencies due to carbide precipitation may be more than offset by the simultaneous degeneration of other cleavage initiating microstructural constituents. (7).

The aim of this investigation is to examine the effects of post weld heat treatment on three representative commercially available weld metals. The weld metals selected have been specifically designed to weld HY80, HY100 and HY130 quenched and tempered steels and as these steels span a strength range from 550 to 900 MN/m^2, the compatible weld metals represent a suitable cross section of high strength ferritic weld metals. The welding wire - parent plate combinations, along with the minimum required yield strength, can be listed as follows:

Bostrand 31 - HY80 - 550 MN/m^2 (80,000 psi)
Linde 120 - HY100 - 690 MN/m^2 (100,000 psi)
AX140 - HY130 - 900 MN/m^2 (130,000 psi)

The compositions of the welding wires, parent plates and weld metals are listed in Table 1. All weld metals were deposited using the submerged arc process with a low heat input (1.2KJ/mm) and using a fully basic flux, OP41TT.

The literature indicates that Bostrand 31 is embrittled by post weld heat treatment and this has been attributed to the precipitation of vanadium carbide. Embrittlement of AX140 has also been noted but no attempts were made to identify the cause of embrittlement.

In this investigation, embrittlement in the three weld metals is investigated in the 450 to 650°C temperature range for times up to 50 hours using Charpy and crack opening displacement (COD) tests to quantify embrittlement. The form of embrittlement is examined using scanning and transmission electron microscopy along with other more conventional optical techniques. The results of the work are discussed in terms of the form of embrittlement, the effects of the principal post weld heat treatment variables, and resulting defect tolerance levels. Specific recommendations for the post weld heat treatment of the three weld metals are made along with broader based guidelines for other high strength weld metals.

CHAPTER 2 - LITERATURE SURVEY

2.1 General introduction

As embrittlement of weld metals is caused by changes occurring in the as deposited microstructure during the heat treatment operation, it is initially necessary to review the compositional and microstructural features that control as deposited toughness. The first section of the literature survey is devoted to this topic while embrittlement mechanisms are reviewed in the second section. Because embrittlement is defined as a decrease in fracture toughness, the fracture toughness of the weld metals needs to be meaningfully established, and the third section of the literature survey is devoted to a discussion of currently available fracture toughness testing techniques and their relation to design against fracture.

2.2 As deposited weld metal microstructures

2.2.1 Solidification structure

The main difference between weld metal microstructures and those of wrought material is that weld metal is in the "as cast" condition, whereas wrought structures are the result of interactions between mechanical deformation and thermal processing. Weld metal microstructures are therefore more closely linked to those of castings where characteristic solidification structures are visible, even though there are subsequent microstructural transformations.

A ferrous weld metal solidifies as either delta ferrite or austenite, depending on the final carbon content of the weld metal after the usually higher carbon plate material has been diluted by the lower carbon welding wire. The growth mode in low alloy weld metals is cellular and normal to the maximum thermal gradient. There is no specific nucleation event at the fusion interface but rather epitaxial growth from grains in the HAZ of the parent plate. (8). The columnar grains grow in the easy growth direction, ⟨100⟩ and as this growth is normal to the maximum thermal gradient, only favourably oriented grains in the HAZ grow. As growth proceeds, the columnar grains converge, with those grains whose easy growth direction is closest to the maximum thermal gradient surviving. The final solidification structure consists of columnar grains growing radially inward from the fusion interface until they converge at the weld centre. Each columnar grain is composed of similarly oriented pencil shaped cells. (9). The cells tend to be oriented with their longitudinal ⟨100⟩ parallel but with no radial texturing.

If the weld has solidified as delta ferrite,then subsequent transformation to austenite may cause some original columnar solidification boundaries to be incorporated into a new grain. This has been observed when solute sensitive etches have indicated segregated impurities apparently in the centre of austenite grains. (9). The overall appearance of the solidification structure remains unaltered however.

2.2.2 Transformation structures

The final transformation products resulting from the decomposition of austenite are complex and depend on the hardenability of the weld metal and the cooling rate. Pro-eutectoid ferrite nucleates at prior austenite grain boundaries and, depending on the alloying content of the weld metal, may thicken or act as a nucleant for parallel ferrite side plates, the classical upper bainite. (9). The enriched austenite between the plates may degenerate to carbides and ferrite, transform to martensite or be retained as austenite.

In low hardenability, slow cooling welds, the bulk of the austenite transforms to coarse plates of ferrite and degenerate pearlite. In welds with a higher hardenability, proeutectoid ferrite decorates the prior austenite grain boundaries while the bulk of the grain transforms to acicular ferrite. The pockets of enriched austenite in the acicular ferrite interstices are either retained or transform to martensite. If the hardenability and/or the cooling rate is sufficiently high, precipitation of proeutectoid and acicular ferrite is suppressed and the entire grain transforms to martensite.

The formation temperature of low carbon martensite is relatively high, and auto-tempering during cooling has been observed where fine carbide rods are precipitated on a number of habit planes. The final structure is composed of lath and auto-tempered martensite with some retained austenite. (10).

The exact nature of acicular ferrite has yet to be clearly resolved. Work by Tuliani is reported to have found that acicular ferrite is precipitate free, has a high dislocation density and has a c/a ratio of approximately 1.01. The ferrite grains occupy different crystallographic habit planes meeting at high angle boundaries. It was consequently proposed that the structure was massive martensite. (11). Other workers have referred to the structure as low temperature bainite (12) and bainite (13). Widgery and Saunders point out that weld metals quenched from within the acicular ferrite temperature formation range contain clearly distinguishable martensite. They go on to argue that while its true structure is not clearly defined, it can be readily identified and the adoption of other titles such as upper or lower bainite and massive martensite is misleading. (9). They also state that they have observed classically defined lower bainite in low alloy weld metals, which is characterized by carbide particles precipitated on a single high angle habit plane within the ferrite grains. This is distinguished from auto-tempered martensite by the observation of carbides precipitated on all three habits in the latter. Unfortunately, they present no pictorial evidence for this distinction.

The appearance of the various microstructures referred to in this section can be illustrated by reference to micrographs of the weld metals examined in this investigation. The general layout of columnar grains in a weld run can be seen in the macrograph, Figure 13, while acicular ferrite and proeutectoid ferrite are shown in Figure 44. What are thought to be islands of martensite in acicular ferrite are shown in Figure 46 and a totally martensitic microstructure is shown in Figure 60.

In multirun deposits, subsequent weld runs form a HAZ in the runs immediately beneath, causing the structure to transform to fine equiaxed grains of ferrite and martensite (Figure 13). This structure is considerably tougher than the columnar region and if the proportion is increased by using more weld runs at a lower heat input, the toughness of the deposit is increased. (14). It has also been pointed out that the lower heat input will lead to a finer structure in the non modified columnar region and thus the improvement in toughness can be attributed both to the increased proportion of refined structure and to the finer, non heat affected structure in the columnar region. (13).

2.2.3 Relationship of structure to properties

In the development of high strength weld metals the two principal property requirements are high strength and high toughness. At the lower end of the strength range (up to 690 MN/m^2) the most satisfactory structure is acicular ferrite which has a high dislocation density and a high yield to ultimate ratio. At higher strengths, there is some confusion about what is the best structure to meet the required strength levels. Connor et al., showed that the necessary strength level in HY130 weld metal could only be achieved above a critical cooling rate (15), and Shackleton inferred from this data that the structure was martensitic. (13). Saunders has examined weld metals at the 900 MN/m^2 level and described all such microstructures as martensitic. (10).

In general terms, the development of adequate strength has not caused as much difficulty as the concurrent requirement for high toughness. Knowledge of the relationship between weld metal microstructure and toughness has been very slowly developed, principally because of confusion in the identification of microstructural constituents.

Toughness is widely described in terms of Charpy or Crack Opening Displacement (COD) transition curves which are a measure of the temperature dependence of the resistance of the material to crack initiation, in the case of COD, and initiation and propogation in the case

Charpy. Upper shelf fracture occurs by microvoid coalescence and resistance to this fracture mode is promoted by reducing the volume fraction of inclusions and therefore increasing the inter-inclusion spacing. Widgery has demonstrated that resistance to microvoid coalescence also decreases with increasing yield stress and decreasing strain hardening exponent (16), and therefore weld metal cleanliness becomes very significant in high strength weld metals which exhibit low work hardening. This has promoted the development of cleaner weld metals where specific steps have been taken to lower sulphur and oxygen levels by using basic slags in submerged arc welding and low oxygen content shielding gasses in metal inert gas (MIG) welding.

The transition region of the Charpy curve is caused by increasing proportions of cleavage fracture until at the lower shelf, fracture occurs entirely by cleavage. Garland and Kirkwood have argued that the best approach to the development of weld metals is to examine the factors which cause cleavage fracture and if these factors can be suppressed, then upper shelf behaviour i.e. microvoid coalescence, can be extended to lower temperatures. (7).

Widgery has examined several microstructural types and concluded that acicular ferrite had a higher cleavage resistance that coarse ferrite/pearlite mixtures or ferrite side plates. Proeutectoid ferrite was also considered undesirable because it is softer than acicular ferrite and strain tends to concentrate in the proeutectoid ferrite bands along prior austenite grain boundaries causing local cleavage cracks. The higher cleavage crack resistance of acicular ferrite was attributed to its fine grain size which meant that ductile tearing was necessary to link cleavage cracks in individual acicular grains, whereas a cleavage crack could propagate undeflected across an entire colony of parallel ferrite side plates. (17, 9).

Shackleton has suggested that minor microstructural constituents may be responsible for the observed scatter in the toughness of acicular ferrite, (13), and this has been confirmed by Garland and Kirkwood who have shown that the onset of cleavage fracture is dominated by pools of martensite retained in the interstices of the acicular ferrite. It was found that increasing proportions of martensite lowered cleavage resistance, while a post weld heat treatment which caused the martensite to degenerate to ferrite and carbides, caused a significant increase in cleavage resistance. Two types of martensite were allegedly observed, "blocky lath martensite" in a carbon, manganese, niobium weld metal and "twinned martensite" in a carbon, manganese, molybdenum weld metal. The evidence for the distinction is based on two, not very clear, electron micrographs and this requires further confirmation. (25).

The blocky lath martensite was found to be more detrimental than the rounded islands of twinned martensite, the inference being that cleavage cracks were more readily nucleated in the former. This appears anomalous as it is generally considered that twinned martensite has a lower cleavage resistance. The islands of blocky lath martensite were observed to be associated with solidification and transformation boundaries, which was also considered undesirable, but the reason for this is not clear as they implied fracture by transgranular cleavage and not by intergranular separation. In summary, it can be concluded that islands of martensite in acicular ferrite adversely affect its cleavage resistance, but the exact micromechanism of fracture has yet to be clearly established.

There has been little work published on cleavage fracture in martensitic weld metals. Saunders examined seven such weld metals and found that they contained lath and auto-tempered martensite. He concluded that, provided sufficient alloying additions were made to ensure that the structure was fully martensitic, there was little scope for structural modification that would improve its cleavage resistance. This, of course, presupposes that the carbon level is restricted to the absolute minimum compatible with the attainment of the required strength level. It was noted that the transition curves of martensitic weld metals are fairly flat and the importance of weld cleanliness to minimize failure by low energy microvoid coalescence was stressed. (10).

The role of microstructural constituents in the resistance to cleavage fracture has been recently reviewed (18), and the effects are summarized in Figure 1. With increasing acicular ferrite contents, the cleavage resistance initially falls, possibly due to strain concentration in proeutectoid ferrite (17), after which the cleavage resistance increases until the formation of martensite begins to lower resistance once again.

2.2.4 Composition and as deposited properties

Alloying element additions to ferrous weld metals are required to fulfill the following requirements:

1. Develop sufficient hardenability to ensure the formation of the desired microstructure (acicular ferrite or martensite).

2. Suppress the formation of undesirable microstructures. (proeutectoid ferrite, ferrite side plates and martensite in acicular ferrite).

3. Ensure adequate deoxidation and nitrogen fixation.

4. Ensure fixation of other undesirable impurities (manganese is added to combine with sulphur).

5. Increase tempering resistance so that softening in multipass welds is minimized.

A broad understanding of the influence of microstructural components on fracture toughness has only evolved relatively recently and there are still some areas that need further clarification, particularly the role of martensite in acicular ferrite. Weld metal development has consequently been based on compositional control where various elements have been evaluated for their effects on strength and toughness. Typical of this approach was work done by Ennis and Telford, who evaluated 60 compositions and subjected the results to a multiple regression analysis relating composition to strength and toughness. (19). While they realized that weld metal at the HY80 level had a bainitic structure (acicular ferrite) and that a martensitic microstructure would probably be required to achieve the necessary strength at the HY130 level, they did not specifically aim to control the microstructure by compositional adjustment. The multiple regression analysis gave two parameters for each element, a strength factor and a toughness factor determined from Charpy tests at -51°C.

The conclusions drawn were that manganese, molybdenum and copper improved toughness and strength, while chromium, carbon, nitrogen and the deoxidants decreased toughness.

It is unnecessary duplication to review, in detail, all the studies on the effects of composition on welded properties as this has been very thoroughly covered by Masubuchi et al., (20) and Shackleton (13). Their findings are summarized below and more recent data added where applicable.

Carbon

Carbon is an efficient strengthening agent, but at the same time causes a severe deterioration in Charpy toughness and can cause weld metal cracking. The optimum range of carbon contents is generally accepted as being 0.06 - 0.12%. Most of the data collected on carbon is presumably based on ferrite side plate/acicular ferrite structures, although recent work by Saunders on martensitic weld metals showed that carbon variation over the narrow range 0.06 - 0.10% did not significantly lower COD toughness. (10).

Manganese

Manganese is added to weld metals to control sulphur and prevent hot cracking, to provide some solid solution hardening and to increase hardenability. Shackleton indicates that there is some dispute in the literature whether manganese actually improves toughness, but concludes that levels up to 2% do not cause a significant deterioration. It has been suggested that a manganese/silicon ratio of 4 - 5 minimizes inclusion content. (16).

Silicon

Silicon is a potent solid solution hardener which can cause a deterioration in toughness. It also acts as a powerful weld metal deoxidant. There is some disagreement on the optimum silicon content, the most widely quoted maximum being 0.5%.

Nickel

Nickel marginally improves strength and is principally used to improve toughness although its effectiveness is not agreed upon. There are some reports of nickel in excess of 2.5% causing hot cracking, but contents up to 5% have been successfully used. (21).

Chromium

Chromium increases weld metal strength and causes a deterioration in Charpy toughness, particularly at levels above 1%. It is reported to promote the formation of acicular ferrite.

Molybdenum

Molybdenum increases strength and toughness at levels up to 0.5% by promoting the formation of acicular ferrite. Toughness tends to deteriorate at higher levels.

Copper

There are several reports of copper improving strength and toughness (up to 0.50%) although it has not been widely used in weld metals.

Titanium, zirconium, aluminium

These elements are all used as deoxidizers or denitriders. They are all reported to adversely affect toughness and their levels are restricted to around 0.01%.

Niobium.

Shackleton indicates that the little information available on niobium indicates that it causes a marked decrease in toughness. This was confirmed in work reported by Almquist et al., where niobium additions of up to 0.06% significantly decreased toughness. (22). Garland and Kirkwood compared a 0.02% niobium weld metal with a niobium free but otherwise identical weld metal and found no significant deterioration in toughness. (7). This would appear to be the maximum tolerable level until further information becomes available.

Vanadium

The general view obtained from the literature indicates that vanadium markedly increases strength and causes a severe deterioration in toughness, although there are reports that vanadium at up to 0.12% can be beneficial. Garland and Kirkwood examined weld metals containing up to 0.12% vanadium and found that it promoted the formation of acicular ferrite and did not cause a significant deterioration in toughness. Their investigation also showed that it interacted with niobium and molybdenum causing a toughness deterioration when molybdenum was present and improved toughness when niobium was present. (23). The effects of vanadium on weld metal toughness after post weld heat treatment are further examined in section 2.3.2.1.

Sulphur, phosphorus, oxygen and nitrogen

These elements are considered to be highly undesirable and welding consumables and processes specifically aim to keep their levels as low as possible. Sulphur and phosphorus promote hot cracking, lower upper shelf Charpy toughness, and are limited to levels less than 0.012% in HY series consumables.

Nitrogen markedly lowers toughness and is usually controlled by the addition of strong nitride formers. Oxygen affects upper shelf fracture behaviour by inclusion formation. (24). The amount of nitrogen absorbed in a weld pool increases with the oxygen content of the weld pool which is an added reason for restricting oxygen contents. (26).

2.2.5 Submerged arc process variables

This work is specifically aimed at examining submerged arc weld metals rather than MIG or manual metal arc (MMA) weld metals. The latter two processes have been successfully used to deposit weld metals up to HY130 strength levels and they have been extensively reviewed by Shackleton. (13). He casts some doubt on the suitability of submerged arc at the HY130 strength level because of high oxygen and nitrogen levels, although the advent of fully basic fluxes such as OP41TT suggests that adequate toughness can be achieved if heat inputs are restricted so that cooling rates are sufficiently high for martensite formation.

A significant variable of the submerged arc process is the flux type. Basic fluxes significantly lower weld metal oxygen and inclusion contents which increase upper shelf Charpy toughness. (24, 27). This has led to a trend to use basic fluxes where high weld metal toughness is required, even though their operating characteristics such as current carrying capacity and slag detachability are considerably inferior to acidic fluxes.

Basicity is measured in terms of the chemical content of the flux:

$$B = \frac{CaO + MgO + CaF_2 + \frac{1}{2}(MnO + FeO)}{SiO_2 + \frac{1}{2}(Al_2O_3 + TiO_2 + ZnO_2)}$$

Acid fluxes have a high silica content and have basicity indexes of about 0.5 to 0.8 while a fully basic flux such as OP41TT has high MgO and CaF_2 contents and has a basicity index of 3. (24, 28).

Recent work by Garland and Kirkwood has indicated that fully basic fluxes are not the universal answer to the attainment of high weld metal toughness. (23). The theory is based on the analysis of Charpy transition curves and they argue that upper shelf behaviour, i.e. microvoid coalescence, can only be achieved if the microstructure is sufficiently resistant to cleavage fracture at a given temperature. In other words, a very low inclusion content is not an automatic guarantee of high toughness if the weld metal fails by cleavage. This point was demonstrated when increasing heat input welds were made with a basic flux (OP41TT) and the transition temperature was found to increase with heat input. The decrease in cleavage resistance was attributed to the increased proportion of lath martensite and upper bainite (ferrite side plates). This was due to the observed increase in carbon content, decrease in manganese and silicon contents and the slower cooling rate as the heat input increased. Heat input is therefore the other significant variable with the tendency for toughness to decrease as heat input increases. (18).

Garland and Kirkwood noted that toughness did not deteriorate as rapidly with an amphoteric alumina based flux which caused a higher oxygen level and hence a higher inclusion content, but did not cause changes in the carbon, manganese and silicon contents with increasing heat inputs, and so the cleavage resistance of the matrix was essentially unaltered. It therefore appears that the use of fully basic fluxes is restricted to low heat inputs, although there are reports of a boron, titanium wire which overcomes this limitation, but no detailed account on how this is achieved has been published.

2.2.6 Summary

The principal microstructural and compositional factors controlling submerged arc weld metal toughness can be summarized as follows. Development of higher strength, high toughness consumables, particularly for the HY series steels, has centred on the nickel, chromium, molybdenum, manganese system where various compositions have been successfully used.

Copper should also be considered as a major alloying element, although it has not been widely exploited. The optimum carbon content appears to be in the range 0.06 - 0.10% to ensure adequate strength without a serious loss of toughness. Silicon is the principal deoxidant in use at levels up to 0.30% and other deoxidants such as titanium, zirconium, and aluminium have been used at lower levels. Sulphur, phosphorus, nitrogen and oxygen are considered undesirable impurities and careful attention has been devoted to keeping their levels as low as possible in consumables and through the use of basic slags in submerged arc and low oxygen content shielding gas in MIG. Vanadium and niobium additions at levels up to 0.12% and 0.02% respectively may or may not be beneficial.

The optimum levels of the major alloying elements appear to vary and undoubtedly interact with each other. This interaction is further complicated by the final transformation structure which may vary from ferrite side plates and acicular ferrite through to martensite and the effects of a given element are difficult to isolate from this interaction. The role of the major alloying elements in determining the structure and amount of martensite in acicular ferrite must also be considered.

While this interaction is complex, the trends are gradually emerging and point the way for further development. It appears that up to the HY100 level, the most suitable microstructure is acicular ferrite and this structure can be further developed by attention to the associated martensite.

Finally, basic fluxes give the lowest inclusion content and the highest upper shelf Charpy toughness, but increasing heat input tends to lower the cleavage resistance of nominally acicular structures and amphoteric fluxes may be more suitable at higher heat inputs.

At the higher strength levels of HY130, it appears that martensitic microstructures are necessary and the scope for compositional development seems much more limited. The obvious requirements are that there is sufficient carbon to give adequate strength, the alloying content is sufficient to ensure martensitic hardenability and that impurity levels are kept as low as possible. The literature on martensitic weld metals is extremely limited and this will undoubtedly be an area of increased research as demand for higher strength weld metal increases.

2.3 Weld metal embrittlement

2.3.1 Introduction

In contrast to the careful development of weld metal microstructures designed to give high toughness, it is quite striking that very little attention has been paid to the effect of post weld heat treatment on weld metal properties. In Shackleton's review of welding

HY100 and HY130 steels the issue is completely ignored, although a passing reference is made to some COD work on manual metal arc weld metals which were embrittled by post weld heat treatment. (29). In the Welding Institute's review of welding QT35 and HY80 it is pointed out that the general position regarding post weld heat treatment of weld metals is not well understood, to quote:-

"Whereas it appears that the HAZ regions in HY80 and QT35 steels significantly improve in toughness on post weld heat treatment, the risk of fracture initiation in a post weld heat treated structure will probably depend on the relative effects of the reduction in residual stresses and deterioration in weld metal toughness that results from heat treatment. An important factor that must always be considered in connection with post weld heat treatment is the likelihood of temper embrittlement occurring in weld metal or in HAZ regions. However, there appears to be little information available with respect to quenched and tempered low alloy steels." (6).

Swift and Rogers have reviewed weld metal embrittlement and they divide it into three categories. (30). Creep embrittlement applies to creep failures in weld metals operating at elevated temperatures and is not really applicable in the present context. Stress relief embrittlement is attributed to carbide precipitation during the post weld heat treatment cycle while temper embrittlement is discussed in terms of toughness deterioration after holding for prolonged periods in the 400 - 600°C range. In this survey, it is intended to examine the possibility of temper embrittlement occurring during a normal post weld heat treatment operation,in a structure not destined for high temperature use. There are, therefore, two possible sources of embrittlement during a treatment cycle, carbide precipitation and classical temper embrittlement and these will be examined in turn.

2.3.2 Carbide precipitation

Swift and Rogers report that some weld metals containing strong carbide formers such as vanadium and molybdenum are embrittled by post weld heat treatment. In cases where a deterioration in Charpy toughness has been noted, secondary hardening occurs. They concluded that precipitation of coherent carbides either locks or restricts dislocation motion which makes the microstructure more susceptible to cleavage fracture. (30).

2.3.2.1 Vanadium

Puzak and Pellini examined a manual metal arc weld metal which contained .06%C, 0.26%V, 1.5%Ni and 0.58%Mo. They found that secondary hardening occurred in the 460 - 680°C temperature range, the time to reach peak hardness decreasing as the temperature increased. Maximum hardness coincided with a maximum deterioration in Charpy toughness as shown in Figure 2. Vanadium carbide precipitation was not specifically identified, but rather inferred from the strong secondary hardening observed. The possible simultaneous precipitation of molybdenum carbide was not considered. (31).

Sagan and Campbell found that a 0.1% vanadium bearing Ni-Mo-V weld metal showed a 22°C upward shift in Charpy transition temperature after 2 hours post weld heat treatment at 620°C, while an identical, vanadium free, weld metal showed no change. (32).

Campbell et al., examined submerged arc weld metals containing 0.12% vanadium made from Bostrand 31 wire and a semi basic flux, Encrex 2/102, and found that there was a deterioration in Charpy toughness after a 1 hour heat treatment at 550°C and 650°C. The 55 joule energy absorbed temperature in the as welded condition was -30°C which increased to -15°C after 1 hour at 550°C and 0°C after 1 hour at 650°C (Figure 3). A simultaneous increase in hardness and yield strength was noted and precipitation of vanadium carbide was inferred but no direct observation of the precipitate was attempted. (33).

Garland and Kirkwood examined the influence of vanadium on submerged arc weld metal toughness using plate dilution as a source of vanadium. They used two levels of vanadium (approx. .03% and 0.12%), two heat inputs (3.3 and 7.5 KJ/mm) and an amphoteric flux, BX200 and a basic flux OP41TT. Stress relief was "carried out in accordance with BS1515" which presumably meant 580 - 620°C for 1 hour. They concluded that the final toughness was a result of the balance between the degeneration of islands of martensite which increased toughness and the adverse effect of precipitation of alloy carbides which decreased toughness. Carbon manganese welds containing up to 0.12%V welded at 3.3 KJ/mm and using OP41TT flux showed a marked toughness increase on heat treatment which is shown in Figure 4. Similar welds made at a higher heat input (7.6 KJ/mm) showed only a marginal improvement. A decrease in toughness was observed at the higher vanadium level and a 3.3KJ/mm heat input using an amphoteric flux, BX200 (Figure 5). In this case it was suggested that precipitation of aluminium nitride aided epitaxial growth of vanadium carbide, but this was not experimentally verified. Precipitation of vanadium carbide was inferred from increases in yield strength rather than by direct observation. (23).

Hannerz and Jonsson-Holmquist (34) examined vanadium in weld metals using single run submerged arc at one heat input (7.2 KJ/mm). Parent plate dilution was used as a vanadium source. Their results indicated that up to 0.10% vanadium did not significantly degrade Charpy toughness in either the as welded condition, or after 2 hours heat treatment at 600°C. There was a progressive decrease in toughness at higher vanadium levels. Examination of thin foils led them to conclude that precipitation of vanadium nitride occurred during transformation from austenite to ferrite (as the weld metal cooled after deposition) and that subsequent heat treatment coarsened the precipitates sufficiently for them to be observed in the electron microscope. This conclusion was based on the observation of rows of precipitates similar to those observed by Batte and Honeycombe (35) who studied the isothermal transformation of 1.0% vanadium steels. The rows of precipitates observed by Hannerz and Jonsson-Holmquist were in a 0.22% vanadium weld after stress relief. They state that "some" precipitates were observed in the as deposited 0.09% vanadium weld and that "more" were observed in the as deposited 0.22% vanadium weld, but they do not present any pictorial evidence. They referred to the precipitate as vanadium nitride but no diffraction evidence was presented.

Work carried out on the post weld heat treatment embrittlement of vanadium bearing heat affected zones is also relevant to the discussion. (36). Vanadium carbide precipitation was identified by electron diffraction, with the precipitate uniformly distributed throughout the proeutectoid ferrite/acicular ferrite structure. The most significant observation was that precipitation of vanadium carbide promoted intergranular failure, the argument being that the vanadium carbide strengthened the grains, thus concentrating strain on the grain boundaries. As far as it is known, no fracture surface observations have been made of vanadium embrittled weld metals.

In summary, it can be concluded that the influence of vanadium on weld metal toughness after post weld heat treatment is complex and related to a number of factors, namely, the vanadium content, the heat input, the flux type and the presence of other alloying elements. It is generally agreed that the precipitation of vanadium as a carbide or nitride causes a deterioration in Charpy toughness, the magnitude of the deterioration increasing rapidly at vanadium levels in excess of 0.12%. Garland and Kirkwood argue that this precipitation cannot be considered in isolation as the post weld heat treatment may remove other cleavage initiating microconstituents and this may more than counteract the deleterious effect of precipitation. The effect is schematically illustrated in Figure 6. It can also be noted from this figure that some investigators have suggested that carbides resulting from the degeneration of retained austenite and/or martensite can themselves lower cleavage resistance. (17, 37). The apparent difference between the results of Campbell et al., who observed a nett toughness deterioration, whereas Garland and Kirkwood observed a toughness increase at the same vanadium level (0.12%) may be explained by a lower martensite content in the former weld metal. Welds made with increasing heat inputs and decreasingly basic fluxes seem to exhibit a greater degree of embrittlement.

The precipitation of vanadium carbide in weld metals has not been studied in any detail. It is suggested that precipitation occurs immediately during weld cooling and that growth occurs on subsequent heat treatment, or alternatively that precipitation and growth occur on heat treatment, but there appears to be no conclusive evidence for either viewpoint at levels around 0.1%. It is also uncertain if vanadium carbide precipitates uniformly throughout the structure or is associated with the degeneration of islands of martensite. Swift and Rogers assert that precipitating species promote cleavage fracture while other work suggests that intergranular failure may occur and direct observation of fracture surfaces is required.

2.3.2.2 Molybdenum

There have been very few detailed studies on the effects of molybdenum carbide precipitation in post weld heat treated weld metal. Bland (38) examined $2\frac{1}{4}$ Cr - 1 Mo and $1\frac{1}{4}$ Cr $\frac{1}{2}$ Mo manual metal arc weld metals after various heat treatments using ductility (elongation on a 50mm. gauge length) as a measure of embrittlement. It was concluded that 1% molybdenum caused severe embrittlement at 565°C and the degree of embrittlement decreased as the treatment temperature was raised to 732°C. Molybdenum at the 0.5% level did not appear to cause any embrittlement over the 565 - 732°C temperature range, although it is doubtful if the test was sufficiently sensitive to detect low levels of embrittlement. As no attempt was made to identify the precipitating carbide, it is difficult to establish if molybdenum carbide was solely responsible, as chromium carbides may have been precipitating simultaneously.

Garland and Kirkwood examined the effect of molybdenum at two levels (0.02% and 0.30%) using a basic flux, OP41TT. (7). After post weld heat treatment there was a significant toughness increase observed in the low molybdenum weld metal, while there was only a slight increase at the higher level. When an amphoteric flux, BX200 was used there was a significant deterioration in toughness accompanied by a marked increase in yield stress. It was argued that aluminium from the alumina based flux precipitated as aluminium nitride which provided epitaxial nuclei for molybdenum carbide and caused a faster precipitation rate. No experimental evidence was presented for this theory and no direct observation of molybdenum carbide was made. It is important to note that the weld metals contained 0.01 - 0.014% niobium which is known to markedly increase precipitation hardening in molybdenum bearing steel (39), and so the true magnitude of the toughness deterioration due to the precipitation of molybdenum carbide alone, at up to the 0.30% level, was not clearly established.

2.3.2.3 Niobium

Garland and Kirkwood examined niobium, gained by parent plate dilution, at levels up to 0.023%. (7). They noted that precipitation occurred from the increase in yield stress after post weld heat treatment. They did not observe a deterioration in toughness after heat treatment with either a basic or amphoteric flux. It is probable that niobium could cause a problem if it was present at higher levels.

2.3.3 Temper embrittlement

Temper embrittlement in wrought alloy steels has been recognized for many decades and is usually measured as a shift in the Charpy transition range to higher temperatures. The subject has been extensively reviewed and while the exact mechanism of embrittlement is still conjectural, the principal characteristics are well known. (40, 41).

1. Embrittlement can occur in alloy steels having a ferrite carbide microstructure when heated into, or slowly cooled through the 375 to 575°C temperature range.
2. Embrittlement only occurs if specific impurities such as phosphorus, tin, antimony and arsenic are present, the degree of embrittlement increasing with the concentration of impurities. (42).
3. In an embrittled steel, the fracture path is along the prior austenite grain boundaries.
4. The degree and rate of embrittlement is affected by the alloying element content of the steel. Chromium and manganese tend to increase it. Small amounts of molybdenum can suppress embrittlement, but larger amounts increase it.

Recent work using Auger spectroscopy has shown that the embrittling species segregate preferentially to the prior austenite grain boundaries, reaching very high concentrations in the surface monolayer. The segregation is concentrated in the immediate vicinity of the boundary and decreases to the bulk level within a few atomic diameters. (43).

The segregating impurity has been shown to markedly lower the free energy of the grain boundary surface which implies that less energy is required to separate two grain boundary surfaces containing a segregant than that required in a segregant free case. Hondros argues that when the segregating species is present above a critical concentration, there will be enough segregant on the boundary surfaces to lower their free energy sufficiently for them to become the lowest energy absorbing fracture path. (44). McMahon has shown also that the cohesion of the ferrite/carbide interface is lowered by impurity segregation, grain boundary carbides tending to fracture in the impurity free case while impurities cause smooth decohesion. (46).

The various models of temper embrittlement can be broadly summarized as follows. If a steel is tempered at 650°C or above, the embrittling elements diffuse into the grains due to strong entropy effects and embrittlement does not occur. If a steel is heated for prolonged periods at 550°C or below, the embrittling elements tend to diffuse back to the prior austenite grain boundaries reaching very high concentrations in the immediate boundary vicinity. As diffusion is strongly temperature dependent, the embrittlement rate decreases with temperature and thus embrittlement exhibits a "C curve" behaviour (Figure 7). The embrittling species cause embrittlement by lowering the cohesion of the ferrite/ferrite boundary interfaces and also the ferrite/carbide interfaces. It has been noted that the alloying elements, nickel, chromium, manganese and molybdenum all modify embrittling behaviour and there have been various explanations offered. (41, 47, 48, 54). It has been suggested that they may increase the diffusivity of the embrittling species (manganese is reported to increase the diffusivity of phosphorus in iron (41)), or that they cause preferential grain boundary carbide precipitation, the cohesion of which is lowered by the embrittling species. Detailed experimental justification for the various theories is lacking and the interaction between alloying elements and embrittling elements is not well understood.

The study of temper embrittlement has concentrated on quenched and tempered martensitic microstructures, the principal microstructural variable being prior austenite grain size. Capus found that embrittlement increased with increasing prior austenite grain size and suggested that for a given amount of segregated solute, the amount per unit boundary area is greater for larger grain sizes. (47).

Woodfine (49) studied the effect of microstructure in a 0.04% phosphorus bearing steel and found that the transition temperature shift after a 500°C embrittling treatment was greatest for a martensitic microstructure and successively less for bainitic and pearlite structures. However, it is important to note that the transition temperatures in the embrittled condition were all roughly equal and the differences in shift on embrittlement were due to large differences in the non embrittled transition temperatures.

Other work has confirmed this view where it was found that the amount of embrittlement in a Ni-Cr-V steel was greater for martensite than bainite, but the nonembrittled bainite had a lower toughness than the embrittled martensite. Auger spectroscopy showed segregation of phosphorus and tin to prior austenite grain boundaries was greater in martensite than bainite. (50).

Geniets and Knott examined the relative embrittlement of martensite and bainite and found that if they were tempered to give identical fracture stresses in a low temperature tension test prior to embrittlement, then embrittlement was greater in the tempered bainite. This was attributed to the presence of coarser carbides in the bainitic steel. (51).

Several studies using pure iron containing small amounts of sulphur, phosphorus or tin have shown that substantial embrittlement can occur in polygonal ferrite structures (49, 52, 53) and so it must be concluded that the effect of microstructure on susceptibility to temper embrittlement has not been clearly established. The precipitation of grain boundary carbides appears to affect the degree of embrittlement, but until the cohesion of an impurity doped ferrite-carbide interface can be compared directly with the cohesion of an impurity doped ferrite-ferrite interface, the relative susceptibilities of the two structural types cannot be established. Another factor to be resolved is that differing response may also be related to the relative high angle grain boundary area per unit volume. Geniets and Knotts' result could possibly be explained by suggesting that there was a similar high angle boundary area in the two structures and the differing embrittlement response was caused by the enhanced carbide precipitation on boundaries in the bainite.

2.3.4 Temper embrittlement in weld metals

Bruscato examined the effects of phosphorus, arsenic, antimony and tin in a 2Cr 1Mo manual metal arc weld metal. (55).. The investigation was designed to study possible embrittlement after prolonged exposure in the embrittlement range as would be experienced during the operation of high temperature pressure vessels. Comparison was made between weld metals in the stress relieved condition before, and after a step age treatment designed to induce a degree of embrittlement similar to the embrittlement caused by prolonged isothermal treatments. Charpy energy absorbed at $10^{o}C$ was related to the manganese plus silicon content and the impurity content factor, (10P + 5 Sb + 4 Sn + As). The degree of embrittlement increased with increasing impurity factor and the manganese plus silicon content (Figure 8). It is unfortunate that no Charpy data was presented for the as welded condition as some embrittlement may have occurred during the initial stress relieving heat treatment. The data presented for the step age treatment is not directly relevant in the present context, as it was designed to assess embrittlement after extended exposure at temperatures in the 400 - 600°C range, but it does show impurities can induce temper embrittlement in weld metals.

Wolstenholme examined a 2% chromium, 1% molybdenum weld metal which contained 0.02% phosphorus and found that embrittlement occurred during slow cooling (25°C/hour) after post weld heat treatment at 680°C for 3 hours. The embrittlement could be suppressed by water quenching. Embrittlement was attributed to phosphorus segregation to prior austenite grain boundaries. (56). This work is important because it positively identifies classical temper embrittlement occurring during a post weld heat treatment cycle. Moreover, the treatment cycle used was one which could reasonably be expected in practice, noting of course that treatment temperatures would be lower for HY series weld metals. This is particularly important in terms of Swift and Rogers' review of weld metal embrittlement, because they did not consider the possibility of temper embrittlement occurring during a normal post weld heat treatment cycle. Wolstenholme's findings demonstrate that temper embrittlement is also possible and this must also be considered along with carbide precipitation as a cause of toughness deterioration after post weld heat treatment.

Rosenstein and Asche noted a deterioration in AX140, MIG weld metal post weld heat treated at 565°C. The degree of embrittlement increased with time at temperature and with decreasing cooling rate. While temper embrittlement was suspected, no attempt was made to identify the cause of the embrittlement. (57).

2.3.5 Summary of weld metal embrittlement

The survey of the literature has shown that the deterioration in toughness caused by a post weld heat treatment cycle is usually ascribed to precipitation of alloy carbides. While classical temper embrittlement has also been suspected, it has only been positively identified in one instance, in a 2Cr 1 Mo weld metal.

It appears from the weight of evidence that vanadium at levels in excess of approximately 0.1% causes a decrease in toughness, while there is some doubt on its deleterious effect at lower levels. Its overall effect is further complicated by the possible removal of cleavage initiating microconstituents during stress relief which may lead to a nett improvement in toughness. The literature on Bostrand 31 indicates that vanadium carbide precipitation does cause a decrease in toughness. There has only been one direct observation of vanadium carbide precipitation in weld metal, but this was at levels above the range under consideration. There is clearly a need to further clarify the mode of its precipitation, particularly in relation to the complex weld metal microstructure detailed in section 2.2.2. The observation that vanadium carbide precipitation promotes HAZ intergranular fracture must also be considered as carbide precipitation has usually been thought to promote cleavage fracture. Similar remarks can be applied to molybdenum carbide precipitation. There appears to be contradictory evidence on its deleterious effects in the 0.30 - 0.50% range. As molybdenum is present at these levels in consumables used for welding HY100 and HY130 steels, its exact effect on toughness needs to be further examined.

There is very little evidence to suggest that temper embrittlement is a contributing factor to weld metal embrittlement, although very few investigations appear to have been carried out with the specific aim of identifying it. It must also be noted that in the development of high strength welding consumables, close attention has been devoted to minimizing phosphorus and sulphur levels and yet it is uncertain if the levels are sufficiently low to preclude the possibility of temper embrittlement during a post weld heat treatment cycle. It is therefore clearly desirable that sources of weld metal embrittlement in high strength weld metals be identified so that consequent modification to compositions can be carried out.

2.4 Considerations of general yielding fracture mechanics

2.4.1 Introduction

Embrittlement can be regarded as the toughness decrease resulting from a given treatment. The question that is considered in this section is what is the best way of measuring toughness and how should this be related to the fracture behaviour of an engineering structure.

In engineering structures, catastrophic failure occurs when the operating stress exceeds a critical level causing a pre-existing defect to propagate. The likelihood of fracture is reduced if the size of the defect is below a critical size and if the material has a high resistance to fracture. This resistance is usually termed fracture toughness, and it is obviously desirable to be able to quantify it so that the microstructural and compositional factors that control it can be identified. In order to achieve this, it is necessary to use defect geometries and loading rates that are applicable to the situation in question.

The traditional and widely used fracture test is the Charpy test in which a notched 10mm. square bar is impact loaded and the energy absorbed in fracturing the bar is measured. Ferritic materials display transitional behaviour with increasing temperature and the Charpy tests are conducted over a range of temperatures giving a low energy absorbing shelf at low temperatures and a transition to a higher energy absorbing shelf as test temperature increases. The Charpy test uses a relatively blunt notch which is impact loaded and is therefore not directly relatable to failure in statically loaded structures where fracture is initiated at a sharp crack. The realization of this limitation has lead to the development of fracture tests which can be directly related to structures and which can be used as a basis for design against fracture.

Fracture mechanics attempts to develop small scale tests which accurately model the actual structural situation, so that the fracture toughness and the resulting defect tolerance of a material can be meaningfully established. It is beyond the scope of this review to discuss in detail the vast amount of material published on fracture mechanics. Instead, it is intended to assess the various techniques available for measuring embrittlement so that a suitable laboratory test can be selected. More comprehensive treatments of fracture mechanics in general are available in the literature. (58, 59).

There are two main approaches to the fracture problem, the first considers the arrest of a propagating crack while the second considers the possibility of crack initiation from a pre-existing defect. The former approach has been developed by Pellini et al., and is based on the analysis of dynamic tear test (DT) results and is fully described in the literature (60, 61). In this test,a full thickness specimen containing a sharp notch is impact loaded. As most ferritic materials exhibit a brittle to ductile transition with increasing temperature, the tests are conducted over a range of temperatures spanning the required service range and the energy absorbed in fracture and the area of the shear lips,as a percentage of thickness, are measured. A material is deemed suitable for a given application if the operating range corresponds to the high energy absorbing upper shelf. Dawes determined dynamic tear curves for twelve low alloy weld metals and found that the normal operating range (-20° to +20°C) fell in the transition region of the curves as shown in Figure 9. (2). Wide plate tests were also performed on these weld metals. In this test a 900mm. square plate which contains a notched weld is loaded in tension at the desired temperature until fracture occurs. A full penetration weld is used which contains a sawn notch of varying geometry. (2). The wide plate tests performed on the weld metals which had shown transitional behaviour over the desired operating range in the DT tests, showed that fracture occurred before general yield and that continued crack propagation occurred once a crack was initiated. The weld metals tested were representative of toughness levels currently available, and it was concluded that they were insufficiently tough to be amenable to the fracture propagation design approach. (2). Alternatively, the fracture initiation approach can be used to relate fracture initiation to crack length and applied stress,despite the fact that the desired operating temperature is in the transition range,and therefore provides a means of fracture design for weld metals at the toughness levels currently available.

2.4.2 Linear elastic fracture mechanics

The crack initiation approach relates variations of load and deformation to some characteristic measure of the resistance of a material to fracture. It assumes that fracture occurs when a critical level of the parameter which characterizes the stress and strain environment at the crack tip is reached. The theory is well established for materials which behave in a linear elastic manner up to fracture. Local plasticity at the crack tip is recognized, but the approach is valid provided the local plastic zone at the crack tip does not significantly disturb the elastic stress field. Irwin (62) showed that, for a centre cracked, infinite plate, the stress intensity factor K is given by:

$$K = \sigma \sqrt{\pi \bar{a}}$$

where σ is the stress and $\bar{a}$ half the crack length. Fracture occurs at a critical value of K which varies with stress state and reaches a minimum under plane strain conditions denoted by K_{1C}.* This parameter can be determined in a laboratory test on a relatively small specimen. The specimen, which contains a fatigue crack, is loaded in tension or bending until fracture occurs and the fracture load is used to calculate K_{1C}. The general layout of typical testing apparatus is shown in Figures 15 and 16, although this particular rig was used for COD testing. Plane strain fracture toughness testing has been standardized with certain restrictions to ensure plane strain validity specified as:

$$(a, B) > 2.5 \left(\frac{K_{1C}}{\sigma_y}\right)^2$$

---

*Fracture mechanics symbols used in this chapter and also Chapters 3 and 5 are listed in Appendix 1.

where a is the crack length, B the specimen thickness and σ_y the yield stress. (63, 64, 65).

Once K_{1C} is determined for a given material, the parameter can be substituted in the general design equation to obtain critical crack lengths for a given working stress.

$$K = \text{const. } \sigma \sqrt{\pi a}$$

The constant is a function of crack geometry and values for different geometries have been proposed. (66). Knowledge of critical crack lengths can then be used as a guide to the suitability of a material and as a criterion for defect acceptability.

In most structural steels and weld metals, the validity criteria for plane strain K_{1C} measurements are not met due to excessive crack tip plasticity. General yielding fracture mechanics has been developed to extend linear elastic concepts to yielding materials, the two principal approaches being crack opening displacement, COD and the recently suggested "J" contour integral.

2.4.3 Crack opening displacement

Crack opening displacement (COD) theory postulates that crack opening, δ, can be used to characterize the stress strain field at the crack tip in a material where excessive plasticity precludes elastic analysis. The strip yield model has been developed to relate applied stress, crack length and COD at the crack tip for an infinite, centre cracked plate. (67).

$$\delta = \frac{8\,\sigma_y\,a}{\pi\,E} \;\ln\sec\left(\frac{\pi\sigma}{2\sigma_y}\right)$$

This model only applies up to yield stress, but beyond nett section yield, all displacements applied at the ends of the plate appear as a displacement between the crack surfaces. (67). This enables COD to be related to crack size well beyond the local yield stress, a situation encountered in high residual stress fields and around stress concentrations.

COD theory predicts that fracture occurs at a critical COD value, δ_c and hence the possibility exists for measuring δ_c on a small, full thickness test piece which breaks well after general yield and using this value to predict the failure stress of a large structure which breaks before general yield. This is the basis of the design approach suggested by Harrison et al., (68) and subsequently modified by Burdekin and Dawes (66), Egan (69) and Dawes (2).

The COD at fracture , δ_c is determined in a laboratory test by loading a cracked specimen in bending or tension and plotting load versus crack opening. The latter is not measured directly, but is obtained by converting the crack mouth opening V, measured with a clip gauge, to the crack tip opening. Specimen configuration, loading geometry and clip gauge can be seen in Figure 16, and Figure 19 shows typical schematic load - clip gauge opening curves obtained in COD tests. Once the COD at fracture, δ_c is determined, the critical crack size for the material operating at a given stress level can be calculated by reference to the Welding Institute's design curve shown in Figure 10. Here non-dimensional COD is plotted versus applied strain and if δ_c and the relevant applied strain are known, then the critical crack size $\bar{a}$ is obtained by calculation.

The design curve has been developed using both the strip yield model previously mentioned, and by using wide plate tests to obtain the actual variation of δ with varying crack lengths, $\bar{a}$ and applied stress. The reliability of the design curve has also been tested using wide plate tests where a weld containing a given defect length is loaded to fracture and the resulting fracture stress used to calculate the predicted critical crack length. These tests showed that the design curve gave conservative estimates of the critical crack size by factors ranging from 1.3 to over 4. (2).

Turner and Burdekin have reviewed general yielding fracture mechanics (59) and note a number of objections to the approach, principally that the experimental results do not follow the crack length/gauge length dependence suggested by the strip yield model. This is thought due to plane strain conditions dominating at crack initiation, whereas the strip yield model assumes plane stress. The observed departure has also been attributed to strain hardening at the crack tip.

Another major problem is that slow crack growth is often observed prior to instability in a COD test. It has been shown that δ_i, the COD at crack initiation is substantially independent of specimen thickness when crack growth is by microvoid coalescence. It is suggested that this reflects a "material property" more realistically than δ_m, the COD at maximum load which varies with thickness. (70). The Welding Institute's design approach assumes fracture on a rising load curve and does not consider slow crack growth. It must be noted that δ_i values can be an order of magnitude lower than δ_m values and therefore predict a much lower defect tolerance which may be over conservative. This is one issue yet to be clearly resolved.

Smith and Knott have demonstrated that δ_i and δ_m are strongly dependent on initial notch width, and it is for this reason that COD testing recommendations require a fatigue crack. This gives lower values of δ_i and δ_m than those determined from machined notches. (71). Most of the data used to formulate the Welding Institute's design approach has been based on machined notches and hence the use of fatigue crack results again reduces apparent defect tolerance.

There are therefore, a number of problems associated with the use of COD data in design which are yet to be resolved. This particularly applies to the relationship between slow crack growth and final instability in a real structure.

2.4.4 The "J" contour integral

The J contour integral has been proposed by Rice in an effort to characterize the elastic plastic stress field around a crack. (72). The derivation is based on determining the change in potential energy when a crack is incrementally extended. Rice showed that this energy term was equivalent to a path independent line integral around the crack. The derivation is based on non-linear, elastic behaviour, and it has been pointed out that the energy concept does not apply to a real elastic-plastic material after general yield where a significant amount of energy is dissipated as plastic work and is therefore not available for crack extension. Finite element analysis has shown that it does, however, retain its path independence after general yield, and so while its physical significance is lost, it does continue to characterize the stress-strain field. (59).

Finite element analysis has also verified the path independence of J for a range of different geometry and loading conditions (73), and has enabled the area under a load/load point displacement curve to be directly related to J. (74). This method has been further modified to enable J to be estimated directly from load/clip gauge traces enabling δ and J to be determined from one trace. (75, 76).

J is equivalent to the elastic energy release rate G in the linear elastic range and is therefore related to K.

$$J = G = \frac{K^2 (1 - \nu^2)}{E}$$

Because J is path independent, J_c at fracture can therefore be determined from a specimen beyond general yield and be used to calculate K_c for an elastically loaded structure which in turn is used to calculate critical crack sizes from:

$$K = \text{const.}\ \sigma\sqrt{\pi a}$$

This then enables J to be used to calculate defect tolerances (75, 77).

Very little work seems to have been done to establish the validity of J_c as a critical fracture parameter. Egan has shown that J_c varies with temperature in a similar manner to δ_c using compact tension and two bend geometries. (78). Begley and Landes (79) determined J_c for two materials using four specimen configurations and found that J_c was substantially independent of specimen thickness and configuration although these results have been criticized because they did not consider slow crack growth prior to instability which would invalidate the results. (59). The problem of slow crack growth was identified in more recent work and a method for J_c testing has been proposed using several specimens to extrapolate J versus crack extension back to zero growth giving a J_c value. Plane strain validity limits have been proposed requiring $B > 25 \frac{J_c}{\sigma_y}$. (80).

2.4.5 J_c and δ_c as fracture criteria

Finite element analysis has shown that J is a valid extension of linear elastic concepts, but similar treatments of δ have lead to problems in defining the exact COD analytically. (59, 73). J and δ are related by:

$$J = M \sigma_y \delta$$

the constant M being geometry dependent and varying between 1.15 and 2.1. Turner and Burdekin conclude that J can be more readily determined by computation because δ is not rigorously defined but neither concept is obviously incorrect. (59). There is a considerable amount of COD data available and as it has been used to formulate the basis of a design approach, the use of the COD criterion cannot be easily discarded. There appears to have been no similar linking of small scale J tests to large scale tests such as wide plate tests and the whole J_c fracture criterion has very limited experimental support at this stage. Additionally there appears to be no widely accepted J testing technique as opposed to COD where a standardized technique is available. (81). Further work will undoubtedly clarify the situation, but until then it appears that a dual approach measuring J_c and δ_c (δ_i and δ_m) is desirable.

A relevant point was made by Harrison, who concluded that J, δ and K, corrected for plasticity, showed the same variation over a number of different materials and that they were obviously interrelatable. He concluded that it was possibly more important to determine how these parameters should be used to relate small specimen behaviour to fracture in engineering structures, than to decide which parameter should be determined in a laboratory test. (82).

This survey has highlighted some of the difficulties encountered in attempting to quantify fracture behaviour, and it cannot yet be said that the use of general yielding fracture mechanics is a straightforward laboratory procedure. In the work on weld metal embrittlement described in Chapter 3, the use of the Charpy test was retained because it requires minimal specimen preparation and testing facilities. COD testing was also performed and from these results, values of J were calculated. The accumulation of fracture mechanics data was important for two reasons. Firstly, it would show if the embrittlement behaviour shown in Charpy tests was accurately reflected under conditions of slowly applied load in the presence of a sharp notch. Secondly, and perhaps more importantly, a fracture mechanics analysis can be used to quantify the amount of embrittlement. Using Charpy data alone, weld metal embrittlement may well be detected, but it is difficult to establish if it is significant as it cannot be directly related to structural performance.

CHAPTER 3 EXPERIMENTAL - HEAT TREATMENT VARIABLES AND EMBRITTLEMENT

3.1 Introduction.

The aim of the investigation was to establish if the three weld metals, Bostrand 31, Linde 120 and AX140 were embrittled by post weld heat treatment, to define the effects of heat treatment variables on the severity of embrittlement and to identify the causes of embrittlement. The experimental strategy adopted was to use extreme heat treatment conditions to cause a large amount of embrittlement so that the cause of embrittlement could be readily identified. Once embrittlement was observed, further tests could be used to define more fully the effects of the heat treatment variables. If the embrittlement conditions could be defined then post weld heat treatment cycles designed to avoid embrittlement could be established, or alternatively, if the embrittlement mechanism could be positively identified then appropriate compositional modifications could be suggested. In this chapter, the effects of heat treatment variables on embrittlement severity are examined, while the metallographic examination of the embrittlement mechanisms is considered in Chapter 4.

The literature has indicated that both precipitation of alloy carbides and classical temper embrittlement may contribute to weld metal embrittlement. Both of these embrittlement mechanisms can be expected to be dependent on time and temperature. Precipitation of alloy carbides can be considered in terms of an ageing curve where, for a given time, a peak is observed in a plot of hardness versus treatment temperature. Increasing treatment time tends to increase the peak height and move it to lower temperatures. This behaviour is consistent with the variation of the diffusion coefficients of carbon and the precipitating alloying elements with temperature. Maximum embrittlement can be expected to be coincident with peak hardness. (31). The degree of temper embrittlement will also be dependent on time and temperature with embrittlement being sluggish at low temperatures because of the low diffusivity of the responsible impurities, while at high temperatures, the impurities are dispersed from the grain boundaries. Embrittlement from each source can therefore be expected to be at a maximum over a specific temperature range, and to increase with time. The initial experimental design was based on establishing this range. Short and long time treatments were used to assess the time dependence of the embrittlement with 1 hour being selected for the short treatment as it is the minimum post weld heat treatment time usually used. A long time treatment of 50 hours was selected which would clearly indicate any embrittling tendencies, even though it was well in excess of times used in industrial practice. The initial treatment temperatures were 450°, 550° and 650°C for times of 1 and 50 hours. The Charpy results from these treatments suggested further treatments to define embrittlement conditions more closely. These consisted of varying times at 550°C and the use of a slow cooling rate, but these can be best understood when discussed in terms of the earlier results. Full treatment details are therefore left to the results section. Before they are examined, the materials used and the experimental methods adopted will be reviewed.

3.2 Materials

The three weld metals examined were Bostrand 31, Linde 120 and AX140 which were deposited using the submerged arc process and a fully basic flux, OP41TT. The welds took the form of full penetration double "V" butt welds in 50mm. plate with HY80, HY100 and HY130 plate material being used respectively. All welding was carried out by the staff of NCRE* and the welded panels were supplied in the as deposited condition. The panels were initially 300mm. wide and 700mm. long. Details of the weld preparation and a macro of a typical weld section are shown in Figure 11. The welding details are shown in Table 2 and can be summarized as follows. A constant wire size of 1.6mm. was used for each material with a constant heat input of 1.18 KJ/mm. An additional panel of Bostrand 31 was supplied with a heat input of 3.15 KJ/mm. The flux was baked at 400°C for 2 to 3 hours immediately prior to use and a preheat of 120°C with a maximum interpass temperature of 150°C was employed for each material.

The chemical analyses of the weld metals, wires and plates are given in Table 1. Weld metal analysis was performed using both vacuum spark emission spectroscopy and conventional chemical techniques and values are appropriately marked. Analysis was performed on weld metals in the low dilution region only. Nitrogen and oxygen were determined by vacuum fusion, with nitrogen additionally being determined chemically.

3.3 Experimental methods

3.3.1 Specimen location

All Charpy and COD specimens were extracted from the low dilution region of the weldment as shown in Figure 12. The specimens were located as close to the plate surface as possible, with the notch in the fracture specimens perpendicular to the plate surface, so that

---

* Naval Construction Research Establishment, Dunfermline, Fife, Scotland.

the direction of crack propagation was parallel to the longitudinal weld axis. There was one exception to this location for COD specimens. To assist with development trials on the COD testing rig, COD specimens were cut from a Bostrand 31 panel supplied for Charpy specimens. The panel had been sawn to size and the specimens were extracted with the main specimen axis parallel with the weld axis, so that the notch was normal to the plate surface but crack propagation occurred transverse to the longitudinal weld axis. These Bostrand 31 specimens were known as the "B" series.

All tensile specimens (Hounsfield No. 12) were extracted from the low dilution region with the tensile axis transverse to the longitudinal weld axis.

Dawes has indicated that the least tough region of a butt weld is the high dilution region at the weld root and has recommended that this region should be assessed in determining the limiting fracture parameters of a weld. (83). This study examined the low dilution region only because it meant that the maximum use of available weld metal could be made and because compositional variation along the bead would be minimal. In the weld root, the amount of parent plate dilution would be expected to vary depending on the final geometry of the back gouged groove and the weld bead placement. This in turn would cause higher scatter in the fracture results with some associated uncertainty in the composition of individual specimens. Additionally, as this investigation was a study of weld metal embrittlement, the results from the low dilution region would give a realistic upper bound to the fracture behaviour expected from the weldment as a whole.

3.3.2 Heat treatment

All specimens were heat treated as sawn blanks and final machining was carried out after heat treatment to ensure the removal of any oxidised or decarburized material. All heat treatments were carried out using an air circulating furnace. The absolute temperature and temperature gradients in the furnace were measured using a calibrated thermocouple connected to a digital thermometer and were found accurate to within ±5°C, with temperature variation over a 50 hour period being less than 2°C. All specimens used to examine the effects of time and temperature on embrittlement were water quenched directly from treatment temperature. The treatment time was measured from the time the specimen attained the required treatment temperature. A cooling rate of 100°C/hour was used to examine the effects of cooling rate and was generated by stepping the furnace controller down 50°C every half hour giving the required mean cooling rate.

3.3.3 Charpy testing

All specimens were machined after heat treatment to give final dimension in accordance with standard practice. (84). Specimens were fractured in an Avery testing machine and the results were used to give energy absorbed versus temperature plots. As the majority of tests were at non-ambient temperatures, an end setting jig was manufactured so that specimens could be accurately positioned on the test anvil and fractured within 5 seconds of being removed from the low or high temperature bath. Specimens tested at sub-ambient temperatures were cooled in an insulated alcohol bath using solid CO_2 as a coolant. Bath temperatures were monitored using an alcohol thermometer.

3.3.4. Analysis of Charpy curves

A conventional Charpy curve can be divided into three regions; a low energy absorbing shelf at low temperatures, a high energy shelf at high temperatures and a transition range between the two. The literature survey indicated that upper shelf fracture is controlled by the volume fraction of inclusions, the inter-inclusion spacing and the work hardening exponent of the material. Heat treatment will not alter the first two factors, but may affect the third. The position of the transition range is a measure of the temperature dependence of the materials resistance to low energy fracture modes such as cleavage. A tough weld metal accordingly displays upper shelf behaviour to low temperatures where the transition to a low energy fracture mode occurs, whereas a less tough weld metal with a similar inclusion distribution may give the same upper shelf level, but will have a transition to a low energy mode at much higher temperatures. The two weld metals can then be compared by the difference in position of the transition range. Similarly, a measure of embrittlement is made by determining the position of the transition range after a given treatment and comparing it with the position of the transition range in the as deposited condition.

Charpy curves are usually presented as a basically free hand curve through the determined points. This is fairly satisfactory for wrought materials where the scatter is low, but in weld metal testing a high degree of scatter is observed and the free hand procedure becomes less satisfactory. There is also a tendency for the curves to be presented without the experimental points giving no indication of scatter. (7). If a large number of specimens are tested a sigmoidal scatter band would be obtained. The scatter is derived from two principal sources, the first being experimental factors such as variations in notch acuity, accuracy of positioning in the test fixture and, accuracy of determining the test temperature and energy absorbed. The second source of scatter is the inhomogeniety of the structure being tested, the principal variables being the relative volumes of columnar and refined structure at the notch root and the orientation of the columnar grains.

This can be illustrated by reference to Figure 13 which shows the full face of a Bostrand 31 Charpy specimen with the notch running down the left-hand vertical edge. The top two thirds of the notch is sited in columnar grains, while the bottom third is in refined structure. If the run placement had been different, there would have been different proportions of columnar and refined structures, for example, at position A, which has a higher refined content, or position B, which has a lower refined content. A batch of Charpy specimens used to obtain a single transition curve can be expected to contain a similar range of structural variations at the notch root and there is, accordingly, a source of scatter built into the test.

To deal with the problem of scatter, the following procedure was adopted. The transition range of the Charpy curve was approximated to a straight line, the position of which was located by determining the regression line for the points falling in the transition range. Any point which was obviously on the upper or lower shelf was discarded. The inclusion or exclusion of points at the top of the transition range which may have in fact been on the upper shelf did not alter the position of the line significantly. This procedure enabled a consistent approach to be adopted in determining the position of the transition range, rather than the arbitrary drawing of a free hand curve which is prone to experimental bias. Similar methods to that outlined have been used elsewhere. (85).

The availability of weld metal was limited and it was not possible to use a large number of specimens for each Charpy curve. The advantage of using large numbers of specimens would be questionable because the results would be prone to the same scatter sources and it was felt that the improvement in precision would be small. It was also considered that a high degree of precision was not as important as obtaining a reliable comparison between the various heat treatments. A minimum of 7 specimens was used to determine points in the transition range and the regression equation and correlation coefficients were calculated.

The degree of embrittlement may be defined as the shift in the transition range after a particular treatment. In this study, the shift was measured in terms of the 55 joule (40ft/lb.) energy absorbed temperature (T_{55J}). When this was plotted versus treatment temperature, it showed the transition range shift for a given treatment and also gave an indication of the absolute toughness so that direct comparison with other weld metals could be made. A typical plot is shown in Figure 25. The selection of the 55 joule level is relatively arbitrary, although it is convenient as it is 1/3 to 1/2 of the upper shelf level of the weld metals. This is not a particularly important issue because the transition regression lines are presented in the results section and if other energy absrobed levels are required, they can be simply acquired from the plots. In general, these will give the same relative toughness rating because the transition curves are reasonably parallel. Varying slope will only cause a different rating when the regression lines are closely bunched, which indicates that differences in absolute toughness are small anyway. It will also be noted on the T_{55J} versus treatment temperature plots, that straight lines have been used to join individual datum points when in fact the true behaviour would be more accurately represented by a smooth curve. Straight lines have been used to indicate that no information was acquired for the intermediate regions and the straight line approximates the expected trend.

The T_{55J} plots (for example, Figure 25) also include the 90% confidence limits of T_{55J} which in some cases appear to be large, spanning up to ±13°C. This scatter was primarily due to structural variation at the notch root as previously discussed, and is magnified because the confidence limits represent a horizontal section across the transition curve. The 90% confidence limits were calculated on the basis of the method suggested in reference 86. The sample variation of y on x (energy absorbed on temperature), $S_{y/x}$, was determined for each transition curve from the residual sum of squares.

$$S_{y/x}{}^2 = \frac{\Sigma(y_i - a_o - a_1 x_i)^2}{n - 2}$$

where $y = a_o + a_1 x$

n - number of tests

y - energy in joules

x - temperature in °C

a_o - coefficient

a_1 - coefficient

As a confidence limit on temperature was required, the confidence limits for y (energy) were calculated and divided by the slope of the curve a_1. The 90% confidence limits were therefore given by:

$$\pm\, t_{(90\%,\ n-2)}\ \frac{S_{y/x}}{a_1\sqrt{n}}$$

Values of $t_{90\%,\ n-2}$ were taken from tables of percentage points on the "t" distribution.

3.3.5 COD testing

3.3.5.1 Specimen size

British Standards draft for development D.D.19 was used as a basis for COD testing. (81). The symbols used in D.D.19 are consistent with those used in the literature and have been adopted in this work. All fracture mechanics symbols are listed in Appendix 1.

D.D.19 recommends a preferred geometry specimen defined as:

$W = 2B$, $a/W = 0.5$, $S = 4W$

where W - specimen width
B - specimen thickness
a - crack length
S - span between supports in 3 point bending.

The specimen should be of full plate thickness and contain a fatigue crack.

It was considered that full thickness tests were impractical due to the prohibitive material requirement and because it was doubtful if the available machine capacity of 50 KN would be sufficient to fracture the specimens. The disadvantage of testing less than full plate thickness specimens was somewhat offset by the possibility of determining δ_i, the COD at crack initiation. Full thickness tests are recommended because δ_m, the COD at maximum load, decreases with increasing thickness. Smith and Knott (70, 71) have explained this variation in terms of crack initiation and growth. When crack growth is by microvoid coalescence, δ_i, appears to be independent of specimen thickness. Crack growth begins in the centre of the specimen where stress triaxiality is highest and as crack growth proceeds, the uncracked outer ligaments work harden, carrying some of the total load. Final instability at δ_m occurs when the change in specimen load carrying capacity due to the extending central crack more than offsets the increasing load carrying capacity of the outer ligaments. The thickness of the outer ligaments was found to be relatively constant at 2mm. and so as the total specimen thickness increases, the relative load carrying capacity of the uncracked regions diminishes and δ_i approaches δ_m. The detection of δ_i in the present work could therefore be reasonably expected to give a thickness independent fracture parameter, at least in the upper shelf region of the curve.

The situation is less clear in the lower shelf region where fracture occurs by cleavage on some other low energy mode. Knott (58) has shown that while sufficient triaxiality may exist in a specimen to give a macroscopically flat fracture, the principal tensile stress may not have reached its limiting plane strain value and further increases in thickness may lower the fracture stress. Less than full thickness specimens could therefore overestimate lower shelf fracture parameters but at least they will give an upper bound value and any indications of embrittlement observed in thin specimens can be confidently expected in full plate thickness specimens.

A specimen thickness of 10mm. was selected as it allowed economical use of material and could be fractured with the available machine capacity. As it was the same thickness as the Charpy specimens it meant that the same order of scatter due to microstructural variation at the notch tip could be expected. This point is also relevant to the discussion of the relative merits of full thickness testing. In section 3.3.1 it was stated that the test criterion was the study of embrittlement in low dilution weld metal only. If full thickness tests had been carried out then the full joint, including the possibly less tough high dilution root area would have been tested which would have made direct comparison of the COD and Charpy results less valid. The principal specimen dimensions are shown in Figure 14. The machined notch was 6mm. deep which was extended by fatigue cracking to 10mm. to give a final a/W of 0.5.

3.3.5.2 Fatigue pre-cracking

D.D.19 recommends that COD specimens should be fatigue cracked as δ_i and δ_m are known to increase with notch width (71). All fatigue cracking was carried out on an Amsler Vibraphore with a 20 KN capacity. The fatigue crack was nucleated from a sharp machined V notch with a typical radius of 0.05mm. While cracks were readily nucleated, they did not usually grow with the crack front normal to the specimen surface, even in apparently stress relieved specimens. The growth of non-uniform fatigue cracks has been observed in full thickness as deposited weld metals and has been attributed to residual stresses. Dawes has recommended a mechanical stress relieving treatment to overcome the problem which entails locally compressing the material at the notch tip to just beyond yield stress. The residual stress pattern so formed enables straighter fatigue cracks to be grown without affecting the COD determined. (87). A

10mm. diameter punch was used to compress the material at the notch tip on one side only. The compression load P was determined from the relation:

$$P = 1.4\ B^2\ \sigma_y$$

σ_y - weld metal yield stress.

Reduction in specimen thickness was typically 0.3 - 0.6%. The compression technique enabled much straighter fatigue cracks to be grown and reduced specimen wastage to reasonable levels.

The maximum load used to initiate a fatigue crack was 8 KN which was progressively decreased and the last 1mm. was grown at loads of 3.6 KN which gave a fatigue stress intensity factor, K_f, of 27 $MN/m^{3/2}$. D.D.19 recommends that the fatigue stress intensity should not exceed the plane strain limit given by:

$$K_f < 0.63\ \sigma_y\ B^{\frac{1}{2}}$$

The lowest yield stress of any material tested was 648 MN/m^2 which gave a limiting K_f of 40.8 $MN/m^{3/2}$, so that the fatigue stress intensity used (27 $MN/m^{3/2}$.) was only 2/3 of the limiting value and was therefore also valid for K_{1C} testing. The loading frequency was 110 cycles per second and cracking took approximately 20 minutes per specimen.

All crack lengths were measured on a projection microscope after COD testing and the results were rejected for any specimens containing cracks outside the limits $0.45 < a/W < 0.55$ and having greater than 5% curvature.

3.3.5.3 COD test rig

All COD testing was carried out on a 50 KN "Mand" servo hydraulic testing machine. In this machine, load is applied by a hydraulically loaded actuator which is controlled by a servo valve in a closed loop feedback circuit. Control is achieved by comparing a command voltage with a signal from the machine (load or position) and the servo valve drives the actuator until the signals are balanced. A constand load point displacement rate is achieved by generating a steadily increasing command voltage using a motor driven potentiometer and comparing it with the voltage from a displacement transducer mounted on the actuator. As the command voltage is steadily increasing, the actuator is driven up and various displacement rates are obtained by varying the speed of the motor driven potentiometer. A displacement rate of 1mm./minute was used for all tests.

While this system is ideal in theory and provides a high stiffness loading system, considerable problems were encountered with the Mand machine. These were manifest as large and random rapid movements of the actuator which were caused by electronic noise emanating from a number of sources. Considerable time was spent tracing and reducing these noise levels and the author is of the opinion that if this type of control system is to be used, considerably more attention needs to be devoted to the quality and stability of the feedback circuits as noise entering at any point can cause actuator movement.

Specimen bending was carried in a three point bending rig designed to comply with D.D.19. Specimen loading was through floating 10mm. rollers which were electrically insulated from the rest of the rig. While only one specimen geometry was to be tested, the fixture was designed to be adjustable using a method suggested by NCRE so that preferred geometry specimens up to 25mm. thick could be tested. All specimens tested at sub-ambient temperatures were fractured in an insulated alcohol bath cooled with solid CO_2 additions. Temperature was monitored by a chromel alumel thermocouple spot welded to the specimen immediately beside the fatigue crack tip. Bath temperature was also monitored with a thermometer and the observed temperature difference did not exceed 2^oC. Specimens were held at temperature for a minimum of 5 minutes prior to testing and temperature drift during a test was less than 2^oC. A general view of the testing machine and instrumentation is shown in Figure 15 and a close up of the bending fixture showing specimen location, thermocouple and potential drop leads is shown in Figure 16.

3.3.5.4 Clip gauge linearity and drift

COD measurements were determined from clip gauge openings, the clip gauge being mounted across the crack on two knife edges screwed to the specimen as shown in Figure 16. The clip gauge used four 300ohm strain gauges connected in a bridge network, the signal from which was amplified and fed to an X-Y recorder where it was plotted versus load to give a load/clip gauge opening or, P/V curve.

The clip gauge was linear over the range 8.8 to 10.5mm. which was well in excess of the testing range required. A constant initial knife edge spacing of 8.9mm. was used for all tests. The low temperature clip gauge drift at -60^oC was found to be 0.005mm. over a 5 minute period. The testing procedure was such that the clip gauge was only placed on the knife edges after temperature stabilization, and the test immediately commenced,and the drift over the testing time of typically 3 minutes, was considered negligible.

3.3.5.5 Calculation of COD

The critical COD (δ_i or δ_m) was determined by converting the clip gauge opening to COD at the notch tip using the Well's equations (81), the accuracy of which have been confirmed by various workers using finite element analysis (73) and by experimental observation (88). The equations can be expressed as follows:

$$\delta = \frac{0.45\ (W-a)}{0.45W + 0.55\ a + z}\left(V - \frac{\Upsilon\sigma_y\ W(1-\nu^2)}{E}\right) \ldots\ldots \quad (1)$$

where $V \geqslant \dfrac{2\ \Upsilon\sigma_y\ W(1-\nu^2)}{E}$

$$= \frac{0.45\ (W-a)}{0.45W + 0.55\ a + z}\left(\frac{V^2 E}{4\Upsilon\sigma_y\ W(1-\nu^2)}\right) \ldots\ldots \quad (2)$$

where $V < \dfrac{2\ \Upsilon\sigma_y\ W(1-\nu^2)}{E}$

V - clip gauge opening

V_i - " " " at initiation

V_m - " " " at maximum load

z - knife edge height

E - Young's modulus

ν - Poisson's ratio

Υ is a non-dimensional function of a/W and values are tabulated in D.D.19. COD was calculated using a programable desk top calculator. Values of a, σ_y and V (either V_i or V_m) were fed into the program and Υ was calculated for the given value of a/W by interpolation between the values given in D.D.19. The program then calculated $\dfrac{2\ \Upsilon\sigma_y\ W(1-\nu^2)}{E}$, compared it with V and selected the appropriate equation to calculate δ, the print out indicating which equation had been used.

The value of yield stress used in the equation was that determined at 20°C, but should strictly have been determined at the test temperature in question. This means that for sub-ambient tests, the calculated COD was above that which would have been determined if the increase in yield stress with decreasing temperature was considered. The magnitude of the error was calculated and found to be insignificant at temperatures down to -75°C, the lowest test temperature used, and this error source was ignored. The calculations are shown in Appendix 2.

As a check that the calculations were giving a fair estimate of the actual COD, four specimens of Bostrand 31 with the notch transverse to the weld axis, (the "B" series) were loaded to points before and just after crack initiation, unloaded and the final clip gauge opening was used to calculate the plastic component of the COD. This was compared with the value measured on the specimen surface using a projection microscope. The measured and calculated values are listed in Table 3 and show reasonable agreement. The error range of the measured value is due to uncertainty in locating the exact corner of the fatigue crack/plastic opening junction.

3.3.5.6 Determination of COD at initiation-δ_i

There are two methods of determining δ_i. In the first method, specimens are loaded to increasing values of V, unloaded and heat tinted. The specimens are then fractured at low temperatures and the crack growth revealed by heat tinting is measured. Crack growth is then plotted versus V and the curve extrapolated to zero crack growth to give a value V_i from which δ_i is determined. While the method gives an unambiguous estimate of δ_i, it was not used in this work because it would have prohibitively raised the number of specimens required. Additionally, weld metals contain significantly variable structures at the notch root and it was unreasonable to expect the form of the P/V curve to be sufficiently similar from specimen to specimen to enable valid extrapolation.

The alternative potential drop technique was used which theoretically enabled a δ_i value to be obtained from one specimen. This technique utilizes the phenomenon that the resistance to current flow in a specimen increases with crack growth. A constant current is passed through the specimen and the voltage between two probes attached on either side of the notch is plotted versus V. When crack initiation occurs, there is an inflection in the potential trace which defines V_i and hence δ_i. The method has been fully described in the literature (81, 89) and has been reviewed by Holder. (90).

A feedback controlled, constant current source was used to give a current density of 0.1 Amp/mm^2 at the notch plane and voltage was measured across two probe wires spot welded diagonally across the notch. A millivolt source was placed in series with the probe wires to back-off the voltage generated across the crack so that the small voltage changes due to crack growth could be amplified. A DC amplifier with a gain of 10^5 amplified the signal which was fed onto the Y axis of an X-Y recorder to give a final sensitivity of 0.4 microvolt per mm. Potential was plotted against clip gauge opening V. Potential was measured across platinum probe wires soldered to heavy gauge copper leads which were twisted together to minimize noise. With the probe wires shorted out, the noise level was ±0.5 microvolt, this being mainly 50 cycle hum from the DC amplifier. Current was carried to the specimen by heavy gauge copper wires screwed to the specimen to give a constant contact resistance. The location of the current carrying leads and voltage probe wires can be seen in Figure 16.

Early trials, especially with the specimens immersed in the cooling bath, revealed excessive voltage drift which was traced to thermocouple voltages generated at the probe-specimen junction. The platinum probe wires were replaced by iron wires and the specimen relocated such that the surface of the specimen was 1mm. above the bath, so that coolant movement could not cause variations in the junction temperature. Although this considerably improved the stability of the signal, the system was still subject to random drift of ± 3 microvolts over 10 - 20 seconds which was thought due to instabilities in the power supply. Continual adjustment during the testing program did not satisfactorily resolve the problem and while some traces were drift free, others had to be discarded.

The other major problem encountered was relating the potential/V trace to the P/V trace. The basis of the method is the detection of a change in slope in the potential/V trace, where potential is thought to vary linearly with V until crack growth occurs. A factor which also causes a change in potential is the growth of the plastic zone from the notch across the specimen. This was also thought to cause an inflection in the trace and consequently there were two inflection points, the first occurring around general yield and a second corresponding to crack initiation. This was particularly noticeable with Linde 120 when fractured in the upper shelf region.

During early trials using Bostrand 31, some specimens were fractured just after general yield and after an observed inflection in the potential/V trace and no crack growth was detected. To overcome this problem, δ_i was defined as the last inflection before maximum load. A trace showing this double inflection is shown in Figure 18. This phenomenon has also been reported elsewhere. (91).

The ease of detection of δ_i was also dependent on the material. This is best illustrated by reference to Figures 17 and 18 where it can be seen that as deposited AX140 has a very peaked P/V curve and where crack initiation was detected just before maximum load giving a large inflection. The rapid decrease in load was indicative of rapid crack growth as the potential/V trace indicates. The behaviour of Linde 120 and to a lesser extent, Bostrand 31 was markedly different. The P/V curve was very flat with a gradual climb to maximum load, followed by an equally gradual decrease and few specimens actually fractured within the clip gauge range. If the potential trace was sufficiently stable to detect initiation, a very small inflection was observed; this was consistent with the gradual decrease in load indicating very slow crack growth and hence crack initiation was very difficult to detect. The few satisfactory potential traces obtained for Linde 120 indicated that crack initiation preceded maximum load by a small amount.

The detection of δ_i under conditions of slow crack growth was considered to be the least satisfactory aspect of the work, and the author is of the opinion that further development of the potential drop technique is required before it can be used to give reliable estimates of δ_i. Similar reservations have been voiced elsewhere in the literature. (58, 80). While attempts were made to detect δ_i in every test, results are only quoted in cases where the trace was sufficiently stable and where δ_i seemed clearly defined.

3.3.5.7 The "pop-in" phenomenon

A feature observed during the testing of some of the weld metals, particularly the 3.15KJ/mm Bostrand 31 weld and several embrittled welds, was the occurrence of small bursts of crack growth similar to the so-called plane strain "pop-ins" observed in K_{1C} testing. These were manifest as small steps in the P-V trace accompanied by a slight decrease in load, a simultaneous step on the potential/V trace and an audible "click". The bursts of crack growth could occur at COD values as low as 10% of the maximum load COD (specimen H1/4). D.D.19 specifies the critical COD as that at which crack growth first occurs, so consequently the pop-ins were used to define δ_i in the absence of a previous inflection in the potential/V trace. It should be noted that the pop-ins were probably associated with a burst of crack growth and subsequent arrest while δ_i values imply the initiation of stable and continuing slow crack growth. For the purpose of a clear definition, the values of δ_i determined from a pop-in are clearly distinguished from those due to stable crack growth in the tables of results.

3.3.5.8 Determination of COD at maximum load - δ_m

The clip gauge opening at the highest load reached was used to determine δ_m. Where the maximum load reached a plateau indicating stable crack growth, the reading at the beginning of the plateau was used. Maximum load readings fell into three categories, fracture on a rising load curve, fracture on a rising load curve preceded by pop-ins and a maximum load plateau as shown in Figure 19. Fracture on a rising load curve is appropriately marked in the tables of results. A problem arose in deciding whether the bursts of crack growth which preceded fracture were significant, since the potential trace indicated that the crack had subsequently arrested and considerably higher loads were reached, suggesting that δ_m defined as the pop-in COD would give an unduly conservative estimate. As the size of the pop-ins varied a cut-off point was defined to classify the results. If the clip gauge opening accompanying a pop-in was less than 0.025mm. which corresponded to a COD of 0.0004mm., the pop-in was ignored and the maximum load reached was used to calculate δ_m. If the gauge opening was greater than 0.025mm., it was considered as δ_m. In most cases where this occurred, the final maximum load reached was only 10 - 20% higher than the pop-in load and while the magnitude of the discriminating pop-in size is arbitrary, it does reasonably reflect specimen performance. The issue of whether the pop-in COD or δ_m is more relevant in estimating defect tolerance is discussed in section 5.2.

3.3.6 Determination of the J contour integral

There were a number of alternatives available for determining J. Two possibilities entailed the use of published finite element solutions for preferred geometry three point bend specimens (2B = W, a/W = 0.5). Hayes (92) has evaluated the variation of J with load, but his solution was not used in this work because the fracture load variations were small and it was felt to be an insufficiently sensitive parameter. Sumpter (75) has evaluated the variation of J with clip gauge opening V for both plane strain and plane stress, assuming work hardening. While this conversion was not used directly, his results were used to calculate the variation of non-dimensional J with non-dimensional δ and the J values actually measured were superimposed on the plot for comparison.

The method adopted for J determination was based on Sumpter's derivation (75, 76) relating the area under a load - load point displacement diagram U_{P-q}, directly to J, which for the preferred 3 point bend geometry reduces to:

$$J = \frac{2\,U_{P-q}}{B(W-a)}$$

U_{P-q} - Area under load, load point displacement diagram.

The relation is not sensitive to small variations of crack length around a/w = 0.5 and therefore, the preferred COD geometry is ideal for calculating J. The COD testing provided a P/V trace and to convert the area under this trace to the equivalent P/q area (U_{P-q}) the relation suggested by Dawes was used where load point displacement is geometrically related to clip gauge opening V.

$$q = \frac{W(V-\delta)}{a+z}$$

$$\therefore J = \frac{q}{V} \quad \frac{2}{(W-a)B} \quad (U_{P-V})$$

$$= \frac{2\,W(V-\delta)}{BV(a+Z)(W-a)} \quad (U_{P-V})$$

The area U_{P-V} shown in Figure 19 was determined by measuring load coordinates on the P-V diagram and the area calculated on a desk top calculator by numerical integration. Because of the difficulties in obtaining unequivocal δ_i values for each test, δ_m values were used in the calculations. While this is reasonable for fracture occurring on a rising load curve, it meant that J was over-estimated for weld metals exhibiting stable crack growth. Some calculations were also performed for δ_i values at around 0°C, giving a lower bound estimate of J and these were found to be only slightly lower than those calculated using δ_m values. The values of J are shown in the results tables and will be referred to in more detail in the results section.

3.4 Hardness and tensile results

Hardness values were determined on low dilution samples of weld metal in the as deposited condition and after 1 and 50 hours treatment in the 450 - 650°C range. The hardness values plotted versus treatment temperature are shown in Figure 20. Each point is the mean of 10 readings on each sample.

The Bostrand 31 weld metal shows a strong secondary hardening peak at 610°C after 1 hour, with the degree of hardening increasing and the peak moving to 550°C after 50 hours. The peak hardness developed after 50 hours, 290 HV30, was slightly higher than the as deposited hardness of 283 HV30.

The Linde 120 did not reveal any secondary hardening peak after 1 hour with the hardness steadily decreasing above 550°C. A small peak was observed at 500°C after 50 hours with the hardness decreasing more rapidly above 550°C.

AX140 did not show a secondary hardening peak after treatment times of 1 or 50 hours. Hardness decreased rapidly above 550°C with the

50 hour treatment giving a consistently lower hardness.

The tensile results generally reflected the trends observed in the hardness results. Tensile data is presented in Table 4 which shows the means of duplicate tests. The yield to ultimate ratio is also stated which is a measure of the work hardening capacity of the material. The variation of yield stress with treatment temperature after 1 and 50 hours is shown in Figure 21 along with the minimum parent plate yield strength requirement. All materials gave clearly defined yield points except for the 650° - 50 hour treatments where yielding was continuous and the 0.2% proof stress was determined.

The yield stress for the higher heat input Bostrand 31 weld metal in the as deposited condition and after 50 hours at 550°C is included with the 1.18 KJ/mm heat input material.

Secondary hardening is again apparent in the Bostrand 31 material. While the yield stress was not as high after 50 hours at 550°C as the hardness results would suggest, there was a pronounced drop in elongation. The yield stress was well in excess of the design requirements up to 650°C.

The Linde 120 results did not reveal any significant secondary hardening, but showed a decrease in yield stress above 550°C. The 550°C, 50 hour yield stress was above the design requirement while the 650°C value was below it.

The yield stress of AX140 after 1 hours treatment was generally just above the minimum plate yield up to 550°C, after which it decreased.

The yield stress was consistently lower after the 50 hour treatment and fell below minimum plate yield above 450°C.

3.5 Charpy results

3.5.1 The effect of treatment temperature and time

The results of this part of the work are presented in a number of ways which require some explanation to avoid confusion. Basically, each weld metal was held at temperatures of 150, 450, 550 and 650°C for periods of 1 and 50 hours and were water quenched. The Charpy curves for the 1 hour treatment are presented on one plot while the curves for the 50 hour treatments are presented on a second plot. Each plot also includes the actual Charpy points so that a visual impression of scatter can be gained. The occurrence of four curves with points on one plot appears confusing, but the points are clearly distinguished and do enable direct comparison. The comparison is more clearly illustrated on a third plot where the temperature corresponding to 55 joules energy absorbed (T_{55J}) is plotted versus treatment temperature. This shows the shift in the transition range after treatment with the amount of embrittlement increasing as T_{55J} increases. All actual Charpy point co-ordinates are listed in Table 14. It will also be noted from the Charpy transition curves that some upper shelf levels are shown and these in turn show the Charpy points which were not used to determine the regression equation, as they were outside the transition range. Additionally, the three as deposited weld metal transition curves are plotted in Figure 22 so that direct comparisons between the weld metals can be made. These lines are also shown on the 1 hour treatment Charpy transition diagrams as a dotted line.

Bostrand 31 (1.18 KJ/mm)

Transition curves were determined after treatments at 150, 450, 550 and 650°C for 1 hour and 50 hours, the specimens being water quenched from treatment temperature. The 1 hour transition curves are shown in Figure 23 and the 50 hour curves in Figure 24. The regression equations, correlation coefficients and T_{55J} are listed in Table 5. Comparison between the treatments is shown in Figure 25 where treatment temperature is plotted versus T_{55J} for the two treatment times. This indicates that significant embrittlement occurs after 1 hour at 550°C with a further large increase after 50 hours. Embrittlement is also observed at 650°C after 1 hour, but there is a nett toughness improvement after 50 hours. This is consistent with the hardness results which indicated an increase in peak hardness and the peak shifting to lower temperatures with increasing time. The improvement in toughness after 50 hours at 650°C is consistent with the overageing observed on the hardness curve and in fact,upper shelf levels were achieved in the testing range. The elevation in upper shelf energy is attributable to the higher work hardening capacity shown by the tensile results.

Linde 120

The heat treatments used were identical to those for Bostrand 31 and the 1 hour and 50 hour transition curves are shown in Figures 26 and 27 with T_{55J} versus treatment temperature in Figure 28. The regression equations and correlation coefficients are shown in Table 6. Comparison with Figures 25 and 31 indicates that the general level of toughness of Linde 120 was significantly higher than either that of Bostrand 31 or AX140. There was a small decrease in toughness at 450°C, but this was within the experimental scatter range and it was not considered significant.

AX140

The same heat treatments were again used and the 1 and 50 hour transition curves are shown in Figures 29 and 31 with the T_{55J} versus treatment temperature in Figure 31. The regression equations and correlation coefficients are listed in Table 7. The 1 hour treatment did not cause a significant toughness change up to 550°C with an increase in toughness at 650°C, which is consistent with the overageing observed on the hardness plots. The 50 hour treatment indicated embrittlement at 450°C which increased markedly at 550°C.

3.5.2 Effect of time at 550°C - AX140

The AX140 weld metal did not appear to be embrittled after 1 hour at 550°C, so further samples were treated at 550°C for 2 hours and 10 hours and water quenched. The 2 and 10 hour regression lines are shown in Figure 32. Figure 33 is a plot of T_{55J} versus log time and shows a steady increase in embrittlement up to 10 hours, with a more rapid increase between 10 and 50 hours. These results indicate that the embrittlement reaction is sluggish and that the degree of embrittlement is low for treatment times up to 10 hours.

3.5.3 Effect of cooling rate - AX140 - Linde 120

All the previously examined Charpy results were obtained from water quenched samples. The effect of cooling rate was investigated by comparing Charpy results obtained after cooling at 100°C/hour with the water quenched results. Previous results indicated that embrittlement of AX140 was sluggish up to 10 hours at 550°C so batches of AX140 were treated for 2 and 10 hours at 550°C and cooled at 100°C/hour. Specimens of Linde 120 were also included to see if any embrittlement occurred, even though the water quenched results indicated only a small level of embrittlement. The Linde 120 regression lines and Charpy points are shown in Figure 34. The AX140 slow cooling regression lines are shown in Figure 35. The regression equations are included in Tables 6 and 7 respectively. Figure 33 illustrates the variation of embrittlement with treatment time at 550°C and cooling rate. Slow cooling from 550°C increases embrittlement in Linde 120 and AX140.

3.5.4 Summary of Charpy results

Both AX140 and Bostrand 31 were significantly embrittled by treatment at 550°C. Significant embrittlement was found for Bostrand 31 after 1 hour which further increased after 50 hours. Embrittlement of AX140 at 550°C was sluggish, but a high degree of embrittlement was observed after 50 hours. A small amount of embrittlement was noted for Linde 120, but was relatively insignificant when compared with the other two weld metals.

Decreasing cooling rate from 550°C increased the amount of embrittlement in AX140 and Linde 120. However, the amount of embrittlement in the latter remained small.

3.6 COD results

The Charpy results indicated that embrittlement occurred in the 450° to 550°C temperature range and was greatest after the 50 hour treatment. COD tests were performed to establish if the degree of embrittlement suggested by the Charpy results was observed under conditions of a slowly applied load in the presence of a sharp notch, and to obtain data from which estimates of defect tolerances could be made.

Tests were carried out on weld metals in the as deposited condition and after 50 hours at 450, 500 and 550°C followed by water quenching. The 500°C treatment was omitted on the AX140 material. Tests were also performed on the high heat input Bostrand 31 (3.15 KJ/mm) material in the as deposited condition and after a 550°C - 50 hour treatment. Tests were not performed on materials heated to higher temperatures because the tensile results indicated that a marked loss of strength occurred.

All COD data is tabulated in Tables 8, 9, 10 and 11, and some of the data is plotted in Figures, 36, 37, 38 and 39. It should be noted that the lines on these figures are to illustrate trends rather than show lines of best fit. The points plotted in these figures are mainly δ_m values, although some δ_i values corresponding to slow crack growth are included and linked to the relevant δ_m values. δ_i values corresponding to "pop-ins" are not included on the graphs, but are appropriately marked in the tables. These figures also show the COD values used for the defect calculations in section 3.8.

<u>Bostrand 31</u>

As deposited δ_m versus test temperature from the 1.18 KJ/mm weld metal is tabulated in Table 8 and plotted in Figure 36, which also includes data from the B series (transverse notch) tests. The results for the 550°C - 50 hour treatment are also included and show a clear reduction in δ_m. The results for the 450° and 500°C treatment are omitted for clarity but fell between the two curves.

δ_m for the 3.15 KJ/mm heat input weld in the as deposited condition and after 50 hours at 550°C is shown in Figure 37 (Table 9). The higher heat input weld shows appreciably higher scatter and this is thought to be directly related to the larger weld run size which caused a greater structural variation at the notch root. The points can be reasonably interpreted as indicating an upper and lower bound, with the lower bound being due to a high proportion of columnar grains at the centre of the notch. The lower values of the 3.15 KJ/mm weld were below those of the 1.18 KJ/mm weld when tested in the same direction, indicating a lower as deposited toughness with increasing heat input although the 3.15 KJ/mm results were similar to the transverse notch 1.18 KJ/mm results. The embrittlement due to heat treatment is again clearly apparent.

Linde 120

Figure 38 shows the variation of δ_m and δ_i with test temperature for the weld metal in the as deposited condition and after heat treatment at 450, 500 and 550°C. All the test results have been included on one plot to demonstrate clearly that any embrittlement in the 450 to 550°C range is minimal. The test details are shown in Table 10. The general level of δ_m is higher than that of as deposited Bostrand 31 and the transition to the lower shelf occurs at lower temperatures. There is a tendency for the 450°C values to be lower than the as deposited values, while the 550°C values tend to be higher. While further tests could have confirmed these trends, it is felt that there is sufficient data to conclude that any embrittlement was minimal especially when compared with the clear indications found for Bostrand 31 and AX140.

AX140

The 550°C treatment caused a clear reduction in δ_m which is illustrated in Figure 39. The 450°C results are not included but fell midway between the two curves (Table 11). The as deposited curve is very flat, showing a low temperature dependence with the 550°C - 50 hour results lying below it. The as deposited δ_m values were significantly lower than the equivalent Linde 120 and Bostrand 31 values.

In summary, the COD results clearly reflected the trends observed in the Charpy tests showing that significant embrittlement occurred at 550°C for both Bostrand 31 and AX140, and that embrittlement of Linde 120 over the 450 - 550°C range was minimal.

3.7 J integral results

J was evaluated for the as deposited tests and the treatments that showed maximum embrittlement and the values are included in Tables 8, 9, 10 and 11. Most J values were calculated using δ_m values, although at least one upper shelf estimate of J based on crack initiation has been made for each weld metal in the as deposited condition. While the neglect of initiation does lead to an over-estimate of J in some cases, the magnitude of the error is fairly small as can be noted by inspecting the tables. In the embrittled weld metals, crack initiation did not occur until maximum load was reached.

The variation of J with temperature and heat treatment reflected the variation of δ_m and no new useful information can be shown by plotting the values. Instead, the J values were converted to non dimensional J and plotted versus non dimensional δ, (Figure 40).

This plot includes every J value irrespective of weld metal type or degree of embrittlement. The effect of embrittlement is to lower J and δ values towards the origin. Sumpter's plane strain and plane stress finite element solutions are included for comparison. (75). The results generally fell between the two curves, tending to be much closer to the plane stress solution as would be expected for this thickness. As the value of non dimensional δ decreased below 2, the results deviated below the plane stress solution when they would have been expected to approach the plane strain solution. It has been suggested that this deviation is due to undetected slow crack growth. (82). This is not the case in this instance, because the deviation is at low values of δ which correspond to fracture on a rising load curve, in, or just beyond the linear elastic range where crack growth was rapid and clearly defined. To confirm the deviation, values of J and δ were determined at regular intervals along a single specimen P-V curve (specimen G1/3) and are shown plotted in Figure 41, where the deviation at low δ values is again apparent. This is probably best explained by the tendency for the Wells equation to over-estimate δ at low values as found experimentally by Archer. (88). The effect of the non detection of initiation can also be seen on the plot. If initiation is neglected, higher values of δ and J further up the plot will be obtained, but there will be no tendency for it to deviate below the plane stress solution. The discontinuity in the plot coinciding with general yield should also be noted.

The question of plane strain validity limits for J testing was mentioned in section 2.4.4. It is not possible to show these limits on the diagram as they vary with σ_y. Calculations showed that all tests met the minimum level suggested which can be stated as:

$$(W-a) > \frac{25J}{\sigma_y}$$

Some of the tests, particularly the Linde 120 and Bostrand 31, as deposited (Specimens G1/- and D1/- respectively) did not meet the more stringent requirement (82):

$$(W-a) > \frac{50J}{\sigma_y}$$

However, Figure 40 clearly illustrates that J varies in a similar manner to δ and that the experimental determinations are in good agreement with the finite element predictions.

3.8 Calculation of defect tolerances

3.8.1 General considerations

The advantage of fracture mechanics techniques over methods like the Charpy test , is that they can be used to calculate the defect tolerance of a material, and so direct comparisons of the fracture characteristics of materials can be made. In this section, the defect tolerance in terms of the critical crack size $\bar{a}$ is calculated for the weld metals in the as deposited and embrittled conditions, assuming an operating temperature of 0°C and a working stress of 2/3 minimum plate yield. The as deposited COD values represent upper shelf levels and the calculations are valid over a wider temperature range e.g. -20 to +10°C. The critical crack size $\bar{a}$ is equivalent to half the crack length of a through thickness defect in a finite plate, and can be modified for other crack shapes using the appropriate shape factors listed in reference 2.

The as deposited values of δ and J used in the calculations corresponded to the lowest crack initiation values in the -20 to +20°C upper shelf range. The values used are indicated in Figures 36, 37, 38 and 39 and are included in the table of results of the defect calculations, Table 12. Two values are used for the 1.18 KJ/mm Bostrand 31 weld, corresponding respectively to the normal notch orientation and the transverse notch (Series B).

The embrittled values used in the calculations all corresponded to fracture on a rising load curve where crack initiation was clearly defined. As Linde 120 was not embrittled, the calculations are repeated on sample G1/3 which had the lowest δ_i at 0°C.

3.8.2 COD calculations

As deposited condition

The Welding Institute design equation was used as a basis for calculation. (2). The defect was assumed to be in weld metal, normal to the applied stress and remote from stress concentrations. The working stress σ_w was assumed to be 2/3 minimum plate yield:

Bostrand 31 / HY80	$\sigma_w = 368$ MN/m^2
Linde 120 / HY100	$\sigma_w = 460$ MN/m^2
AX140 / HY130	$\sigma_w = 598$ MN/m^2

The design equation is given by:

$$\Phi = \left(\frac{e}{e_y}\right)^2 \quad \text{for } \frac{e}{e_y} < 0.5 \qquad \text{.... (i)}$$

and

$$\Phi = \left(\frac{e}{e_y}\right) - 0.25 \text{ for } \frac{e}{e_y} > 0.5 \qquad \text{.... (ii)}$$

where

$$\Phi = \frac{1}{2\pi\bar{a}}\left(\frac{\delta}{e_y}\right) \qquad \text{.... (iii)}$$

In the as deposited weld, nett strain is the sum of the strain due to residual stresses, assumed to be equal to the yield stress, and the working stress:

$$\frac{e}{e_y} = \frac{\sigma_w}{\sigma_y} + \frac{\sigma_y}{\sigma_y} \qquad \text{.... (iv)}$$

Substituting (iv) in (ii) and (iii)

$$\bar{a} = \frac{\delta E}{2\pi(\sigma_w + 0.75\sigma_y)} \qquad \text{.... (v)}$$

Post weld heat treated condition

In this derivation, the complete removal of residual stress is assumed. Therefore, the nett strain is due to the working stress alone.

$$\frac{e}{e_y} = \frac{\sigma_w}{\sigma_y} \qquad \text{.... (vi)}$$

From (ii) and (iii)

$$\bar{a} = \frac{\delta E}{2\pi(\sigma_w - 0.25\sigma_y)} \qquad \text{.... (vii)}$$

In the case of the Bostrand 31 welds, the elevation in weld metal yield stress was sufficient to reduce $\frac{\sigma_w}{\sigma_y}$ to$<$0.5. In these instances, from equation (i).

$$\bar{a} = \frac{\delta E}{2\pi\left(\frac{\sigma_w}{\sigma_y}\right)^2} \qquad \text{.... (viii)}$$

Calculations were also performed assuming that 25% of the original residual stress remained after heat treatment. In this case, the nett strain is given by:

$$\frac{e}{e_y} = \frac{\sigma_w}{\sigma_y} + \frac{0.25\sigma_y}{\sigma_y}$$

Therefore, from equations (ii) and (iii)

$$\bar{a} = \frac{\delta E}{2\pi\ \sigma_w} \qquad \text{.... (ix)}$$

3.8.3 J calculations

As deposited condition

J can be used to calculate K_c, the stress intensity at fracture, up to yield stress provided plastic zone corrections are used when $\sigma_w > 0.8\ \sigma_y$. (77). In the as deposited condition, the effective stress was assumed equal to σ_y even when the working stress was superimposed because any stress in excess of yield would be relaxed by plastic flow.

$$J = \frac{K_c^2}{E'}$$

$$E' = \frac{E}{1 - \nu^2} \quad \text{for plane strain}$$

$K = \sigma\sqrt{\bar{a}'\pi}$ for a wide plate (66) where $\bar{a}'$ is the uncorrected crack length.

$$\bar{a}' = \bar{a} + r_y$$

$$r_y = \frac{1}{6\pi}\left(\frac{K}{\sigma}\right)^2 \quad \text{for plane strain}$$

$$\therefore \quad \bar{a} = \frac{JE}{\pi\sigma_y^2(1 - \nu^2)} - \frac{JE}{6\pi(1 - \nu^2)\,\sigma_y^2}$$

$$= \frac{5\ JE}{6\pi\ \sigma_y^2(1 - \nu^2)} \qquad \text{.... (x)}$$

Post weld heat treated condition

As $\sigma_w < 0.8\sigma_y$ no plastic zone correction is required.

$$\therefore \quad \bar{a} = \frac{JE}{\pi\ \sigma_w^2\ (1 - \nu^2)} \qquad \text{.... (xi)}$$

If 25% of the original residual stress remains after heat treatment then $\sigma_w + 0.25\sigma_y > 0.8\sigma_y$ and

$$\bar{a} = \frac{JE}{\pi(1 - \nu^2)\,(\sigma_w + 0.25\sigma_y)^2} - r_y$$

where $r_y = \frac{1}{6\pi}\left(\frac{K}{\sigma}\right)^2$

$$\therefore \quad \bar{a} = \frac{5JE}{6\pi(1 - \nu^2)\,(\sigma_w + 0.25\sigma_y)^2} \qquad \ldots\ldots \text{(xii)}$$

The results of the calculations are shown in Table 12, and the equation numbers referred to, relate to the equations shown in this section. It can be noted from these results that the defect tolerances of AX140 and Bostrand 31 actually increase after post weld heat treatment, even though the weld metal is embrittled while if 25% residual stress is assumed, the defect tolerances decrease. The significance of these calculations will be further discussed in section 5.4.3.

CHAPTER 4 EXPERIMENTAL - METALLOGRAPHIC EXAMINATION OF WELD METAL EMBRITTLEMENT

4.1 Experimental methods

The metallographic examination of the weld metals was carried out in both the as deposited and embrittled conditions and the results of these examinations are described separately. Weld metals in the as deposited condition were studied using optical and transmission electron microscopy and a quantitative estimate of the microstructural constituents was made.

The embrittlement study concentrated on a scanning electron microscope (SEM) comparison of as deposited and embrittled fracture surfaces mostly taken from COD specimens. Transmission electron microscopy was used to examine the carbide distribution and identify carbide types present after heat treatment. As deposited COD fracture surfaces, produced at upper shelf temperatures, were compared to embrittled weld metal fracture surfaces produced at similar temperatures. The observations could therefore be directly linked to the observed decrease in COD. In each case, the specimen number from which a given fractograph was taken, is quoted and the corresponding COD can be found by reference to Tables 8, 9, 10 and 11.

Optical and electron microscopy was performed on sections transverse to the weld axis unless otherwise stated and were confined to the columnar regions.

An initial study of carbide precipitation after the maximum embritelment treatment (550°C - 50 hours for Bostrand 31 and AX140) was performed on thin foils so that precipitating carbides could be identified and their location and orientation relative to the ferrite determined. This turned out to be a formidable task: the main problems can be listed as follows and should be borne in mind if further similar work is attempted. The ferrite grain size, acicular or lath, was essentially unchanged after 50 hours at 550°C indicating effective carbide pinning of grain boundaries and the grain size was of the same order as the smallest, field limiting diffraction aperture available. Consequently, it was not usually possible to obtain diffraction patterns from one grain only and spots from other grains made interpretation difficult. It also became apparent that more than one carbide type was precipitating which further complicated interpretation. Another difficulty was the ferromagnetic interaction between the elctron beam and the specimen. This resulted in image shift as the specimen was tilted and the need to constantly make objective lens astigmatism corrections. Because the carbides were still small after the 550°C treatment (50 - 200 Å), further work was carried out on specimens aged at 650°C and above.

The switch to unshadowed or self shadowed extraction replicas overcame most of the difficulties. These were prepared by coating a nital etched specimen with carbon, blanking off unwanted areas with lacquer and floating off the replica in a solution of 10% HCl in alcohol using an applied potential of 30 volts for 5 - 10 seconds. Carbide dissolution was negligible and the technique was extremely consistent. Basic features, such as prior austenite grain boundaries and acicular boundaries, could still be identified although gold-palladium shadowing was used to examine as deposited structures.

Diffraction patterns were measured using a projection microscope with a travelling stage. The limit of accuracy was controlled by locating the centre of diffuse spots rather than measurement limitations. The diffraction data are presented as a photograph of the pattern, an indexed diagram of the pattern and a list of experimentally determined "d" spacings which are compared with published d spacings. Interplanar angles are not quoted, but the indexing was checked using published interplanar angles in the case of cubic carbides and cementite (93), while the interplanar angles of M_7C_3 and Mo_2C were obtained using a computer program. In cases where identification was still uncertain, relative intensities published in the powder file (94) were used. The symbols d and c/a are freely used and stand for the interplanar spacing for a given set of planes and the axial ratio of a tetragonal unit cell respectively and should not be confused with the fracture mechanics symbols. The system adopted in naming the carbides follows that usually found in the literature. (96). A metal symbol is often used to name a carbide even though the carbide may contain significant amounts of other metal atoms e.g. Fe_3C can contain significant amounts of manganese and chromium. It would be more rigorous to define all carbides as M_xC_y, but the usual notations are retained for clarity. The carbides identified in the present study were consequently Fe_3C, Mo_2C, V_4C_3, M_7C_3 and $M_{23}C_6$. The latter two carbides are chromium rich, but are usually defined as mixtures (96). It should also be noted that nitrogen may replace carbon in the carbides but this is difficult to detect from lattice parameter measurements.

4.2 As deposited microstructures

4.2.1 Bostrand 31

Weld metal deposited at each heat input was examined and appeared similar except that the acicular ferrite in the 3.15 KJ/mm weld seemed coarser than that in the 1.18 KJ/mm weld. Proeutectoid ferrite decorating the prior austenite grain boundaries can be seen in Figure 42, while Figures 43 and 44 show each weld at higher magnifications. The structures were predominantly acicular ferrite with some proeutectoid ferrite. There was a tendency for some of the proeutectoid ferrite in the higher heat input weld to develop small sideplates which could be considered as embryonic upper bainite (Figure 45). However, the usual definition of ferrite sideplates or upper bainite tends to imply that the plates are well developed and extend well into, or across, a grain and as the development of sideplates in the present case was minimal, all such structures were counted as proeutectoid ferrite.

The other microstructural component identified was revealed by etching in 4% picral and appeared as small angular lumps about 1 micron across and is shown in Figure 46. Their angular nature suggests that they occupy acicular ferrite interstices while the elongated areas could be between parallel acicular ferrite grains. These areas therefore appear to be the pockets of martensite referred to by Garland and Kirkwood. (7). While the term martensite is adopted in this work, there is considerable uncertainty about its true nature and this is discussed later in this section.

The area fractions of the three constituents, acicular ferrite, proeutectoid ferrite and martensite were measured and are shown in Table 13 along with an estimate of the acicular ferrite needle width. The measurement methods are detailed in Appendix 3. The results indicated that the percentage of proeutectoid ferrite increased with increasing heat input along with a small increase in the acicular ferrite grain width. There was an apparent decrease in the amount of martensite with increasing heat input, but the difference was small and was within the measurement errors and so is not considered significant.

Examination of extraction replicas showed that there was some fine carbide precipitation associated with the edges of the acicular ferrite grains as shown in the upper centre of Figure 47. The carbides were identified as Fe_3C (Figure 48). There appeared to be no evidence of V_4C_3 precipitation.

Thin foils of each weld metal were prepared to obtain micrographs of the internal structure of the so called martensite and to determine the c/a ratio of these areas so that they could be compared with those of the acicular ferrite. The results of this work were somewhat inconclusive. Figure 49 shows acicular ferrite in the 1.18 KJ/mm weld with a prior austenite boundary running down the right-hand side. Examination of this structure at higher magnifications did not reveal readily identifiable martensite, although some areas did suggest lath martensite (Figure 50). However, this could equally be interpreted as parallel acicular ferrite similar to that in the centre of Figure 49. Parallel laths were also noted in the 3.15 KJ/mm weld (Figures 51 and 52). Diffraction patterns from the laths shown in Figure 51 indicated a suggestion of tetragonality with a c/a ratio of 1.004 (Figure 53). Other patterns from similar laths were solved giving c/a values between 1 and 1.004, but it must be noted that this variation was of the same order as the measurement accuracy which was limited by the diffuse nature of the spots caused by the high dislocation density.

Figure 52 can also be interpreted as parallel acicular ferrite, but the dark band suggests an area of martensite similar to the elongated areas noted in Figure 46. A similar area is shown in Figure 54 with its diffraction pattern in Figure 55, the solution of which indicated that any tetragonality was very small. An unexpected observation was the occurrence of a streaked $V_4C_3[111]$ zone. The pattern suggests an orientation relationship of $\{111\}_{V_4C_3}$ // $\{110\}_\alpha$ which is actually 9° away from the established relationship (97) of $\{100\}_{V_4C_3}$ //$\{100\}_\alpha$. However, this apparent misalignment is not uncommon in heavily dislocated structures at early stages of precipitation and Tekin and Kelly have published an identical pattern for V_4C_3 precipitating in martensite.(110). The responsible precipitates were not located, but Figure 56 is from an adjacent area and appears to show very fine precipitates. Attempts were made to interpret the pattern in terms of spots from another grain or from a cementite particle but neither assumption could be made to fit. This observation therefore indicates that precipitation of V_4C_3 is occurring during cooling in Bostrand 31 when welded at 3.15 KJ/mm. Evidence for similar precipitation in the lower heat input weld was not obtained, but the search was not exhaustive and this coupled with the extreme difficulty of obtaining carbide patterns in these materials does not rule out its possible occurrence.

Returning to the question of martensite, none of the results have really confirmed its existence, although lath type structures were identified. Garland and Kirkwood have indicated that both lath and twinned martensite can occur in weld metals of a similar composition (7), but the present observations have not confirmed either. An apparent martensite phase can be found by picral etching, but this is difficult to relate to the transmission micrographs. Parallel lath structures can be found, but the lath width is comparable to that of the acicular ferrite and while the laths appear to have some tendency to tetragonality , they do not have significantly higher c/a ratios than the ferrite and it is difficult to discriminate between the structures on this basis. The situation is further complicated by the occurrence of precipitation which would rapidly deplete the lattice of carbon, thus lowering its c/a. As indicated previously, the word "martensite" will be used to denote the component identified by picral etching while the realism of attempts to clearly define a structural difference between this component and acicular ferrite will be considered in the discussion section.

The relationship between the martensite and the cleavage path in as deposited Bostrand 31 was examined by initiating a cleavage crack at -60°C in a COD specimen and sectioning. Multiple cracking is shown in Figure 57 and the dark areas indicate the so-called martensite. As this is a section and the structure underneath could be controlling the cracks, conclusions drawn must be tentative, but the cracks at A tend to cut across the long axis of the martensite while the cracks at B appear to be in line with the martensite. The crack lengths also appear to be large in relation to the martensite islands. If Figure 57 is compared with Figure 43, which is at the same magnification, it appears that the facet length is also considerably greater than the acicular ferrite grain size. If the pockets of martensite were controlling cleavage fracture it could be expected that the facets would be more directly associated with the pockets and the facet length should be of the same order as the acicular ferrite width. This point will also be further discussed in the discussion section.

4.2.2 Linde 120

This structure was essentially similar to that of the Bostrand 31 and a typical micrograph is shown in Figure 58. The microconstituents, acicular ferrite, proeutectoid ferrite and martensite were identified and their area fractions are shown in Table 13. Also included are estimates of the acicular ferrite and prior austenite grain size. The fractions of proeutectoid ferrite and martensite were both significantly lower than in Bostrand 31. The martensite pockets were noticeably smaller than those in Bostrand 31 and the area fraction is definitely an upper estimate as it was difficult to discriminate between the martensite and coarse inclusions at magnifications of 2000X. The martensite is shown as small islands in Figure 59. There was again evidence of Fe_3C precipitation on the edges of the acicular ferrite grains.

4.2.3 AX140

The structure of AX140 was markedly different from either Bostrand 31 or Linde 120. The structure did not contain any proeutectoid ferrite and was noticeably finer than the other two weld metal types. The structure is shown in Figures 60 and 61 and if Figure 61 is compared with the micrograph of Linde 120 at a similar magnification, Figure 59, the much finer structure can be noted. The as deposited hardness of the structure was 358 HV30 which was significantly higher than either the Linde 120 at 287 HV30 or Bostrand 31 at 283 HV30. Samples of AX140 weld metal were held at 1150°C for 30 minutes and water quenched, but this treatment did not cause a hardness increase, whereas a similar treatment caused a significant hardness increase in the other two weld metals. On the basis of each of these factors, the structure was termed martensite. Because the carbon content was low, M_s would be relatively high and some auto-tempering could be expected, although no evidence of carbide precipitation was found from extraction replicas. Carbides may have been detected if a thin foil had been prepared, but previous experience on as deposited thin foils suggested that obtaining diffraction evidence in a highly dislocated structure with a fine effective grain size would be difficult. While no as deposited thin foils were prepared, Figure 62 shows AX140 after 50 hours at 650°C and the lath structure is clearly visible. Again carbide precipitation has effectively pinned the boundaries and prevented any substructural growth. X-ray diffraction analysis indicated that the structure contained approximately 1.5% retained austenite. (Appendix 4 and Table 13).

4.3 Metallographic examination of embrittlement

4.3.1 Bostrand 31

Fracture surfaces of the lower heat input Bostrand 31 weld metal were examined using a scanning electron microscope in both the as deposited condition and after treatment at 550°C for 50 hours. The fractographs were obtained from COD specimens fractured at similar temperatures and show areas in the immediate vicinity of the notch, with the notch at the bottom and the direction of crack propagation upwards.

Upper shelf as deposited failure was by microvoid coalescence (Figures 63 and 64). The corrugated appearance of the surface in Figure 63 was typical of upper shelf failures in the three weld metals and has been observed in other high strength weld metals. (10). Examination of specimens treated at 550°C and fractured at temperatures corresponding to microvoid coalescence in the as deposited weld metal, showed that the failure mode was mixed but was predominantly cleavage. Figure 65 shows a low magnification view of specimen D4/6 fractured at -20°C and Figure 66 is a close up of the same area showing cleavage and a small amount of microvoid coalescence. Cleavage also predominated in specimen D4/2 fractured at -6°C (Figure 67). Specimens of the higher heat input weld were also examined and again showed that cleavage was the dominant fracture mode in the embrittled condition.

The pronounced secondary hardening peak observed at 550°C indicated the precipitation of a carbide was promoting cleavage failure and as vanadium was present at 0.12%, vanadium carbide was suppodedly responsible. Initial attempts to locate the carbide using thin foils ran into difficulties as previously mentioned and unshadowed extraction replicas were used. It was found expedient to overage the material to coarsen the carbides; this was not regarded as invalidating the analysis, as pronounced secondary hardening had been observed, and the responsible carbides could reasonably be expected to be present in a coarser form.

Vanadium carbide was found to be extremely resistant to coarsening and final examination was performed on specimens treated at 700°C for 10 hours. Vanadium carbide appeared to be the only carbide present and its distribution is shown in Figure 68, with extremely fine carbides (20 - 50Å) distributed evenly throughout the grains and with coarser carbides (100 - 250Å) along the acicular ferrite grain boundaries. The coarser carbides on the grain boundaries reflect the enhanced diffusional mobility of vanadium and carbon at those sites. The coarser carbides also appeared in patches which could have been associated with the martensitic areas in the as deposited weld metal (Figure 69). A ring pattern of the carbides in Figure 69 showed that they were V_4C_3 (Figure 70).

4.3.2 AX140

Examination of COD fracture surfaces in the as deposited condition showed that upper shelf failure occurred by microvoid coalescence (Figure 71) with a transition to cleavage at lower temperatures. Figure 72 is taken from specimen E1/6 fractured at -64°C and shows mixed cleavage and microvoid coalescence.

Specimens treated at 550°C failed by smooth decohesion along the prior austenite columnar grain boundaries (Figures 73 and 74). Some microvoid coalescence was observed which was due to ductile tearing linking cracks on different boundaries and can be seen on the left of Figure 75. Inspection of the grain surfaces at high magnifications did not show any evidence of films or particles (Figure 76).

A Charpy specimen treated at 550°C for 10 hours, cooled at 100°C/hour and fractured at 2°C was also examined and again exhibited smooth intergranular decohesion with some cleavage and microvoid coalescence (Figures 77 and 78).

Carbide identification was performed on extraction replicas taken from a specimen aged at 650°C for 50 hours and a typical area is shown in Figure 79 which shows rods of Mo_2C and larger carbides which were either Fe_3C, M_7C_3 or in one instance $M_{23}C_6$. Diffraction patterns were obtained by tilting this area. Mo_2C was identified from ring patterns and also from a single crystal pattern shown in Figure 80, while a pattern of $M_{23}C_6$ is shown in Figure 81. This latter result was unexpected as 4 - 5% chromium is required for its stabilization. However, the pattern could not be solved as Fe_3C, Mo_2C or M_7C_3 and additionally, the intensity of the spots correlated with relative X-ray intensities published in the powder file which indicated that 660, 440 and 333 planes gave high intensities. Other patterns were solved as M_7C_3 and Fe_3C.

An extraction replica was also made from a transverse section through a COD specimen treated at 550°C, with the replica being taken immediately adjacent to the crack surface and this presented a section across the longitudinal axes of the columnar grains. Heavy carbide precipitation on the prior austenite boundaries was noted (Figure 82) and diffraction patterns were obtained from the grain boundary carbides shown in Figure 83. These indicated the presence of M_7C_3 (Figure 84) and Fe_3C (Figure 85). Rods of Mo_2C were also observed (Figure 83), although no patterns were obtained. While it was not possible to accurately quantify the carbide distribution, which would entail identifying each particle, the general tendency was for Mo_2C to be precipitated in clusters similar to that shown in Figure 79, while M_7C_3 and Fe_3C were more evenly distributed and were associated with either lath boundaries or heavily concentrated on prior austenite columnar boundaries.

Relating the identified carbide types to those predicted by published phase diagrams was not straightforward as the latter are based on less complex compositions and tend to use long ageing times to approach an ostensibly true equilibrium state. However, a diagram published by Andrews et al., can be used as a guide, noting that it was established for 1000 hours ageing and for a carbon content of 0.12% which is significantly higher than the 0.09% AX140. (98). The diagram is shown in Figure 86 and it includes composition points corresponding to AX140 and Linde 120. This suggests that Fe_3C, M_7C_3 and Mo_2C should be present in the AX140 which is therefore in agreement with the results. The occurrence of $M_{23}C_6$ is unexpected, but it can be suggested that it was due to a local concentration of chromium which is perhaps not unexpected in a rapidly solidifying weld metal.

4.3.3 Auger analysis of AX140 fracture surfaces

The intergranular fracture mode was indicative of classical temper embrittlement and it was therefore necessary to establish by direct measurement which of the known embrittling elements was responsible. The chemical analysis results indicated that 0.011% phosphorus and up to 0.015% tin were present and while these levels were lower than those generally considered to cause embrittlement (41), they were the likely responsible elements.

Two specimens of AX140 were treated at 550°C for 50 hours, notched in the columnar region and fractured in an Auger spectrometer* where the surface monolayer was analysed.

---

* Analysis performed at the National Physical Laboratories, Teddington by Dr M P Seah.

Typical figures from these analyses were as follows, the results being in fractions of an equivalent monolayer.

P	0.23 ± 0.03	Cr	0.26 ± 0.04	Mn	0.42 ± 0.08
Mo	0.25 ± 0.05	Sn	0.02 ± 0.01	Sb	0.01
As	0.06	Ni	0.23 ± 0.03	Al	0.08
Si	0.04				

Molybdenum and chromium were present as carbides and so the monolayer equivalent becomes 0.09 and 0.06 of the grain boundary area covered by carbides. Therefore, the significant segregants were phosphorus, manganese and nickel.

4.3.4 Linde 120

The Linde 120 COD curves shown in Figure 38 reflect similar upper shelf COD values for the as deposited condition and after 50 hours treatment at 450, 500 and 550°C. The fracture surfaces of these specimens were all similar showing failure by microvoid coalescence (Figure 87). At -66°C, the as deposited weld metal failed by cleavage whereas the weld metal treated at 550°C failed by intergranular fracture (Figure 88). This form of failure was also observed in the Charpy specimens which were held at 550°C for 10 hours and cooled at 100°C/hour. Figure 89 shows a low magnification view of a Charpy specimen fracture at -16°C and suggests some form of intergranular failure. Examination at higher magnifications showed that there were three types of fracture surface, cleavage, microvoid coalescence and intergranular decohesion. Cleavage and microvoid coalescence can be seen in Figure 90, while cleavage and intergranular decohesion is shown in Figure 91. The three failure modes can also be seen on the right-hand side of Figure 92 which shows the junction between the columnar region and the refined region, the latter fracturing by microvoid coalescence. A particle in the walls of microvoid coalescence shown in Figure 92 and 90 was analysed using X-ray dispersive analysis. The particle is located in the centre of Figure 90 and is shown in Figure 93, and the resulting trace in Figure 94. This indicates the presence of silicon, aluminium, iron and manganese and the particle was therefore considered to be an inclusion. Similar results were obtained for particles analysed in the refined structure shown on the left of Figure 92.

These results suggest that temper embrittlement was responsible for the slight decrease in toughness observed in the slow cooled Charpy specimens as shown in Figure 33. There was also a tendency for temper embrittlement to cause failure along prior austenite grain boundaries after prolonged heating at 550°C (Figure 88), although the COD results showed that any embrittlement was negligible (Figure 38).

Extraction replicas were prepared from a sample held at 650°C for 50 hours. Mo_2C and Fe_3C were identified with the Mo_2C present in the form of high aspect ratio rods which were found in patches and not generally distributed throughout the structure (Figure 95). The ring pattern used to identify Mo_2C is shown in Figure 96. Fe_3C was more generally precipitated throughout the structure with some tendency to precipitate on acicular ferrite grain boundaries (Figure 95). A cementite pattern from the area of Figure 95 is shown in Figure 97. A COD specimen treated at 550°C for 50 hours was examined and no evidence of heavy prior austenite grain boundary carbide precipitation could be found (Figure 98). The phase diagram (Figure 86) suggests the Mo_2C and Fe_3C should be present which is in agreement with these findings.

4.3.5 Summary of embrittlement in Bostrand 31, AX140 and Linde 120

The metallographic examination showed that all as deposited weld metals failed by microvoid coalescence in the upper shelf region with a transition to cleavage fracture as the temperature was lowered. Embrittlement of Bostrand 31 was caused by precipitation of V_4C_3 throughout the structure and this promoted cleavage failure. Temper embrittlement was identified as the cause of embrittlement of AX140 and was caused by segregation of phosphorus to prior austenite columnar grain boundaries. Complex carbide precipitation was also noted, although precipitation of Mo_2C did not promote cleavage failure. Heavy precipitation of Fe_3C and M_7C_3 on columnar grain boundaries was noted. In Linde 120 there were only small indications of embrittlement, but where it did occur, it appeared attributable to temper embrittlement.

CHAPTER 5 DISCUSSION

5.1 INTRODUCTION

The investigation has involved a detailed study of the properties and microstructures of the weld metals in the as deposited and post weld heat treated conditions. It has been demonstrated that embrittlement can occur in these weld metals and has given insight into the form such embrittlement can take. Data has been obtained on properties and microstructures of as deposited weld metal and this has been examined in terms of the proposed weld metal toughness models. The embrittlement studies included the determination of COD data for as deposited and post weld heat treated weld metals and this has enabled the calculation of defect tolerances so that the significance of the observed embrittlement can be discussed in these terms. Considerations of the data accumulated in the work, together with the defect tolerance calculations, has enabled specific recommendations for the post weld heat treatment of the three weld metals to be made, along with broader based guidelines for the post weld heat treatment of other high strength ferrous weld metals. All these aspects are therefore considered in the following discussion.

5.2 Weld metal embrittlement

5.2.1 Embrittlement of Bostrand 31, Linde 120 and AX140

The Charpy data presented in section 3.5 showed that embrittlement of each weld metal occurred after post weld heat treatment in the temperature range of 450° to 650°C. The severity of embrittlement, if embrittlement did indeed occur, was dependent on the major heat treatment variables, treatment temperature, treatment time and cooling rate. Figure 25 shows the variation in the degree of embrittlement of Bostrand 31 as a function of treatment temperature and treatment time where it can be noted that embrittlement was observed after 1 hour in the 550 to 650°C range. After 50 hours, embrittlement increased at 550°C with embrittlement also occurring at 450°C, but there was a nett toughness increase at 650°C. Reference to Figures 28 and 33 show that Linde 120 was not significantly embrittled by treatments in the 450 to 650°C range when water quenched following heat treatment but was embrittled on slow cooling from 550°C. Figures 31 and 33 show that AX140 could be severely embrittled by prolonged treatment at 450 and 550°C, and that embrittlement increased as cooling rate decreased after a given time at treatment temperature.

The metallographic studies showed that embrittlement was caused by two distinct processes, precipitation of alloy carbides and classical temper embrittlement. These forms of embrittlement are now examined in turn to identify the role of microstructure, composition and heat treatment variables on the severity of embrittlement.

5.2.2 Precipitation hardening

Precipitation hardening was found to cause severe embrittlement in Bostrand 31 through the precipitation of vanadium carbide. The low dilution regions of the weld contained 0.10 to 0.13% vanadium which was sufficient to cause significant secondary hardening after 1 hour with peak hardness being developed at 610°C. As ageing time increased to 50 hours, the peak hardness increased and the peak hardness temperature decreased to 550°C (Figure 20). The secondary hardening was accompanied by a marked decrease in Charpy toughness, the

55 joule energy absorbed temperature increasing by 44°C after 1 hour at 550°C and 97°C after 50 hours (Figure 25). This trend was also reflected in the COD toughness measurements. Examination of the embrittled fracture surfaces showed that precipitation promoted cleavage fracture.

In section 4.3.1, it was noted that vanadium carbide precipitated as a fine dispersion throughout the acicular ferrite with larger particles on the acicular ferrite grain boundaries and also in pockets which could have been associated with islands of martensite in the as deposited structure (Figure 69). The growth of coarser carbides on the grain boundaries was probably a direct function of the material being overaged. Tekin and Kelly (110)studied precipitation in martensitic vanadium bearing alloys and noted that coarse grain boundary carbides were only present after peak hardness, whereas carbide precipitation was confined to precipitation on dislocations within the grains before and at peak hardness. It accordingly seems likely that the vanadium carbide distribution in Bostrand 31 at peak hardness was a fine matrix precipitate on dislocations. Coarser precipitates could have been present in the areas occupied by the martensite islands as a result of growth on pre-existing vanadium carbide,precipitated on cooling in the original weld as discussed in section 4.2.1.

Tekin and Kelly attributed the secondary hardening caused by vanadium carbide to the precipitating carbides pinning dislocations and severely restricting their mobility. This was confirmed by the appearance of a sharp yield point in tensile tests on material aged to peak hardness and which was absent in non aged or overaged material.(110). Similarly, if the precipitates pin the dislocations, the precipitates will effectively raise the friction stress on dislocations and promote cleavage fracture as predicted by the cleavage fracture models proposed by Cottrell (104) and Knott (58). (These models will not be discussed here but are described in detail in reference 58 Chapter 7).

The severity of embrittlement of Bostrand 31 summarized in Figure 25 can therefore be explained in terms of the kinetics of vanadium carbide precipitation. At 450°C, precipitation is sluggish with only a small amount of embrittlement after 50 hours. At 550°C, precipitation is more rapid causing significant embrittlement after 1 hour which further increases after 50 hours. At 650°C rapid precipitation leads to embrittlement after 1 hour, but longer times cause overageing with a nett toughness increase after 50 hours.

The effect of molybdenum as a potential precipitation hardening element could be assessed from the Linde 120 and the AX140 weld metals which contained 0.47% and 0.55 to 0.59% respectively. The Linde 120 exhibited a small secondary hardening peak after 50 hours at 500°C (Figure 20) while the AX140 ageing curve was essentially flat in the 450 to 550°C range indicating that any hardening due to molybdenum carbide precipitation was slight and was tending to retard structural softening rather than increase overall hardness.

In section 4.3.2 it was noted that the embrittled fracture mode of AX140 was intergranular decohesion, a characteristic of temper embrittlement and there appeared to be no indications of precipitation hardening promoting cleavage fracture. The Linde 120 fracture surfaces also indicated that the small amount of embrittlement observed was caused by temper embrittlement. While it can be argued that temper embrittlement may have been masking the potential of molybdenum carbide precipitation to promote cleavage, the virtual absence of temper embrittlement in the Linde 120 water quenched COD specimens should have enabled precipitation promoted cleavage to be observed. As it was not detected, even after long ageing times, it can be considered that molybdenum carbide precipitation is not likely to cause embrittlement in weld metals containing up to 0.6% molybdenum.

Garland and Kirkwood observed an apparent interaction between molybdenum and alumina bearing, amphoteric fluxes and suggested that the presence of AlN in the weld metal improved the kinetics of molybdenum carbide precipitation and caused embrittlement. Amphoteric fluxes were not used in this work, although the weld metal aluminium levels were similar to those in Garland and Kirkwood's work (0.014 to 0.016%). (7). In this study, prolonged ageing in the region of the peak hardness temperature (500°C) was used and additionally, Mo_2C was identified in overaged material and yet molybdenum carbide precipitation did not appear to be deleterious. Little more can be said about Garland and Kirkwood's observation of embrittlement until the precipitating carbides in the weld metals they examined, are identified.

The minimal effect of molybdenum, compared to vanadium, can be illustrated by data published by Irvine and Pickering (105) which has been replotted in Figure 99. The vertical axis is the intensity of secondary hardening following solution treatment and it is plotted against alloy content. This plot shows that 3% molybdenum is required to cause as much hardening as 0.2% vanadium, and that molybdenum at the levels present in AX140 and Linde 120 (up to 0.6%) will only cause minimal hardening while vanadium at 0.12%, the level in Bostrand 31, will cause significant hardening.

In section 2.3.2.1 it was noted that heat treatment will remove the islands of martensite in acicular ferrite and this may offset the deleterious effect of precipitation. This phenomenon was used by Garland and Kirkwood to explain a nett improvement in toughness in a 0.12% vanadium weld metal after heat treatment. (7). In this work, a nett decrease was observed after 1 hour at 550°C or 650°C. Comparisons between their Charpy curves (Figure 3) and those obtained in this work (Figure 23) shows that the as deposited toughness was higher in this work. In the weld metals examined by Garland and Kirkwood, the martensite islands were up to 4 microns across whereas, in Bostrand 31, the islands were much smaller, being generally less than 1.5 microns across. The implication is that while the relative amounts of martensite were similar, the larger island size was having a more pronounced effect on cleavage fracture and their removal caused a large potential increase in toughness, whereas the removal of the smaller islands in Bostrand 31 did not have the same potential for improvement. Their weld toughness model can therefore be adapted to explain the present observations, but it must be noted that their conclusion, that vanadium at up to 0.12% will not cause a loss of toughness on heat treatment, was not found correct and large decreases in toughness were observed. The practical implication of these findings will be further discussed in section 5.5.

5.2.3 Temper embrittlement

The examination of fracture surfaces detailed in section 4.3.2 showed that classical temper embrittlement was the principle embrittlement mechanism in AX140. The slow cooled Charpy results indicated that temper embrittlement could also occur in Linde 120, although to a much smaller extent. Temper embrittlement was not detected in Bostrand 31 due to the overriding effect of vanadium carbide precipitation promoting cleavage fracture.

The Auger analysis of an AX140 fracture surface showed that phosphorus, manganese and nickel were the principal segregating elements on the prior austenite grain boundaries. Phosphorus has been identified as a strong embrittling element which significantly lowers the surface energy and hence the energy required to separate prior austenite boundaries. (41, 44). Manganese is also thought to contribute to embrittlement although its potency is apparently less than phosphorus. (106). Joshi and Stein (48) observed segregation of nickel to grain boundaries only when embrittling elements were present. They therefore argued that any effects of nickel on grain boundary cohesion could not be isolated from the effects of the known embrittling elements. It accordingly appears likely that phosphorus is the major embrittling element in the present case. It is also worth noting that tin was not detected as a significant segregant, even though the chemical analysis figures indicated a relatively high bulk concentration of up to 0.015%.

As noted above, temper embrittlement was largely confined to AX140 with Linde 120 showing a much lower susceptibility. Table 1 shows that each weld metal contained the same amount of phosphorus, 0.009% being determined by conventional chemical analysis and 0.011% by vacuum spark emission spectroscopy. The marked difference in their susceptibilities must therefore be attributed to their different microstructures and compositions. AX140 was almost totally martensitic whereas Linde 120 was predominantly acicular ferrite. It can be argued that each martensite grain i.e. a cell enclosed by a prior austenite grain boundary, contains few high angle boundaries. This can be qualitatively justified by inspection of Figure 61 which shows that the martensite has formed in colonies of laths and as cleavage fracture has been observed to run straight across such colonies, only being deflected at the colony boundaries (107), it can be suggested that the inter lath boundaries are low angle, while the inter colony boundaries are high angle. In an acicular ferrite structure, the ferrite grains meet at high angle boundaries (11) and these boundaries can also act as sites for Gibbsian segregation. Therefore, for a given prior austenite grain size, there will be a greater area of internal grain boundary segregation sites in acicular ferrite than in martensite. Internal absorption on these boundaries will lower the amount of phosphorus available for the prior austenite grain boundaries and hence, the phosphorus levels on prior austenite grain boundaries will be lower in acicular ferrite than in martensite.

An alternative or additional reason for the differing responses of the two microstructures can be attributed to the higher chromium content of AX140. In section 4.3.2 it was noted that this weld metal contained sufficient chromium to cause precipitation of chromium rich M_7C_3 which tends to nucleate and grow on grain boundaries rather than on dislocations as is the case for Mo_2C and V_4C_3. In Figure 82, the heavy precipitation of M_7C_3 and Fe_3C on prior austenite boundaries in AX140 was noted while no equivalent heavy precipitation could be found in Linde 120 (Figure 98).

Theories of temper embrittlement are as yet uncertain about the interaction of grain boundary carbides and the embrittling elements, although it has been observed that decohesion of the carbide/ferrite interface occurs in embrittled steel, while carbide cracking occurs in non embrittled steels. (106, 108). As this interface is usually highly tenacious, it is suggested that the embrittling elements reduce the cohesion of the ferrite/carbide interface as well as the ferrite/ferrite interface.

A high magnification view of the fracture surface of embrittled AX140 is shown in Figure 76 and it can be noted that it is relatively featureless, with some surface tears and holes, the latter probably being associated with inclusions being pulled out of the boundary. If preferential weakening of the ferrite/carbide interface had occurred, then dimpled microvoid coalescence centred on carbide particles would have been expected but was not observed. The slow cooled Linde 120 samples represented a lower level of embrittlement and it was initially suspected that the walls of microvoid coalescence observed in the columnar region, as shown in Figure 90, could have been due to void formation around grain boundary carbides but X-ray dispersive analysis showed that the particles were inclusions (Figure 94). These findings accordingly lead to the conclusion that the segregating elements lower the cohesion of both interface components and while carbides are undoubtedly present on the interface, their exact role in the embrittlement mechanism is yet to be established.

In summary, it appears that phosphorus is the element primarily responsible for temper embrittlement. The reason for the higher susceptibility of AX140 compared to Linde 120 appears to lie in their differing microstructure with Linde 120 being less susceptible because its acicular ferrite structure enables more phosphorus to be absorbed on to internal acicular ferrite grain boundaries lowering the amount available for prior austenite boundaries. Carbide precipitation on prior austenite boundaries is associated with embrittelment, but its exact role in the embrittlement mechanism is not clearly known.

The influence of the principal heat treatment variables on the severity of embrittlement of AX140 and Linde 120 can be explained in terms of the kinetics of temper embrittlement. The severity of embrittlement of AX140 increased with time at 550°C because this temperature was within the embrittlement range, while at 650°C there was no embrittlement because phosphorus tended to diffuse away from the grain boundary surfaces. Similarly, embrittlement increased as cooling rate decreased after a given time at 550°C as more time was spent in the embrittlement range. Temper embrittlement of Linde 120 followed along similar lines except that prolonged exposure at 550°C did not cause any detectable decrease in toughness, although Figure 88 shows that sufficient segregation of phosphorus had occurred to make the prior austenite grain boundaries the preferred low temperature fracture path. The increase in embrittlement as cooling rate decreased is also in line with temper embrittlement behaviour.

An important point that should be noted was that the only improvement in toughness over as deposited levels was accompanied by a significant decrease in yield strength and occurred when Linde 120 and

AX140 were heat treated at temperatures above the temper embrittlement range. Bostrand 31 behaved in a similar manner with toughness increasing after 50 hours at 650°C. The increase in toughness can be attributed to the coarsening of precipitating alloy carbides which in turn increased cleavage resistance. Treatment at 650°C reduced the yield strengths of Linde 120 and AX140 below the minimum parent plate yields of HY100 and HY130 respectively. The yield strength of Bostrand 31 was just in excess of the minimum yield strength of HY80 after treatment at 650°C for 50 hours.

5.2.4 Summary of weld metal embrittlement

Embrittlement of the three weld metals occurred when they were post weld heat treated in the 450 to 650°C temperature range. Weld metal embrittlement took two forms; precipitation of alloy carbides which promoted transgranular cleavage fracture and classical temper embrittlement which promoted intergranular decohesion. The severity of embrittlement was dependent on the principal heat treatment variables, treatment temperature, time and cooling rate; the exact nature of this dependence being dictated by which of the two forms of embrittlement occurred. Bostrand 31 was embrittled by precipitation of vanadium carbide which effectively restricted dislocation motion and promoted cleavage fracture. The greatest level of embrittlement coincided with the temperature at which peak hardness was developed and the magnitude of embrittlement increased with time. Vanadium contents of 0.12% were sufficient to cause embrittlement by the formation of alloy carbides, while precipitation of molybdenum carbide did not cause embrittlement for molybdenum levels up to 0.6%.

Temper embrittlement was found to cause severe embrittlement in AX140 and minor embrittlement in Linde 120. Embrittlement occurred over the 450 to 550°C temperature range, being greatest at 550°C, and the severity of embrittlement increased with time. Embrittlement severity also increased with decreasing cooling rates after heat treatment. Embrittlement was caused by the segregation of phosphorus to prior austenite grain boundaries and phosphorus levels of 0.011% were sufficient to cause embrittlement. Martensitic weld metal microstructures were more susceptible to temper embrittlement than acicular ferrite microstructures. The only observed increases in toughness over as deposited toughness levels were accompanied by significant reductions in yield strength and occurred when the weld metals were heat treated at 650°C. This reduced the yield strengths of Linde 120 and AX140 below their matching parent plate minimum yield strengths.

5.3 The relationship of as deposited properties to microstructure

The main emphasis of this study was an examination of weld metal embrittlement although it did present an opportunity to examine the relationship between as deposited microstructures and their toughness, and to relate the microstructures to the proposed weld toughness models. (7, 18).

In Figure 22, the as deposited Charpy transition curves of the three weld metals are shown. Insufficient tests at high temperatures mean that upper shelf levels cannot be accurately compared, although the trend is for AX140 to lie below the other two weld metals. This was confirmed by the COD tests which showed that the AX140 upper shelf level was significantly lower (Figures 36, 37 and 39). Table 13 showed the three weld metals contained similar inclusion contents and the reason for the lower upper shelf levels of AX140 is because of its increased yield stress and lower work hardening capacity (Table 4) which is in agreement with established models. (16).

The observation of an apparent decrease in COD when Bostrand 31 was tested with the notch transverse to the weld axis ("B" series specimens) could possibly be explained by a differing inclusion spacial distribution in this direction and is worth further investigation.

The relative resistance to cleavage is best considered in terms of the Charpy curves in Figure 22 which show that Linde 120 had the highest resistance followed by Bostrand 31 and AX140. Bostrand 31 and Linde 120 were both predominantly acicular ferrite and can be compared in terms of the weld toughness models discussed in section 2.2.3. Table 13 shows that Linde 120 contained less proeutectoid ferrite and martensite than Bostrand 31, both factors leading to a higher resistance to cleavage in terms of Garland and Kirkwood's model. (7). Similarly, increasing heat input increased the proportion of proeutectoid ferrite in Bostrand 31,lowering its cleavage resistance (Figures 36 and 37). However, the higher resistance to cleavage of Linde 120 compared with the two Bostrand 31 weld metals could equally be explained by other unmeasured parameters, particularly differing levels of solid solution hardeners, such as silicon and the possibility of vanadium carbide precipitation in Bostrand 31.

Vanadium carbide was found in the higher heat input weld but not in the lower heat input weld used for Charpy testing, although its non detection did not mean it was absent as detection was extremely difficult in the fine grained, heavily dislocated structure. The lower heat input used in this case would increase the cooling rate and make precipitation less likely but as cementite was detected, it also seems likely that vanadium carbide precipitation could have occurred. If this was the case, then it would lower the weld metal's cleavage resistance.

The basis of Garland and Kirkwood's model is that the islands of martensite in the acicular ferrite dominate cleavage performance. In section 4.2.1, the attempts to identify the islands of martensite shown in Figure 46 using thin foils was described and it was concluded that,while lath type areas could be identified, the laths could equally be interpreted as parallel acicular ferrite grains with some indications of tetragonality. The presence of martensite as a discrete microstructural component was therefore not positively established although Figure 46 suggests its existence.

The existence of martensite in acicular ferrite appears to be conceptually reasonable as carbon would be expected to be rejected at the growing acicular ferrite interfaces, thus stabilizing pockets of austenite in the acicular ferrite interstices. These could then transform to martensite on further cooling. The presence of cementite on acicular ferrite boundaries (Figure 47) confirms that some carbon is being rejected, although the observation of carbide precipitation throughout the grains after heat treatment (Figure 68) suggests that some carbon is retained in the acicular ferrite as postulated by Tuliani et al., (11). This then leads to semantic arguments about when acicular ferrite is martensite and if the so-called islands of martensite are, in reality, a truly different crystallographic structure. This is further complicated by the possibility of the martensite islands autotempering as suggested by the presence of vanadium carbide in the dark band between the acicular ferrite plates in Figure 54. If the reason for a crystallographic difference was initially a higher carbon content, then autotempering removes this distinction.

If the model is to be clearly proven, direct evidence of the islands of martensite causing cleavage crack initiation is required. In this context there appear to be two possibilities; the islands of martensite crack and the crack propogates into the surrounding ferrite in a manner analogous to cleavage cracks caused by lamellar carbides (103), or the angular nature of the martensite islands causes local stress concentrations in the adjacent ferrite and promotes cleavage crack nucleation. The site of cleavage cracks in Bostrand 31 was examined in section 4.2.1, Figure 57, but the cleavage cracks were large in comparison with the islands of martensite and no definite interrelationship could be established. It is considered that this structure was not really suitable for such an examination because the islands of martensite were extremely small (up to 1.5 micron). The martensite in the weld metals studied by Garland and Kirkwood appeared to be much larger,with sizes ranging up to 4 microns,and cleavage fracture paths could be more readily studied in this structure. This is an area of fruitful further work, and while the apparent dependence of cleavage properties on these islands of martensite has been noted, direct crystallographic information on the martensite and its role in cleavage fracture is required.

The martensitic microstructure of AX140 had a much lower fracture toughness - temperature dependence indicating that the resistance to microvoid coalescence was not significantly higher than the resistance to cleavage. This shows that inclusion contents have to be reduced to raise upper shelf levels to those of the lower strength weld metals. The factors controlling cleavage fracture in this microstructure are not readily discernible. Saunders (10) showed that the major hardenability elements did not significantly alter the cleavage resistance and it appears that the main variable is carbon content, which should be kept as low as possible commensurate with achieving the necessary strength and hardenability.

In summary, the fracture properties of the three weld metals were in broad agreement with the various models proposed to relate toughness to microstructure. Linde 120 and Bostrand 31 were both predominantly acicular ferrite with Bostrand 31 having a higher pro-eutectoid ferrite and martensite content. The cleavage resistance of Bostrand 31 was less than that of Linde 120 as predicted by the proposed weld metal toughness models. Attempts made to clarify the role of martensite in acicular ferrite showed that its effect is complex and its relationship to cleavage fracture is not easy to establish. The need for further work in the area was highlighted. The limiting aspect of martensitic weld metal toughness appeared to be the inclusion content which would have to be decreased to raise upper shelf fracture resistance to the same levels as the lower strength weld metals.

5.4 COD data and defect tolerance calculations

5.4.1 Introduction

The COD and J contour integral results enabled the calculation of as deposited and post weld heat treated defect tolerance levels and this has enabled quantitative assessments of the significance of the observed embrittlement. In this section, the significance of the defect calculations are examined and the importance of residual stress levels remaining after heat treatment is noted. Before, the defect tolerance calculations are considered in detail, some further brief comments on the magnitudes of the COD and J results are necessary.

5.4.2 COD and J results

The as deposited COD results are best considered by reference to Figures 36, 38 and 39 which show the variation of δ_m and δ_i with temperature for the three weld metals deposited at 1.18 KJ/mm. Upper shelf values of δ_m are in the range of 0.21 to 0.24mm. for Linde 120, 0.16 to 0.21 mm. for Bostrand 31 and 0.10 to 0.12mm. for AX140. Comparison between these values and other published weld metal data initially indicates that these values appear to be low: upper shelf values of 0.4 to 0.6mm. have been recorded for Bostrand 31 (99), while values of up to 0.8mm. have been recorded for low strength manual metal arc weld metals. (29). However, the low δ values obtained in this work were a direct consequence of two principal factors; the use of a fatigue cracked specimen and the use of the Well's equations (equations 1 and 2 section 3.3.5.5) to calculate δ from the clip gauge opening. The published values quoted above were determined from specimens containing a slit notch, typically 0.15mm. wide, and by using the equation suggested by Ingham et al., to calculate δ(100). Both of these factors cause a considerable increase in apparent δ (58, 73) and this has been confirmed with weld metals. (2). Saunders (10) measured δ in 900 MN/m^2 martensitic weld metals using fatigue cracked specimens and obtained upper shelf values in the range of 0.10mm. to 0.20mm. which further suggests the magnitude of the values obtained in this work are of the right order.

The attempted determination of δ_i was discussed at length in Chapter 3, section 3.3.5.6, where it was noted that while δ_i was difficult to detect, indications were that it was not significantly lower than δ_m in the as deposited weld metals.

The occurrence of pop-ins was also noted and the problem arose of deciding whether the pop-in value of COD or the subsequent higher maximum load COD was the critical fracture characterizing parameter. Pop-ins were observed in all the embrittled weld metals and also in the 3.15 KJ/mm Bostrand 31 weld. The potential drop trace indicated that arrest of the crack occurred and this arrest could be attributed to a number of possibilities.

(a) The crack propagated into a metallurgically tougher microstructure.

(b) The stress intensity at the tip of the advancing crack was reduced by load shedding on to microstructural regions capable of withstanding higher strains (or δ).

(c) Load was shed on to the plane stress regions near the specimen surface again lowering the stress intensity at the tip of the propagating crack..

Figure 100 shows a specimen where the behaviour in cases (b) and (c) appeared possible. Shear lips can be seen on either side of the specimen with two bands of brittle intergranular fracture separated by a more ductile region in the centre. The brittle bands coincide with columnar regions while the more ductile central region is associated with the reheated refined zone. It can also be noted that the fatigue crack is shortest in the area of the left side columnar grains which would cause the highest stress intensity to be located in the least tough microstructure. The pop-in observed on this specimen was very large and was considered as a δ_m value, but this type of structure could be envisaged as causing small pop-ins if the crack extended preferentially into the columnar regions and load was shed on to the metallurgically tougher central region and on to the shear lips. The pop-ins could therefore be directly attributable to the bands of embrittled columnar structure, the magnitude of the pop-in and whether macroscopic failure occurred being controlled by the relative amounts of brittle columnar material at the notch tip and its position relative to the centre of the specimen. While pop-ins gave an indication of brittle components within the structure, the maximum load COD, δ_m, was considered as giving a more realistic value of the overall fracture characteristics of the composite structure.

The difficulties encountered in determining the appropriate critical value of δ applied equally to J. In terms of J determination in general, it appeared that the values determined were of the correct order and showed good agreement with published finite element solutions (Figures 40 and 41). The deviation of the δ-J curve at low values of δ indicated that the use of δ to calculate J would underestimate it in this range, but as this range was in, or just above the linear elastic region it would be more appropriate to calculate corrected K_c values directly. This would present no additional work provided the compatible specimen geometry was used. Apart from this restriction, the determination of J from load/clip gauge opening traces was straightforward, the only major experimental difficulty being the detection of slow crack growth, a problem which equally affects δ_i determinations.

5.4.3 Defect tolerance calculations

The defect tolerance calculations described in section 3.8 used COD values corresponding to crack initiation in the as deposited case and corresponding to fracture in the embrittled case, there being no preceding slow crack growth. All tests were performed on 10mm thick specimens and it is not possible to categorically state that the results are thickness independent, although δ_i has been found to be independent of thickness in some materials. (70). This will not change the implication of the findings as the same defect tolerance variation could be expected in thicker specimens. What should be noted is that increasing the specimen thickness will decrease the defect tolerance, all other factors, such as notch acuity being equal.

The use of less than full plate thickness specimens could also be criticized on the grounds that they did not test material from the high dilution root region. In terms of the two types of embrittlement found, examination of the low dilution area may not have revealed any embrittlement. In the case of the vanadium bearing weld metal, dilution from the vanadium free parent plate material would have lowered the vanadium content in this region and lowered embrittlement levels. Where temper embrittlement caused embrittlement, especially in AX140, susceptibility at the root should again have been lower because the HY130 had a lower phosphorus content (0.005%) and dilution from this source would have lowered the nett weld metal phosphorus level.

The results of the defect tolerance calculations using the Welding Institute design equation and the J contour integral and assuming a working stress of $\frac{2}{3}$ minimum plate yield are shown in Table 12. If the Welding Institute design equation results are initially considered, they show that Linde 120 has the highest defect tolerance followed by the 1.18 KJ/mm Bostrand 31, the 3.15 KJ/mm Bostrand 31 and AX140. As noted in section 3.8, the quoted defect sizes correspond to the half length of a through thickness crack and inspection of Table 12 shows that the lengths of critical defects are very small e.g. 6.5mm. for Linde 120 which was the toughest weld metal. However, it should be stressed that these defect estimates are conservative because they are based on fatigue crack initiation values of δ, whereas the usual use of the design equation is based on maximum load δ values obtained from a 0.15mm. slit notch. (2). If the as deposited design equation* is considered, from section 3.8:

$$\bar{a} = \frac{\delta E}{2\pi(\sigma_w + 0.75\sigma_y)} \qquad \text{.... (i)}$$

It can be seen that $\bar{a}$ varies proportionally with δ for a given stress level. The considerably lower value of δ determined from crack initiation in a fatigue cracked specimen will therefore be directly

---

*NB. The equation numbers refer to equations in this section only.

reflected in a lower predicted value of $\bar{a}$.

Dawes has shown that **critical** crack lengths predicted from δ_m in 0.15mm. notch COD specimens give conservative estimates of the defect length necessary to cause fracture in a wide plate test, the ratio of $\bar{a}$ measured in the wide plate test to $\bar{a}$ predicted by the use of COD data in the design equation varying from 1.3 to 4.5. (2). Therefore, if the use of δ_{max} measured on 0.15mm. notch specimen gives a conservative estimate of defect tolerance, the use of fatigue crack δ_i values, which are considerably lower than the former for a given material, will further increase the conservatism of the defect tolerance estimate.

There is, however, one necessary qualification for the above conclusion. The wide plate tests reported by Dawes contained 0.15mm. sawn notches and if fatigue cracks had been used, it is probable that the resulting defect tolerance would have been reduced. Dawes argues that the sawn notches should be considered as "natural" defects as they contained hydrogen cracks at the notch tip. It is not possible to categorically state if these "natural" defects were as severe as a fatigue crack: if they were not then the level of conservatism is critical crack length predictions, based on fatigue cracked δ_i values, would be reduced if the wide plate tests used fatigue cracks.

Defect tolerances calculated for the post weld heat treated weld metals show that the defect tolerances **for** Bostrand 31 and AX140 actually increase if it is assumed that the treatment completely removes residual stresses (Table 12). This result initially appears anomalous as it would be expected that the marked embrittlement observed (Figures 36 and 39) would cause a decrease in defect tolerance. What the results in fact imply, is that the removal of residual stresses completely offsets the effect of embrittlement. If 25% of the original residual stress level remains after heat treatment then the defect tolerance is lower than the as deposited value. The importance of remaining residual stress levels can be clearly illustrated if the critical crack size is plotted against residual stress levels after heat treatment as is shown in Figure 101. The appropriate embrittled values of δ and J for Bostrand 31 (1.18 KJ/mm) and AX140 were used to calculate values of the critical predicted crack length $\bar{a}$ over the range of residual stress levels, zero to equal to the yield strength. The calculations were based on the Welding Institute design equation, Figure 101 (a) and the J integral design equation Figure 101 (b).

The equations for the curves were derived as follows:

COD case (Figure 101 (a))

For zero residual stress, from section 3.8.

$$\bar{a} = \frac{\delta E}{2\pi(\sigma_w - 0.25\sigma_y)} \qquad \text{.... (ii)}$$

If a residual stress σ_R is present where $0 < \sigma_R < \sigma_y$, the total strain is given by:

$$\frac{e}{e_y} = \frac{\sigma_w}{\sigma_y} + \frac{\sigma_R}{\sigma_y} \qquad \text{.... (iii)}$$

$$\therefore \quad \bar{a} = \frac{\delta E}{2\pi(\sigma_w - 0.25\sigma_y + \sigma_R)} \qquad \text{.... (iv)}$$

The abscissa of Figure 100 (a) is the percentage of residual stress remaining after heat treatment i.e. $\frac{\sigma_R}{\sigma_y} \times 100$. The as deposited defect tolerances of Bostrand 31 and AX140 are indicated as D1 and E1 respectively.

J design case (Figure 101 (b))

For zero residual stress and using a plane strain plastic zone correction, from section 3.8.

$$\bar{a} = \frac{5}{6} \frac{J.E.}{\pi(1 - \nu^2)(\sigma_w)^2} \qquad \text{.... (v)}$$

(The zero residual stress defect tolerances calculated in Table 12 do not contain the plastic zone correction factor 5/6 because $\sigma_w < 0.8\sigma_y$ but a plastic zone correction is used here for continuity as $\sigma_w + \sigma_R$ increases).

If a residual stress σ_R is present where $0 < \sigma_R < \sigma_y$:

$$\bar{a} = \frac{5}{6} \frac{J.E.}{\pi(1 - \nu^2)(\sigma_w + \sigma_R)^2} \qquad \text{.... (vi)}$$

The abscissa of Figure 101 (b) is the percentage residual stress remaining after heat treatment i.e. $\frac{\sigma_R}{\sigma_y} \times 100$.

The rapid decrease in defect tolerance with increasing amounts of residual stress remaining after heat treatment,is clearly demonstrated with the defect tolerance falling below the as deposited defect tolerance level when the remaining residual stress exceeds very low values.

The important implication of this result is that it is necessary to know the actual residual stress level after post weld heat treatment if the heat treatment causes embrittlement. The limited material published on residual stress levels in HY series plate materials and weld metals, indicates that post weld heat treatments of six hours in the 500 to 600°C range do not totally remove residual stresses (Figure 102). (21). As relatively low levels of residual stress can critically alter the nett defect tolerance of a material embrittled by heat treatment, the frequently used assumption that post weld heat treatment leads to the complete removal of residual stresses can lead to a non conservative estimate of defect tolerance.

While it is possible to raise many conjectural arguments about the validity of some of the assumptions implicit in the derivation of the design equations, their correlation with wide plate test behaviour for the as deposited case is established, and these correlations represent the best available fracture theory to-date. However, when the stress relieved assumptions are considered, there appears to be only one instance where wide plate tests have been made to check COD predictions. This information is contained in a paper by Dawes (102) and unfortunately, he gives very little information about the wide plate tests, although sufficient data is presented to enable some defect tolerance calculations to be made here. The weld metal considered has a composition very similar to Bostrand 31 and COD tests showed that the critical COD decreased after stress relief. Defect tolerance calculations using this data can be made. In this instance, a working stress of 2/3 plate yield is assumed and equation (i) is used to calculate the critical crack size in the as deposited case, while equation (ii) is used for the stress relieved case (assuming zero residual stress).

$$\bar{a} = \frac{E}{2\pi(\sigma_w - 0.25\sigma_y)} \qquad \text{.... (ii)}$$

	δ_c mm	σ_y MN/m^2	σ_w MN/m^2	$\bar{a}$ mm
As deposited	.07	704	380	2.53
Stress relieved	.025	809	380	4.61

The increase in defect tolerance, despite embrittlement reducing δ_c, is clearly illustrated. The wide plate tests carried out on the as deposited and stress relieved welds contained predetermined defect lengths and so the predicted critical crack lengths were calculated from the fracture stress. The two results obtained for the stress relieved weld are marked SR in Figure 103 which also includes results from other tests. The significance of this result is that the predicted defect size is again less than the critical defect size to cause fracture, which means that equation (ii) gives a realistic estimate of the effect of the removal of residual stress. The calculation was based on assuming zero residual stress (equation (ii)) and if residual stresses had been present, they would tend to reduce the conservatism of the defect tolerance estimate. The fact that assuming zero residual stress still gave a conservative estimate of the critical crack size means that either the actual residual stress level was very low or that there is a sufficient margin of conservation in equation (ii) to accommodate some residual stress without giving non conservative critical crack sizes.

It cannot be argued that the use of the Welding Institute design equation for weld metals embrittled by stress relief has been positively substantiated when only two tests have been performed on one weld metal. It is hoped that further work, considering the effects of residual stresses on wide plate test results, will be carried out so that correlations with COD behaviour can be further reinforced. This is very important because the use of such a detailed design approach appears to enable embrittled weld metals to be safely used provided residual stress levels after post weld heat treatment are known.

Table 12 also shows defect tolerance calculations based on J values and assuming the same working stress levels. The absolute magnitudes of the critical crack sizes are approximately 3 times greater than the equivalent COD - Welding Institute design equation predictions, although no safety factor has been included in the calculation, whereas the latter approach has been shown conservative. These results also indicate a substantial improvement in defect tolerance after heat treatment if zero residual stress levels are assumed.

There are no obviously incorrect assumptions in the calculations, although the factoring of the plastic zone conections could be disputed. The assumption that the effective stress in the as deposited case is equal to σ_y, the yield stress, undoubtedly underestimates the true effective stress due to the superimposition of the working stress on the residual stress. On the other hand, adding the stresses would result in an over-estimate of the true stress intensity. This is because the actual loading in such cases is strain, rather than stress, controlled. The true effective stress would lie between the two extremes and therefore, the J based, as deposited crack sizes listed in Table 12 are likely to be an over-estimate of the true critical crack size. The use of a true effective stress value would then reduce these values towards the COD, as deposited values. However, this factor does not change the main point of the argument. The reduction in as deposited crack lengths would further increase the magnitude of the nett defect tolerance improvement after post weld heat treatment.

This nett improvement is due to the dominant effect of σ^2 in the general design equation (including plastic zone correction).

$$\bar{a} = \frac{5}{6} \frac{J.E.}{\sigma^2 \pi(1 - \nu^2)} \quad .... \text{(vii)}$$

The importance of residual stresses remaining after post weld heat treatment is through its effectively squared effect i.e.

$$\bar{a} = \frac{5}{6} \frac{J.E.}{\pi(1 - \nu^2)(\sigma_w + \sigma_R)^2} \quad .... \text{(vi)}$$

Small changes in the level of residual stress can therefore offset changes in J due to embrittlement and the importance of knowing residual stress levels after post weld heat treatment where the weld metal is embrittled is again demonstrated (Figure 101). Little further comment can be made on these results as the whole J concept in terms of defect tolerance is untested and the validity of the approach needs to be confirmed by large scale simulative tests such as wide plate tests. However the J results confirm the trends shown by the COD results, the only difference being in the magnitude of the critical predicted crack sizes.

The main points from the preceding discussion can be summarized as follows:

1. The apparently low magnitudes of upper shelf, as deposited δ_m and δ_i values were directly attributable to the use of fatigue cracked specimens. Comparisons with other weld metals tested using fatigue cracked specimens showed that the magnitude of the results was of the right order.

2. The use of δ_i values obtained from fatigue cracked specimens in the Welding Institute design equation resulted in very low as deposited defect tolerances which were possibly over-conservative because the equation had been derived from machined notch, δ_m values.

3. The Welding Institute design equation predicted a nett improvement in defect tolerance after post weld heat treatment for Bostrand 31 and AX140, even though substantial embrittlement had occurred. This assumed total removal of residual stresses, but if some residual stresses remained after heat treatment, defect tolerance decreased rapidly as remaining residual stress levels increased above zero.

4. Values of J determined from load/clip gauge traces showed good agreement with published finite element solutions with some tendency to under-estimate J at low COD values.

5. Defect tolerances derived from J values showed the same trends as those from COD values, although they were up to 3 times larger in magnitude.

5.5 Practical implications and further work

The work discussed in the previous sections has shown that each of the three high strength weld metals examined could be embrittled to varying extents by post weld heat treatment. Two types of embrittlement were identified; precipitation hardening which promoted cleavage fracture and temper embrittlement which caused failure along prior austenite grain boundaries. The heat treatments used were deliberately extreme to cause a large amount of embrittlement, so that the cause of embrittlement could be readily identified. What is now required is the development of post weld heat treatment procedures which are more directly applicable to industrial fabrication practice and through which the positive advantages of heat treatment can be realized while any embrittlement tendencies are minimized. While the treatments detailed in section 3.5 did not cover every combination of treatment temperature, time, and cooling rate, sufficient information was gained so that appropriate recommendations can be made for the three weld metals examined and, additionally, guidelines for the heat treatment of other high strength, alloy bearing weld metals can be suggested.

For a given weld metal, the maximum treatment temperature will be dictated by either the temperature at which the weld metal is softened, lowering its room temperature strength below the design requirement, or by the tempering temperature of the plate material, the lower of the two being used for treatment. The weld metals must therefore be considered in combination with the appropriate parent plate. While lower treatment temperatures could be used, this would necessitate longer treatment times for the same level of stress relaxation (21) and as the likely treatment temperatures are in, or just above the 400 to 550°C temper embrittlement range, as high a treatment temperature as possible avoiding plate or weld metal softening should be used. Further considerations of appropriate heat treatment procedures are better illustrated by considering each weld metal in turn.

Linde 120 used in conjunction with HY100 plate was found to be only slightly susceptible to temper embrittlement, but it must be stressed that other treatment schedules, particularly using very slow cooling rates may have increased embrittlement. The treatment cycle should therefore be designed to avoid embrittlement from this source. The maximum temperature to avoid weld metal softening is approximately 600°C which is similar to the plate tempering temperature and if this treatment temperature was used it would give maximum stress relaxation in minimum time. Linde 120 did not appear to be embrittled by prolonged exposures at high temperatures (Figure 33), but the bulk of stress relaxation would probably occur in the first two hours as found in other high strength weld metals (21), so treatment times should be restricted to similar periods. The final level of embrittlement will then be dictated by the maximum cooling rate after treatment. Figure 33 shows that cooling rates of 100°C/hour or greater will not cause marked embrittlement, but embrittlement could be expected to increase if slower cooling rates were used. The actual cooling rate achieved will be dependent on the structural configuration of the fabrication and the section thicknesses. If slower cooling rates do occur then it would be necessary to simulate them in a weld sample and evaluate the effects by Charpy testing. If these tests in turn showed marked embrittlement then a fracture mechanics analysis would be required. This will be further discussed after the other two weld metals have been considered.

AX140 was significantly more susceptible to temper embrittlement than Linde 120. Similar treatment constraints apply to this weld metal as outlined above for Linde 120, with the additional factor that as treatment temperatures will be in the embrittlement range (HY130 is tempered at 565°C (21)), the treatment time should be kept very short e.g. 2 hours. Figure 33 indicated that at 100°C/hour cooling rates, there will be some embrittlement which could be expected to increase for slower cooling rates, so it appears that some embrittlement must be expected unless very high cooling rates are used. Again the significance of this embrittlement can only be evaluated by a fracture mechanics analysis.

Bostrand 31 was embrittled by vanadium carbide precipitation which promoted cleavage fracture and embrittlement was detected after 1 hour in the 550 to 650°C temperature range. The design of a suitable treatment for this material is therefore severely restricted. The possibilities appear to be either overageing by holding for prolonged periods at 650°C or by treating at temperatures below the vanadium carbide precipitation range. The former alternative would probably be unsuitable as it would lead to plate softening (HY180 is tempered at 650°C (6)). With the second alternative, very low treatment temperatures would be required as vanadium carbide can begin to precipitate at 450°C after 15 hours(110) and embrittlement was detected after 50 hours (Figure 24). This means that temperatures around 400°C would be required and it is doubtful if significant stress relaxation would occur. If HY80 fabrications require post weld heat treatment,it would be more advisable to change to a vanadium free consumable. Vanadium was undoubtedly added to promote acicular ferrite formation but this could also be achieved by increasing molybdenum and nickel as in Linde 120. With suitable modification, a heat treatable weld metal could be developed, although precautions against temper embrittlement should still be taken.

The above discussion has been based on avoiding or minimizing any embrittlement. In section 3.8, defect tolerance calculations showed that the defect tolerance of the embrittled weld metals actually increased if total removal of residual stresses was assumed. Additionally, it must be emphasized that these calculations were based on extremely severe embrittlement treatments e.g. 550°C for 50 hours for Bostrand 31 and AX140. A less severe treatment, for example AX140 treated at 550°C for 2 hours and cooled at 100°C/hour, causes much less embrittlement (Figure 33) and would therefore result in a higher defect tolerance, thus increasing the magnitude of the improvement in defect tolerance after heat treatment. This therefore suggests that, provided treatment times are kept short and fairly rapid cooling rates are used, Bostrand 31 and AX140 can be post weld heat treated safely. The qualification must be added that the final defect tolerance will be dictated by the remaining residual stress levels after heat treatment, as shown in section 5.4 and Figure 101. This then means that prospects of post weld heat treatment should not be abandoned if, for example, Charpy testing shows that embrittlement occurs. What is then required are COD (or J) tests on weld metal which has been cycled through the actual proposed heat treatment cycle. This data, along with stress relaxation data to indicate remaining residual stress levels, can be used to calculate defect tolerance levels. These results may then indicate that while embrittlement occurs, residual stress levels are sufficiently reduced to actually increase defect tolerance.

Also noted in section 5.4 was the observation that the satisfactory use of the Welding Institute design equation has only been demonstrated in one instance for post weld heat treated weld metal and this is possibly the most important area for future work. If further COD or J, and wide plate test correlations confirm the reliability of the Welding Institute design approach in dealing with stress relieved weld metals, then some weld metal embrittlement may well be tolerable.

The findings from this work can be used to establish guidelines for the post weld heat treatment of other high strength weld metals. The most important consideration is that temper embrittlement can occur during a normal heat treatment cycle, as shown by the 10 hours at 550°C, 100°C/hour cooling rate, cycles for AX140 and Linde 120. The manufacturers of Linde 120 are currently contemplating a treatment of 50 hours at 607°C and cooling at 5.5°C/hour (95) which demonstrates that the slow cooling rate cycles used in this work were by no means extremely unrealistic. Temper embrittlement could be expected to be significant in the proposed Linde 120 treatment. If the possibility of temper embrittlement is acknowledged then the basic heat treatment cycle should be designed on the basis of using the highest possible temperature for a short time, e.g. 2 hours, and cooling as fast as possible. This cycle should be checked by doing an exact simulation on a weld sample and performing Charpy test comparisons with the as deposited weld metal. If embrittlement is detected then a more detailed fracture mechanics analysis, as outlined earlier in this section, would be required. Such a simulative cycle would also indicate if embrittlement caused by precipitating carbides was present; vanadium, niobium and possibly titanium being the likely responsible alloying elements. Molybdenum at levels up to 0.6% did not appear to promote embrittlement in this work, although there are contrary reports in the literature (7) which were discussed in section 5.2.2. These findings should be relatively independent of the welding process used and could equally be expected in MIG welds as the impurity content or strong carbide forming alloy content will be dominated by the welding wire composition. The only additional factor to consider is that it appears that martensitic weld metal microstructures are more susceptible than acicular ferrite and so temper embrittlement will be a greater problem at higher strength levels where martensitic structures are required (above 896 MN/m^2).

In the preceding discussion, attention has been focussed on the weld metal, but it should be noted that temper embrittlement is also possible in the plate material (109) along with problems such as reheat cracking. These considerations are beyond the scope of this work, but plate material should also be examined prior to embarking on post weld heat treatment. The problem of reheat cracking is usually more common in creep resisting steels, although many aspects of it are related to segregation of impurities to prior austenite grain boundaries. This subject has been comprehensively reviewed by Boniszewski. (111).

Possible future work on the problem of embrittlement caused by post weld heat treatment can be divided into two areas. The first is further confirmational work on the fracture mechanics predictions as has been previously mentioned. While this does not overcome the problem of embrittlement, it may well show that embrittlement is not a problem, the effect of removing residual stresses completely overriding any embrittlement. The second is work to remove, or minimize any embrittlement. This should be straightforward in the case of embrittlement caused by precipitation hardening by discontinuing the use of vanadium and niobium to promote acicular ferrite and suitable compositions free of this problem, such as Linde 120, are already available. The problem of temper embrittlement is less straightforward as indicated by the sustained research in this area over the last few decades. Further reduction of phosphorus levels is an obvious solution and it is interesting to note that this is the exact solution suggested by Wolstenholme when he observed temper embrittlement in a manual metal arc weld metal. (56). The phosphorus levels he examined were 0.02% which have been halved in AX140 and yet temper embrittlement persists. A relatively simple further step would be to reduce the phosphorus level in AX140 to the same level as that in the parent plate, HY130, which is 0.005%. If this does not solve, or reduce the problem, it is difficult to see that the economic penalty in further reducing phosphorus levels will be justified by the improved temper embrittlement resistance. This again suggests that the fracture mechanics analysis may hold the solution, or at least the final compromise.

CHAPTER 6 CONCLUSIONS

The effects of post weld heat treatment on the properties of three high strength submerged arc weld metals spanning a yield strength range of 550 to 900 MN/m^2 were examined and the following conclusions drawn.

1. Post weld heat treatment over the temperature range of 450 to 550°C causes embrittlement of each of the three weld metals. Bostrand 31 and AX140 could be severely embrittled while Linde 120 was only slightly embrittled.

2. Bostrand 31 was embrittled by the precipitation of vanadium carbide which promoted transgranular cleavage fracture. Embrittlement occurred over the 450 to 650°C temperature range and was greatest at 550°C. The embrittlement severity increased with treatment time.

3. Vanadium contents of 0.12% were sufficient to cause severe precipitation hardening embrittlement. Molybdenum at levels up to 0.6% did not cause precipitation hardening induced embrittlement after 50 hours at temperatures corresponding to the peak secondary hardening temperature (500°C).

4. Embrittlement of AX140 was caused by classical temper embrittlement which caused decohesion of prior austenite columnar grain boundaries. This form of embrittlement was also responsible for the slight embrittlement of Linde 120.

5. Temper embrittlement was caused by the migration of phosphorus to prior austenite grain boundaries during post weld heat treatment in the 450 to 550°C temperature range. A bulk phosphorus content

of 0.011% was sufficient to cause severe embrittlement. The amount of embrittlement increased with treatment time and decreasing cooling rate after post weld heat treatment.

6. Martensitic weld metal microstructures appeared to be more susceptible to temper embrittlement than acicular ferrite microstructures.

7. Heat treatment at relatively high temperatures (650°C) could cause an increase in toughness over as deposited toughness levels, but caused an unacceptable decrease in yield strength.

8. The relative as deposited toughness levels of the three weld metals could be successfully related to their microstructures in terms of existing weld metal toughness models. The role of martensite in acicular ferrite was examined and it was concluded that its relationship to cleavage fracture needs further clarification.

9. Defect tolerance calculations based on COD and J contour integral data showed that the defect tolerance of AX140 and Bostrand 31 increased after post weld heat treatment, even though the treatment caused severe embrittlement. It was found that residual stress levels remaining after heat treatment could critically affect the final defect tolerance with defect tolerance decreasing rapidly as residual stress levels increased above zero.

10. The results of the embrittlement study suggested that Linde 120 and AX140 could be heat treated with minimum embrittlement by using a treatment temperature equal to the plate tempering temperature, a short treatment time and as high a cooling rate as possible. Bostrand 31 cannot be post weld heat treated without substantial embrittlement. However, the fracture mechanics analysis showed that some embrittlement could be tolerated and still lead to an increase in defect tolerance after heat treatment.

11. The possibility of both temper embrittlement and precipitation hardening embrittlement should be recognized when designing post weld heat treatment procedures for high strength weld metals.

APPENDIX 1

Fracture mechanics notation

P - Load
a - Crack length
$\bar{a}$ - Critical crack length predicted by design equations
B - Specimen thickness
W - Specimen width
S - Specimen span between supports in 3 point bend test
V - Clip gauge opening
V_i - Clip gauge opening at crack initiation
V_m - Clip gauge opening at maximum load
δ - Crack opening displacement
δ_i - Crack opening displacement at crack initiation
δ_m - Crack opening displacement at maximum load
δ_c - Critical crack opening displacement at fracture
Y - Non dimensional function of a/W
z - Height of knife edges
σ_y - Weld metal yield stress
σ_w - Working stress
σ_R - Residual stress
σ - Stress
e - Strain
e_y - Yield strain
E - Young's modulus
ν - Poisson's ratio
J - J contour integral
J_i - J contour integral at crack initiation
J_c - J contour integral at fracture

K - Stress intensity

K_c - Stress intensity at fracture

K_{1C} - Plane strain fracture toughness

K_f - Fatigue stress intensity

q - Load point displacement

U_{p-q} - Area under load/load point displacement curve

U_{p-v} - Area under load/clip gauge opening curve

T_{55J} - 55 joule energy absorbed temperature in Charpy test

T - Test temperature

APPENDIX 2

Calculation of errors in the determination of COD

It was noted in section 3.5.5.5 that the Well's equations contain a value of σ_y, the weld metal yield stress and as this varies with temperature, a rigorous calculation of δ should use a value of σ_y determined at the test temperature in question. In this work, the value of σ_y used in all calculations was determined at 20°C only. As σ_y increases with decreasing temperature, the 20°C value would underestimate the true σ_y value at low temperatures and hence, δ values calculated from the 20°C value of σ_y would over-estimate the true COD as test temperature decreased. An estimate of the maximum likely error was calculated from data presented by Saunders (reference 10) who determined the variation of yield stress with temperature for a series of high strength martensitic weld metals. These results indicated that σ_y could increase by up to 25% over the 20° to -75°C range. The maximum error would therefore be represented by the increase in yield stress at -75°C. COD values were calculated for values of clip gauge opening V, ranging from 0.10 to 1.50mm., the range covered in the present work. A constant a/W of 0.5 was assumed and the calculations were based on the as deposited yield strength of AX140 assuming zero increase and a 25% increase in yield stress.

			V							
σ_y	MN/m^2		0.1	0.2	0.3	0.4	0.5	0.8	1.0	1.5
Zero Increase	887	δ	.004	.018	.040	.062	.084	.150	.195	.306
25% Increase	1108		.004	.015	.034	.056	.078	.144	.189	.300

If σ_y increased by 25% the calculated COD was lowered by 0.006mm. down to a clip gauge opening of 0.3mm. whereafter the difference tended to zero. The over-estimation of δ due to using the room temperature value of σ_y was accordingly 0.006mm. maximum and would decrease as test temperatures increased above -75°C. The magnitude of this over-estimation was small in relation to the scatter and to the absolute values of δ and was accordingly considered negligible.

APPENDIX 3

Quantitative Metallography

The area fractions of the constituents, proeutectoid, ferrite, acicular ferrite and martensite were determined for the three weld metals, Linde 120, Bostrand 31 (1.18 KJ/mm) and Bostrand 31 (3.15 KJ/mm). Martensite was assumed to be present in the acicular ferrite and so the area fractions of proeutectoid ferrite and acicular ferrite plus martensite were initially determined. The percentage of martensite in the acicular ferrite was then determined, giving absolute values of the martensite and proeutectoid ferrite and the percentage of acicular ferrite was obtained by subtraction. Determination of proeutectoid ferrite and acicular ferrite plus martensite was carried out on nital etched specimens at 200X magnification while the area fraction of martensite was measured at 2000X magnification on specimens etched in 4% picral.

A "Swift" point counting system was used for all determinations, in which, a cross is displayed in the eyepiece of a conventional optical microscope. The structure under the cross is identified and counted on the appropriate register of a cummulative counting machine. As each count is made, the cross hairs are moved by a predetermined amount and thus, counts along a line can be made. To generate a grid pattern, the cross hairs are moved at 90° to the counting direction and a new line count is made. Thus, a grid can be built up by performing several line counts with a constant spacing between the lines.

In this work, it was noted that proeutectoid ferrite was very directional and therefore required a square grid count to arrive at an unbiased estimate. The grid used was 50 counts at 0.02mm. intervals, which were repeated for 10 lines, 1mm. apart, giving 500 counts over a 10mm. by 10mm. area. (These were the actual displacements of the cross hairs in the eyepiece. The actual movement over the specimen is found by dividing the displacements by the magnification factor). As the martensite was uniformly distributed throughout the acicular ferrite, the grid adopted for the high magnification work was more directional, using 5 lines of 100 counts in 0.1mm. steps with a line spacing of 2mm., again giving 500 counts over a 10 x 10mm. area. Three randomly selected areas were measured at the high and low magnifications on each specimen and the mean of the three determinations was used to calculate the final results which are shown in Table 13.

The volume fractions of inclusions were obtained by calculation, following a method proposed by Steel (101) where it was assumed that all sulphur was combined as MnS and all oxygen was combined as $2MnOSiO_2$. The volume fraction of each inclusion type can therefore be calculated directly from the chemical analysis assuming the inclusion density is half that of iron.

Estimates of the acicular ferrite grain size were made by counting linear intercepts on a 0.1mm. gauge length. Each determination was the mean of 5 counts. The prior austenite grain sizes of Linde 120 and AX140 were estimated by counting linear intercepts on a 0.4mm. gauge length with the counting direction normal to the longitudinal austenite grain axes. Ten counts were made on each specimen.

APPENDIX 4

Determination of retained austenite in AX140 weld metal

The method used was based on the recommendations of a Philips Scientific Report No. 79.136/RD1 "The determination of retained austenite by quantitative X-ray diffraction". This method is based on the ratio of the integrated intensities of a selected ferrite and austenite line being proportional to the ratio of the volume fractions of each phase. If the intensity ratio is determined, the volume fraction of austenite can be calculated.

The two lines chosen for comparison were $(200)_\alpha$ and $(220)_\gamma$. The derivation in the above reference shows that for MoK_α radiation:

$$\frac{I_\gamma}{I_\alpha} = 1.31 \frac{V_\gamma}{V_\alpha} \qquad \text{.... (1)}$$

I_γ - integrated intensity of $(220)_\gamma$ line

I_α - integrated intensity of $(200)_\alpha$ line

V_γ - volume fraction of austenite

V_α - volume fraction of ferrite

$$V_\alpha + V_\gamma = 1 \qquad \text{.... (2)}$$

$$\therefore \quad V_\gamma = \frac{I_\gamma}{I_\alpha} \frac{1}{\frac{I_\gamma}{I_\alpha} + 1.31} \qquad \text{.... (3)}$$

Measurement was performed on a Philips X-ray set with a wide angle goniometer. The experimental conditions were as follows:

Radiation	Mo K_α
Voltage	48KV
Current	20 mA
Divergence slit	1°
Receiving slit	0.2mm.
Scatter slit	1°
Detector	scintillation counter
Scanning speed	0.25°/min.

The Bragg angle (2θ) range scanned was from 27° to 30° to cover the $(200)_\alpha$ at 28.6° and from 31° to 33.5° to cover the $(220)_\gamma$ at 32.5°. Counts were printed out at 4 second intervals and the integrated intensity was measured by adding the counts under the peak and subtracting the background counts which were determined on either side of the peak.

Five scans of each peak were made and the means of the five scans were used to calculate the mean volume fraction.

I_α mean = 14258

I_γ mean = 293

From equation (3)

$V_\gamma = 1.5\%$

The highest value of I_α was linked with the lowest value of I_γ to calculate the minimum V_α and vice versa to calculate the maximum giving a final value of:

$V_\gamma = 1.5 \pm 0.4\%$

This value is at the limit of detection of retained austenite and must therefore be considered with caution. An even stronger objection is that preferred orientation in the weld metal was noted by rotating the sample through 90° which changed the I_α integrated intensity. The derivation of equation (1) assumes random orientation and is not valid if preferred orientation is present, principally through its effect on the Lorentz-Polarisation factor used in the derivation. This further throws the value determined into question. It was concluded that a peak corresponding to the presence of austenite was detected, and was due to a small quantity of retained austenite.

APPENDIX 5

Acknowledgements

The author gratefully acknowledges the supervision and continued enthusiastic support of Dr M F Jordan throughout this project. Thanks are also due to Professor R H Thornley, Head of the Department of Production Engineering for providing laboratory facilities and also to the Metallurgy Department for the use of their metallographic facilities. The work was supported by the Procurement Executive of the Ministry of Defence and special thanks go to Mr I Kilpatrick of NCRE for initially suggesting the project, supplying the welded panels and for his valued remarks during the course of the work. The assistance of members of staff, technicians and fellow postgraduates in the Departments of Production Engineering and Metallurgy is also acknowledged. The author also wishes to thank Christine Maddison for patiently typing this thesis.

BIBLIOGRAPHY

1. Doty W.D.; Welding J., 1965, <u>44</u>, 289s-309s.

2. Dawes M.G.; Welding Institute Research Report E/58/74, 'Brittle fracture in high strength weldments.' 1974.

3. BS 1500, 'Fusion welded pressure vessels: General purposes.' 1958.

4. BS 1515, 'Fusion welded pressure vessels (advanced design and construction for use in the chemical, petroleum, and allied industries). 1965.

5. ASME Section VIII Pressure Vessels: Division 1. 1968.

6. Welding Institute Report; 'The metallurgy and welding of QT 35 and HY 80 steels.' 1974.

7. Garland J.G. and Kirkwood P.R.; Metal Construction, 1975, <u>7</u>, 275-283 and 320-330.

8. Davies G.J. and Garland J.G.; International Metallurgical Reviews No. 196, 1975, <u>20</u>, 83-106.

9. Widgery D.J. and Saunders G.G.; Welding Institute Research Bulletin, 1975, <u>16</u>, 277-281.

10. Saunders G.G.; Welding Institute Research Report M86/75, 'Effect of major alloying elements on the toughness of high strength weld metal.' 1975.

11. Farrar R.A., Tuliani S.S. and Norman S.R.; Institute of Metallurgists, 'The practical implications of fracture mechanisms.' 1973, 142-144.

12. Dorschu K.E. and Lesnewich A.; Welding J., 1964, <u>43</u>, 564s-576s.

13. Shackleton D.N.; Welding Institute Report, 'Welding HY 100 and HY 130 steels.' 1973.

14. Stout R.D. et al.; Welding J., 1969, <u>48</u>, 155s-160s.

15. Connor L.P. et al.; Welding J., 1967, <u>46</u>, 309s-321s.

16. Widgery D.J.; Welding J., 1976, <u>55</u>, 57s-68s.

17. Widgery D.J.; Welding Institute Research Report M46/69, 'The influence of microstructure on fracture initiation in mild steel weld metals.' 1969.

18. Dolby R.E.; Welding Institute Report 14/1976/M, ' Factors controlling weld toughness - the present position. Part 2. Weld metals.' 1976.

19. Enis A. and Telford R.T.; Welding J., 1968, <u>47</u>, 271s-278s.

20. Masubuchi K. et al.; Welding Research Council Bulletin No. 111, 1966.

21. Rosenstein A.H.; NSRDC Report 2843, 'Stress relief characteristics of HY 130 weld metal.' 1969.

22. Almqvist G. et al.; CEGB, Int. Conf. on Welding Research Related to Power Plant.' 1972, 204-231.

23. Garland J.G. and Kirkwood P.R.; BSC Open Report PROD/643/1/75/C, 'The influence of vanadium on submerged arc weld metal toughness.' 1975.

24. Taylor L.G. and Farrar R.A.; Weld. and Metal Fab., 1975, <u>43</u>, 305-310.

25. Garland J.G. and Kirkwood P.R.; BSC Open Report PROD/499/1/74/C, 'The notch toughness of submerged arc weld metal in micro alloyed structural steels.' 1974.

26. Uda M. and Ohno S.; J. Japan Weld. Soc., 1972, <u>41</u>, 772-776.

27. Hughes P.C.; BWRA Research Bulletin, 1967, <u>8</u>, 206-212.

28. Garland J.G. and Kirkwood P.R.; BSC Open Report PROD/176/21/75/C, 'A reappraisal of the relationship between flux basicity and mechanical properties in submerged arc welding.' 1975.

29. Dawes M.G.; Welding Institute Research Report E33/70, 'Fracture initiation in weld metals.' 1970.

30. Swift R.A. and Rogers H.C.; Welding J., 1971, <u>50</u>, 357s-373s.

31. Puzak P.P. and Pellini W.S.; Welding J., 1952, <u>31</u>, 521s-526s.

32 Sagan S.S. and Campbell H.C.; Welding Research Council Bulletin No. 59, 1960.

33. Campbell D.J. et al.; Weld. and Metal Fab., 1974, <u>42</u>, 104-110.

34. Hannerz N.E. and Jonsson-Holmquist B.M.; Metal Construction, 1974, <u>6</u>, 64-67.

35. Batte A.D. and Honeycombe R.W.K.; J.I.S.I., 1973, <u>211</u>, 284-289.

36. Bentley K.P.; Brit. Weld. J., 1964, <u>11</u>, 507-515.

37. Wheatley J.M. and Baker R.G.; Brit. Weld. J., 1962, <u>9</u>, 378-387.

38. Bland J.; Welding J., 1956, <u>35</u>, 181s-194s.

39. Honeycombe R.W.K.; 'Structure and strength of alloy steels.' Climax Molybdenum Co., Publication, 1973.

40. Woodfine B.C.; J.I.S.I., 1953, <u>173</u>, 229-240.

41. McMahon C.J.; ASTM STP 407, 'Temper embrittlement in steel.' 1968, 127-167.

42. Steven W. and Balajiva K.; J.I.S.I., 1959, 193, 141-147.

43. Marcus H.L. et al.; ASTM STP 499 'Temper embrittlement of alloy steels.' 1971, 90-103.

44. Hondros E.D.; Conf. on the mechanics and physics of fracture. Inst. of Physics and Metals Soc., 1975. Paper 21.

45. Saunders G.G.; I.S.I. Report, 'Heat treatment aspects of metal joining processes.' 1972, 18-28.

46. McMahon C.J.; Conf. on the mechanics and physics of fracture. Inst. of Physics and Metals Soc., 1975. Paper 20.

47. Capus J.M.; J.I.S.I., 1962, 200, 922-927.

48. Joshi A. and Stein D.F.; ASTM STP 499, 'Temper embrittlement of alloy steels.' 1972, 59-89.

49. Woodfine B.C.; J.I.S.I., 1953, 173, 240-255.

50. Viswanathan R. and Joshi A.; Met. Trans.A., 1975, 6A, 2289-2297.

51. Geniets L.C.E. and Knott J.F.; Met. Sci. J., 1972, 6, 69-71.

52. Jolly P. and Goux C.; Mem. Sci. Rev. Metallurgy., 1969, LXVI, 605.

53. Thwaites C.J. and Chatterjee S.K.; J.I.S.I., 1972, 210, 581-587.

54. Ohtani H.C. et al.; Met. Trans., 1974, 5, 516-518.

55. Bruscato R.; Welding J., 1970, 49, 148s-156s.

56. Wolstenholme D.; Int. Conf. on Welding Research Related to Power Plant. 1972, 310-325.

57. Rosenstein A.H. and Asche W.H.; MEL R & D Report 116/67, 'Stress relief embrittlement of AX140 and E-11018 weld metals.' 1967.

58. Knott J.F.; 'Fundamentals of fracture mechanics.' Butterworths, London, 1973.

59. Turner C.E. and Burdekin F.M.; Atomic Energy Review, 1974, 12, 439-503.

60. Lange E.A.; 'Toward improved ductility and toughness.' Climax Molybdenum Co. Publication, 1971, 33-44.

61. Loss F.J. and Pellini W.S.; 'Practical fracture mechanics for structural steel.' UKAEA, 1969. Paper J.

62. Irwin G.R.; Trans. ASME, J. App. Mechs., 1957, 24, 361-364.

63. Brown W.F. and Scrawley J.E.; ASTM STP 381, 1965, 133-196.

64. Brown W.F. and Scrawley J.E.; ASTM STP 410, 1967, 1-129.

65. British Standards Draft for Development D.D.3., 'Methods for plain strain fracture toughness testing.' 1972.

66. Burdekin F.M. and Dawes M.G.; Proc. I. Mech. E. Conf., 'Practical application of fracture mechanics to pressure vessel technology.' 1971, 28-37.

67. Burdekin F.M. and Stone D.E.W.; J. Strain Analysis, 1966, 1, 145-153.

68. Harrison J.D. et al.; Second Conf. Significance of Defects in Welded Structures, 1968, 65-79.

69. Egan G.R.; Welding Institute Research Report E/52/72, 'Some relationships between fracture toughness, applied stress or strain and flaw size.' 1971.

70. Smith R.F.; Institute of Metallurgists, 'The practical implications of fracture mechanisms.' 1973, 28-40.

71. Smith R.F. and Knott J.F.; I. Mech. E. Conference, 'Practical application of fracture mechanics to pressure vessel technology.' 1971, 65-72.

72. Rice J.R.; Trans. ASME, J. App. Mech., 1968, 35, 379-386.

73. Hayes D.J. and Turner C.E.; Int. J. of Fracture, 1974, 10, 17-31.

74. Rice J.R. et al.; ASTM STP 536, 1973, 231-244.

75. Sumpter J.D.G.; Material presented at the 3rd International Post Experience Course on Fracture Mechanics, Imperial College, London, 1974. See also; Sumpter J.D.G. Ph.D. Thesis, Imperial College, London, 1974.

76. Dawes M.G.; Welding Institute Research Report E/65/75, 'J estimation procedures for weldments.' 1975.

77. Sumpter J.D.G. and Turner C.E.; ASME 2nd Int. Conf. on Pressure Vessel Technology, Part II, 1973, 1095-1103.

78. Egan G.R.; Engineering Fracture Mechanics, 1973, 5, 167-185.

79. Begley J.A. and Landes J.D.; ASTM STP 514, 1972, 1-23.

80. Begley J.A. and Landes J.D.; ASTM STP 560, 1973, 170-186.

81. British Standards, Draft for Development DD 19, 'Methods for crack opening displacement (COD) testing.' 1972.

82. Harrison J.D.; Welding Institute Research Report, E/64/75, 'A comparison between four elasto plastic fracture mechanics parameters.' 1975.

83. Dawes M.G.; Welding Institute Research Bulletin, 1973, 14, 157-161.

84. BS 131 : Part 2 : 1972, 'The Charpy V - notch impact test on metals.'

85. Strunck S.S. and Stout R.D.; Welding J., 1972, 51, 508s-520s.

86. Chatfield C.; 'Statistics for Technology.' Penguin Books, 1970, 174.

87. Dawes M.G.; Welding Institute Research Report E/39/70, 'Fatigue pre-cracking weldment fracture mechanics specimens.' 1970.

88. Archer G.L.; Welding Institute Research Report E/63/75, 'The relationship between notch tip and notch mouth displacements in SENB fracture toughness specimens.' 1975.

89. Ritchie R.O. et al.; Int. J. of Fracture Mechanics, 1971, 7, 462-467.

90. Holder R.; Ph.D. Thesis, Univ. of Aston in Birmingham. 1976.

91. Barnby J.T. and Al-Daimalani I.S.; To be published in J. Materials Science, 1976.

92. Hayes D.J.; Data quoted in reference number 78.

93. Andrews K.W., Dyson D.J. and Keown S.R.; 'Interpretation of electron diffraction patterns.' Adam Hilger Ltd., 1971.

94. Powder Diffraction File; Joint committee on powder diffraction standards.

95. Lyttle K.A.; Union Carbide Corporation, Private communication to M.F. Jordan, University of Aston.

96. Woodhead J.H. and Quarrell A.G.; 'The role of carbides in low-alloy creep-resisting steels.' Climax Molybdenum Co. Publication, 1965.

97. Baker R.G. and Nutting J.; Iron and Steel Institute Special Report No. 64, 1959, 1-22.

98. Andrews K.W. et al.; J.I.S.I., 1972, 210, 337-350.

99. McInnes D.R. and Smith E.; Metal Construction, 1975, 7, 35-40.

100. Ingham T. et al.; I. Mech. E. Conference, 'Practical application of fracture mechanics to pressure vessel technology.' 1971, 200-208.

101. Steel A.C.; Welding Institute Research Report M/64/71, 'The effects of sulphur and phosphorus on the toughness of mild steel weld metal.' 1971.

102. Dawes M.G.; Welding J., 1974, 42, 369s-379s.

103. Lindley T.C. et al., Iron and Steel Institute Special Report, 'Effects of second phase particles on the mechanical properties of steel.' 1971, 54-59.

104. Cottrell A.H.; Trans AIME, 1958, 212, 192-203.

105. Irvine K.J. and Pickering F.B.; J.I.S.I., 1960, 194, 137-153.

106. Schulz B.J. and McMahon C.J.; ASTM STP 499, 'Temper embrittlement of alloy steels.' 1972, 104-135.

107. Knott J.F.; Conf. on the mechanics and physics of fracture. Inst. of Physics and Metals Soc., 1975. Paper 9.

108. Ouchi C. et al.; 'Towards improved ductility and toughness.' Climax Molybdenum Co. Publication, 1971, 67-82.

109. Yoshino K. and McMahon C.J.; Met. Trans. 1974, 5, 363-370.

110. Tekin E. and Kelly P.M.; J.I.S.I., 1965, 203, 715-720.

111. Boniszewski T.; I.S.I. Report, 'Heat treatment aspects of metal joining processes.' 29-43.

Table 1.

Chemical Analysis of weld metal, Filler wire and Parent Plate

Material	C	Si	Mn	P	S	Cr	Mo	Ni	Al	Co	Cu	Nb	Sn	V	As	Sb	Ti	N	O
Weld Metal																			
BOSTRAND 31/HY80 (1.18 KJ/mm)	†0.07	0.37	1.11	0.014	0.008	0.26	0.39	1.53	0.01	0.03	0.05	0.01	0.009	0.12	-	-	-	.0042	.0283
	0.07	0.41	1.10	0.013	0.013	0.29	0.39	1.47	0.016	-	0.06	-	0.012	0.10	0.005	<0.005	-	.0095	-
BOSTRAND 31/HY80 (3.15 KJ/mm)	†0.06	0.45	1.14	0.012	0.001	0.18	0.42	1.39	0.02	0.03	0.11	0.00	0.009	0.13	-	-			
LINDE 120/HY100 (1.18 KJ/mm)	†0.07	0.25	1.26	0.011	0.010	0.36	0.46	2.65	0.01	0.03	0.21	0.00	0.004	0.00	-	-	-	.0078	.0350
	0.07	0.26	1.25	0.009	0.013	0.44	0.47	2.32	0.014	-	0.22	-	0.011	<0.05	<0.005	<0.005		.0096	
AX 140/HY130 (1.18 KJ/mm)	†0.08	0.27	1.49	0.011	0.009	1.02	0.55	2.82	0.01	0.01	0.07	0.01	0.006	0.02	-	-	-	.0078	.0326
	0.09	0.30	1.52	0.009	0.013	0.97	0.59	2.54	0.016	-	0.08	-	0.015	<0.05	<0.005	<0.005	-	.0060	
Welding Wire																			
Bostrand 31	0.07	0.45	1.41	0.011	0.006	0.05	0.40	1.31	0.005	-	0.05	-	-	0.16	-	-	-		
Linde 120	0.08	0.36	1.64	0.010	0.009	0.31	0.45	2.41	0.11	0.07	0.20	<0.005	<0.01	0.01			0.03		
AX 140	0.08	0.35	1.82	0.011	0.006	1.04	0.61	2.30	0.01	0.05	0.08	<0.005		0.04			0.01		
Parent Plate																			
HY80	0.15	0.19	0.31	0.013	0.020	1.73	0.32	2.79	0.035	-	-	-	<0.005	<0.01	<0.005	<0.005	<0.005	.0077	
HY100	0.17	0.22	0.31	0.011	0.019	1.65	0.47	2.77	0.018	-	-	-	<0.005	<0.01	<0.005	<0.005	<0.005	.0067	
HY130	0.11	0.14	0.68	0.005	0.013	0.59	0.47	5.09	0.008	-	-	-	<0.005	0.09	<0.005	<0.005	<0.005	.0096	

Compositions given in wt. %.

† denotes vacuum spark emission spectroscopy. All other compositions determined by conventional chemical techniques.

Wire	Flux	Plate	Heat input KJ/mm	Amps	Volts	Speed mm/sec	No.of runs	Pre-heat C
Bostrand 31	OP41TT	HY80	1.18	360	28	8.5	46	120
Bostrand 31	OP41TT	HY80	3.15	-	-	-	-	120
Linde 120	OP41TT	HY100	1.18	360	28	8.5	46	120
AX140	OP41TT	HY130	1.18	380	32	10.6	62	120

All wires 1.6mm in diameter.

Maximum interpass temperature 150 C.

OP41TT marketed by Oerlikon Electrodes Ltd.

Bostrand 31 made by B.O.C.

Linde 120 made by the Union Carbide Corp. Linde Division. USA.

AX 140 made by the Air Reduction Co. USA.

Table 2 ; Welding parameters.

Specimen	Crack length a mm.	Predicted* δ mm.	Measured δ mm.
B1/4	9.42	0.104	0.121 ± 0.012
B1/6	10.10	0.052	0.038 ± 0.012
B1/7	10.29	0.081	0.079 ± 0.012
B1/8	10.25	0.103	0.119 ± 0.012

* δ calculated from Well's equation.(DD 19. (81)).

Table 3 ; Comparison of calculated δ values with those measured on the specimen surface.

Weld Metal		150 C		450 C		550 C		650 C	
		1Hr	50Hr	1Hr	50Hr	1Hr	50Hr	1Hr	50Hr
Bostrand 31 (1.18KJ/mm)	σ_y MN/m^2	717	702	723	709	781	763	781	550
	σ_u MN/m^2	754	754	781	778	822	828	820	648
	El %	15	16	14	15.5	13	10.5	13	17
	RA %	64	71	71	72	69	67	71	77
	σ_y/σ_u	.95	.93	.93	.91.	.95	.92	.95	.85
Bostrand 31 (3.15KJ/mm)	σ_y MN/m^2	648					740		
	σ_u MN/m^2	764					826		
	El %	24					22		
	RA %	71					68		
	σ_y/σ_u	.85					.90		
Linde 120	σ_y MN/m^2	737	730	723	745	760	721	680	583
	σ_u MN/m^2	807	784	797	837	866	795	791	768
	El %	20	22	22	18	21	21	21	30
	RA %	70	70	70	66	70	69	69	71
	σ_y/σ_u	.91	.93	.91	.89	.88	.91	.86	.76
AX 140	σ_y MN/m^2	892	918	905	871	901	803	786	610
	σ_u MN/m^2	944	967	958	950	961	857	871	799
	El %	17	16	17	16	21	15	20	15
	PA %	66	62	62	62	69	58	66	60
	σ_y/σ_u	.94	.95	.94	.92	.94	.94	.90	.76

σ_y - Yield stress. σ_u - Ultimate tensile stress.

Table 4 ; Tensile test results.

Code	Heat Treatment		Cooling Rate °C/Hr.	Regression Equation y - Energy, joules x - Temp. °C.	Correlation Coefficient	Range °C	T°_{55J}	90%C.I. ± °C
	Temp. °C	Time Hr						
A	150	1	WQ	$y = 109 + 1.07x$	0.962	-80_+60	-50	8
B	150	50	WQ	$y = 133 + 1.26x$	0.901	-80_+20	-62	9
C	450	1	WQ	$y = 110 + 1.17x$	0.968	-80_+60	-47	9
D	450	50	WQ	$y = 77 + 0.75x$	0.970	-80_+60	-29	8
E	550	1	WQ	$y = 59 + 0.66x$	0.971	-80_+80	-6	7
F	550	50	WQ	$y = 34 + 0.43x$	0.982	-80_+80	+49	5
G	650	1	WQ	$y = 78 + 0.90x$	0.981	-80_+60	-25	8
H	650	50	WQ	$y = 431 + 4.90x$	0.983	-80_-40	-93	8

Table 5 ; Charpy transition curve regression equations for Bostrand 31.

Code	Heat Treatment		Cooling Rate °C/Hr.	Regression Equation y - Energy, Joules x - Temp. °C.	Correlation Coefficient	Range °C	T°_{55J}	90%C.I. ± °C
	Temp °C	Time Hr						
I	150	1	WQ	$y = 130 + 0.87x$	0.954	-80_+40	-86	7
J	150	50	WQ	$y = 129 + 1.06x$	0.973	-80_+40	-70	6
K	450	1	WQ	$y = 114 + 1.06x$	0.990	-80_+40	-56	5
L	450	50	WQ	$y = 102 + 0.94x$	0.971	-80_+40	-50	9
M	550	1	WQ	$y = 135 + 1.04x$	0.973	-80_+40	-77	12
N	550	50	WQ	$y = 122 + 0.95x$	0.972	-80_+40	-71	12
O	650	1	WQ	$y = 151 + 1.07x$	0.944	-80_-10	-90	10
P	650	50	WQ	$y = 161 + 1.70x$	0.938	-80_-10	-62	10
G1S	550	2	100	$y = 124 + 1.02x$	0.987	-80_+20	-68	7
G2S	550	10	100	$y = 112 + 1.05x$	0.955	-80_+20	-54	8

Table 6 ; Charpy transition curve regression equations for Linde 120.

Code	Heat Treatment		Cooling Rate °C/Hr	Regression Equation y - Energy, joules. x - Temp. °C.	Correlation Coefficient	Range °C	T°_{55J}	90%C.I. ± °C
	Temp °C	Time Hr						
Q	150	1	WQ	$y = 90 + 0.80x$	0.958	-80_+60	-44	6
R	150	50	WQ	$y = 89 + 0.65x$	0.931	-80_+60	-52	7
S	450	1	WQ	$y = 84 + 0.64x$	0.934	-80_+60	-45	7
T	450	50	WQ	$y = 68 + 0.72x$	0.985	-80_+60	-18	6
U	550	1	WQ	$y = 98 + 0.83x$	0.948	-80_+60	-52	7
V	550	50	WQ	$y = 52 + 0.46x$	0.964	-80_+60	+7	6
W	650	1	WQ	$y = 125 + 0.88x$	0.883	-80_+60	-79	12
X	650	50	WQ	$y = 153 + 1.48x$	0.976	-80_+60	-66	6
E1	550	2	WQ	$y = 116 + 1.35x$	0.987	-80_+20	-45	3
E2	550	10	WQ	$y = 84 + 0.84x$	0.957	-80_+20	-35	7
E1S	550	2	100	$y = 69 + 0.50x$	0.883	-80_+20	-28	13
E2S	550	10	100	$y = 71 + 0.69x$	0.909	-80_+20	-23	13

Table 7 ; Charpy transition curve regression equations for AX 140.

Spec.	Temp/Time °C/Hour	Crack Length a mm	σ_y MN/m^2	V_i mm	V_m mm	δ_i mm	δ_m mm	J KNm/m^2	Test Temp °C
D1/1	AD	10.45	717	-	1.130	-	0.216	242	-3
D1/2	AD	10.26	"	-	1.105	-	0.216	234	-20
D1/3	AD	9.72	"	0.810	0.826	0.164	0.168	157 †	-31
D1/4	AD	10.01	"	-	0.838	-	0.164*	157	-16
D1/5	AD	10.25	"	0.354	0.356	0.054	0.055*	49	-73
D1/6	AD	10.64	"	0.343	0.662	0.049^x	0.111*	38 †	-39
D1/7	AD	9.99	"	-	0.965	-	0.193	-	+20
D1/8	AD	10.22	"	-	1.270	-	0.253	-	+20
D2/1	450/50	10.08	709	0.559	0.559	0.102	0.102*	-	-1
D2/3	450/50	9.94	"	-	0.318	-	0.050*	-	-39
D2/5	450/50	9.93	"	0.610	0.610	0.115	0.115*	-	-40
D2/6	450/50	9.97	"	0.508	0.584	0.092	0.109*	-	-31
D2/7	450/50	10.04	"	0.533	0.648	0.096	0.122	-	-19
D3/1	500/50	9.76	736	0.610	0.610	0.117	0.117*	-	-2
D3/2	500/50	9.77	"	-	0.406	-	0.070*	-	-20
D3/3	500/50	9.96	"	0.305	0.305	0.046	0.406*	-	-42
D3/7	500/50	9.69	"	0.381	0.381	0.065	0.065*	-	-32
D4/2	550/50	9.89	763	0.330	0.330	0.051	0.051*	48	-6
D4/3	550/50	10.01	"	0.318	0.318	0.047	0.047*	40	-16
D4/4	550/50	9.84	"	0.203	0.381	0.023^x	0.063*	56	-29
D4/5	550/50	10.34	"	0.260	0.267	0.034	0.036*	27	-40
D4/6	550/50	10.99	"	0.279	0.318	0.033	0.040*	30	-20
B1/3	AD	10.49	717	0.635	0.635	0.111	0.111	117	+20
B1/4	AD	10.01	"	0.660	0.660	0.125	0.125	134	+20
B1/5	AD	10.96	"	0.699	0.825	0.116	0.141	122	+20
B1/7	AD	10.24	"	0.749	0.749	0.140	0.140	147	+20
B1/8	AD	10.27	"	0.820	0.825	0.135	0.140	163	+20

x - Pop in. $z = 5.77$ mm.

* - Fracture on a rising load curve. AD - As deposited

† - J value at initiation. 1 mm/min. strain rate.

Table 8 ; COD and J results for the low heat input Bostrand 31 (1.18KJ/mm). Transverse notch " B series " included.

Spec	Temp/Time °C/Hour	Crack Length a mm	σ_y MN/m^2	V_i mm	V_m mm	δ_i mm	δ_m mm	J KNm/m^2	Test Temp °C
H1/1	AD	9.23	648	0.500	0.699	0.102	0.150*	82 †	+20
H1/2	"	10.06	"	0.445	0.851	0.079^{x}	0.168*	150	-1
H1/3	"	9.51	"	0.660	0.902	0.136	0.193*	215	-23
H1/4	"	9.70	"	0.178	0.965	0.021^{x}	0.203*	188	-39
H1/5	"	9.66	"	-	0.508	-	0.098*	84	-30
H1/6	"	9.83	"	0.216	0.546	0.029^{x}	0.104*	97	-12
H1/7	"	9.22	"	0.343	0.940	0.063^{x}	0.209*	212	-5
H1/8	"	10.43	"	-	0.343	-	0.053*	50	-43
H1/9	"	10.47	"	0.241	0.635	0.031^{x}	0.114*	111	-35
H4/1	550/50	9.80	740	-	0.432	-	0.076*	74	+20
H4/2	"	9.78	"	0.241	0.445	0.032^{x}	0.074*	76	+22
H4/3	"	10.46	"	0.216	0.394	0.023^{x}	0.061*	59	0
H4/4	"	10.31	"	0.127	0.368	0.008^{x}	0.057*	49	-21
H4/5	"	10.12	"	-	0.178	-	0.042*	15	-40

x - Pop in. $z = 5.77$ mm.

* - Fracture on a rising load curve. AD - As deposited

† - J value at initiation. 1 mm/min strain rate.

Table 9 ; COD and J results for the high heat input Bostrand 31 (3.15KJ/mm).

Spec.	Temp/Time C/Hour	Crack Length a mm	σ_y MN/m^2	V_i mm	V_m mm	δ_i mm	δ_m mm	J KNm/m^2	Test Temp C
G1/2	AD	10.61	737	1.181	1.181	0.221	0.221	243	-32
G1/3	"	10.50	"	1.070	1.118	0.201	0.211	220 †	-3
G1/4	"	10.30	"	-	0.826	-	0.155*	166	-66
G1/5	"	10.35	"	-	0.914	-	0.172*	189	-46
G1/6	"	10.33	"	-	1.245	-	0.243	269	-20
G1/7	"	10.40	"	-	1.448	-	0.292	-	+21
G1/8	"	10.12	"	-	1.295	-	0.261	-	+19
G2/1	450/50	10.71	745	0.890	1.020	0.159	0.185	263	-6
G2/2	"	10.17	"	-	1.041	-	0.204	225	-22
G2/3	"	10.38	"	-	0.914	-	0.171	194	-32
G2/4	"	10.51	"	-	1.143	-	0.216	238	-38
G2/5	"	10.44	"	-	0.394	-	0.061*	56	-65
G3/1	500/50	11.00	733	-	1.359	-	0.244	-	-30
G3/2	"	10.34	"	1.070	1.143	0.206	0.221	-	-5
G3/3	"	10.33	"	-	0.940	-	0.178	-	-40
G3/4	"	10.36	"	0.292	0.508	0.040x	0.086*	-	-64
G3/5	"	10.54	"	1.072	1.245	0.200	0.236	-	-20
G4/1	550/50	10.58	721	-	1.245	-	0.235	-	-33
G4/2	"	10.45	"	-	1.270	-	0.245	-	-2
G4/3	"	10.66	"	-	1.270	-	0.238	-	-35
G4/4	"	10.19	"	-	1.397	-	0.281	-	-21
G4/5	"	10.44	"	-	0.673	-	0.120*	-	-66

x - Pop in.

* - Fracture on a rising load curve.

† - J value at initiation.

z = 5.77 mm.

AD - As deposited

1 mm/min strain rate.

Table 10 ; COD and J results for Linde 120.

Spec	Temp/Time °C/Hour	Crack Length a mm	σ_y MN/m^2	V_i mm	V_m mm	δ_i mm	δ_m mm	J KNm/m^2	Test Temp °C
E1/1	AD	9.76	892	0.648	0.648	0.121	0.121	143	-5
E1/2	"	10.13	"	0.229	0.470	0.023^x	0.076^*	79	-74
E1/3	"	9.82	"	0.559	0.635	0.100	0.117	114†	-39
E1/4	"	10.25	"	-	0.622	-	0.107	124	-18
E1/5	"	9.90	"	0.432	0.673	0.070^x	0.124^*	138	-16
E1/6	"	9.91	"	-	0.540	-	0.094^*	99	-64
E1/7	"	10.08	"	0.660	0.660	0.118	0.118^*	137	-31
E1/8	"	10.92	"	-	0.724	-	0.117	143	+20
E1/9	"	10.39	"	0.635	0.647	0.108	0.110	156	+20
E2/3	450/50	10.08	871	-	0.559	-	0.097	-	+20
E2/4	"	10.03	"	0.508	0.711	0.086	0.131^*	-	-2
E2/5	"	10.05	"	0.432	0.457	0.069	0.075^*	-	-29
E2/6	"	9.87	"	0.318	0.318	0.045	0.045^*	-	-41
E2/8	"	9.62	"	0.419	0.419	0.071	0.071^*	-	-18
E4/1	550/50	9.86	803	0.267	0.267	0.036	0.036^*	33†	-8
E4/2	"	9.90	"	-	0.318	-	0.047^*	44	-19
E4/3	"	9.99	"	0.356	0.406	0.055^x	0.066^*	62	-31
E4/4	"	9.92	"	0.165	0.324	0.014^x	0.048^*	41	-40
E4/5	"	10.01	"	0.254	0.495	0.032^x	0.086^*	87	-19
E4/10	"	9.60	"	-	0.361	-	0.059^*	52	+7
E4/11	"	10.01	"	-	0.300	-	0.042^*	35	-2
E4/12	"	9.37	"	-	0.430	-	0.078^*	71	-14

x - Pop in.

z = 5.77 mm.

* - Fracture on a rising load curve.

AD - As deposited

† - J value at initiation.

1 mm/min strain rate.

Table 11 ; COD and J results for AX 140.

AS DEPOSITED

Weld Metal	Spec	δ_1 mm	σ_y MN/m^2	σ_w MN/m^2	J KNm/m^2	$\bar{a}$ mm Weld Inst. Method. Equn.(v)	$\bar{a}$ mm J Method Equn.(x)
Bostrand 31 (1.18KJ/mm)	D1/3	0.164	717	368	157	5.9	18.3
"B"series	B1/3	0.111	717	368	117	4.0	13.7
Bostrand 31 (3.15KJ/mm)	H1/1	0.102	648	368	82	3.9	11.7
Linde 120	G1/3	0.201	737	460	220	6.5	24.3
AX 140	E1/9	0.108	892	598	114	2.6	8.6

AFTER PWHT

Weld Metal	Spec	δ_1 mm	σ_y MN/m^2	σ_w MN/m^2	J KNm/m^2	$\bar{a}$ mm Weld. Inst. Method		$\bar{a}$ mm J Method	
						Zero Residual Stress Equn.(vii)	25% Residual Stress Equn.(ix)	Zero Residual Stress Equn (xi)	25% Residual Stress Equn.(xii)
Bostrand 31 (1.18KJ/mm)	D4/2	0.051	763	368	48	9.4	4.5	25.5	10.2
Bostrand 31 (3.15KJ/mm)	H4/3	0.061	740	368	59	10.9	5.4	31.4	12.7
Linde 120	G1/3	0.201	737	460	220	23.9	14.3	74.9	35.0
AX 140	E4/1	0.036	803	598	33	3.0	2.0	6.7	3.1

Equation numbers refer to equations in section 3.8.

Table 12 ; Defect tolerance results for the four weld metals in the as deposited and post weld heat treated (PWHT) conditions.

	Bostrand 31 1.18KJ/mm	Bostrand 31 3.15KJ/mm	Linde 120	AX 140
Area fraction of proeutectoid ferrite %	12	16	7	0
" " " acicular ferrite %	71	69	84	0
" " " martensite %	17	15	9	98.5
" " " retained austenite %	ND	ND	ND	1.5
Calculated volume fraction MnS %	0.07	ND	0.07	0.07
" " " 2MnO SiO_2 %	0.18	ND	0.22	0.21
" " " Total %	0.25	ND	0.29	0.28
Acicular ferrite grain size (micron)	2.0	2.9	1.9	-
Prior austenite grain size (micron)	ND	ND	43	48

Calculation and measurement details given in appendix 3.

ND - Not determined

Table 13 ; Area or volume fraction of microstructural constituents in the four weld metals

Code												
A	T	68	20	-66	-37	-18	-2	-1	-79	41	-50	
	E	171	141	27	42	97	102	119	26	156	78	
B	T	70	20	-66	-37	-18	-2	-79	41	-50		
	E	152	150	49	111	134	123	39	154	32		
C	T	74	20	-66	-37	-18	-2	-77	41	-50		
	E	164	137	21	82	84	128	24	144	43		
D	T	72	20	-66	-35	-17	-2	-79	41			
	E	116	89	24	52	62	79	16	128			
E	T	18	-76	-60	-39	-20	1	-30	40			
	E	79	16	16	37	48	56	28	85			
F	T	18	-76	-60	-40	-20	1	-30	40			
	E	42	6	8	12	25	40	20	52			
G	T	69	20	-66	-34	-18	-2	-77				
	E	151	92	24	34	59	70	19				
H	T	70	20	-66	-37	-18	-78	40	-50			
	E	297	246	98	235	228	45	241	208			
I	T	76	42	-70	-55	-30	-9	9				
	E	164	160	52	92	109	135	132				
J	T	79	42	-69	-55	-29	-9	9				
	E	168	166	48	66	105	137	132				
K	T	75	43	-72	-55	-30	-9	9				
	E	159	157	37	51	85	116	118				
L	T	78	43	-72	-54	-30	-9	9				
	E	152	137	32	44	78	112	105				
M	T	18	-76	-60	-40	-20	1					
	E	148	52	72	107	106	146					
N	T	18	-76	-60	-40	-20	2					
	E	144	48	78	78	93	128					
O	T	81	43	-72	-55	-30	-9	9				
	E	168	182	53	96	136	158	160				
P	T	80	43	-70	-52	-30	-10	9				
	E	177	162	54	76	75	155	185				
G1S	T	17	-16	-62	-90	-50	-39	-25	1			
	E	141	110	64	26	74	94	102	117			
G2S	T	17	-16	-62	-90	-50	-39	-25	1			
	E	124	78	40	28	60	70	98	130			
Q	T	72	42	-71	-53	-53	-30	-30	-10	-10	9	9
	E	117	130	30	44	46	84	72	84	80	90	86
R	T	73	42	-70	-54	-29	-9	9				
	E	130	104	30	59	76	94	101				

Table 14 ; Continued overleaf.

S	T	75	42	-70	-53	-29	-9	9		
	E	96	114	49	33	75	77	85		
T	T	76	42	-71	-53	-29	-9	9		
	E	112	74	20	25	42	67	80		
U	T	18	-76	-60	-39	-20	2			
	E	106	26	58	60	97	99			
V	T	18	-76	-60	-39	-20	1	-30		
	E	59	20	22	28	50	53	37		
W	T	83	41	-71	-55	-30	-9	9		
	E	150	147	48	63	134	124	131		
X	T	69	41	-70	-53	-29	-9	9		
	E	164	162	51	80	94	152	165		
E1	T	20	6	-2	-22	-32	-44	-50	-55	-66
	E	105	108	112	86	80	52	46	36	32
E2	T	20	4	-14	-4	-24	-35	-54	-65	-48
	E	98	100	62	86	61	52	40	34	44
E1S	T	17	2	-20	-80	-60	-40	-30	-10	
	E	79	60	61	18	44	56	68	60	
E2S	T	17	2	-20	-80	-60	-40	-30		
	E	92	68	60	16	45	26	44		

Table 14 ; Individual Charpy energy absorbed values E (joules) at temperature T °C. Specimen codes and heat treatments given in tables 5,6 and7.

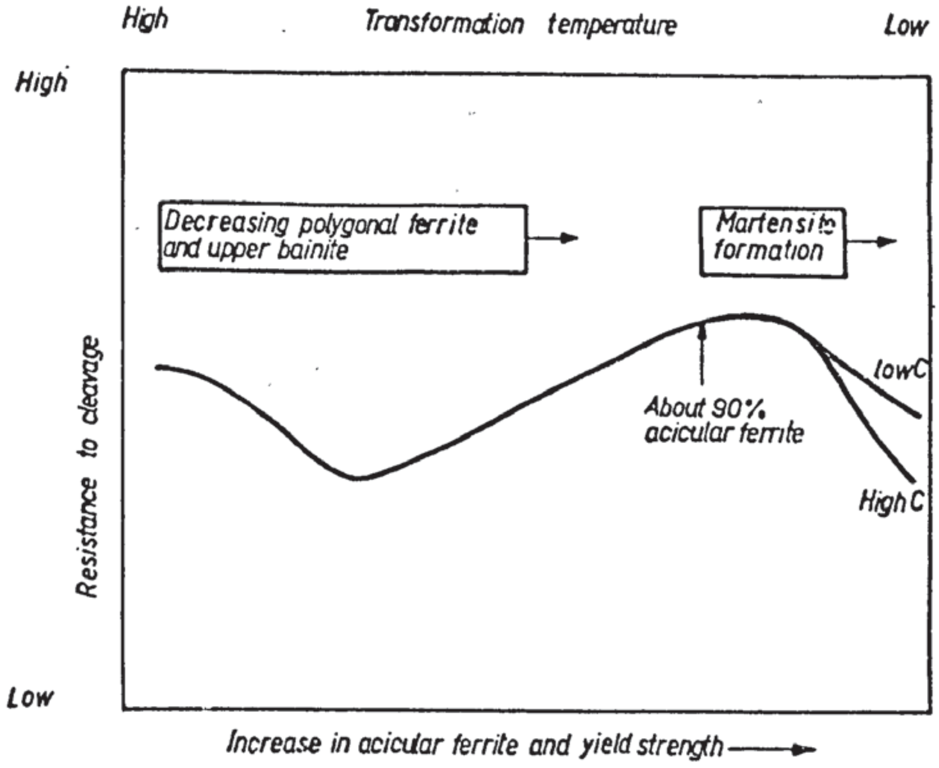

Figure 1 Schematic diagram showing relationship between microstructure and cleavage resistance. (18).

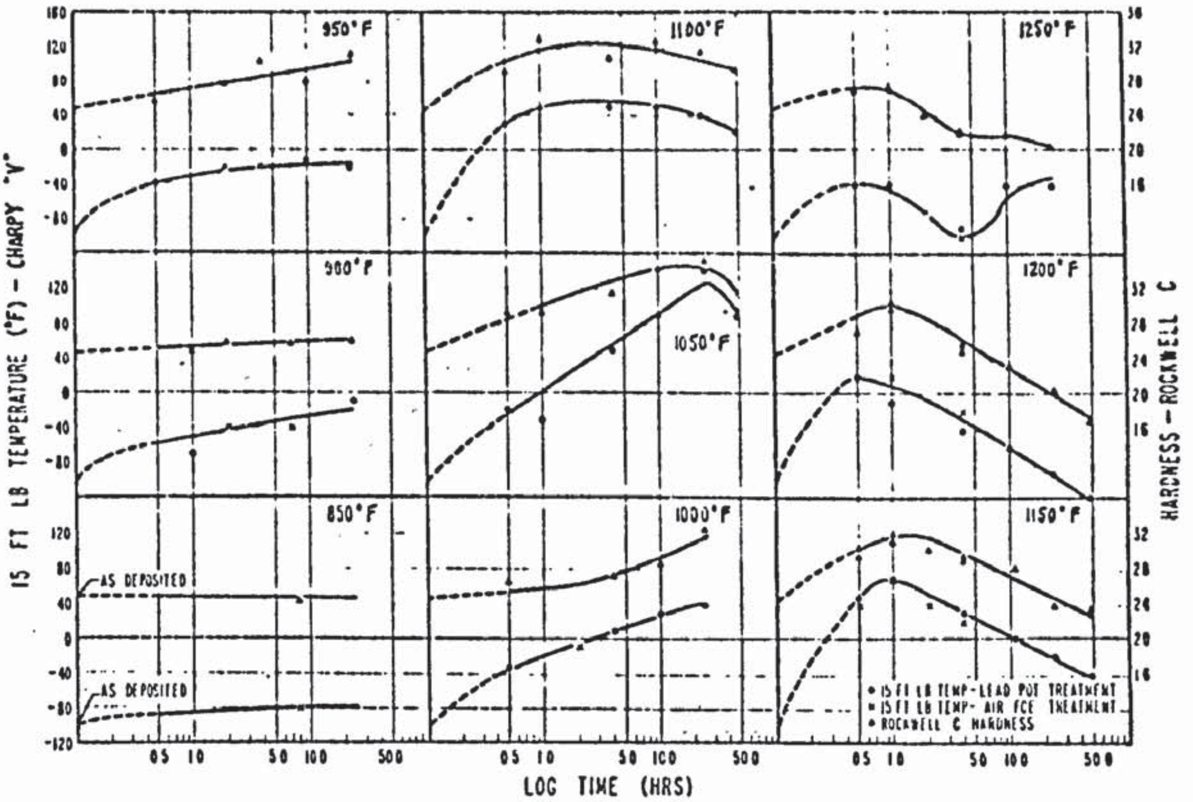

Figure 2 Effect of heat treatment on the Charpy V 15 ft - lb (20 J) transition and hardness (Rockwell C) of a 0.06%C, 1.5%Ni, 0.58%Mo, 0.26%V weld metal. (31).

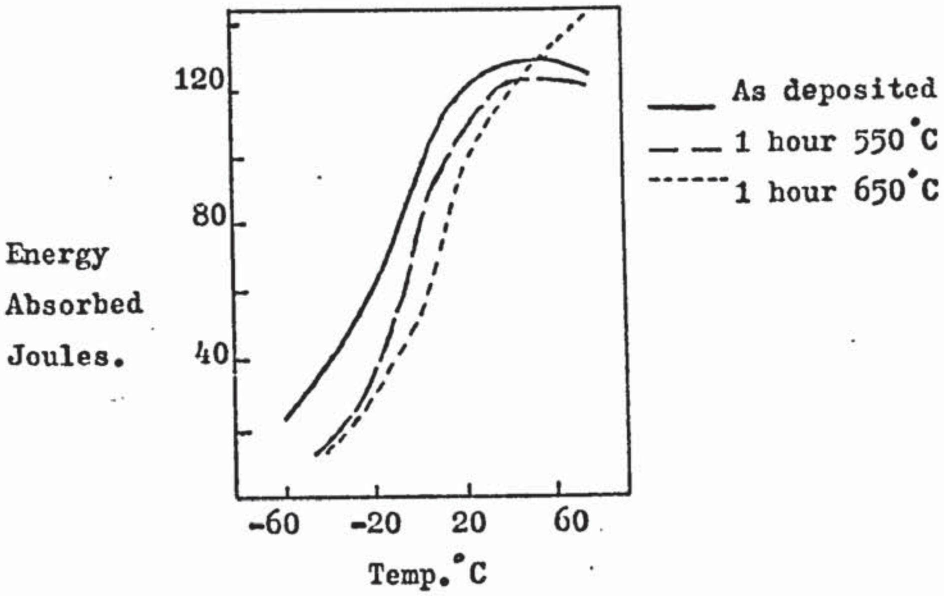

Figure 3 Effect of post weld heat treatment on the Charpy impact properties of Bostrand 31 weld metal deposited with Encrex 2/102 flux (Basicity 2.3). (33).

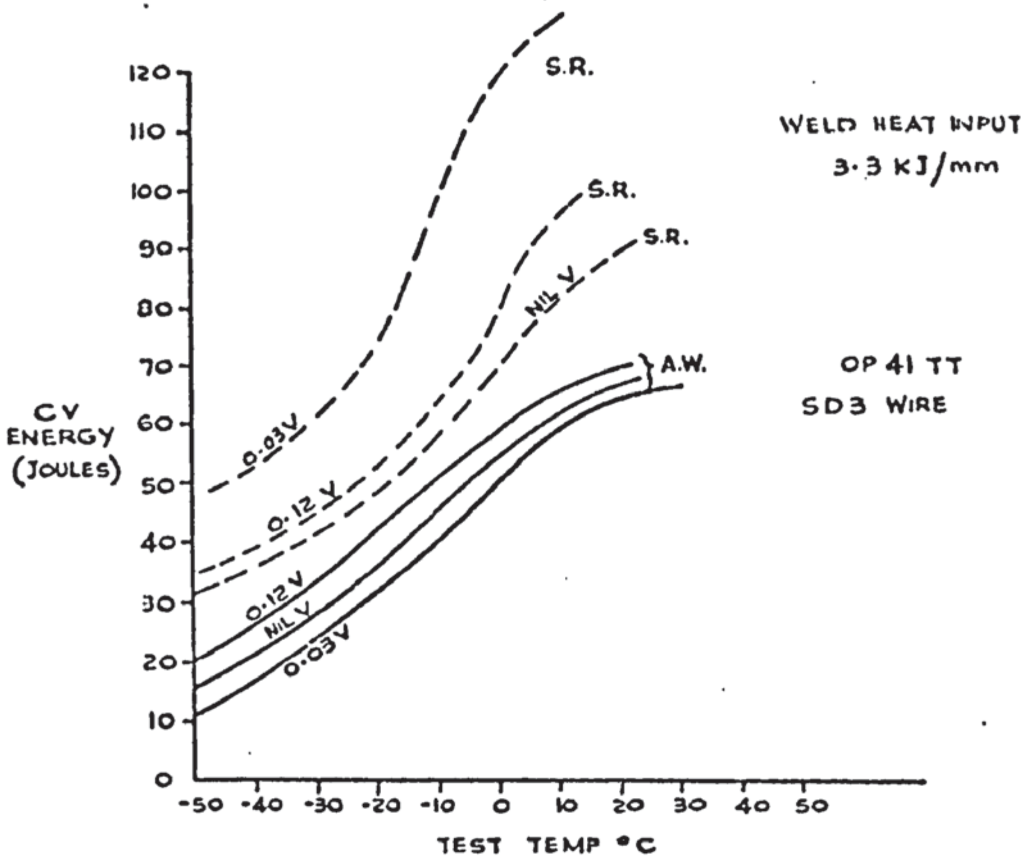

Figure 4 The influence of vanadium on Charpy impact properties of weld metal deposited using a basic flux, in the as deposited condition and after stress relief at 580 to 620°C for 1 hour.(23)

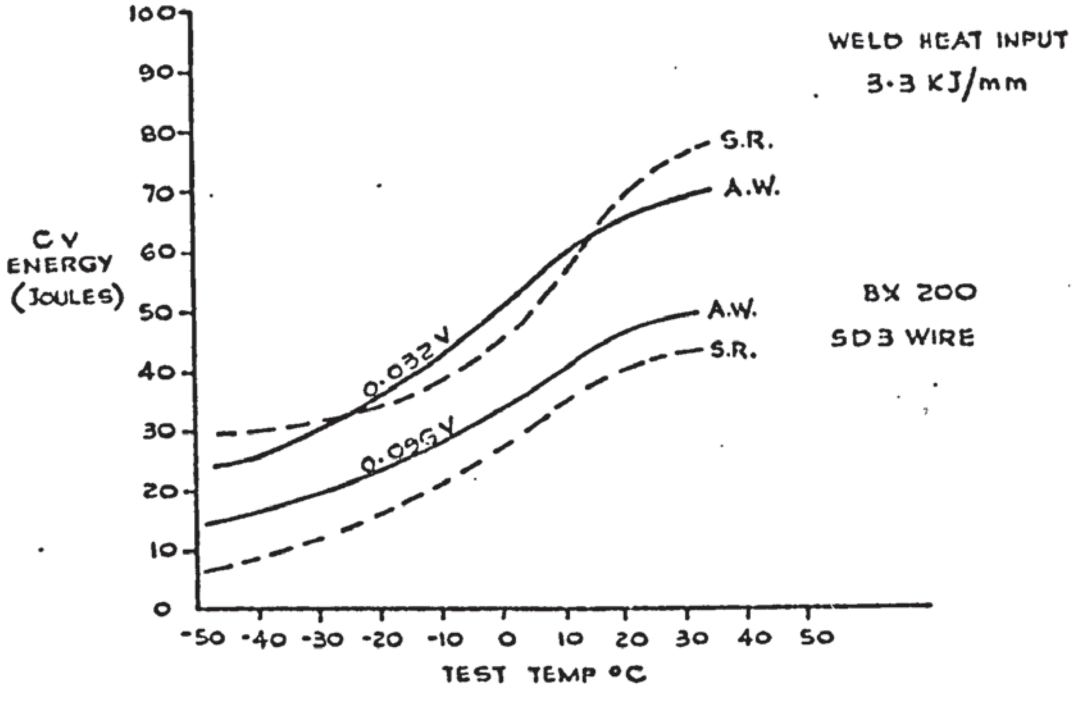

Figure 5 As for Figure 4 with an amphoteric flux being used instead of a basic flux.(23)

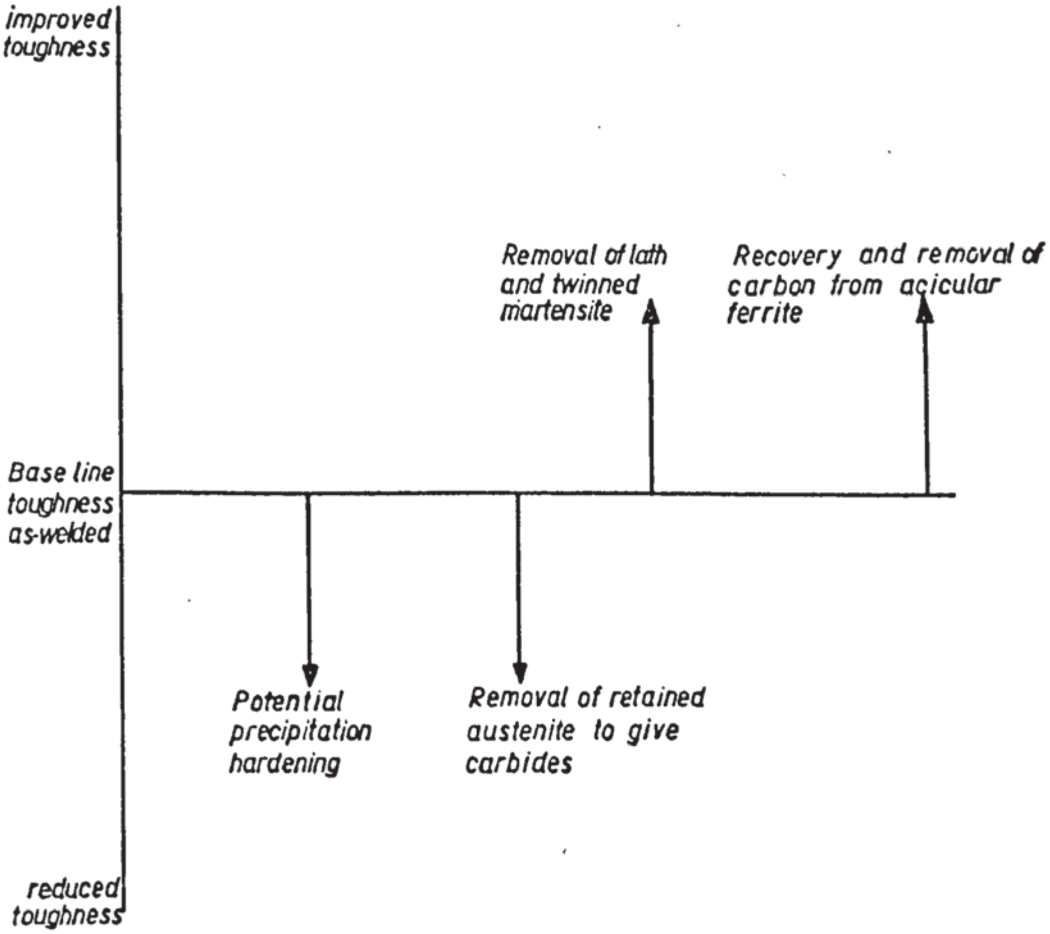

Figure 6 Schematic diagram showing the various metallurgical changes that can take place during stress relieving post weld heat treatments. (18).

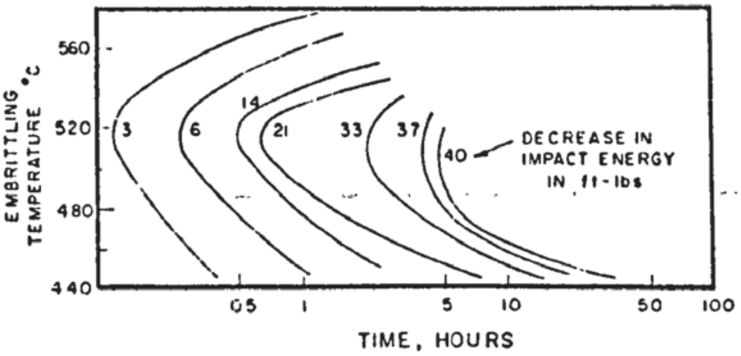

Figure 7 C - curve behaviour of a 0.26%C, 0.66%Mn, 3.53%Ni, 0.84%Cr, 0.026% P steel showing the decrease in impact energy after heat treatment in the temper embrittlement range. (41).

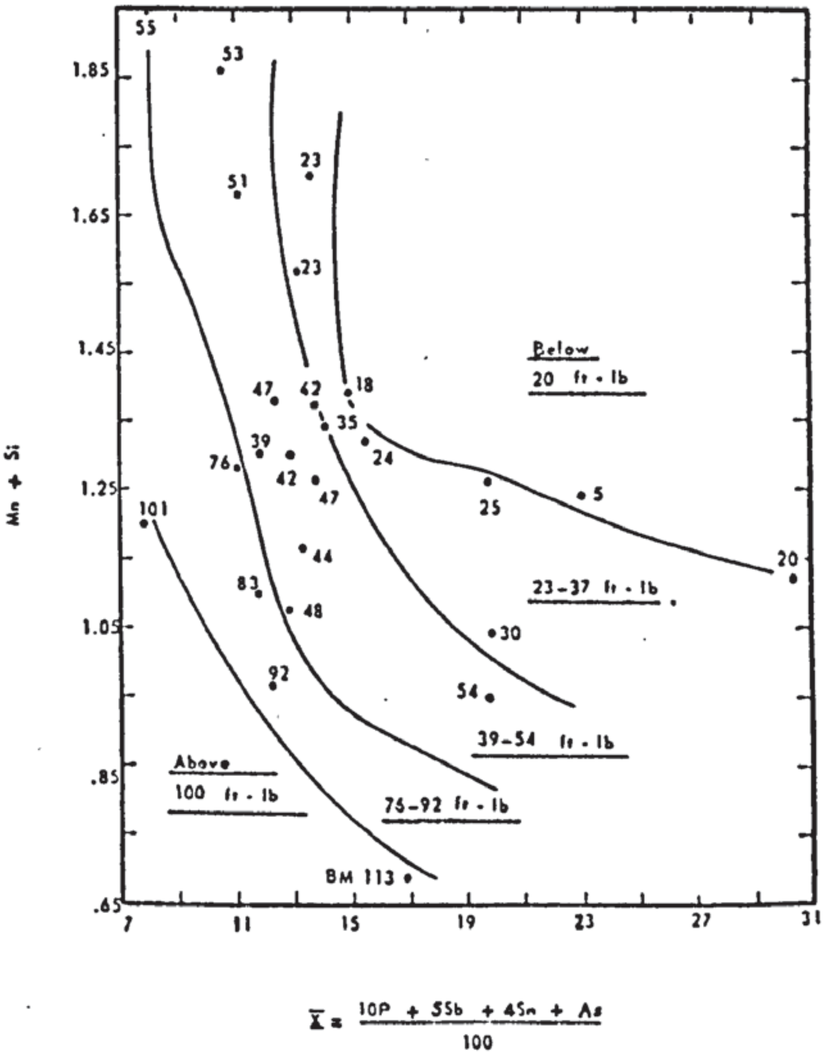

Figure 8 Effect of impurity factor $\overline{X}$ and Mn + Si on the Charpy energy absorbed at $-46^{\circ}C$ for a $2\frac{1}{4}$ Cr - 1 Mo manual metal arc weld metal after a step age embrittling treatment. (55).

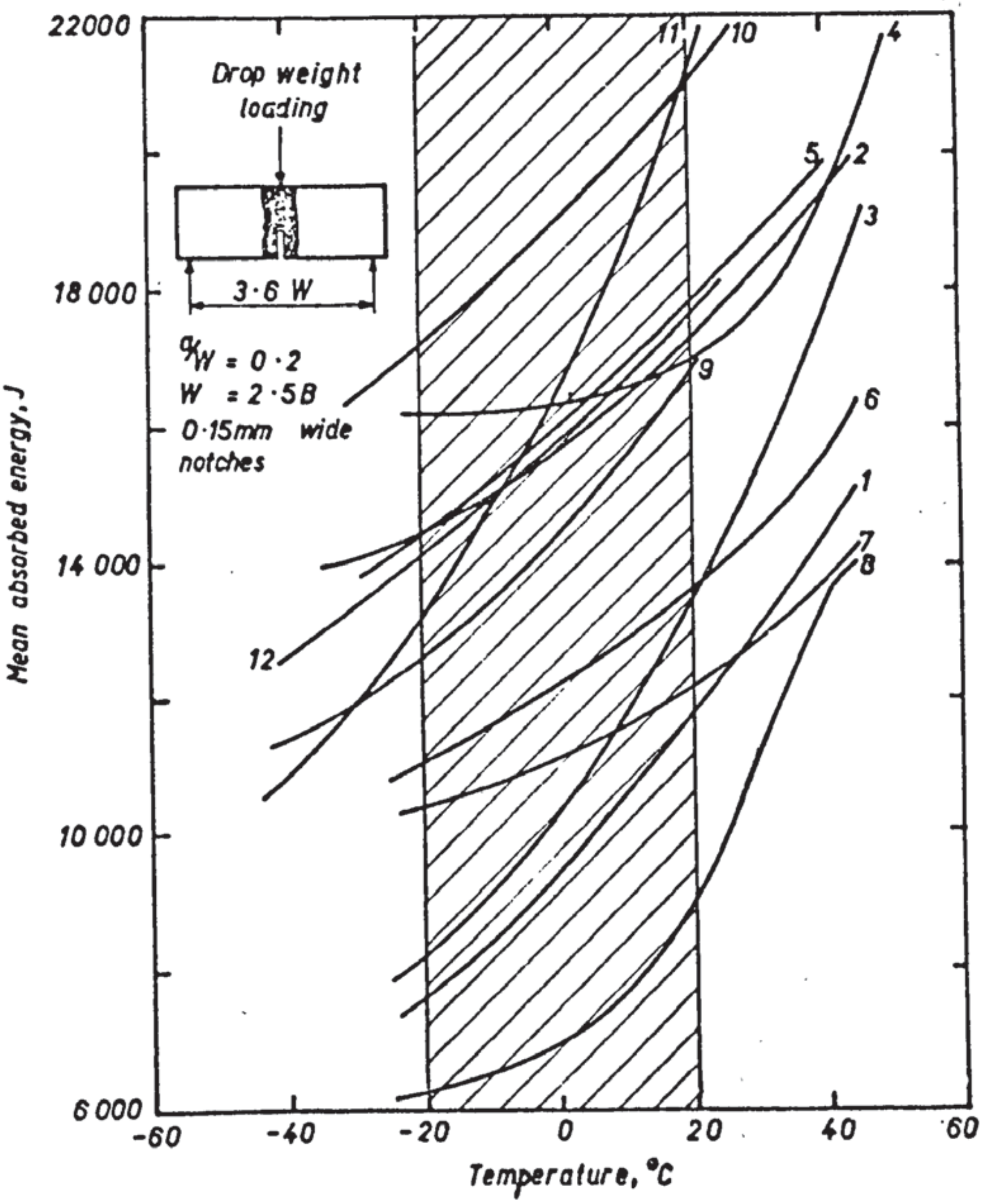

Figure 9 Results of drop weight tear tests on 51mm. thick manual metal arc, submerged arc and MIG weld metals. Shaded area shows desired operating temperature range which coincides with the energy transition range. (2).

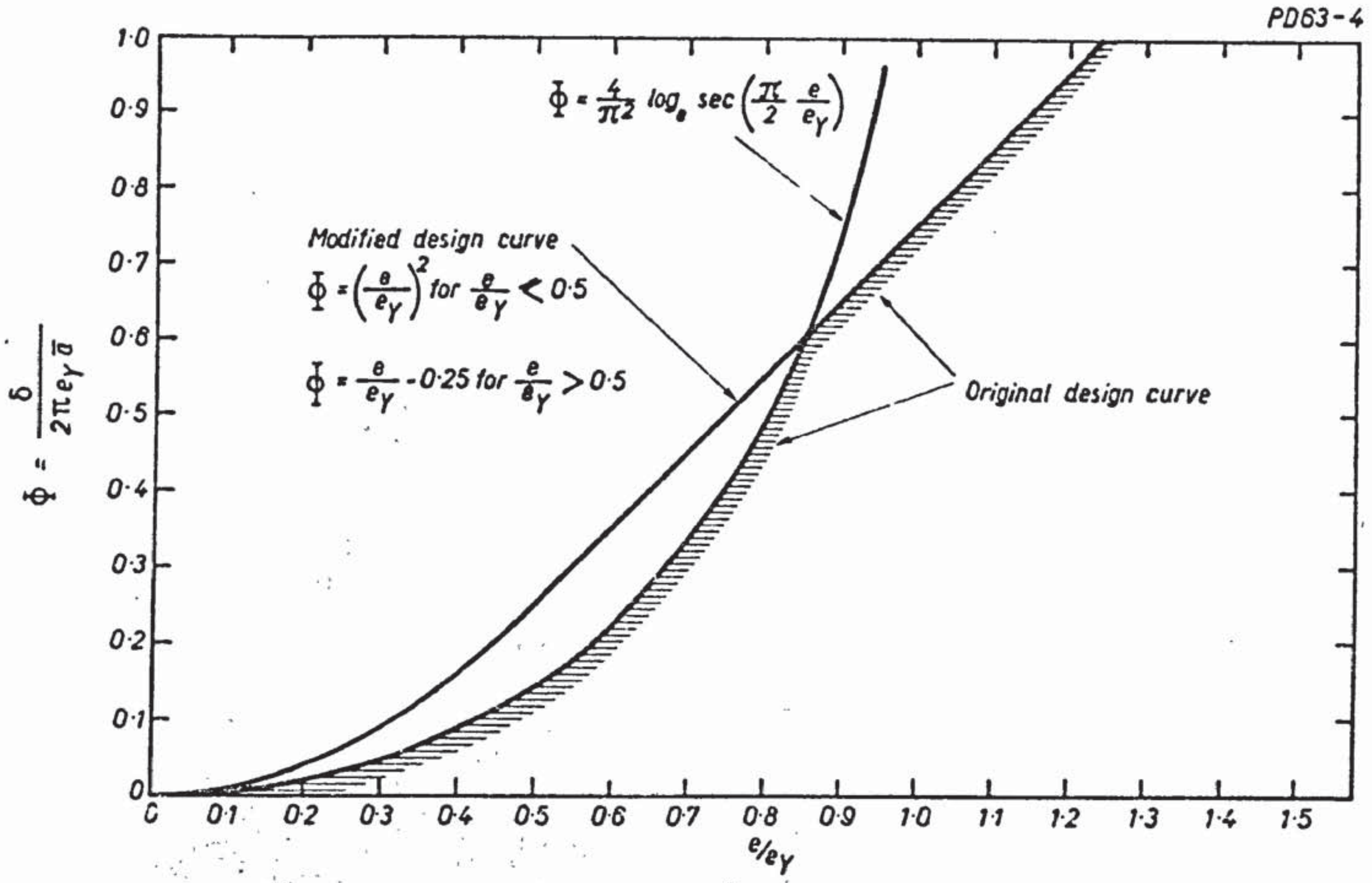

Figure 10 The Welding Institute COD design curve used to calculate critical crack size $\overline{a}$ if δ, $\frac{e}{e_y}$ and e_y are known. (2).

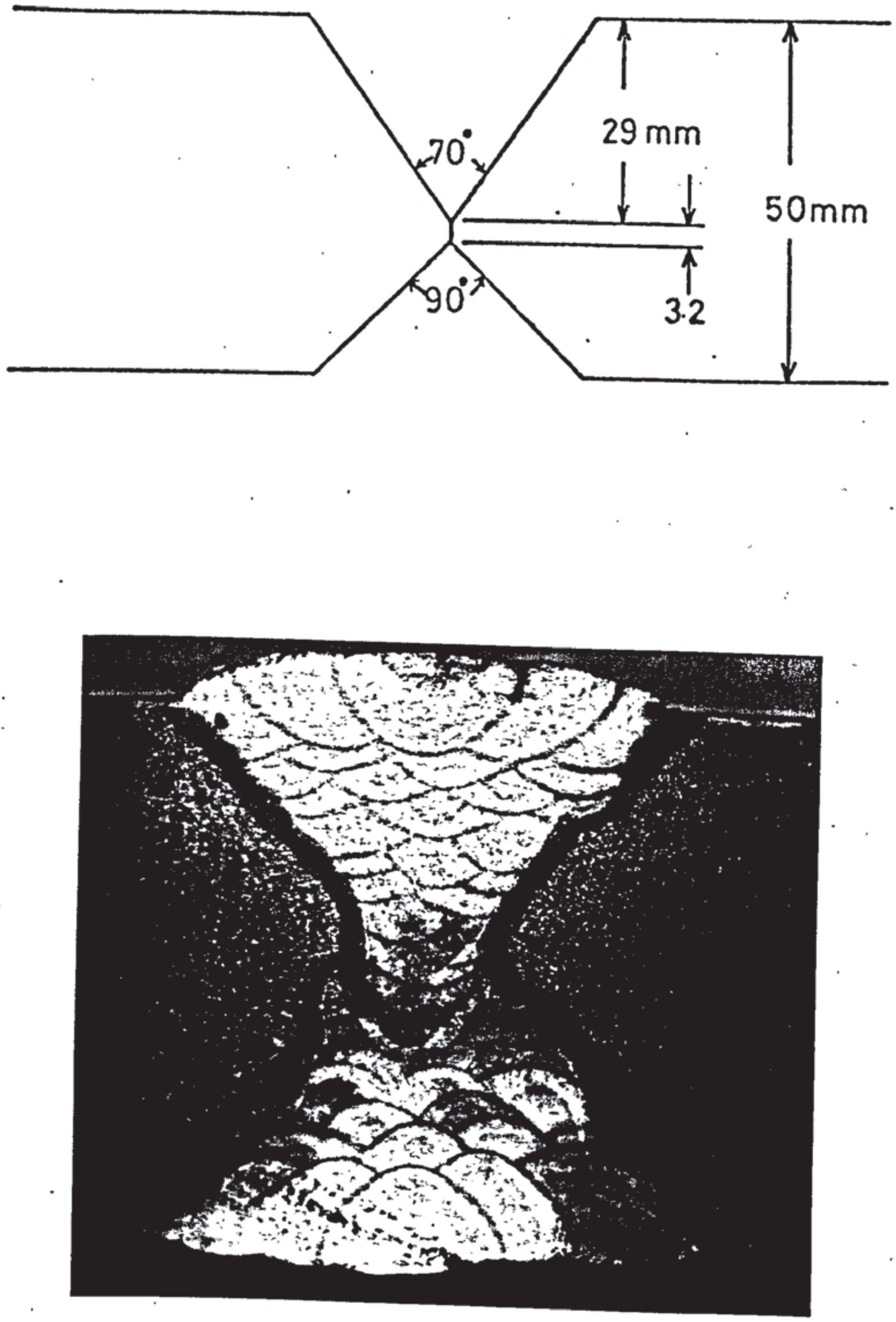

Figure 11 Plate preparation for all full penetration butt welds used. The macro is a section through a completed AX140 weld.

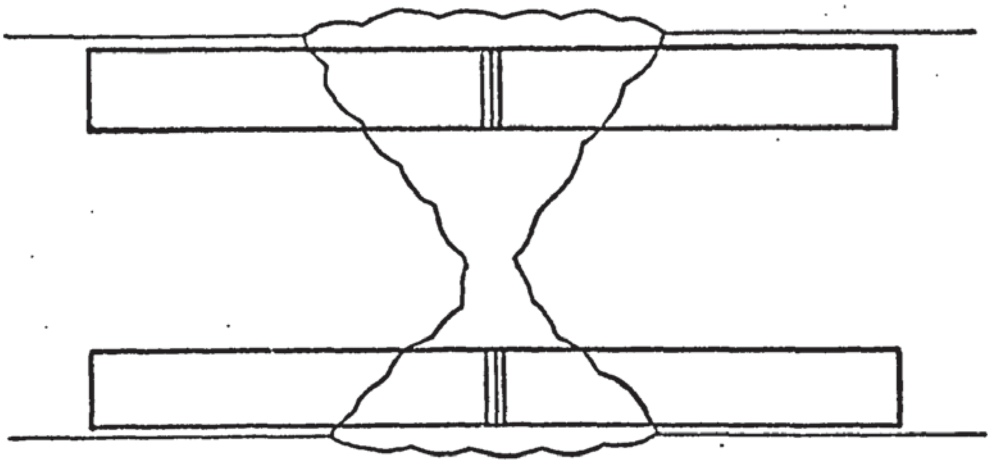

Full size

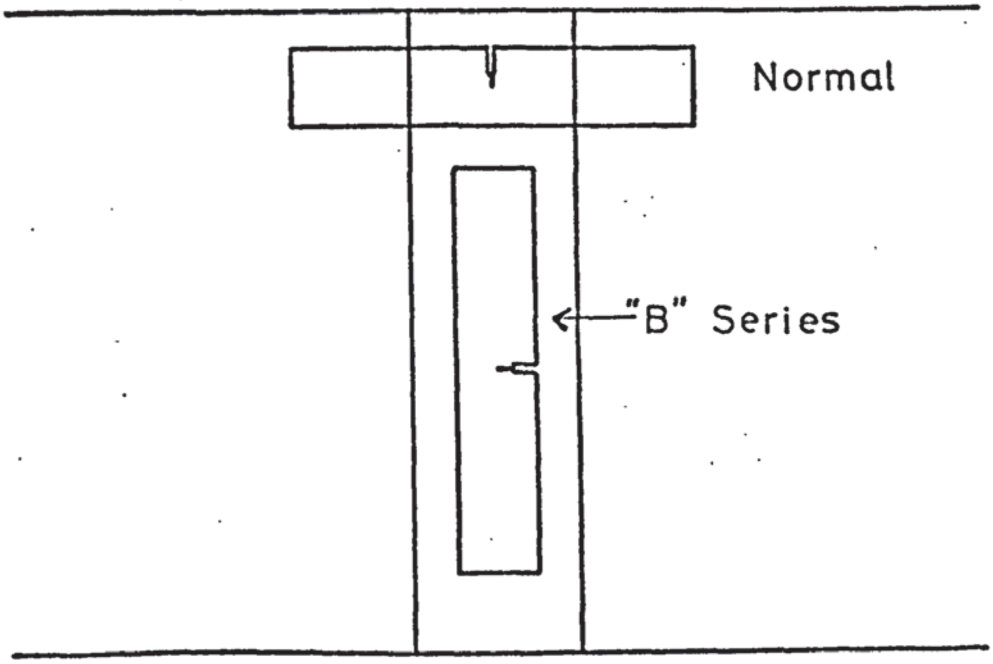

Half size

Figure 12 Specimen location of all Charpy and COD specimens. The orientation of the "B" series is also shown.

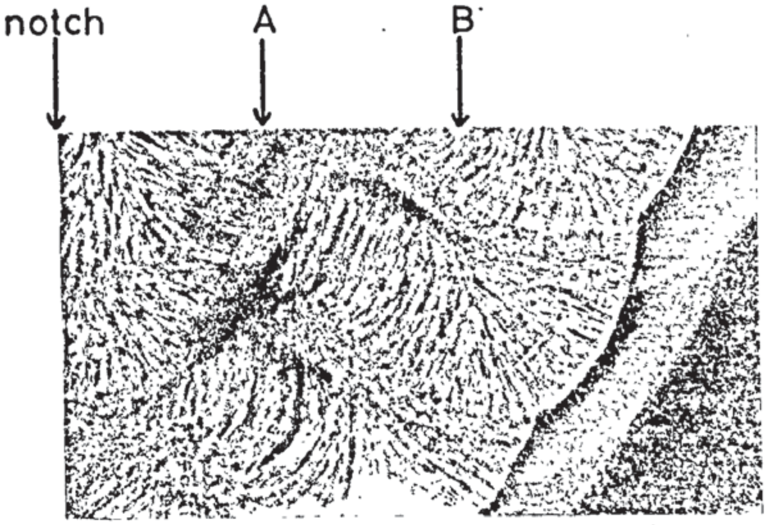

Figure 13 Half Charpy specimen with the notch running down the left-hand side. This figure shows the possible variation in structure at the notch tip. The notch passes through approximately 30% refined structure while at A the % refined structure increases and at B it decreases. X 5. 2% Nital.

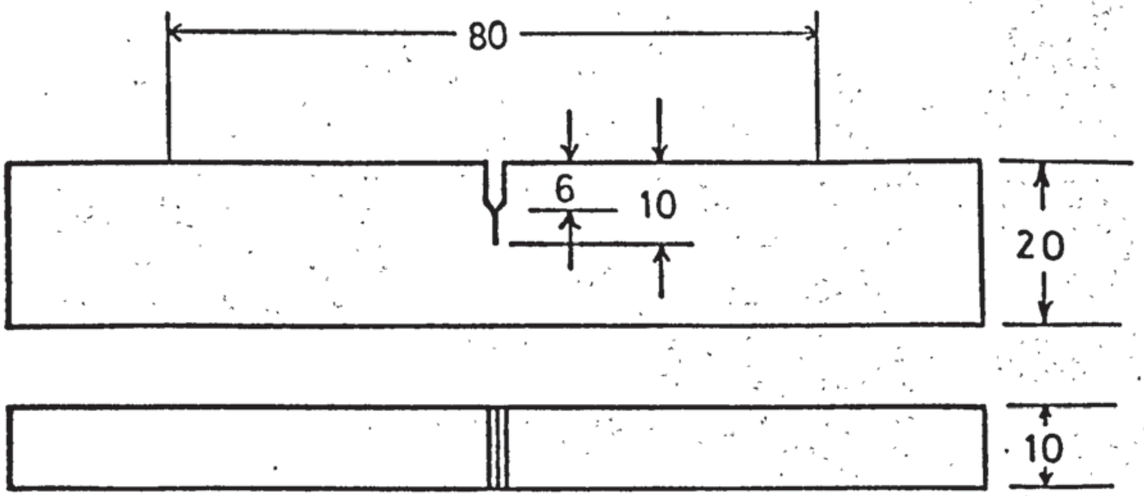

Figure 14 Principal dimensions of the COD specimens. The notch root radius was less than 0.1mm. and contained a fatigue crack giving a total crack length of 10mm.

Figure 17

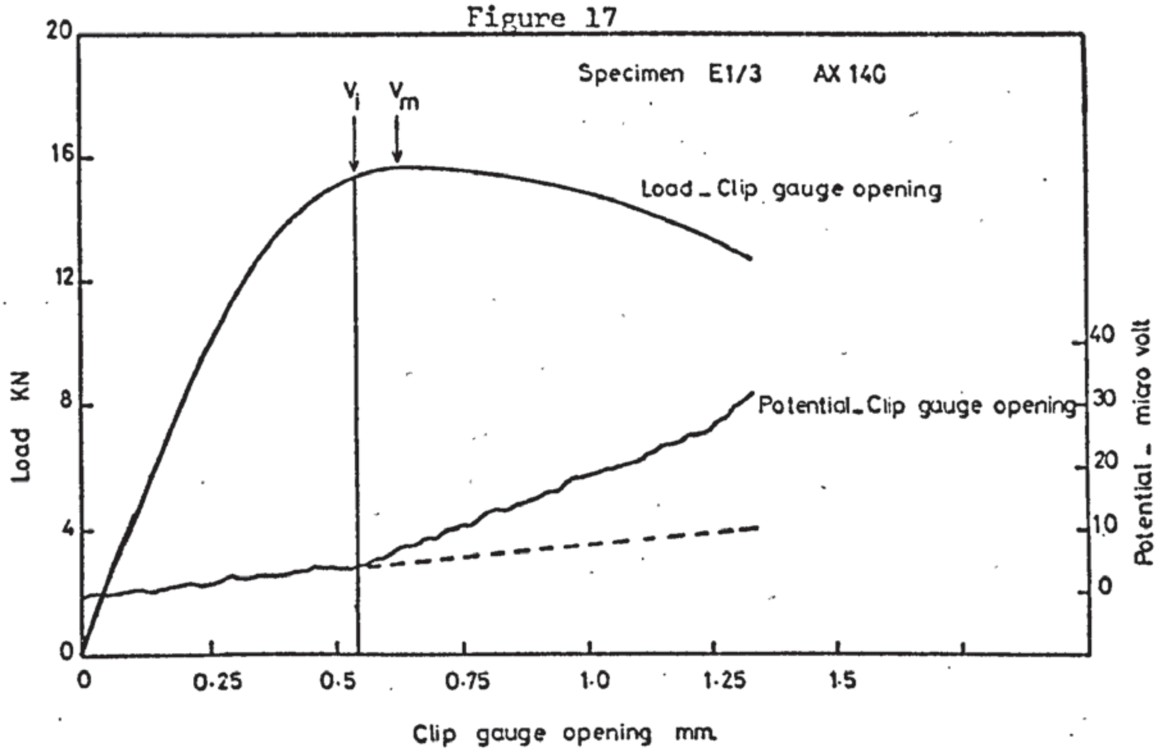

Figure 18

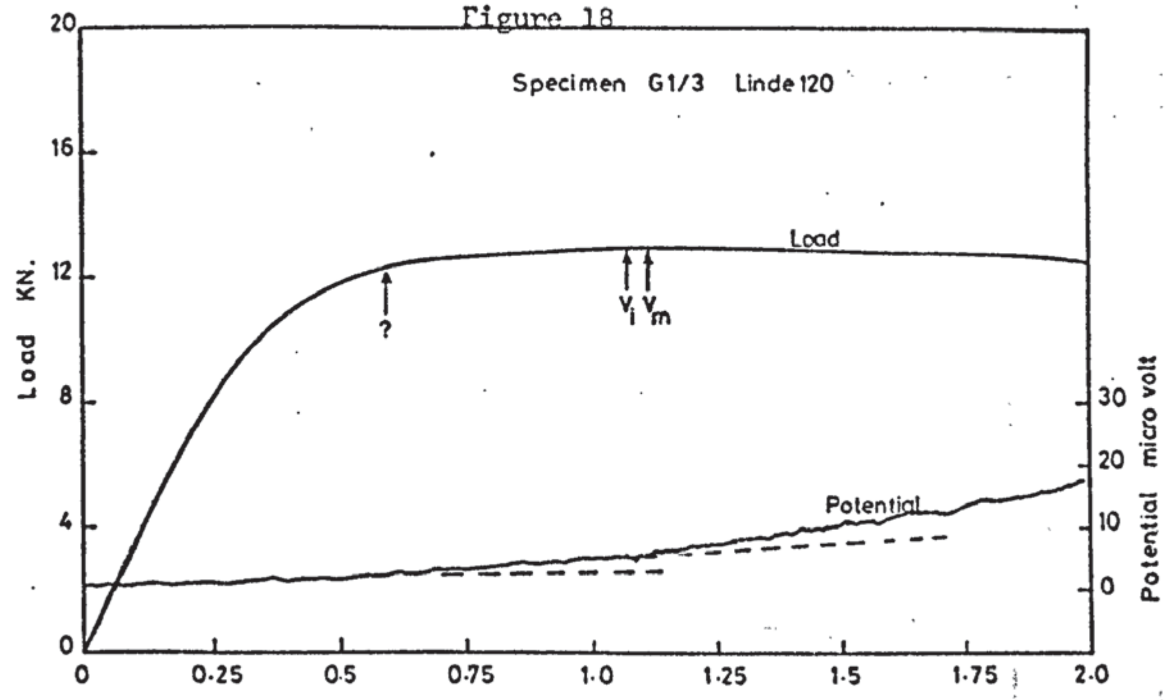

Figures 17 and 18 Clip gauge opening V versus load P and potential drop across crack for Linde 120, AX140 (E1/3, Figure 17) and (G1/3, Figure 18) as deposited weld metals. Note small doubled inflection in potential trace for G1/3 and large inflection for E1/3.

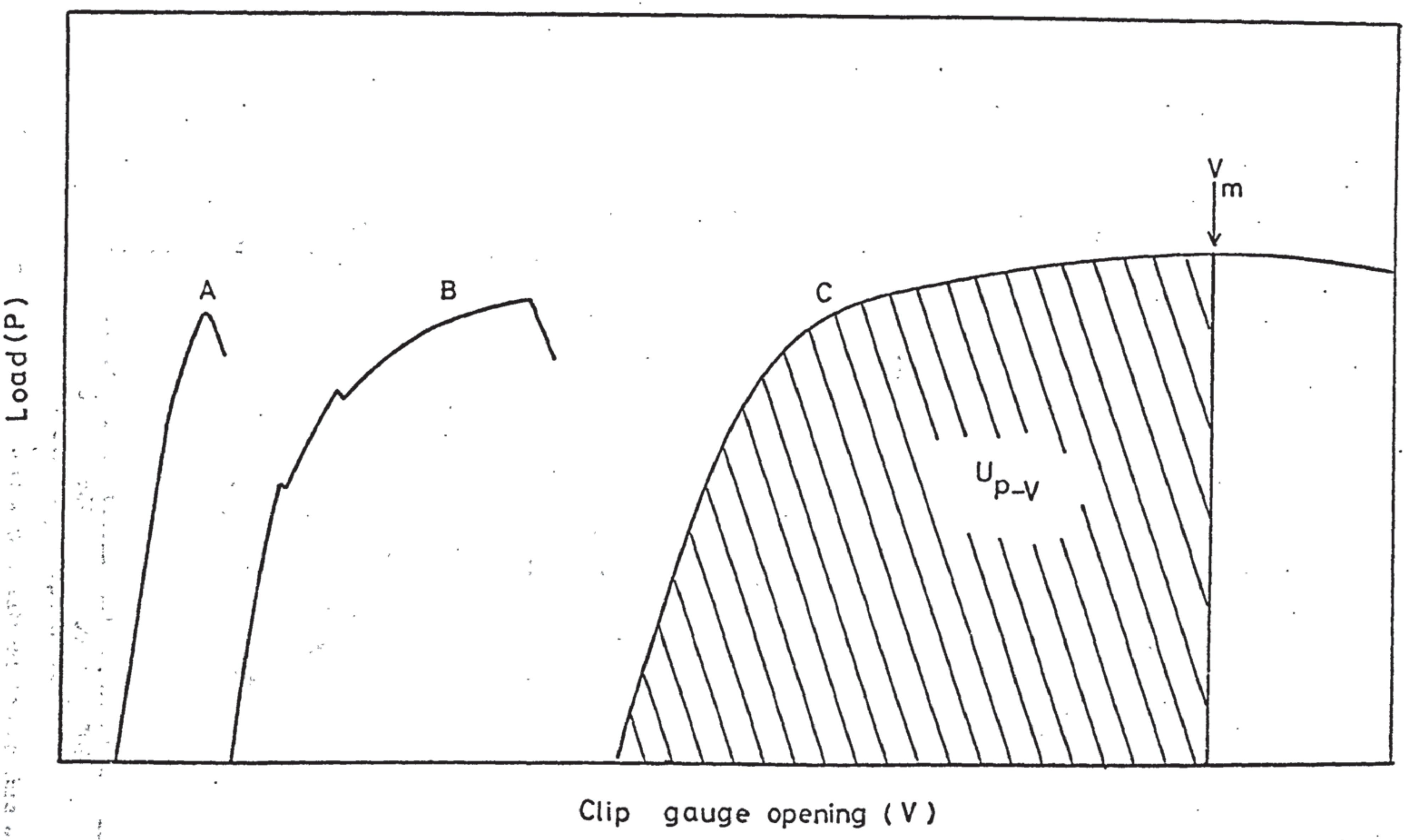

Figure 19—Three types of load - clip gauge opening curves obtained in test program. A - fracture on a rising load curve. B - fracture on a rising load curve preceded by pop-ins. C - maximum load plateau. Area U_{p-V} was used to calculate J.

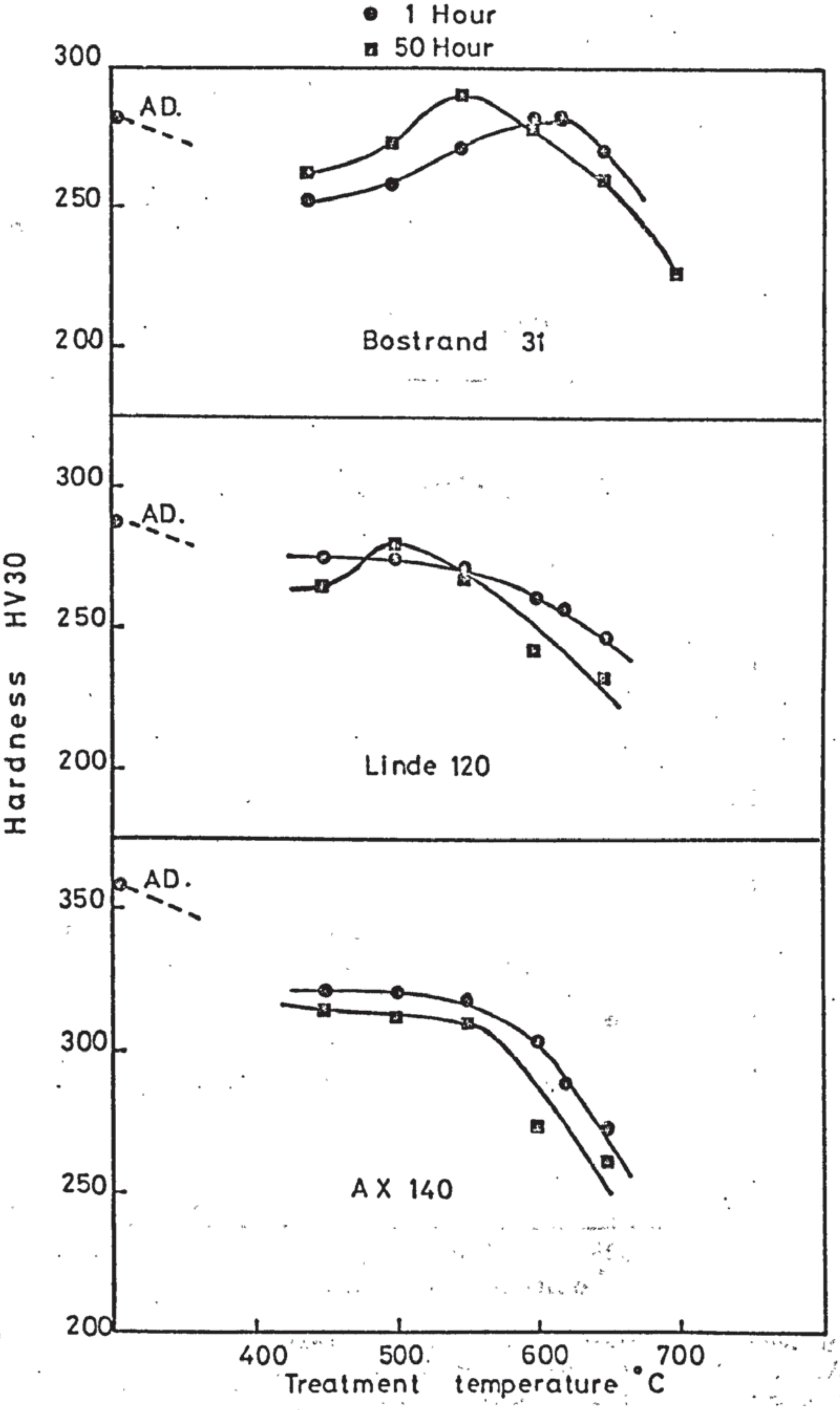

Figure 20 The variation of hardness with treatment temperature after 1 and 50 hours.

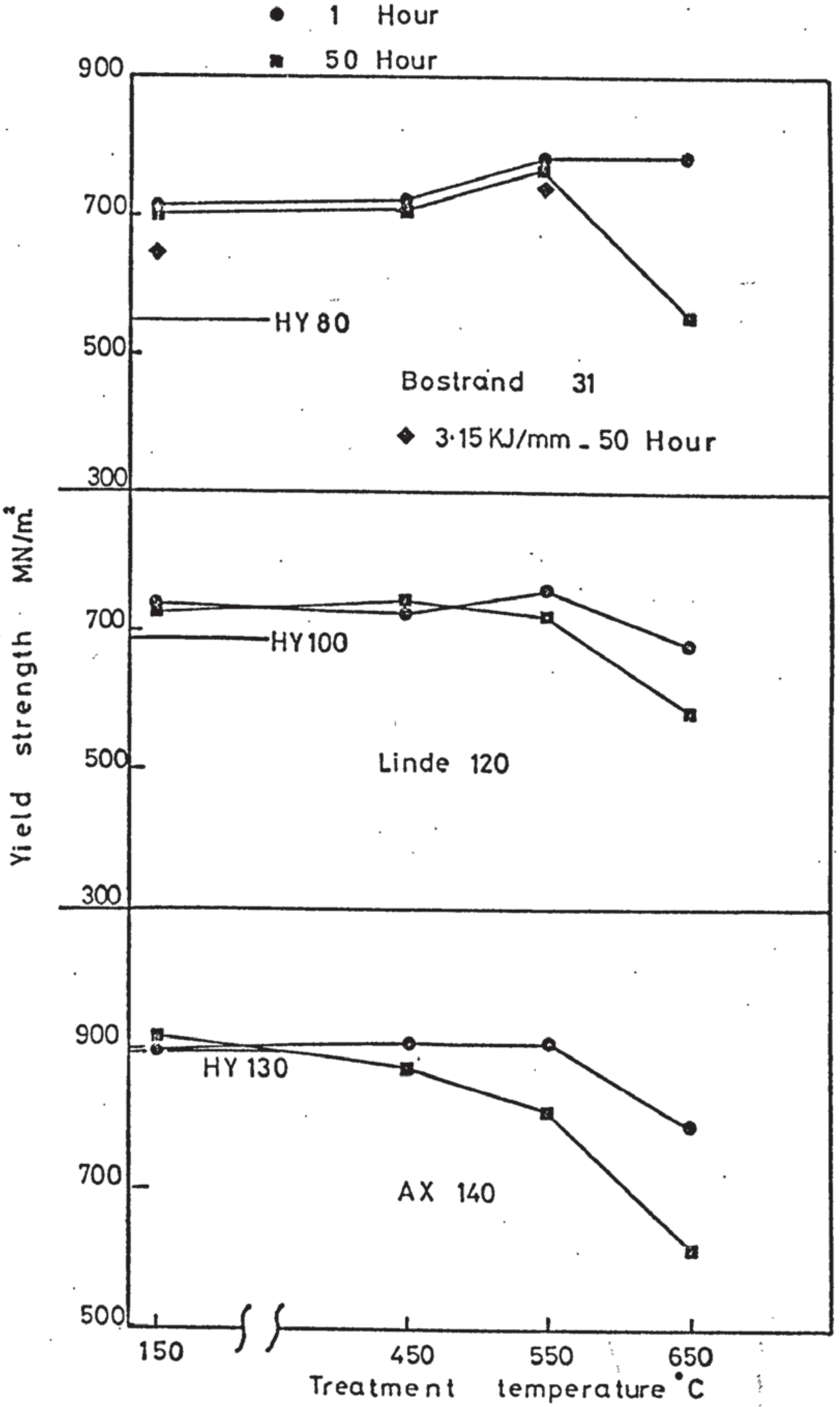

Figure 21 The variation of yield strength with treatment temperature after 1 and 50 hours. As deposited Bostrand 31 (3.15 KJ/mm) and 550°C - 50 hours results included with 1.18 KJ/mm results.

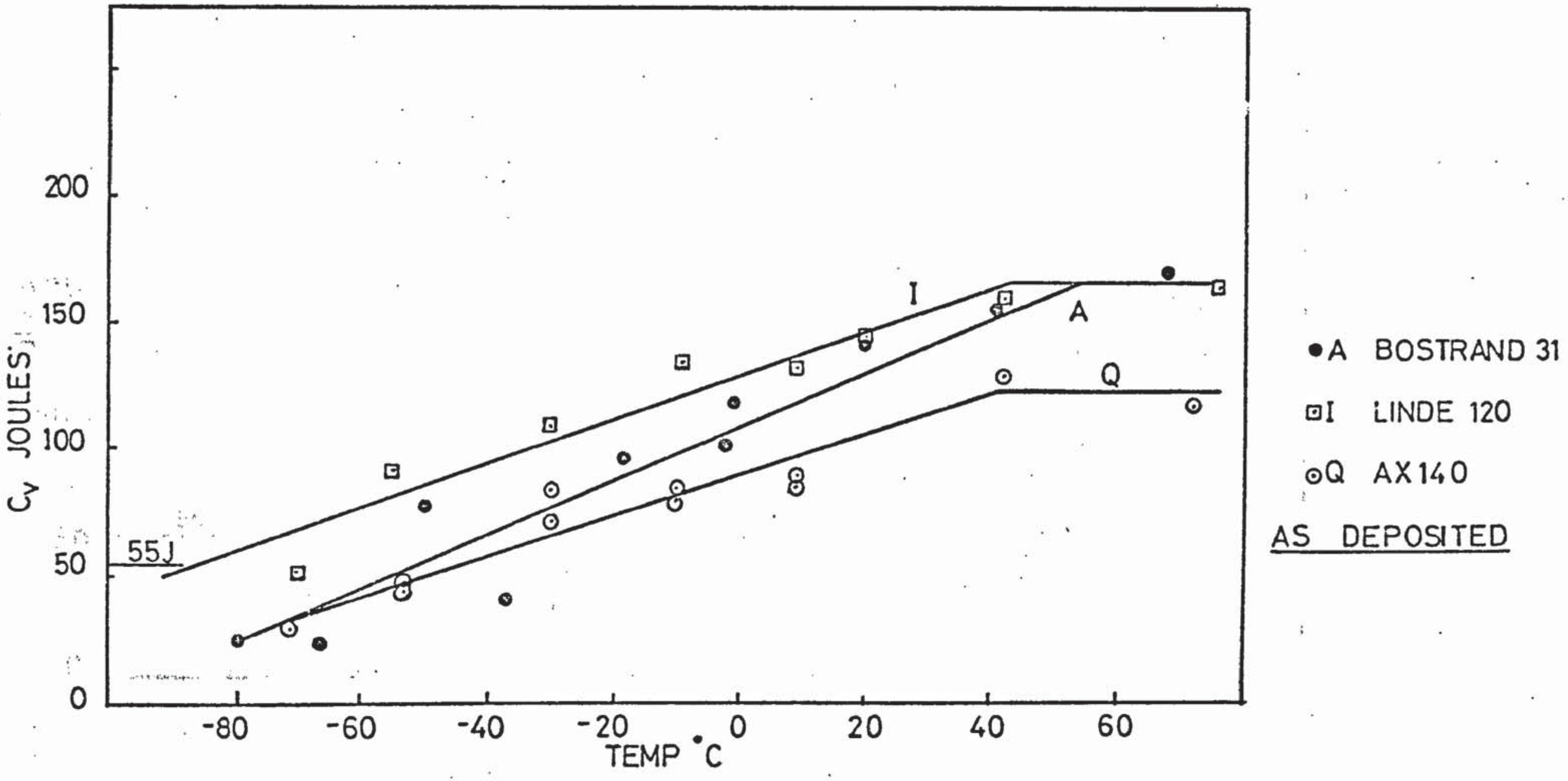

Figure 22 Charpy energy absorbed (C_v) transition curves for as deposited Bostrand 31, Linde 120 and AX140.

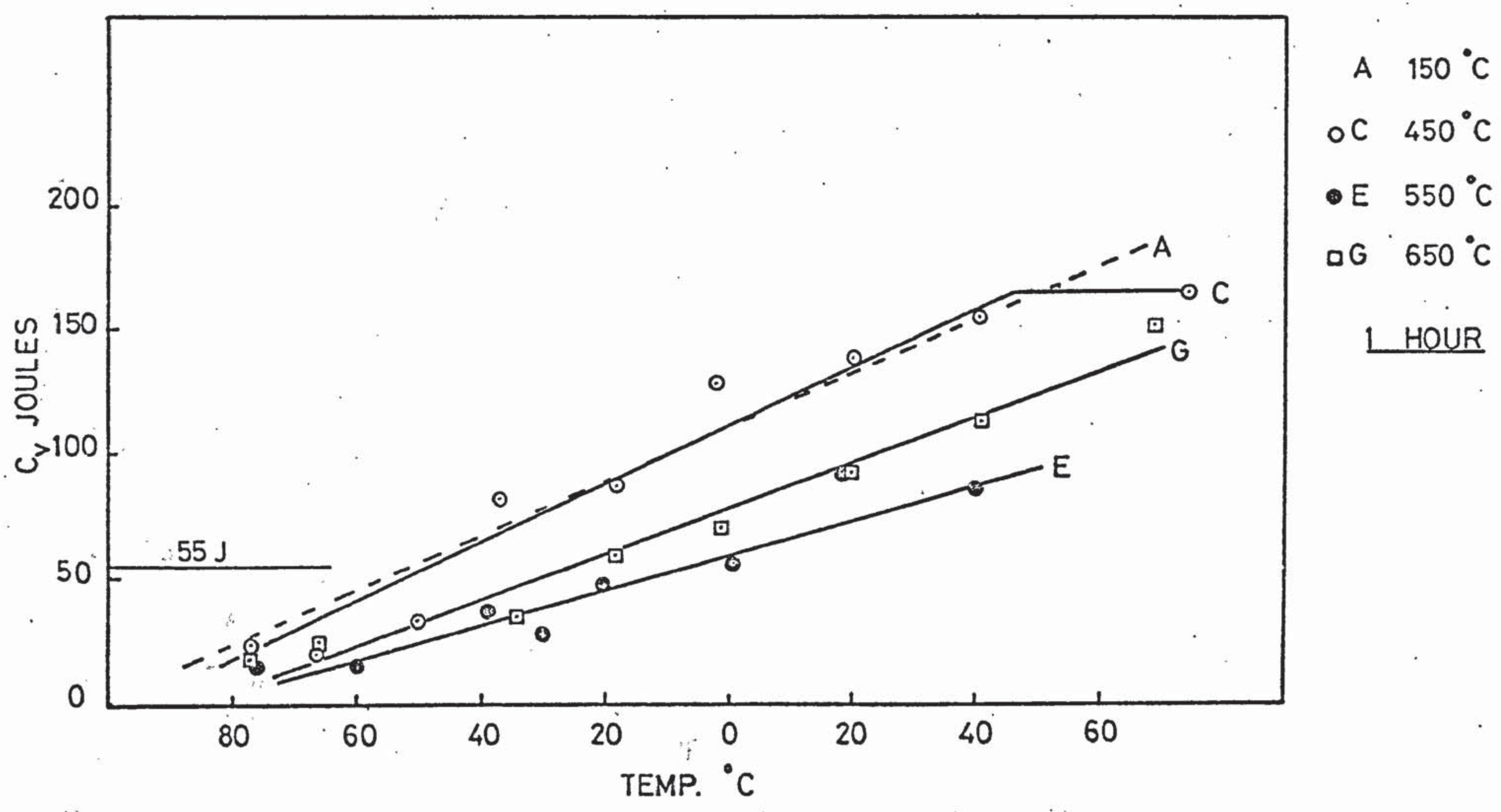

Figure 23 Charpy transition curves for Bostrand 31 after 1 hour at 150, 450, 550 and 650°C.

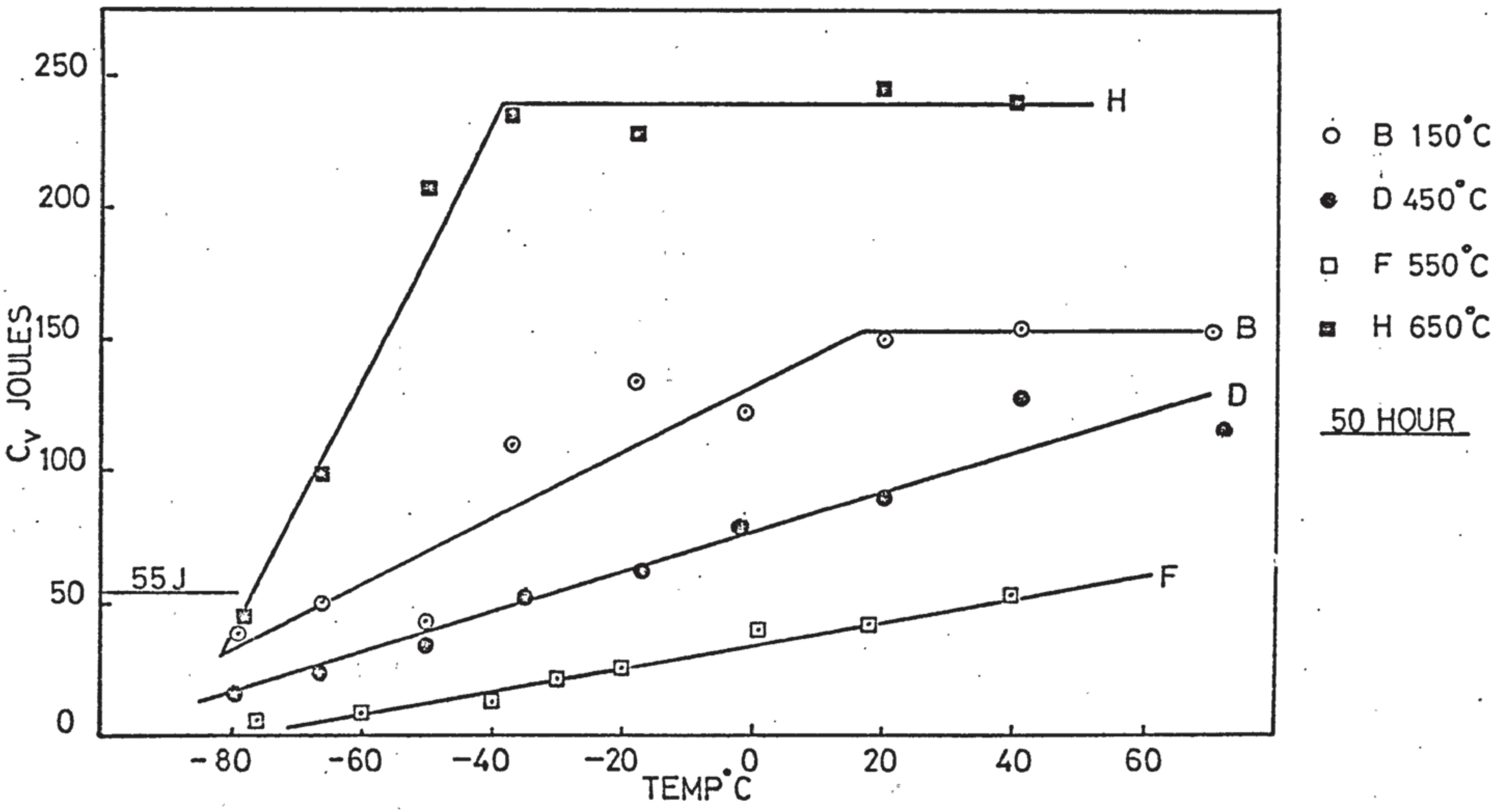

Figure 24 Charpy transition curves for Bostrand 31 after 50 hours at 150, 450, 550 and 650°C.

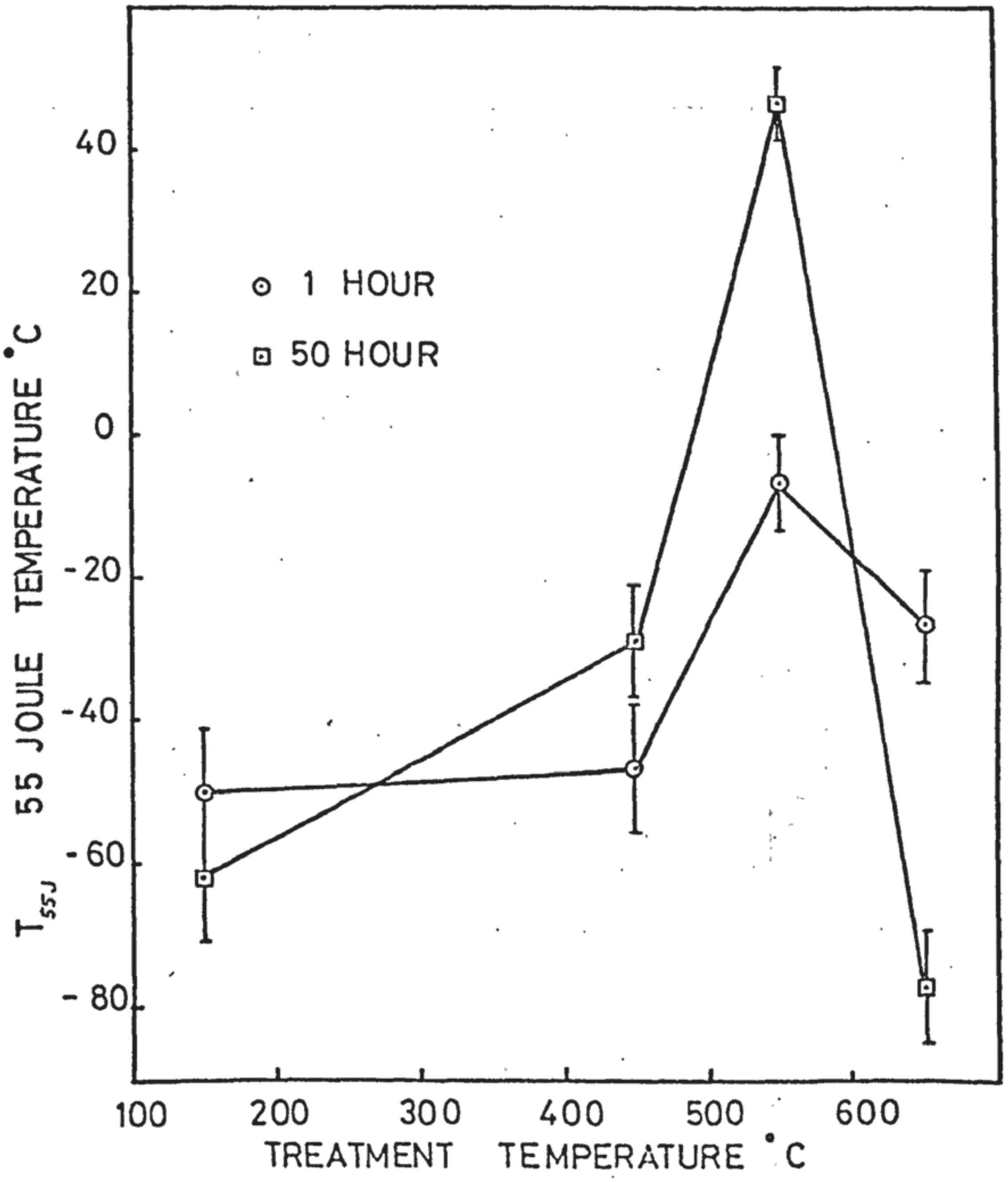

Figure 25 The variation of the 55 joule energy absorbed temperature (T_{55J}) with treatment temperature after 1 hour and 50 hours. The bars indicate 90% confidence limits. Note severe embrittlement in the 450 - 550°C range.

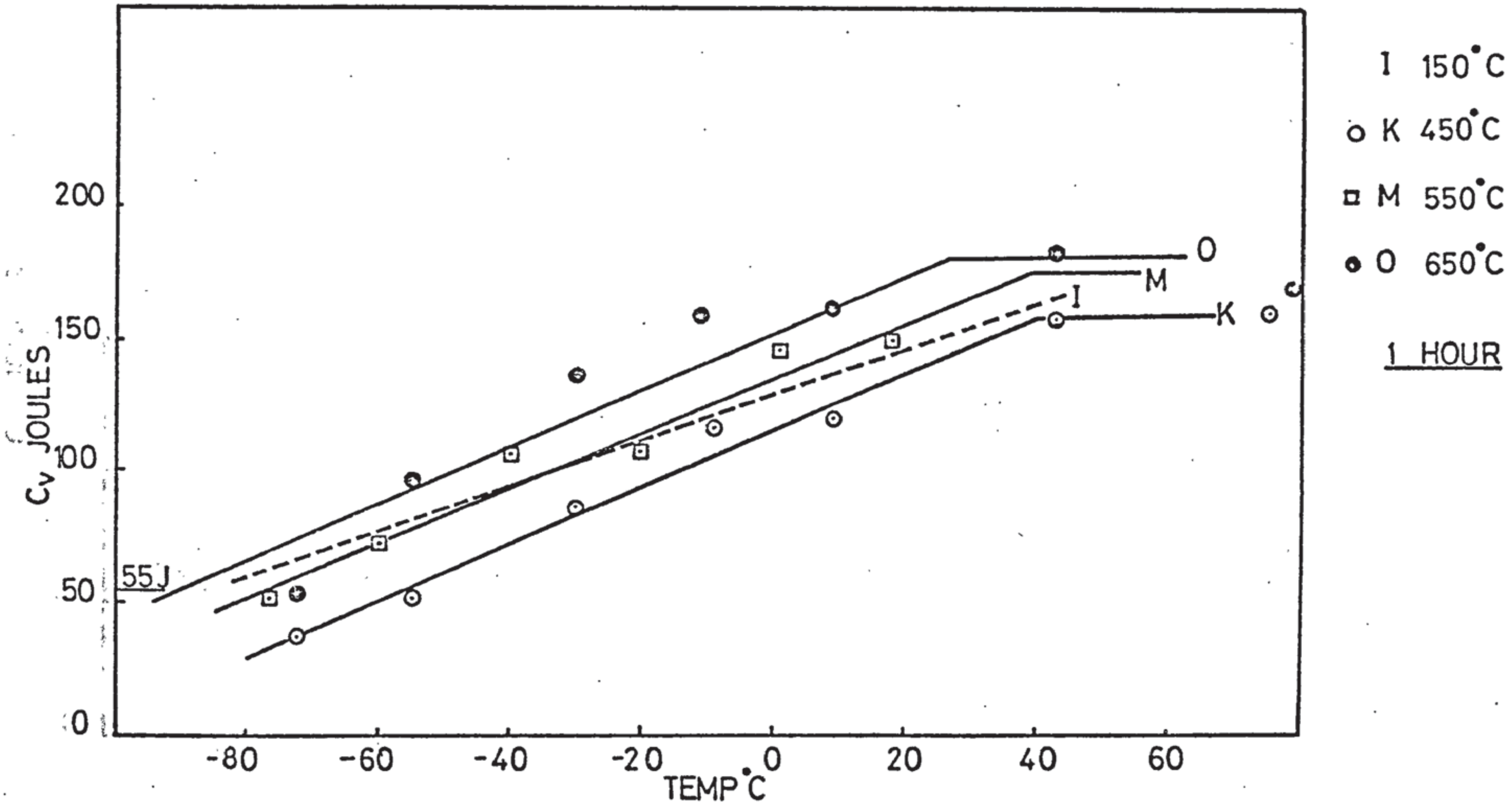

Figure 26 Charpy transition curves for Linde 120 after 1 hour at 150, 450, 550 and 650°C.

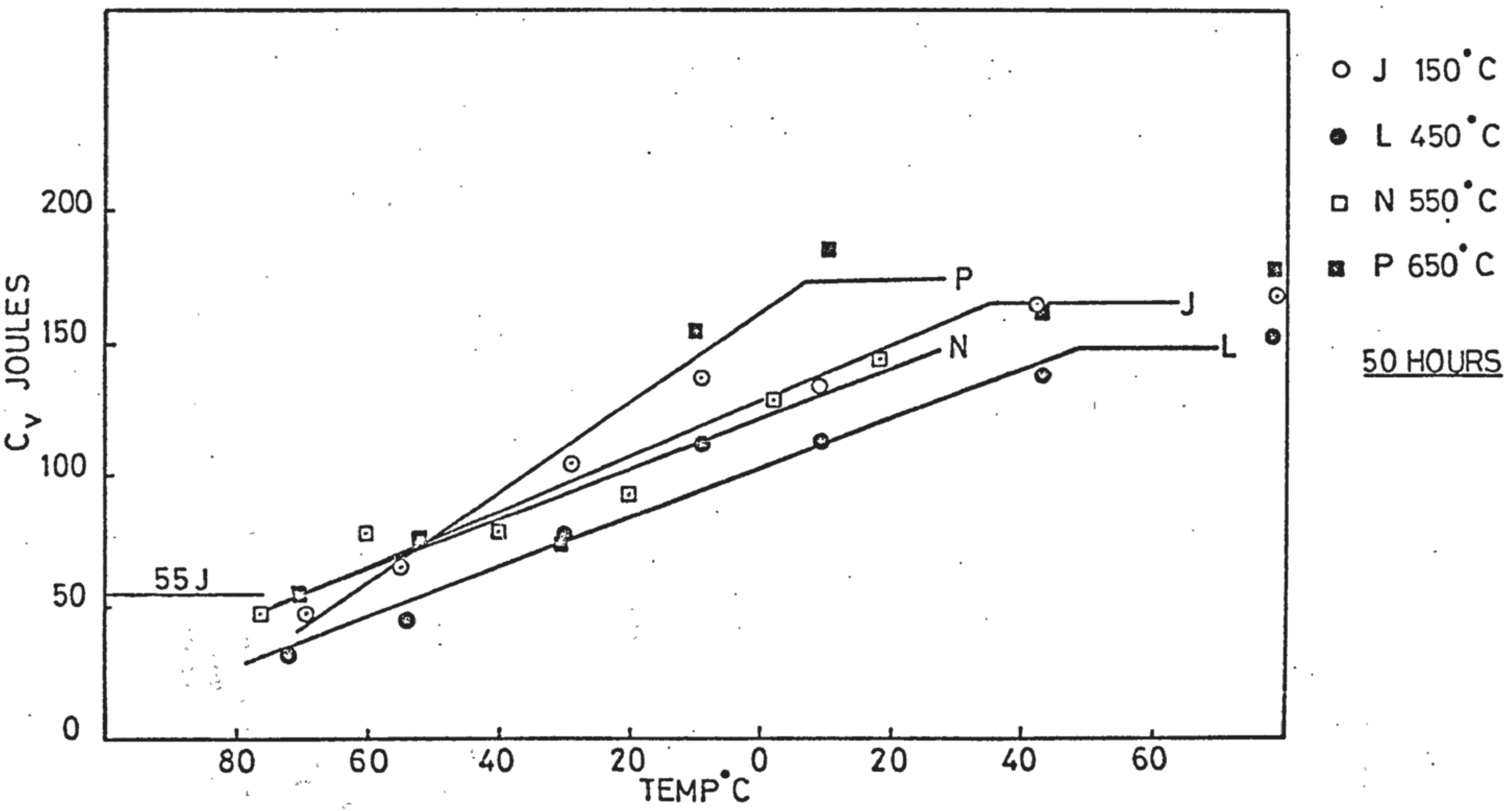

Figure 27 Charpy transition curves for Linde 120 after 50 hours at 150, 450, 550 and 650°C.

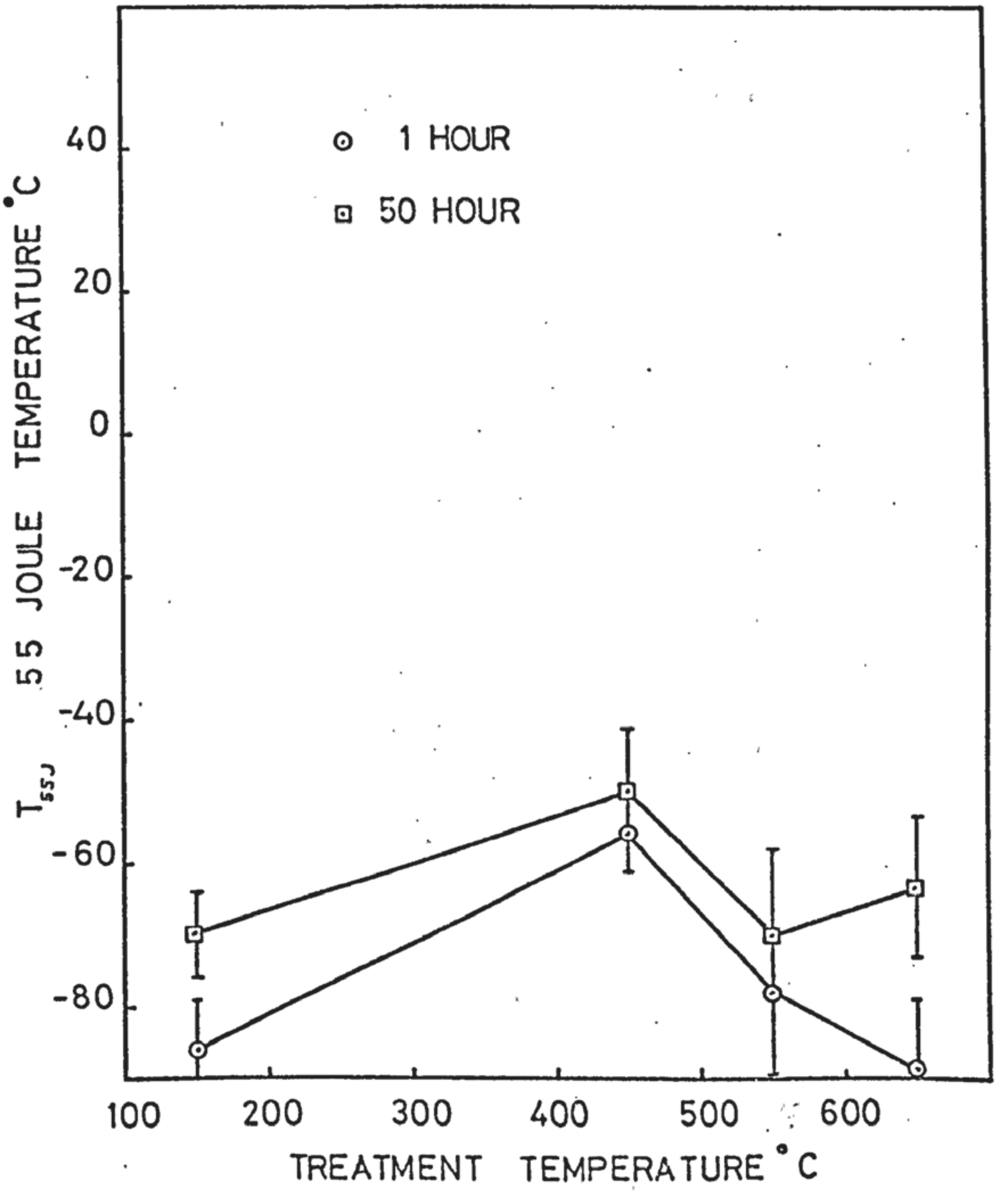

Figure 28 The variation of the 55 joule energy absorbed temperature (T_{55J}) with treatment temperature after 1 hour and 50 hours. The bars indicate 90% confidence limits.

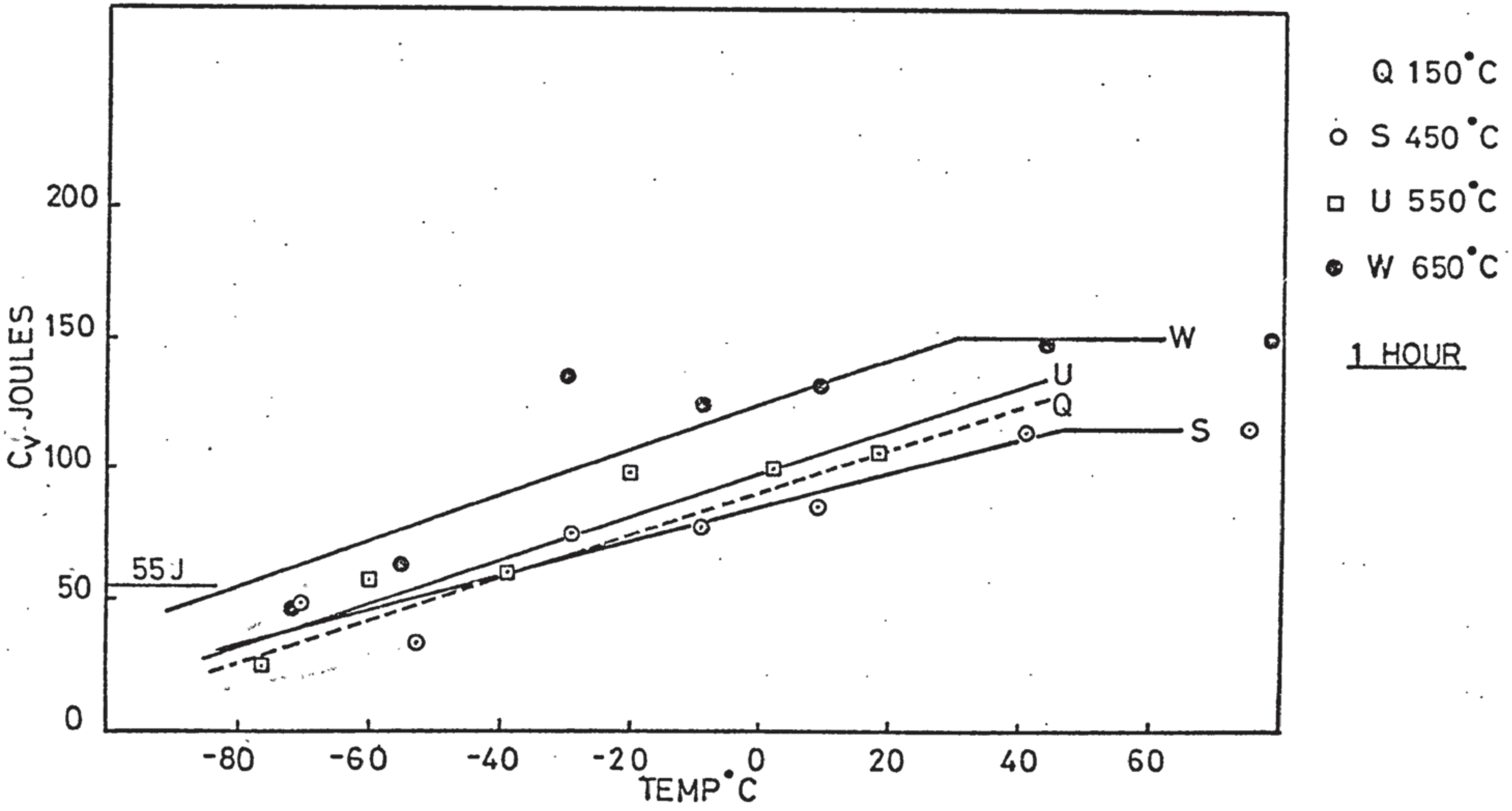

Figure 29 Charpy transition curves for AX140 after 1 hour at 150, 450, 550 and 650°C.

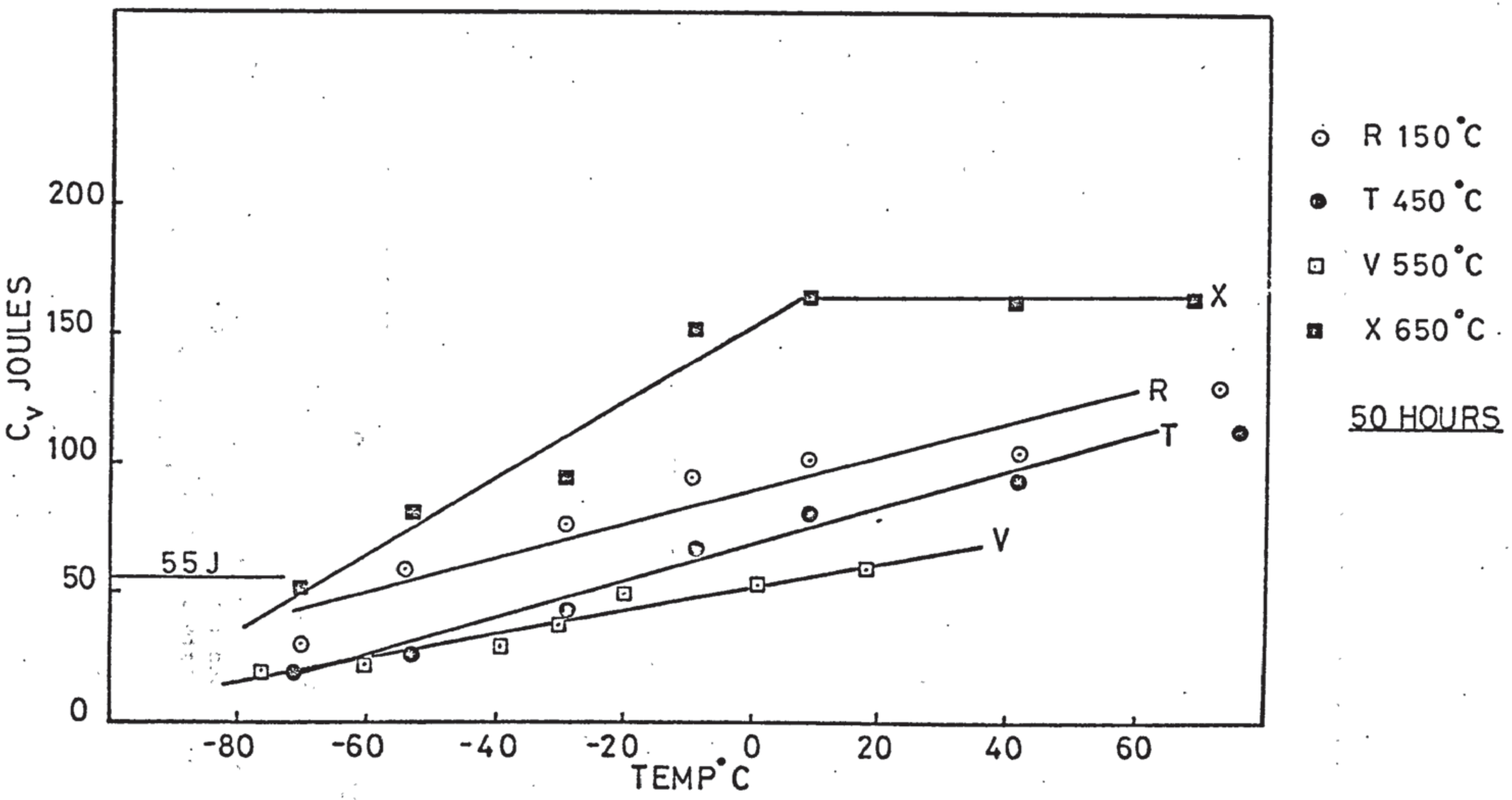

Figure 30 Charpy transition curves for AX140 after 50 hours at 150, 450, 550 and 650°C.

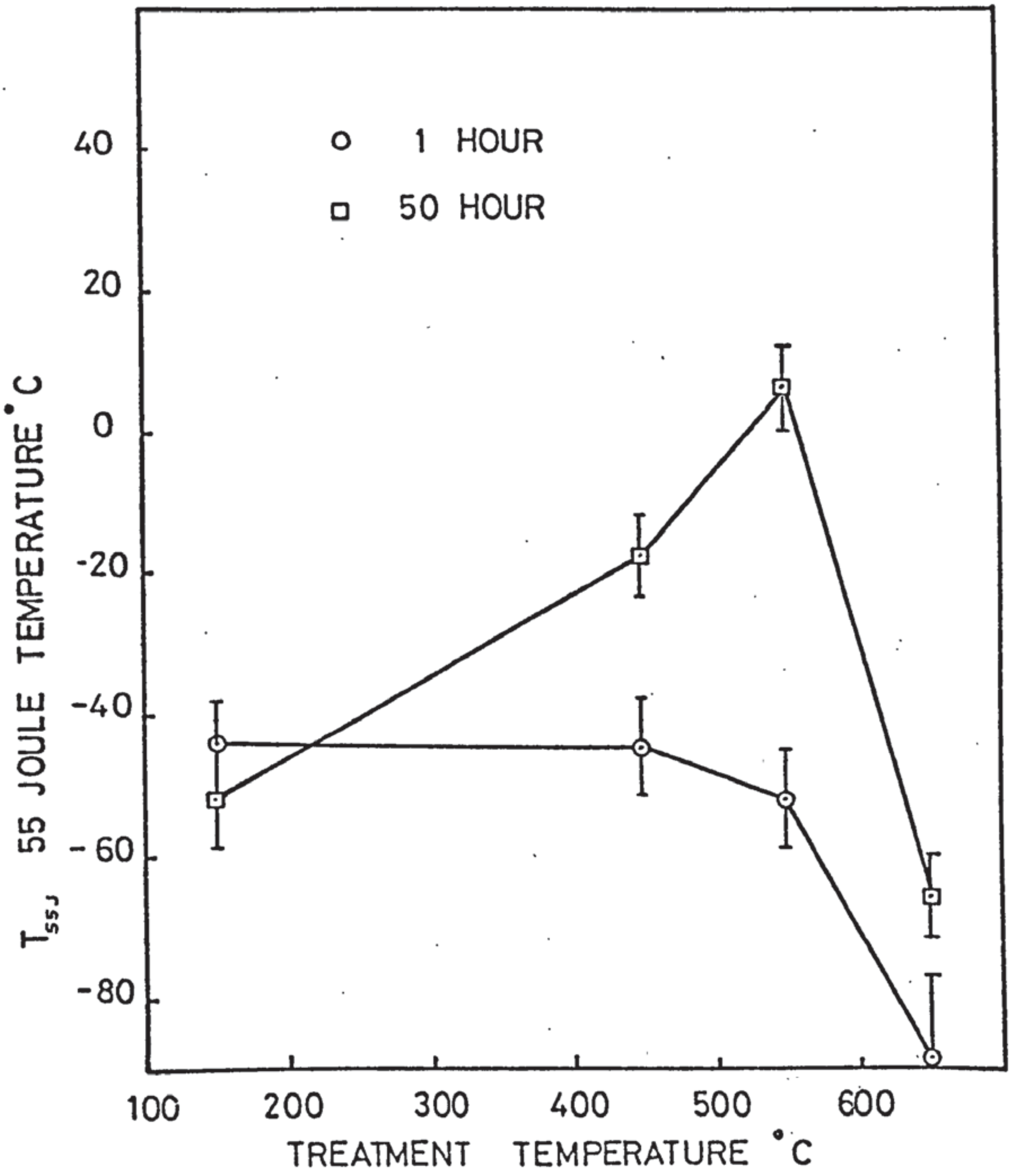

Figure 31 Variation of the 55 joule energy absorbed temperature with treatment temperature (T_{55J}) after 1 hour and 50 hours. The bars indicate the 90% confidence limits. Note embrittlement at 450 and 550°C after 50 hours.

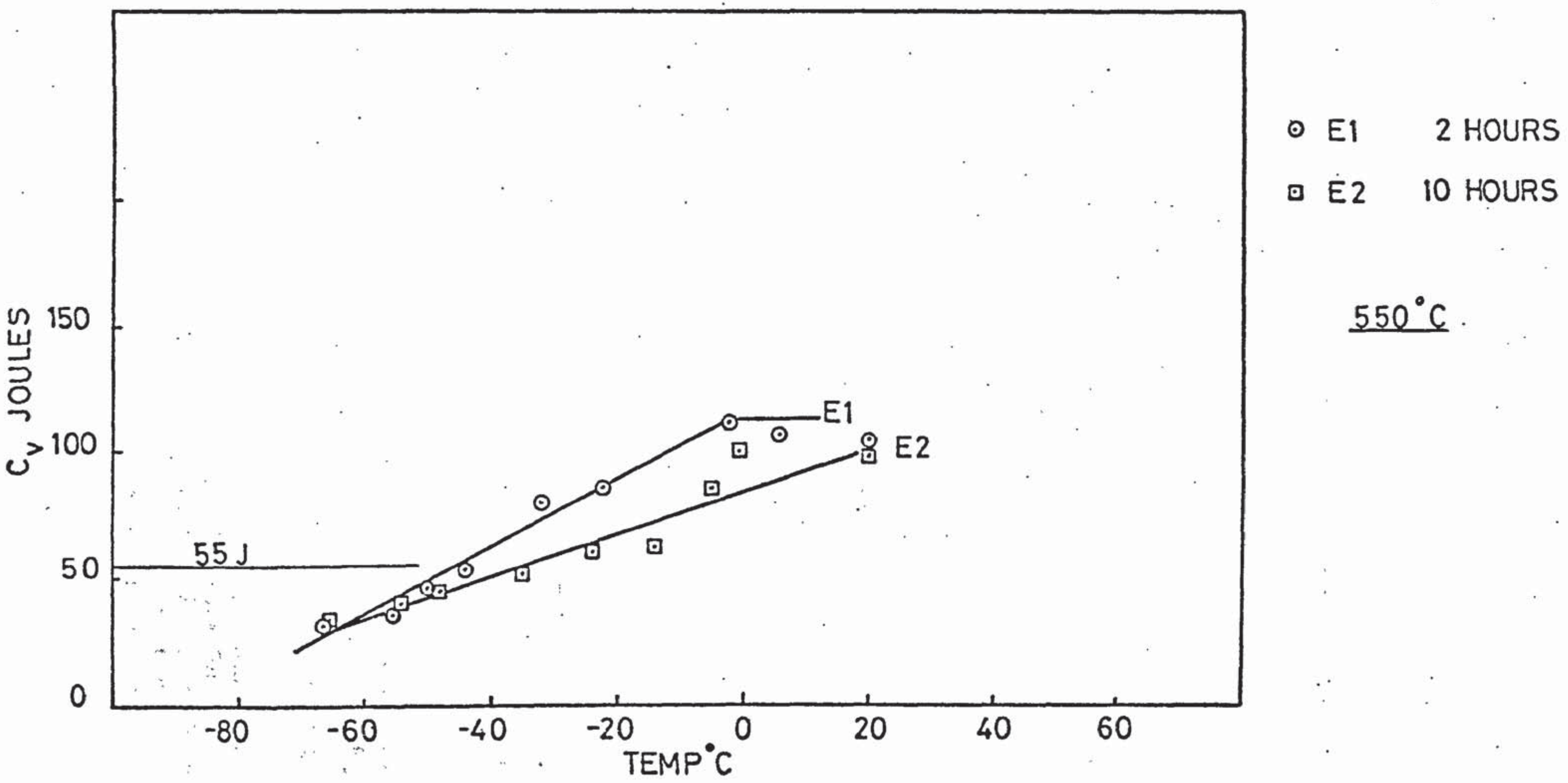

Figure 32 Charpy transition curves for AX140 after 2 and 10 hours at 550°C.

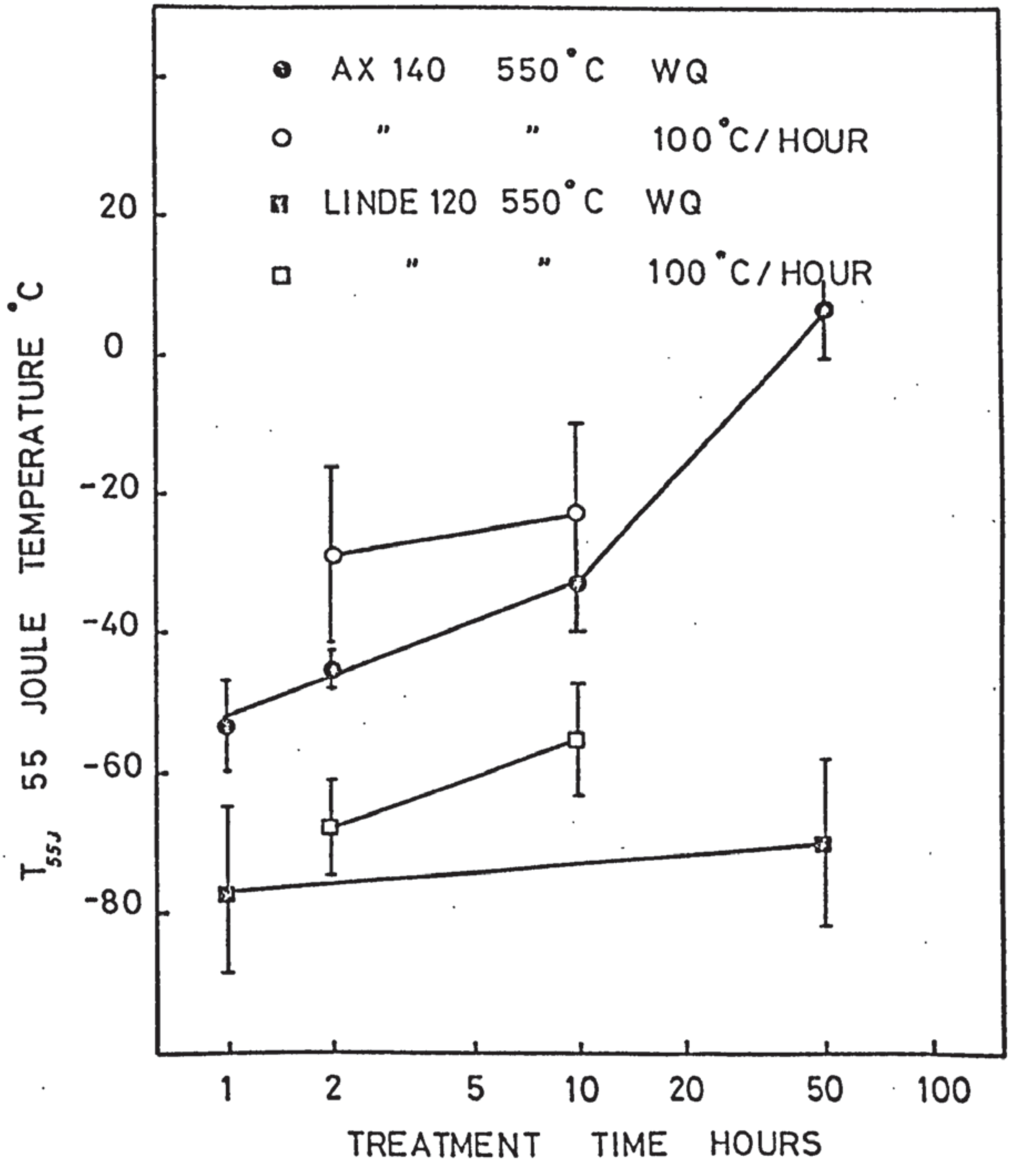

Figure 33 The variation of the 55 joule energy absorbed temperature with treatment time and cooling rate for AX140 and Linde 120 heat treated at 550°C. The bars indicate the 90% confidence limits. The figure shows that embrittlement of AX140 increases with time and decreasing cooling rate.

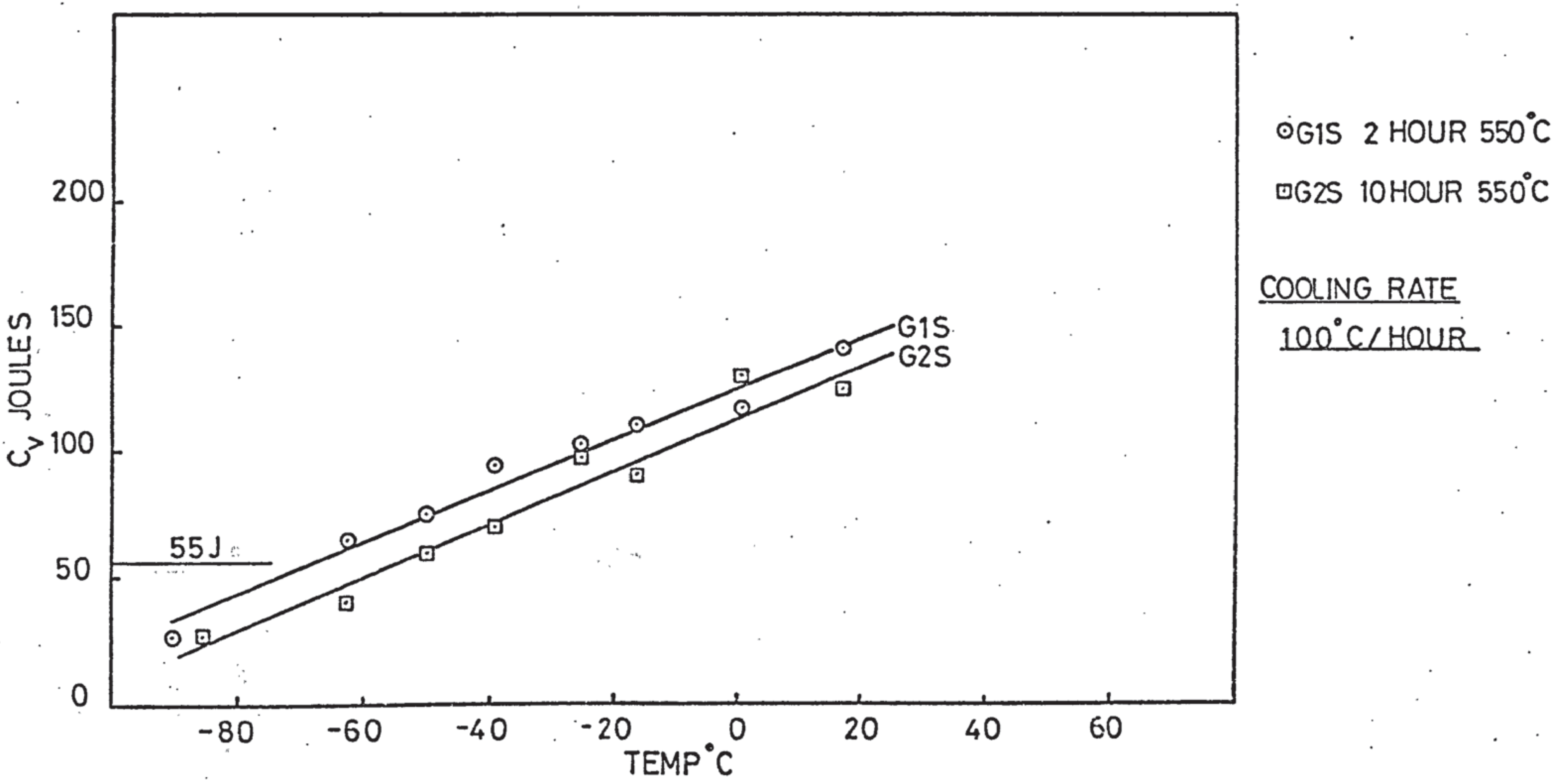

Figure 34 Charpy transition curves for Linde 120 treated at 550°C for 2 and 10 hours and cooled at 100°C/hour.

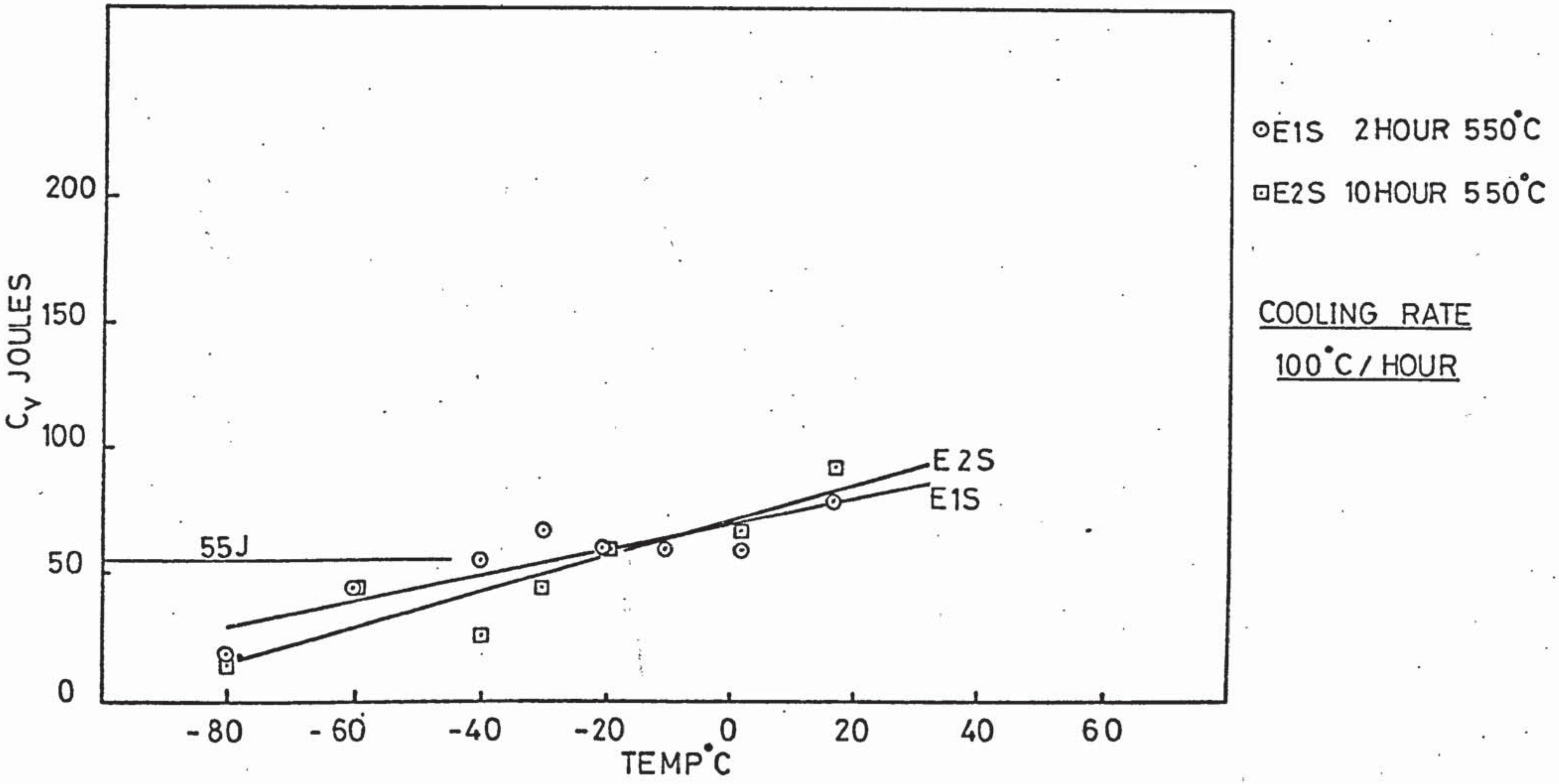

Figure 35 Charpy transition curves for AX140 treated at 550°C for 2 and 10 hours and cooled at 100°C/hour.

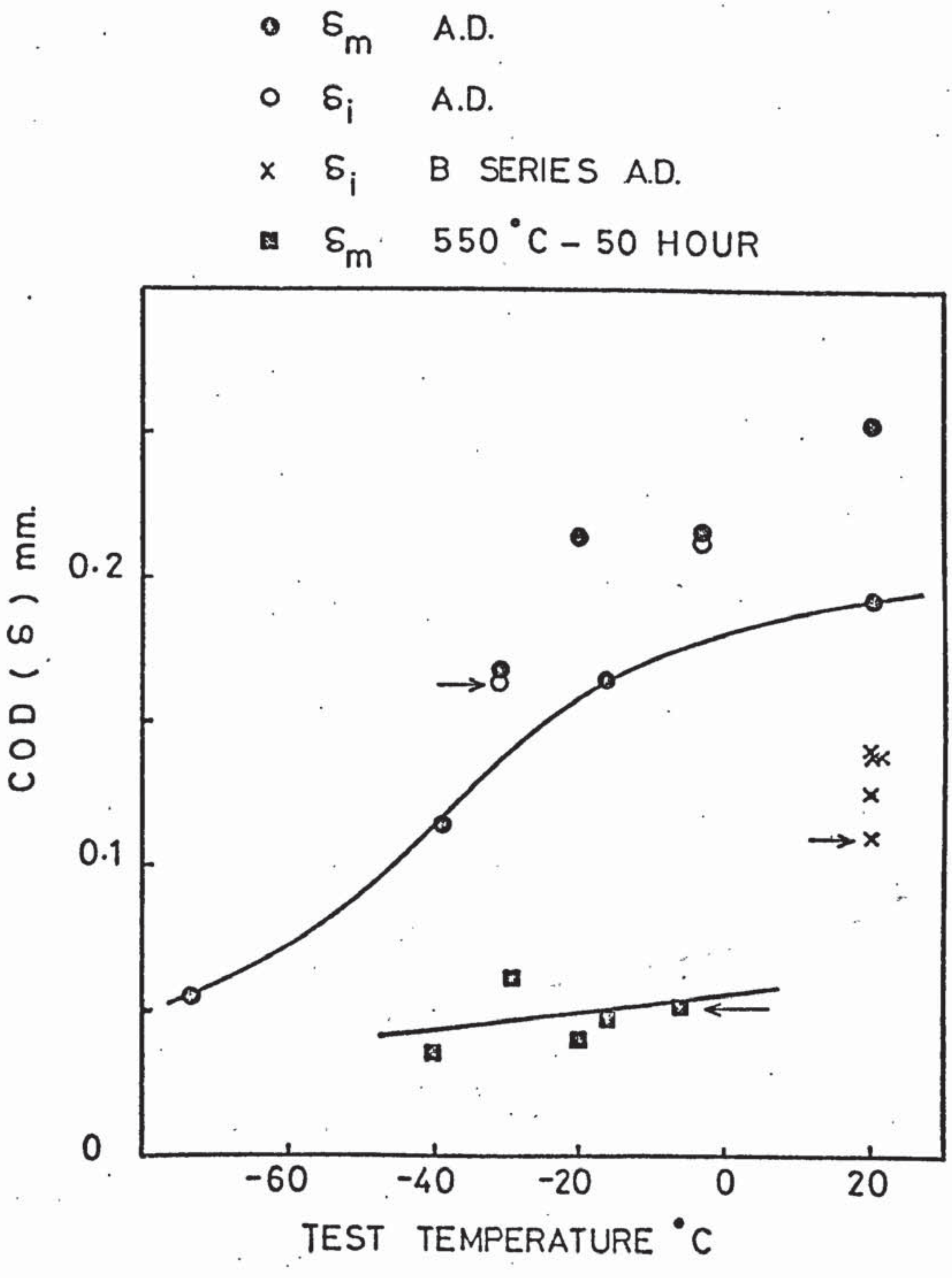

Figure 36 The variation of COD (δ_m and δ_i) with testing temperature for Bostrand 31 (1.18 KJ/mm) in the as deposited condition (A.D) and after 50 hours at 550°C. The as deposited (transverse) notch results (B series) are also included. The figure shows the reduction in COD caused by heat treatment. Arrows indicate values used in the defect tolerance calculations.

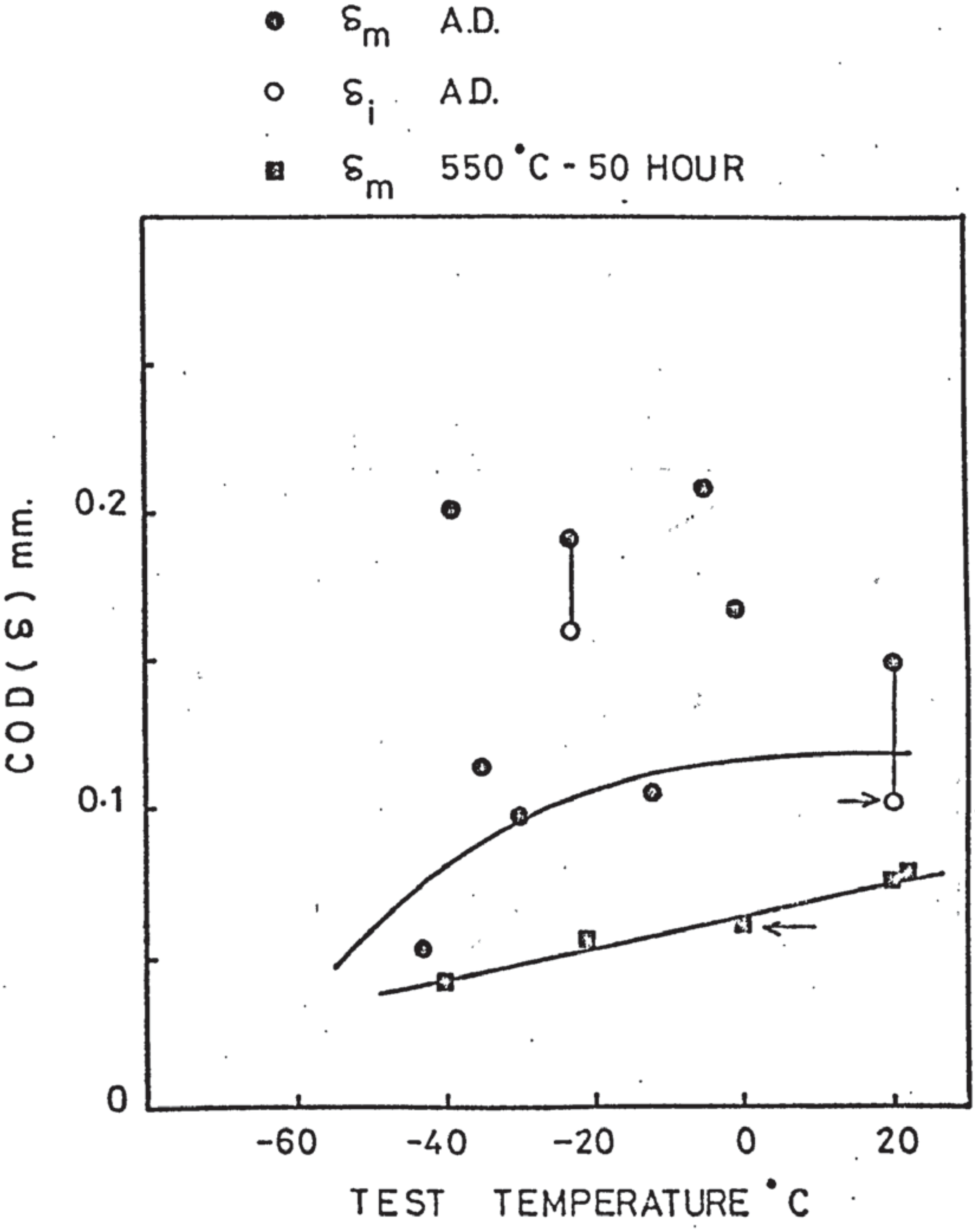

Figure 37 The variation of COD (δ_m and δ_i) with test temperature for Bostrand 31 (3.15 KJ/mm) in the as deposited condition (A.D) and after 50 hours at 550°C showing the reduction in COD caused by heat treatment. Arrows indicate the values used in the defect tolerance calculations.

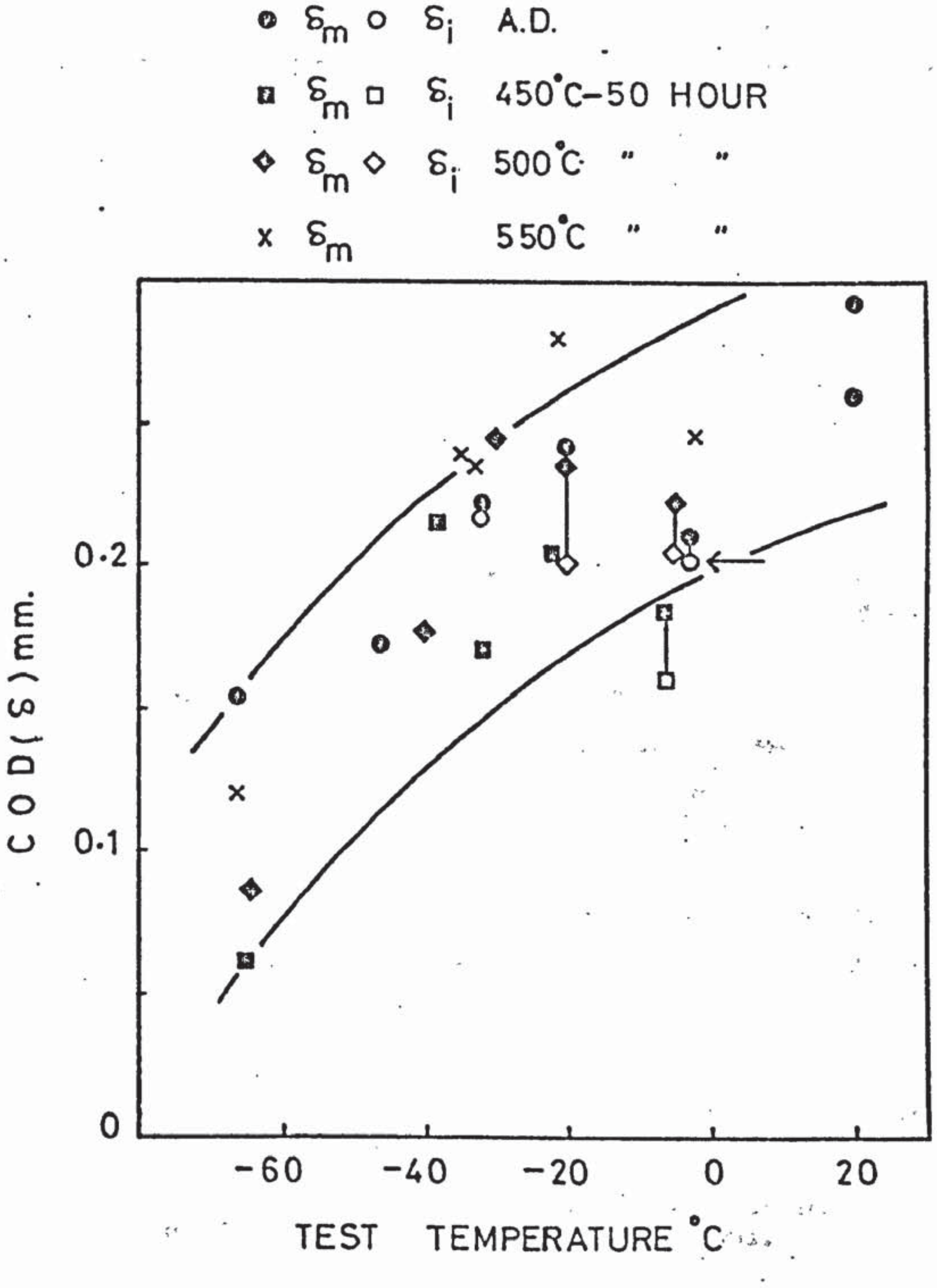

Figure 38 COD (δ_i and δ_m) versus test temperature for Linde 120 in the as deposited condition (A.D) and after 50 hours at 450, 500 and 550°C. The figure shows that any embrittlement due to heat treatment is minimal. The arrow indicates the value used in the defect tolerance calculations.

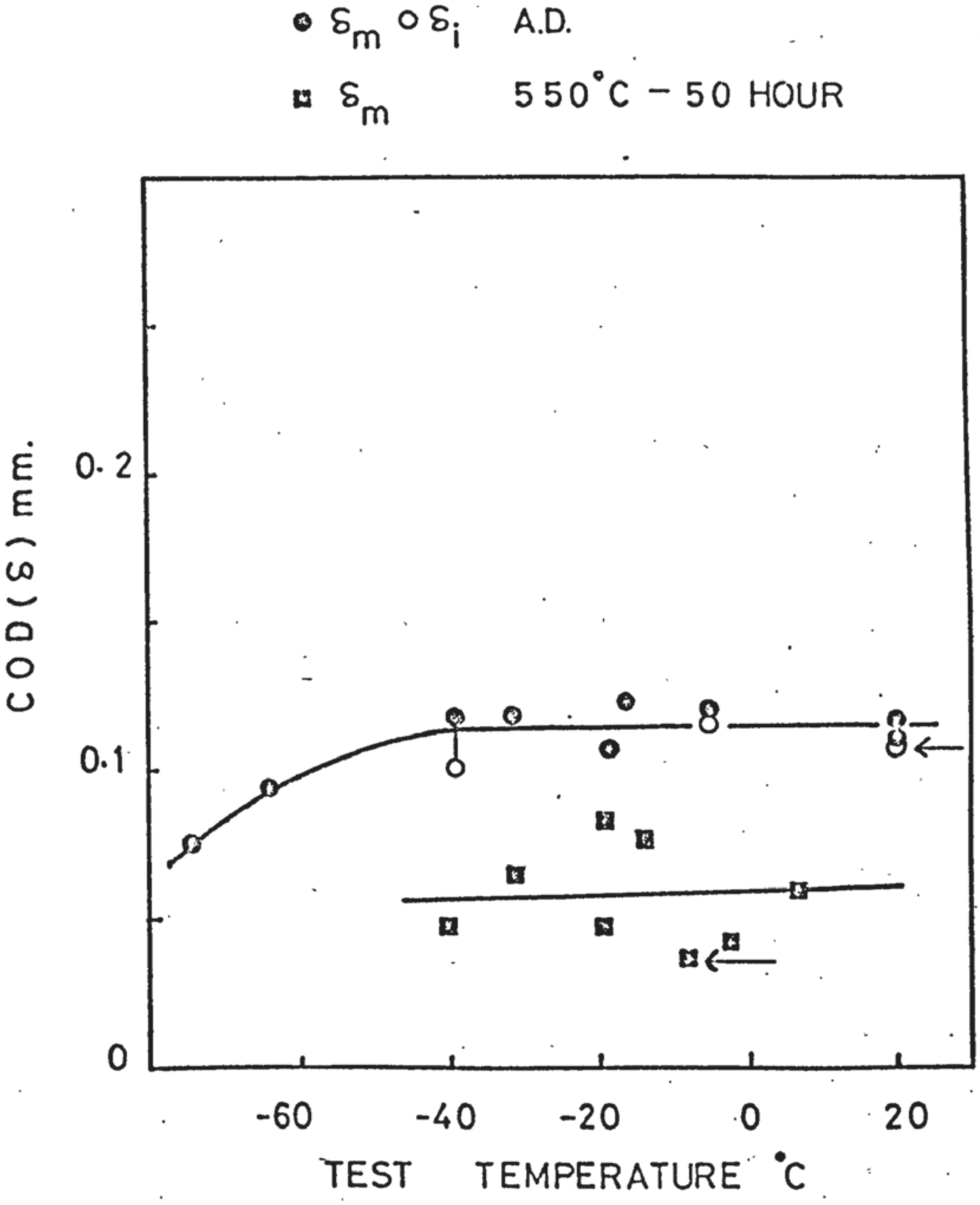

Figure 39 COD (δ_i and δ_m) versus test temperature for AX140 in the as deposited condition (A.D) and after 50 hours at 550°C. Note the low temperature dependence and the reduction of COD caused by heat treatment. Arrows indicate the values used in the defect tolerance calculations.

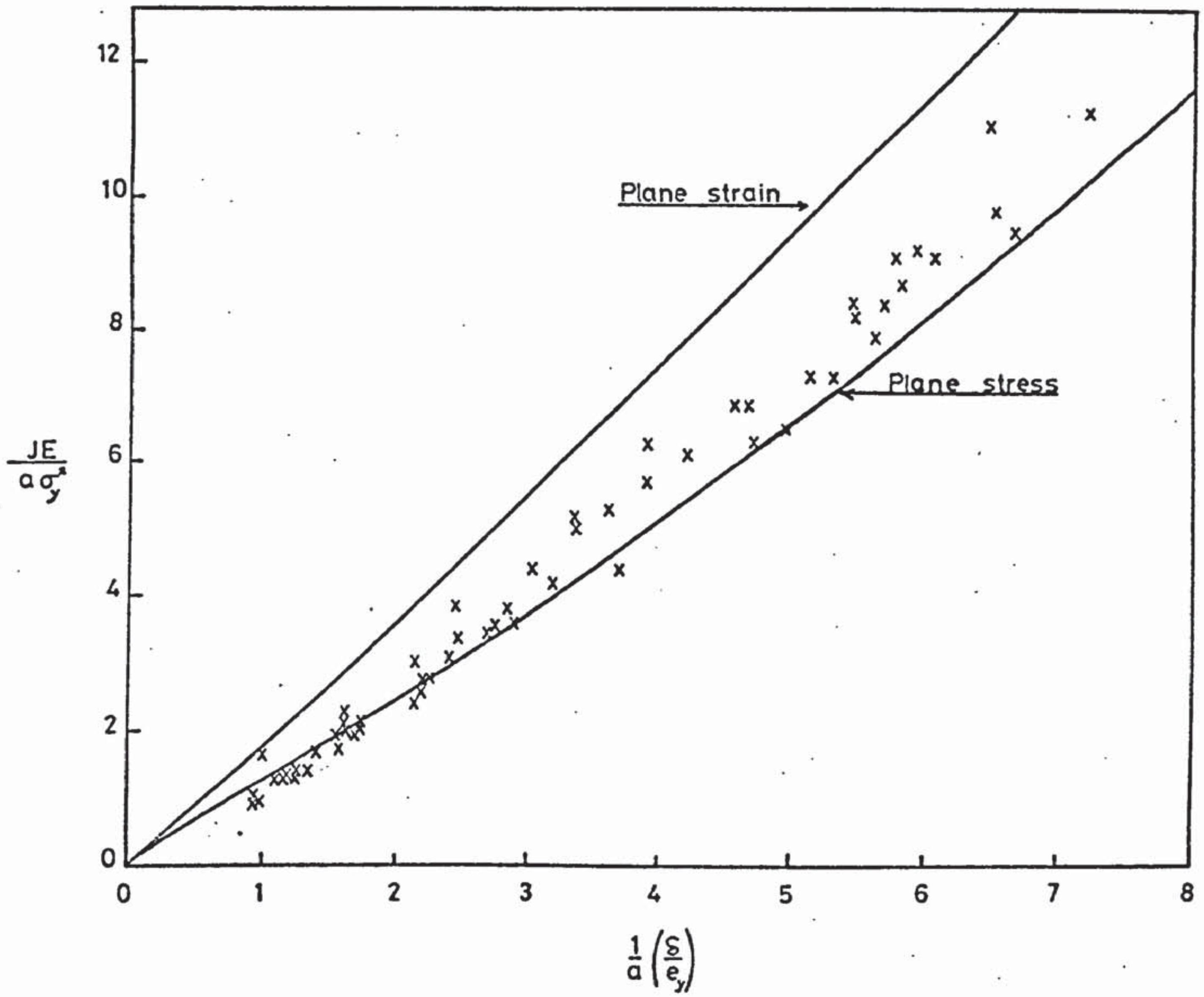

Figure 40 Plot of non dimensional δ versus non dimensional J including all J results from each weld metal regardless of heat treated condition. Finite element solution assuming plane strain and stress are included (from reference 75).

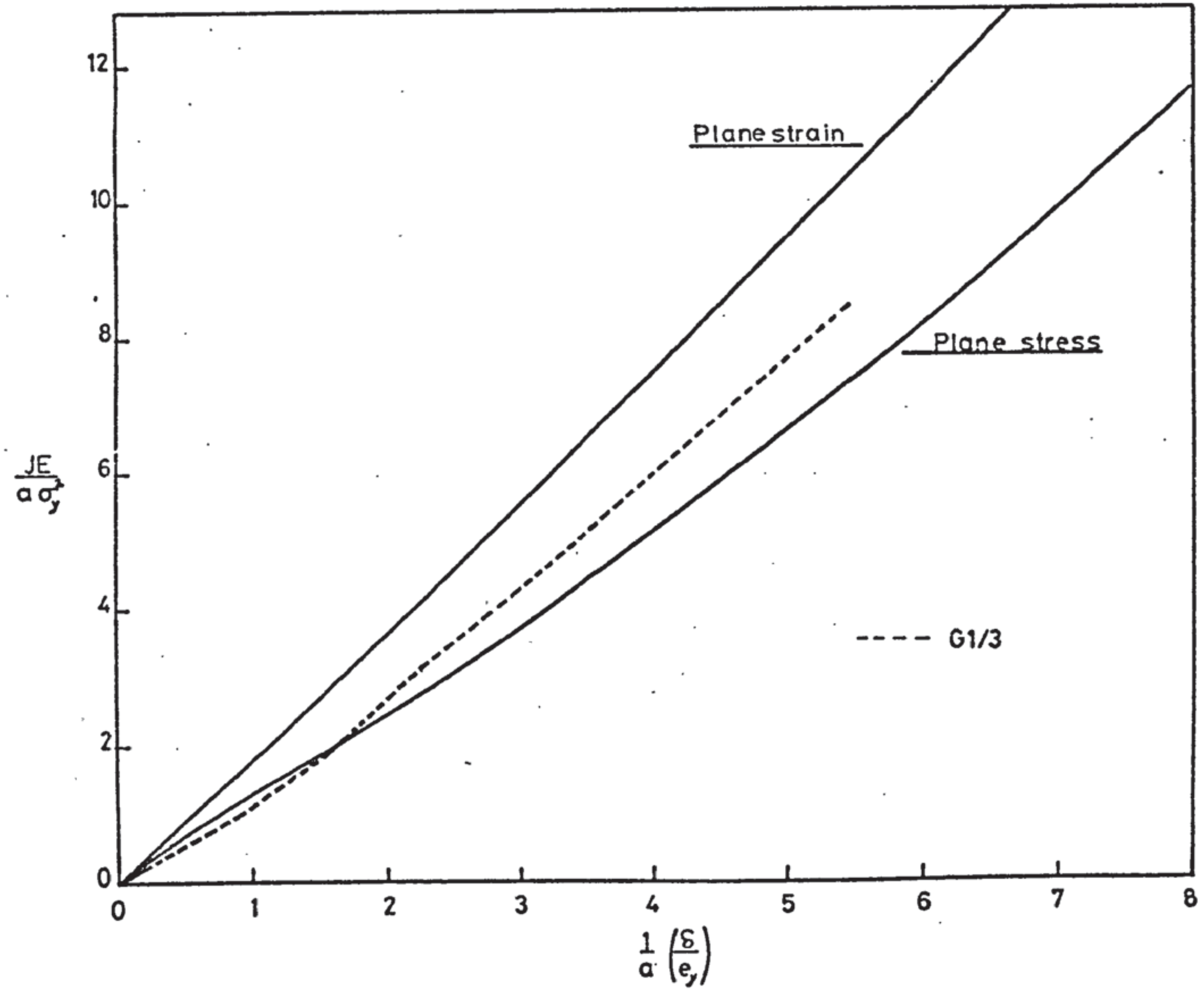

Figure 41 Continuous variation of J and δ along a single load-clip gauge opening curve for specimen G1/3. Note deviation below finite element plane stress solution at low δ values.

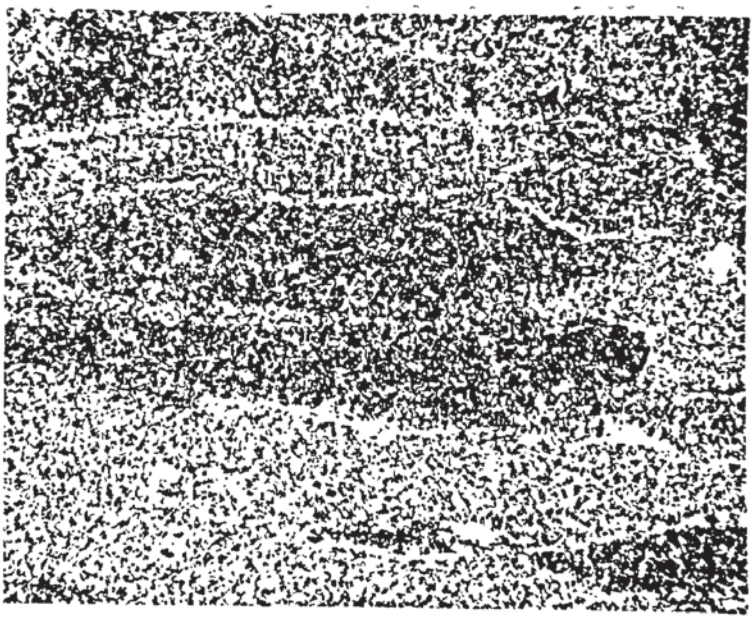

Figure 42 Columnar grains containing acicular ferrite and outlined by proeutectoid ferrite in Bostrand 31 (3.15 KJ/mm). 2% Nital. X 200.

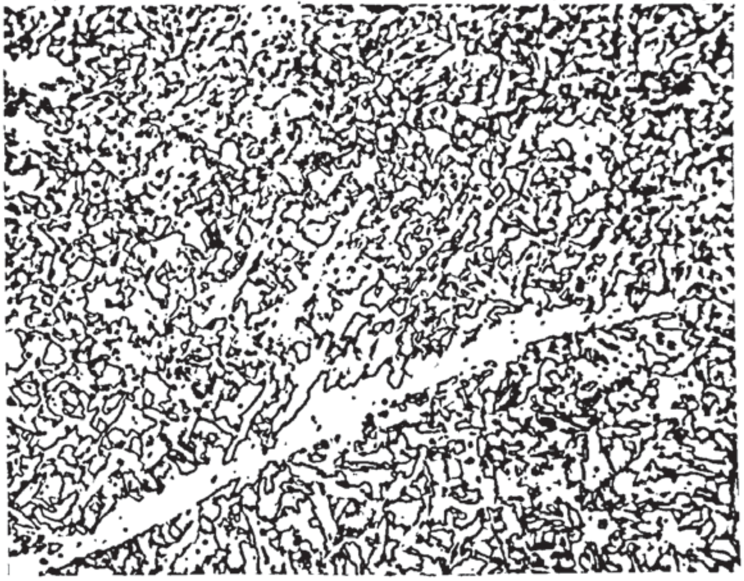

Figure 43 Acicular ferrite and a band of proeutectoid ferrite in Bostrand 31 (3.15 KJ/mm). 2% Nital. X 600.

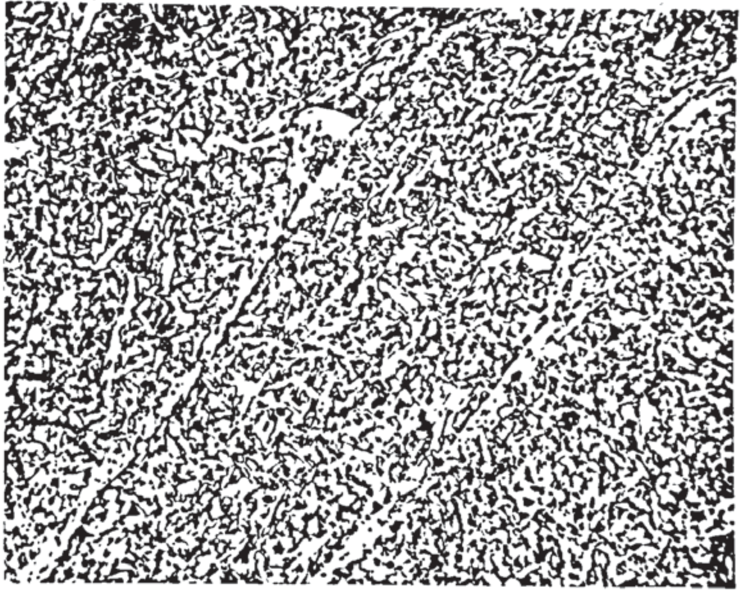

Figure 44 Acicular ferrite and proeutectoid ferrite on columnar grain boundaries in Bostrand 31 (1.18 KJ/mm). 2% Nital. X 600.

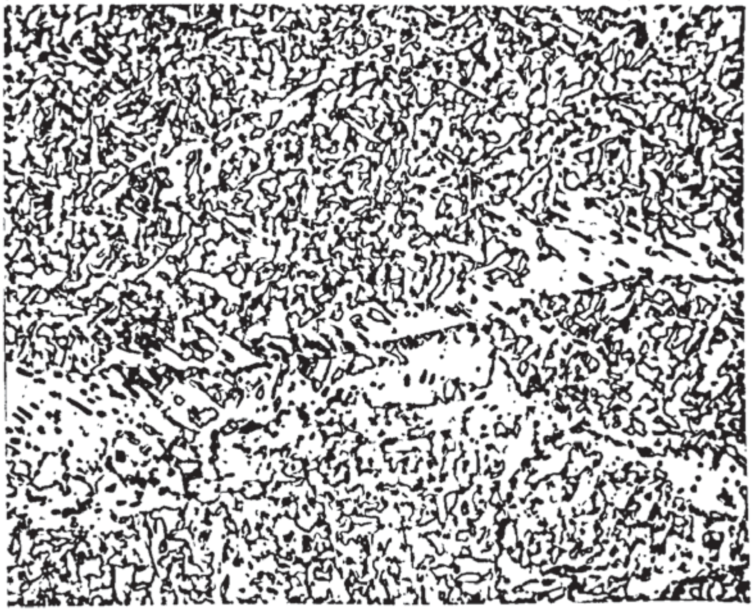

Figure 45 Acicular ferrite and proeutectoid ferrite showing a tendency towards ferrite side plates in Bostrand 31 (3.15 KJ/mm). 2% Nital. X 600.

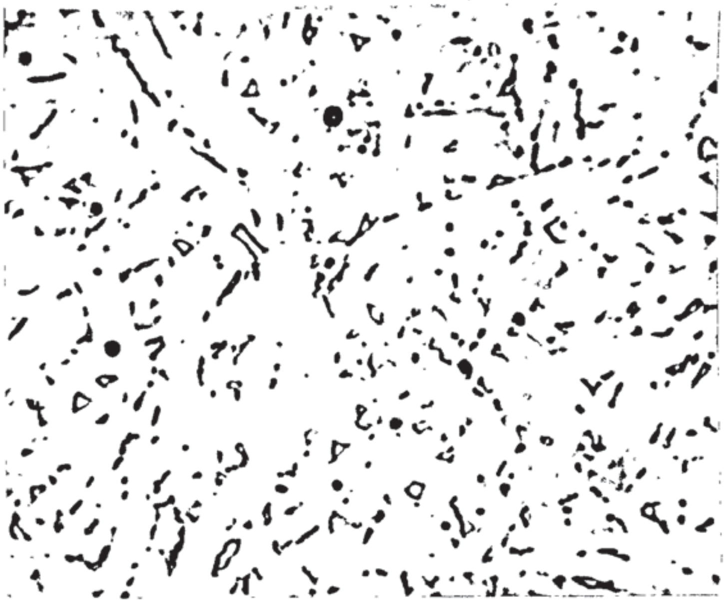

Figure 46 Islands of martensite in acicular ferrite. 4% picral. Bostrand 31 (3.15 KJ/mm). X 2000.

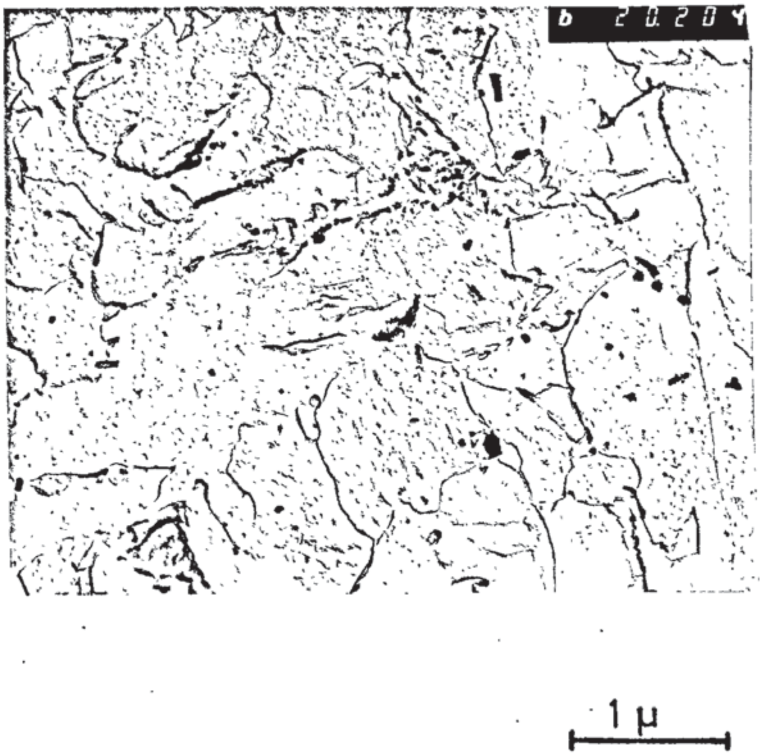

Figure 47 Cemenitite particles (upper left) on acicular ferrite grain boundaries in Bostrand 31 (1.18 KJ/mm). Self shadowed extraction replica.

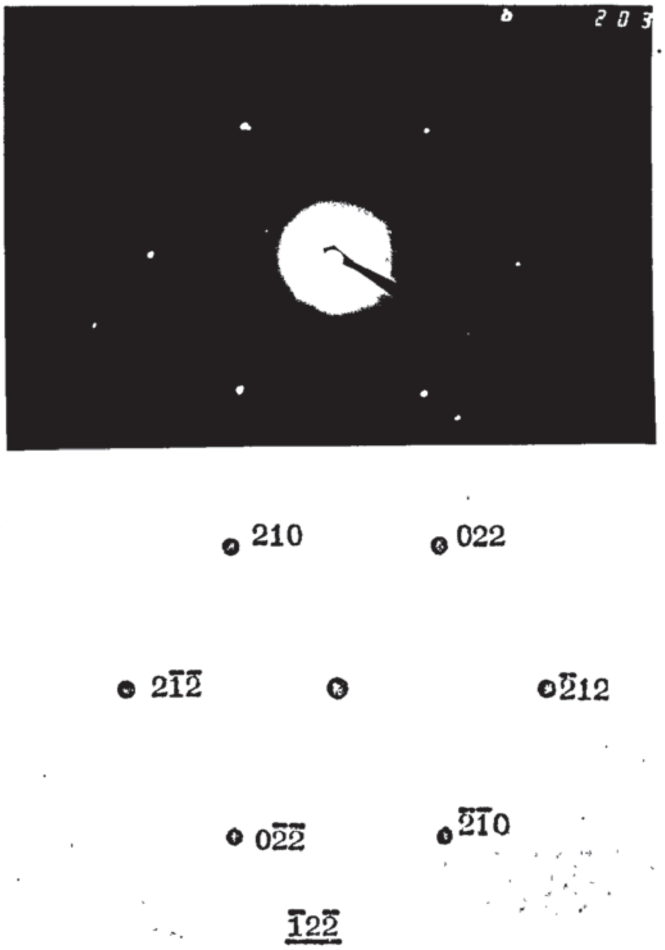

d spacings Å

Plane	Measured	Fe_3C(Ref 93)
210	2.069	2.067
022	2.040	2.031
212	1.770	1.762

Figure 48 Cementite diffraction pattern of particles in Figure 47.

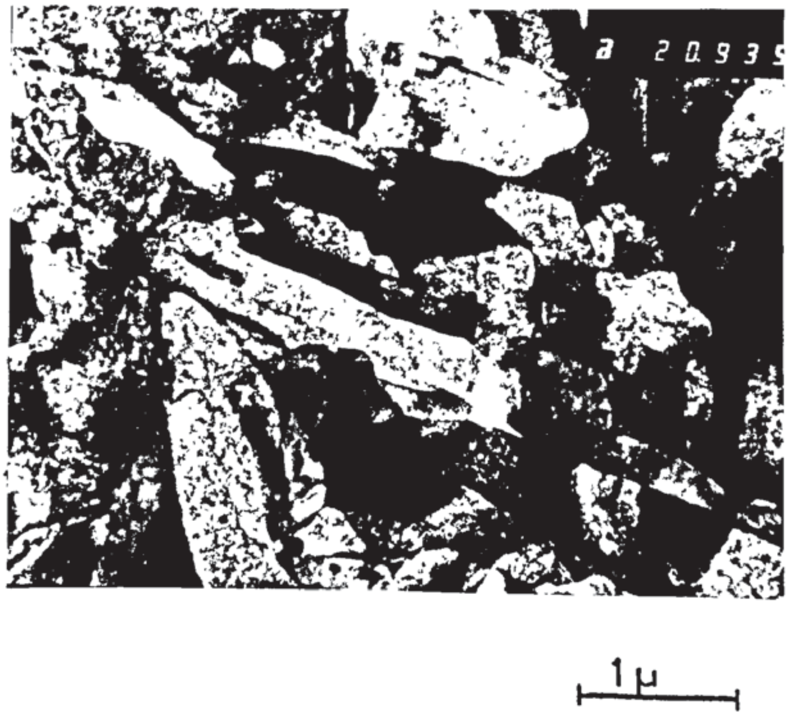

Figure 49 Acicular ferrite with prior austenite grain boundary running down the right-hand side in as deposited Bostrand 31 (1.18 KJ/mm). Thin foil.

Figure 50 Lath type structure in as deposited Bostrand 31 (1.18 KJ/mm). Thin foil.

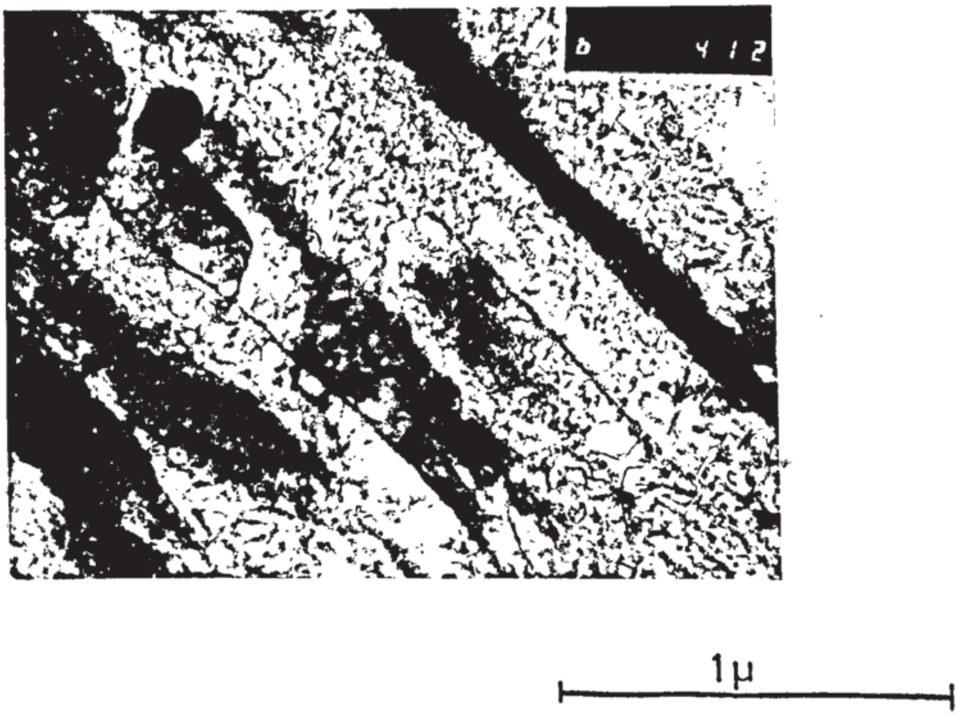

Figure 51 Lath type structure in as deposited Bostrand 31 (3.15 KJ/mm). Thin foil.

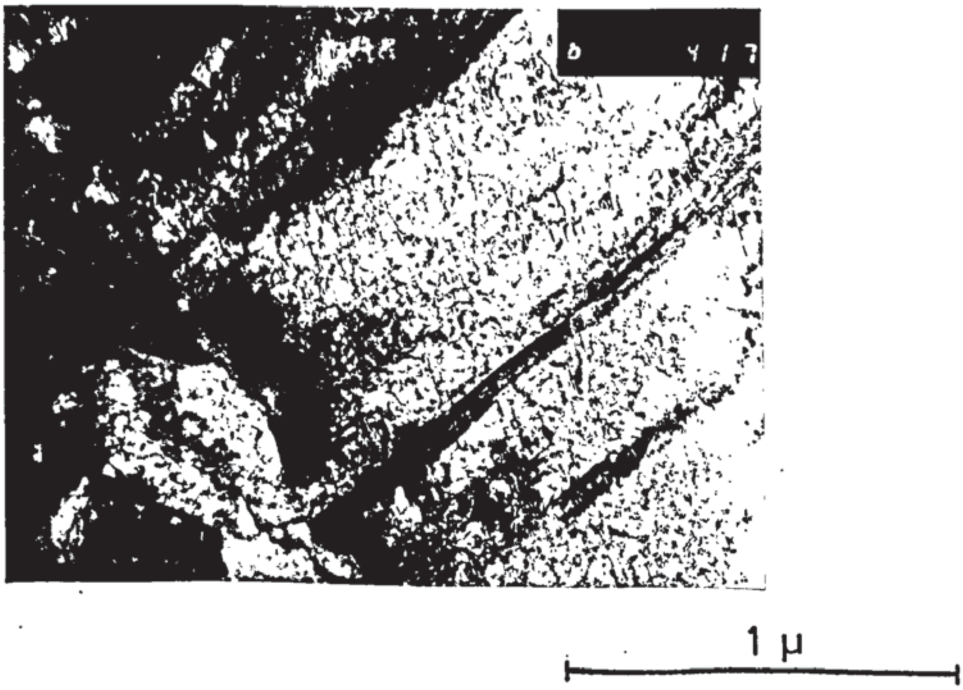

Figure .52 Parallel ferrite grains growing from a prior austenite boundary. Acicular ferrite to left of boundary. Dark band at right centre possibly martensite. Bostrand 31 (3.15 KJ/mm), as deposited, thin foil.

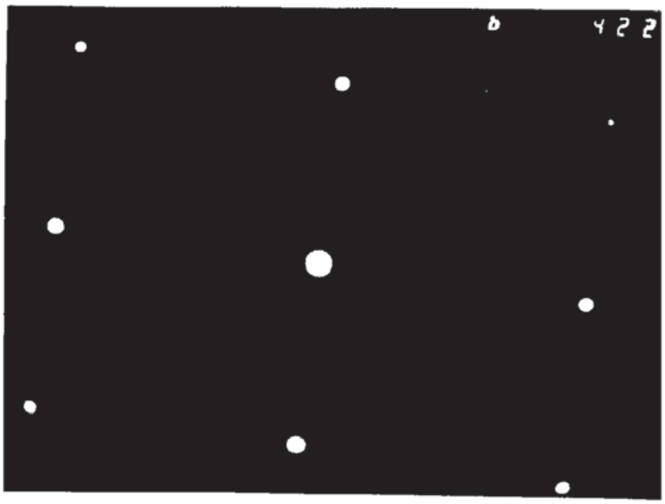

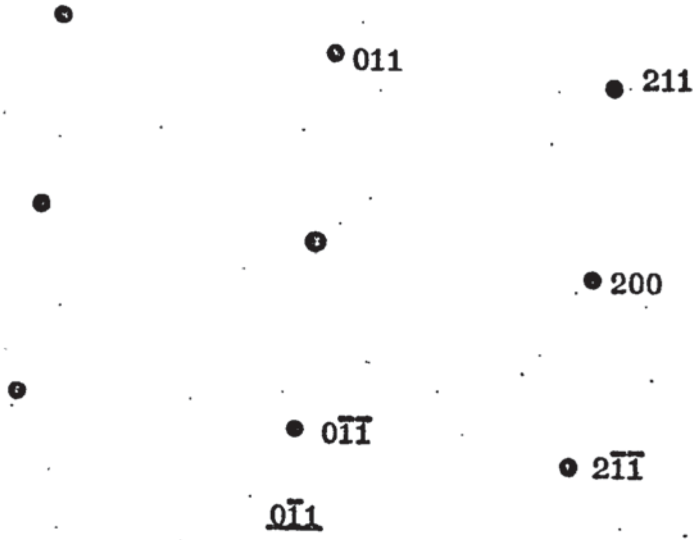

d spacings Å

Plane	Measured	Ferrite
011	2.062	2.027
200	1.433	1.433
211	1.171	1.170

$c/a = 1.004$

Figure 53 Diffraction pattern from large grain on upper right of Figure 52. Solution suggests a small amount of tetragonality.

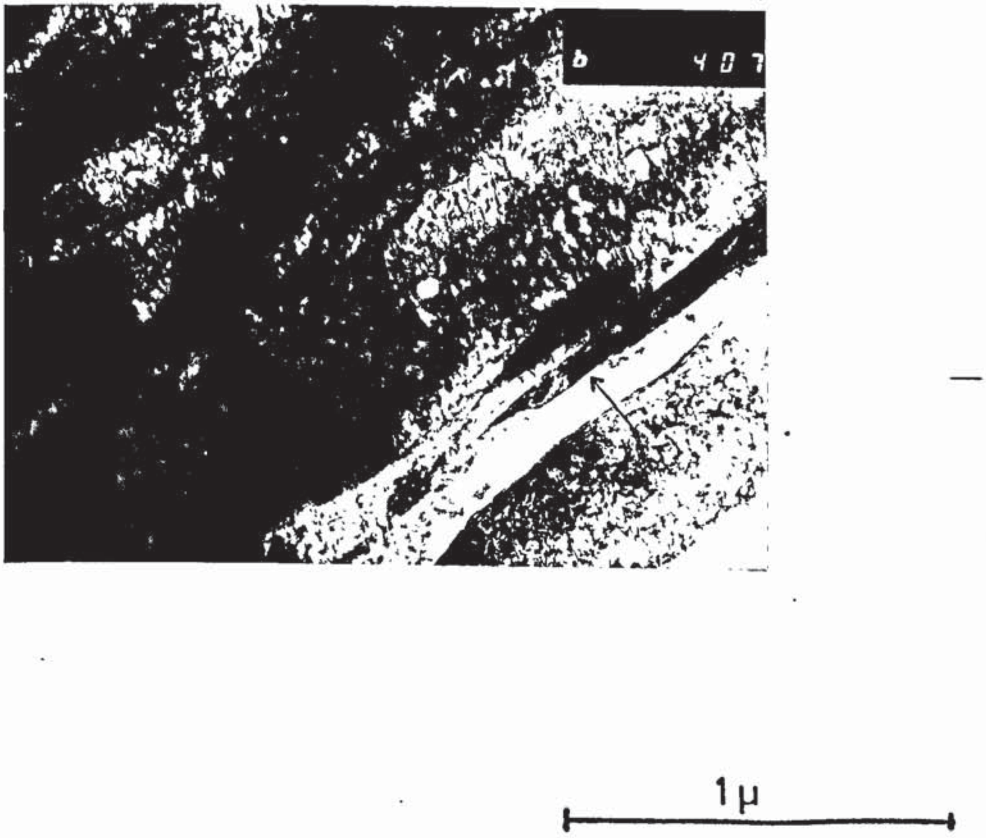

Figure 54 Lath structure in as deposited Bostrand 31 (3.15 KJ/mm). Diffraction pattern in Figure 55 taken from the dark band indicated by the arrow. Thin foil.

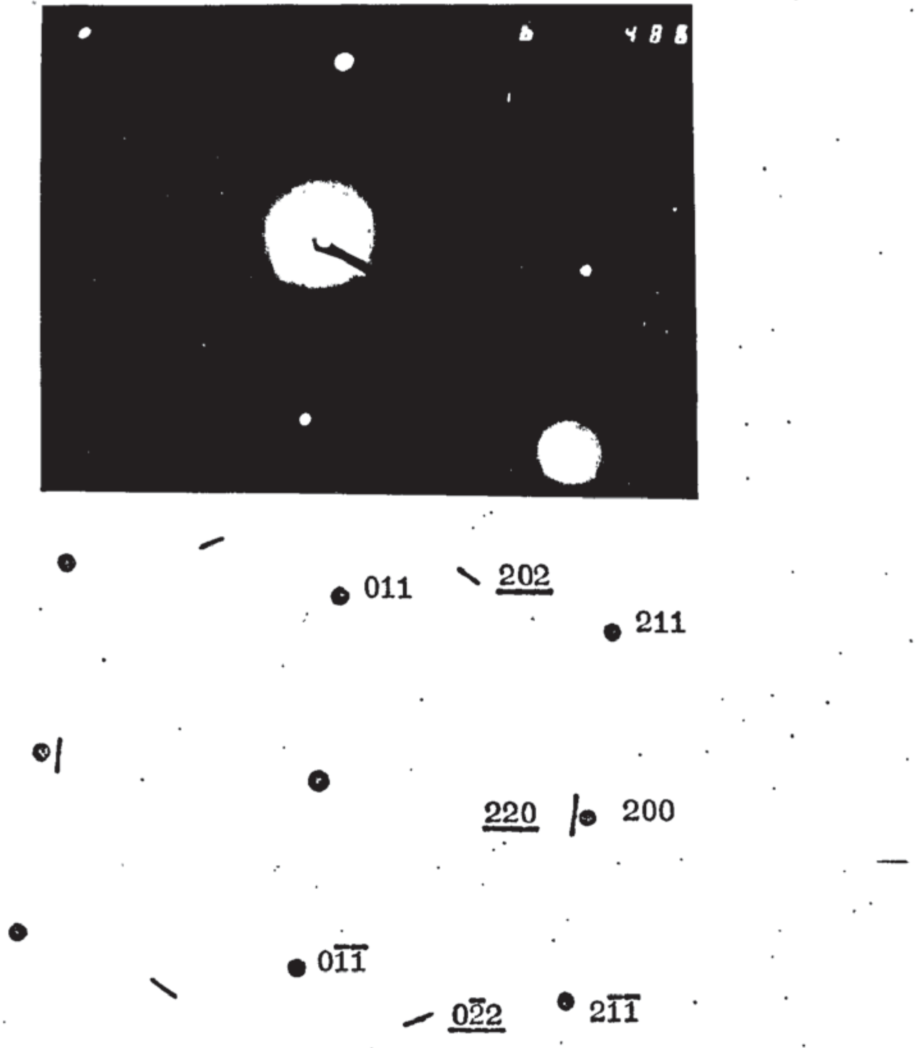

Zones $[01\bar{1}]$ ferrite

$[\bar{1}11]$ V_4C_3

d spacings

Plane	Measured	Ferrite(Ref 93)
011	2.046	2.027
200	1.433	1.433
211	1.170	1.170
		V_4C_3
(220)	1.481	1.471

Figure 55 Diffraction pattern from dark band shown in Figure 55. showing ferrite spots [110] zone and a V_4C_3 [111] zone. The indices of the V_4C_3 poles are underlined.

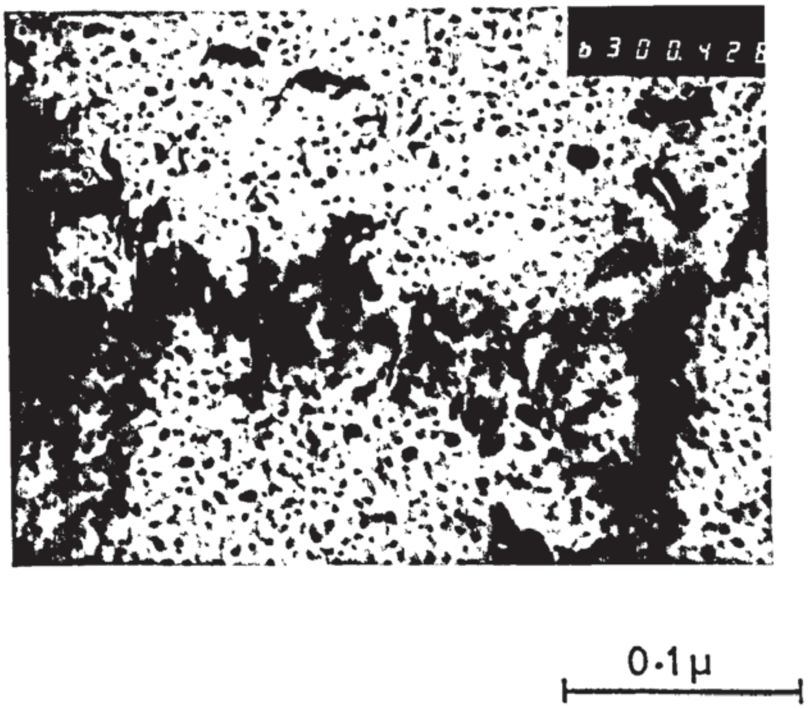

Figure 56 Apparent V_4C_3 precipitate in as deposited Bostrand 31 (3.15 KJ/mm). Thin foil.

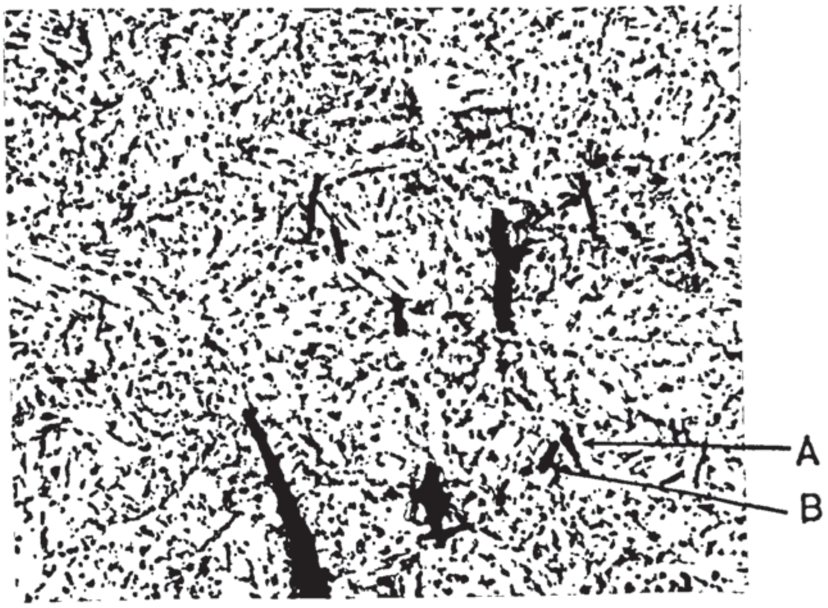

Figure 57 Cleavage cracks in as deposited Bostrand 31 (3.15 KJ/mm). White areas are acicular ferrite and dark areas are martensite. Cracks A and B possibly associated with the martensite - see text, page 95. 4% Picral. X 600.

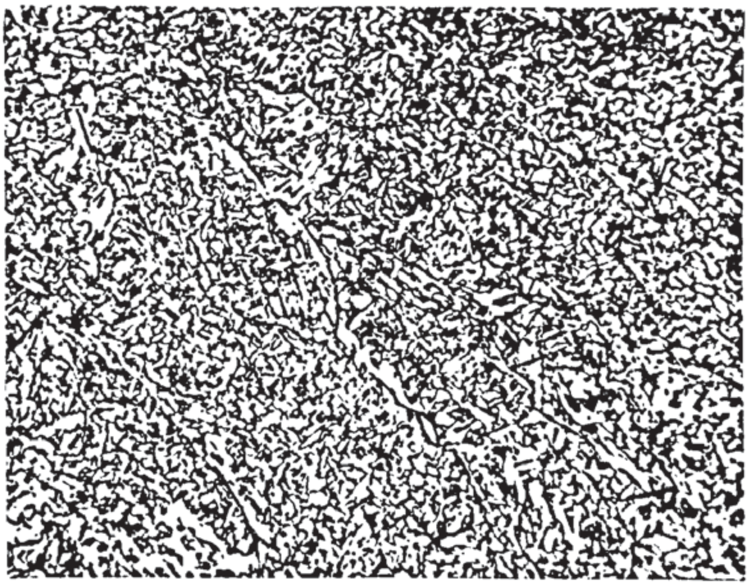

Figure 58 As deposited Linde 120 showing acicular ferrite and some proeutectoid ferrite decorating prior austenite grain boundaries. 2% Nital. X 600.

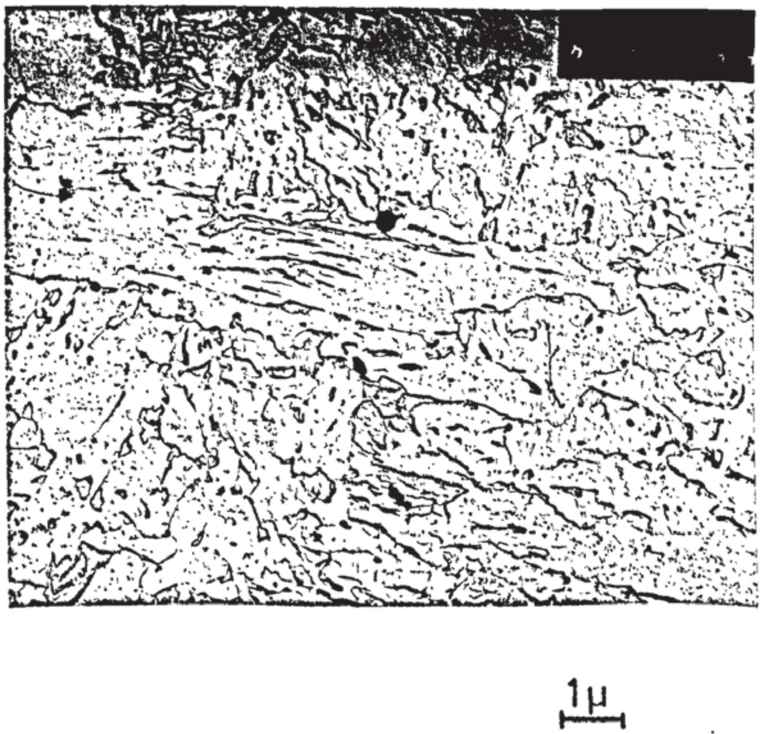

Figure 59 As deposited Linde 120 showing acicular ferrite with small islands of martensite (darker areas). Shadowed extraction replica.

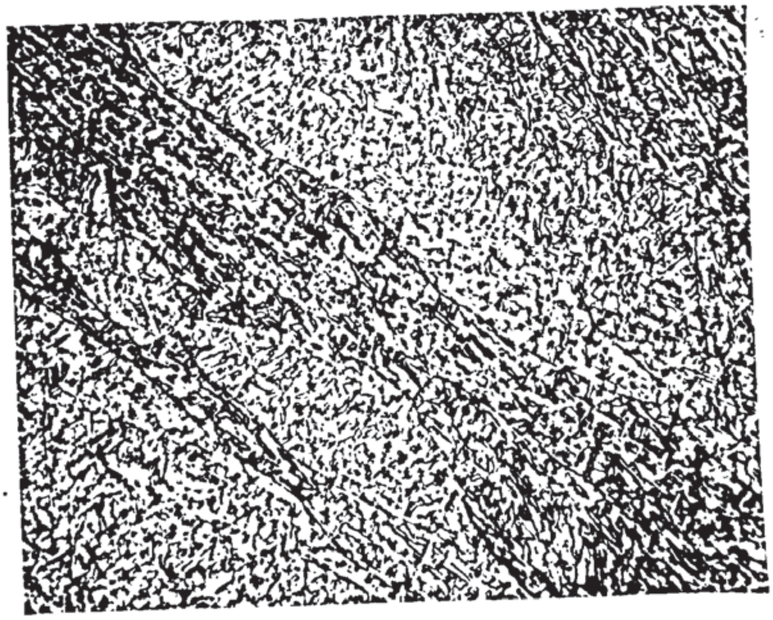

Figure 60 As deposited AX140 showing totally martensitic structure and prior austenite grain boundaries. 2% Nital. X 600.

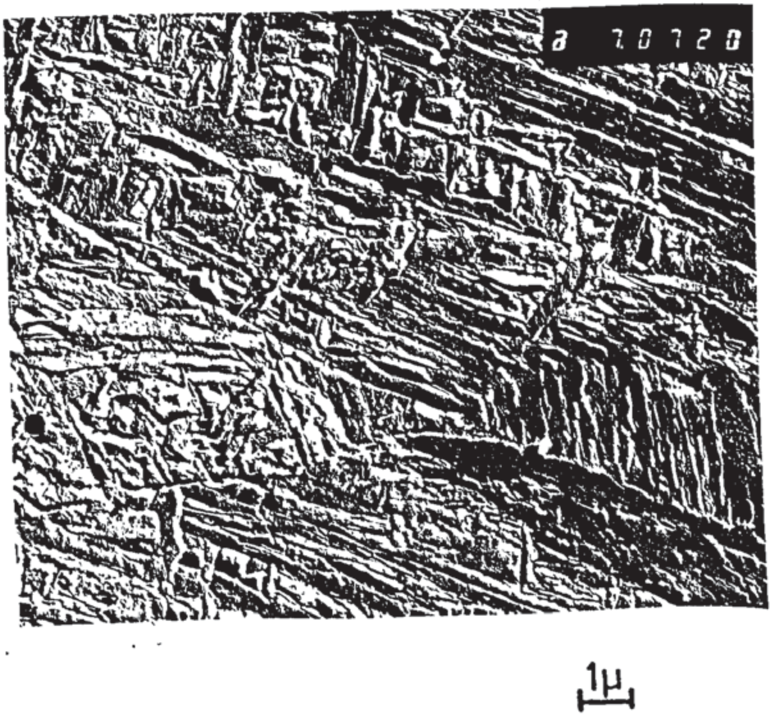

Figure 61 As deposited AX140 showing lath martensite in clearly defined colonies. Shadowed extraction replica.

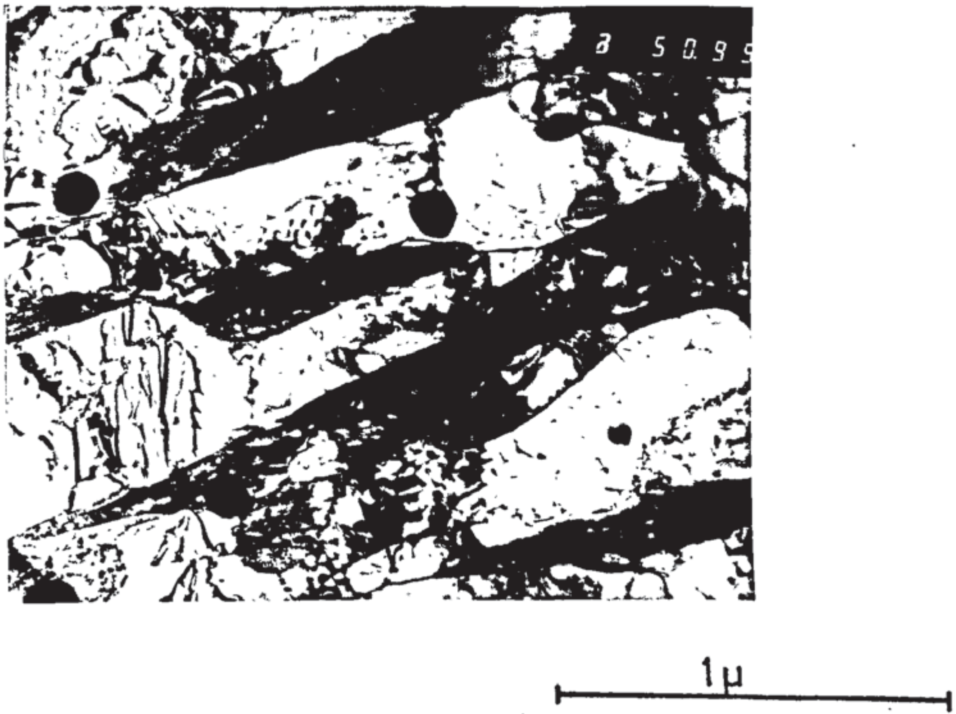

Figure 62 AX140 heat treated at 650°C for 50 hours. Lath structure persists indicating effective grain boundary pinning by carbides. The rounded lumps are inclusions. Thin foil.

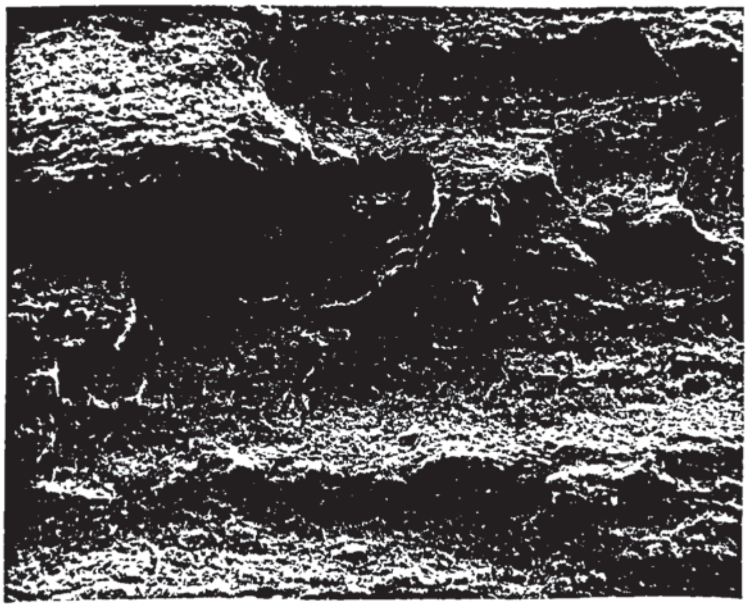

Figure 63 S.E.M. of as deposited Bostrand 31 (1.18 KJ/mm) COD fracture surface. Note rumpled appearance typical of all as deposited upper shelf fractures in each weld metal. Specimen D1/2. X 120.

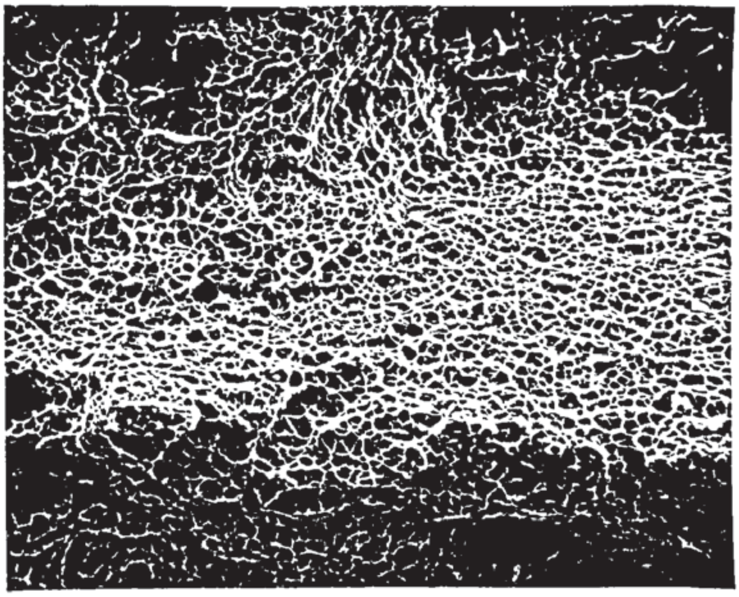

Figure 64 S.E.M. of as deposited Bostrand 31 showing microvoid coalescence. Specimen D1/2. X 550.

Figure 65 S.E.M. of Bostrand 31 (1.18 KJ/mm) treated at 550°C for 50 hours showing extensive cleavage. Note fatigue crack tip at lower right. Specimen D4/6. X 120.

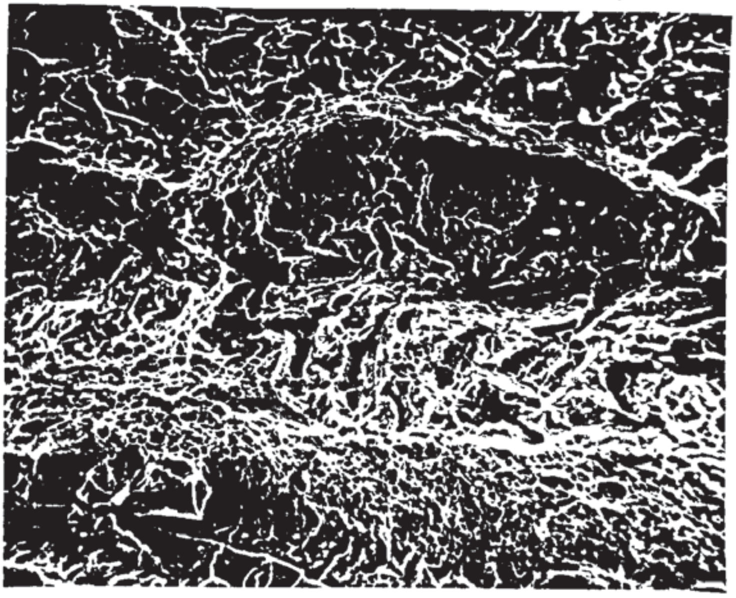

Figure 66 Close up of Figure 65 showing cleavage and microvoid coalescence. X 600.

Figure 67 Cleavage in Bostrand 31 treated at 550°C for 50 hours and fractured at -6°C. Specimen D4/2. X 1300.

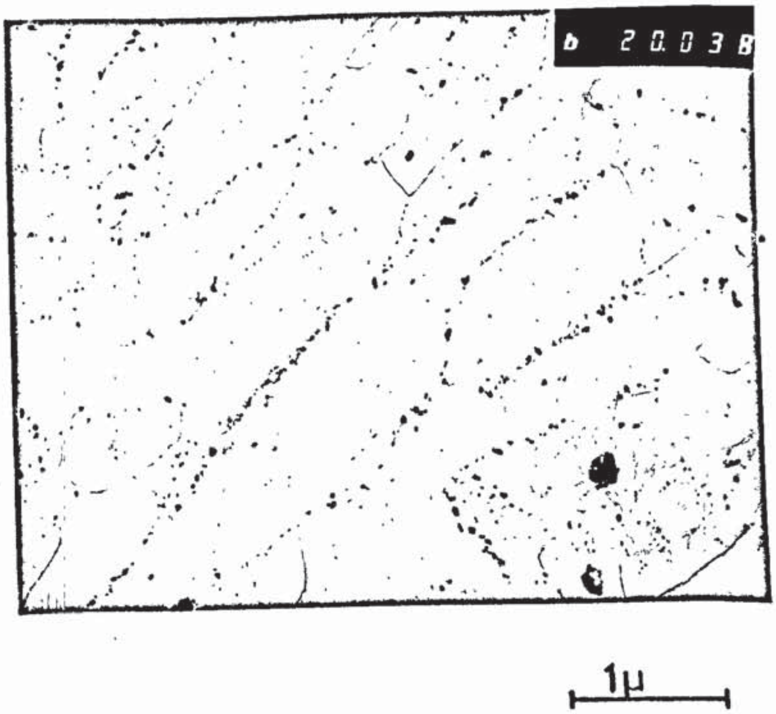

Figure 68 Very fine V_4C_3 precipitates in acicular ferrite with coarser V_4C_3 an acicular ferrite grain boundaries. Bostrand 31 treated at 700°C for 10 hours. Extraction replica.

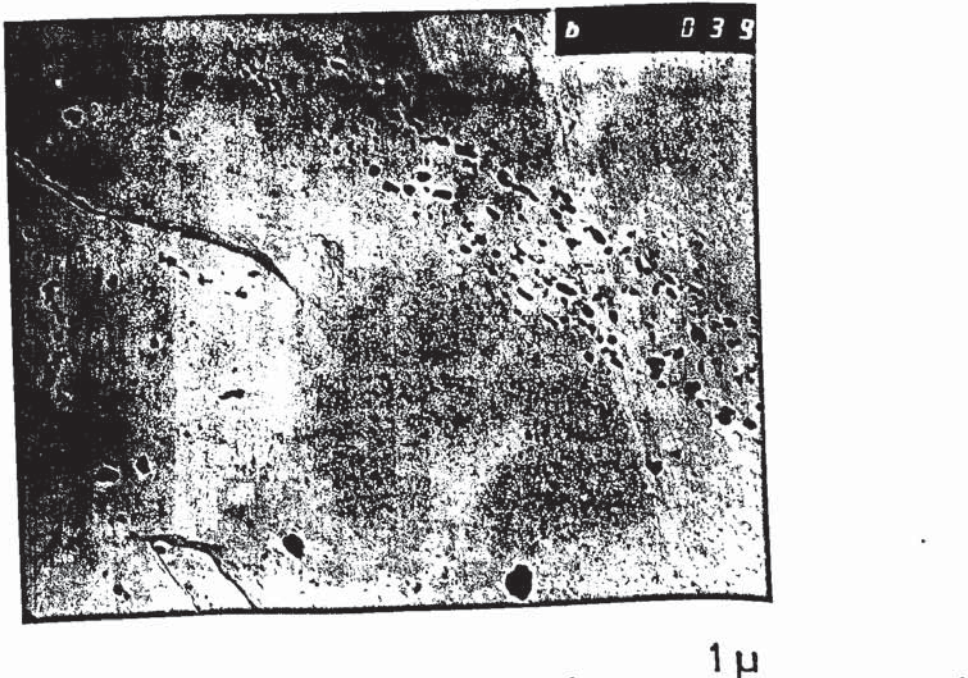

Figure 69 Fine matrix precipitates of V_4C_3 and coarser precipitates possibly caused by growth of V_4C_3 in martensite islands. Bostrand 31 treated at 700°C for 10 hours. Extraction replica.

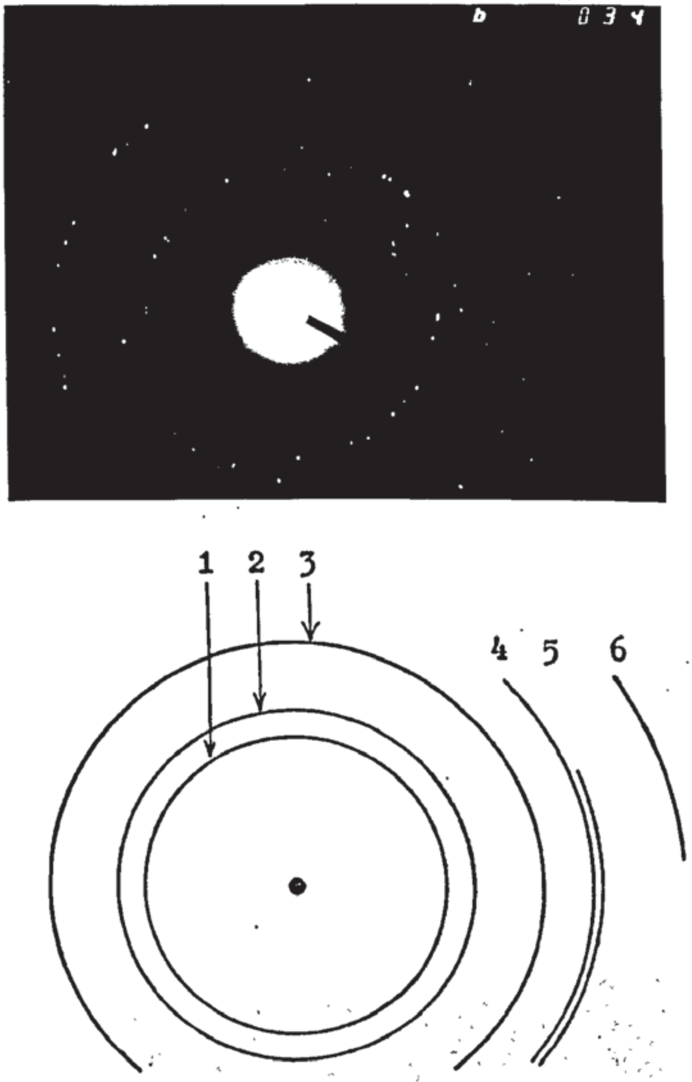

d spacings Å

Plane	Measured	V_4C_3 (Ref 93)
1 111	2.396	2.402
2 002	2.064	2.080
3 022	1.465	1.471
4 113	1.261	1.254
5 222	1.205	1.201
6 004	1.045	1.040

Figure 70 Ring diffraction pattern of V_4C_3 particles shown in Figure 69. Fine matrix precipitates contributed to the pattern as well as the coarser particles.

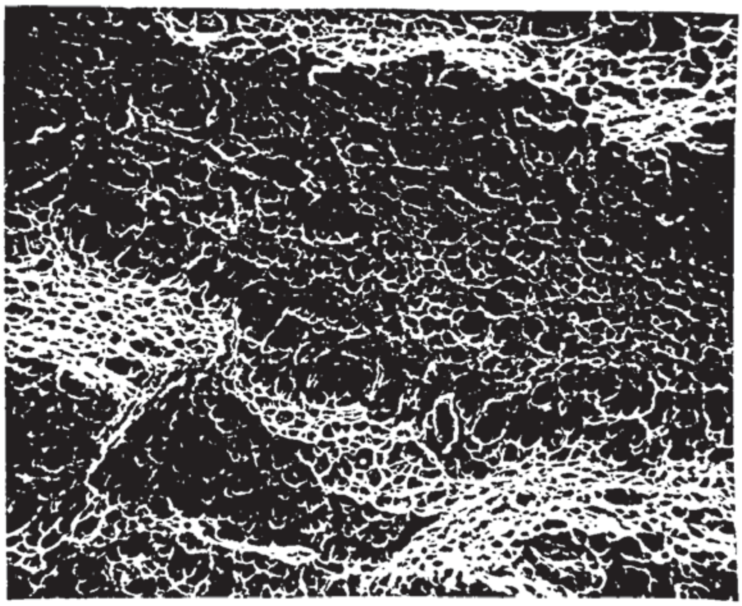

Figure 71 S.E.M. of as deposited AX140 fractured in upper shelf range and showing microvoid coalescence. Specimen E1/1. X 550.

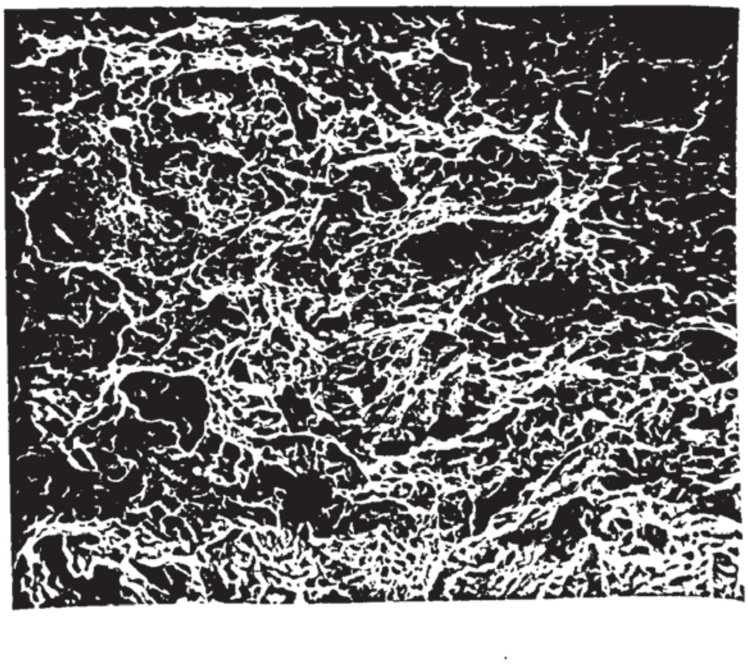

Figure 72 S.E.M. of as deposited AX140 fractured at -64°C showing mixed cleavage and microvoid coalescence. Specimen E1/6. X 550.

Figure 73 S.E.M. of AX140 heat treated at 550°C for 50 hours showing smooth decohesion along prior austenite columnar grain boundaries. Specimen E4/1. X 120.

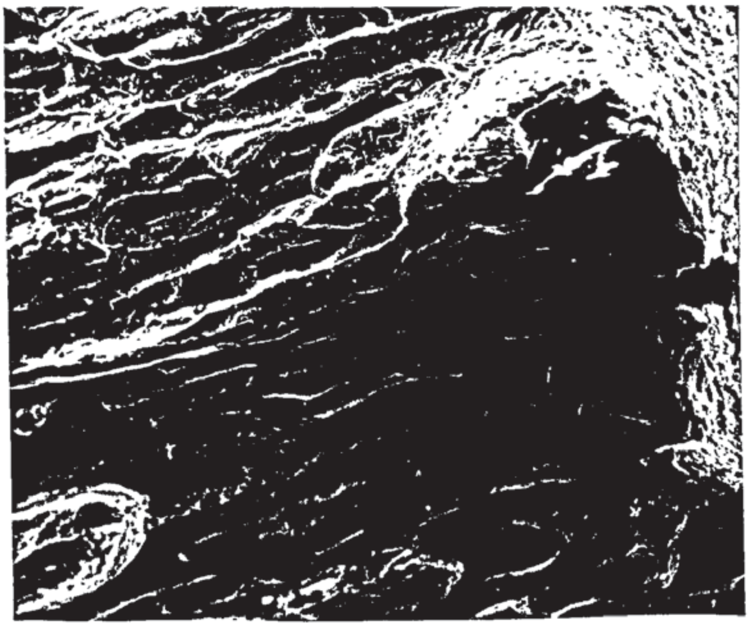

Figure 74 S.E.M. of intergranular decohesion in AX140 heat treated at 550°C for 50 hours. Specimen E4/5. X 220.

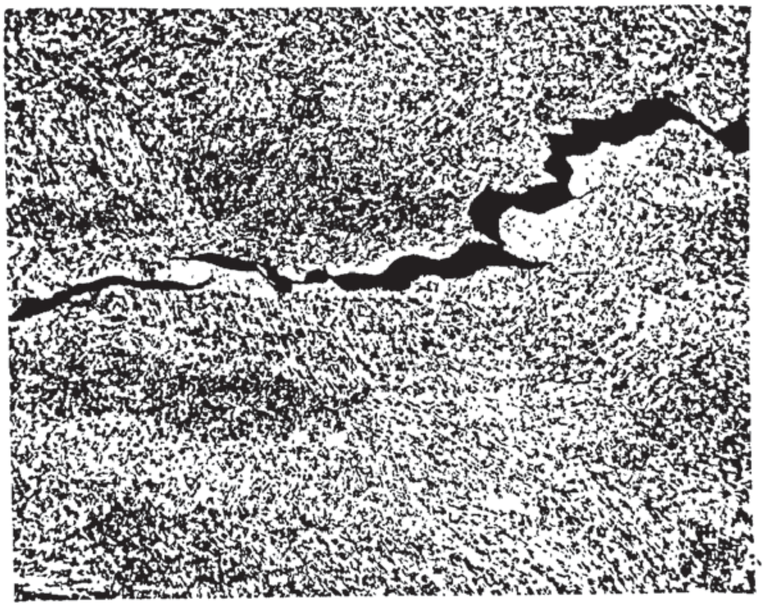

Figure 75 Intergranular fracture path along prior austenite grain boundaries in AX140 heat treated at 550°C for 50 hours. Ductile tearing has linked individual cracks at left centre. 4% Picral. X 150.

Figure 76 S.E.M. of prior austenite boundary fracture surface showing holes associated with inclusion pull out and some surface tears. AX140 - 550°C - 50 hours. X 2700.

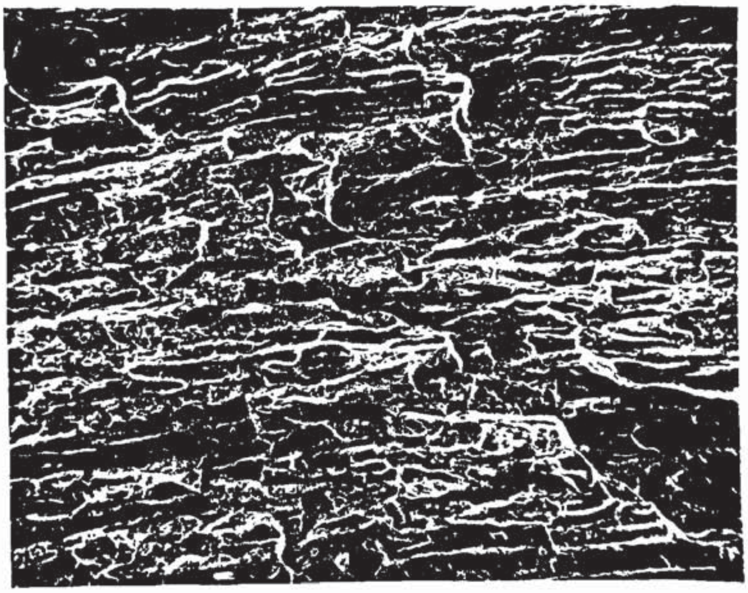

Figure 77 S.E.M. of AX140 heat treated 550°C for 10 hours and cooled at 100°C/hour, showing intergranular decohesion along prior austenite grain boundaries. X 130. Charpy specimen fractured at 2°C.

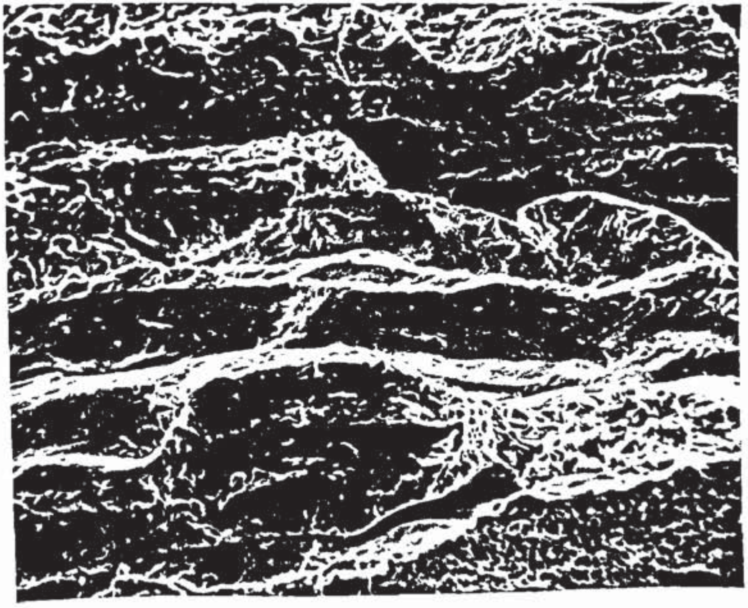

Figure 78 Close up of area in Figure 77 showing intergranular failure and some microvoid coalescence. X 650.

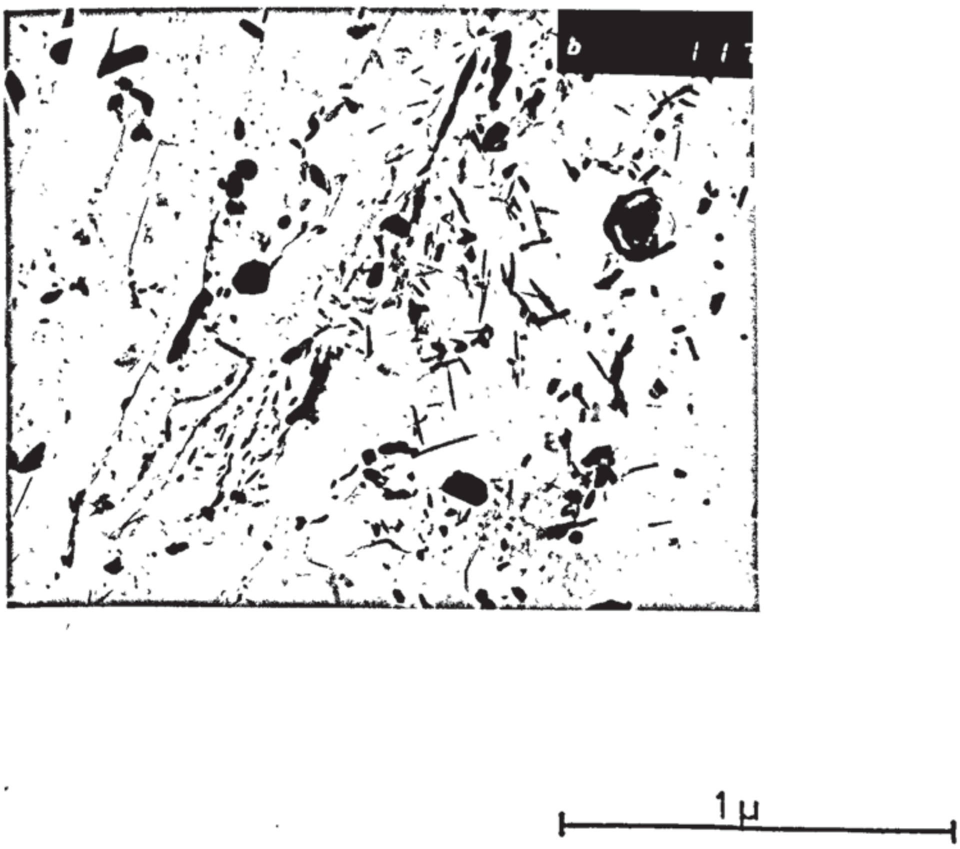

Figure 79 Carbides in AX140 heat treated at 650°C for 50 hours. Note concentration of Mo_2C needles in centre right and association of coarser, more rounded Fe_3C and M_7C_3 with lath boundaries. Extraction replica.

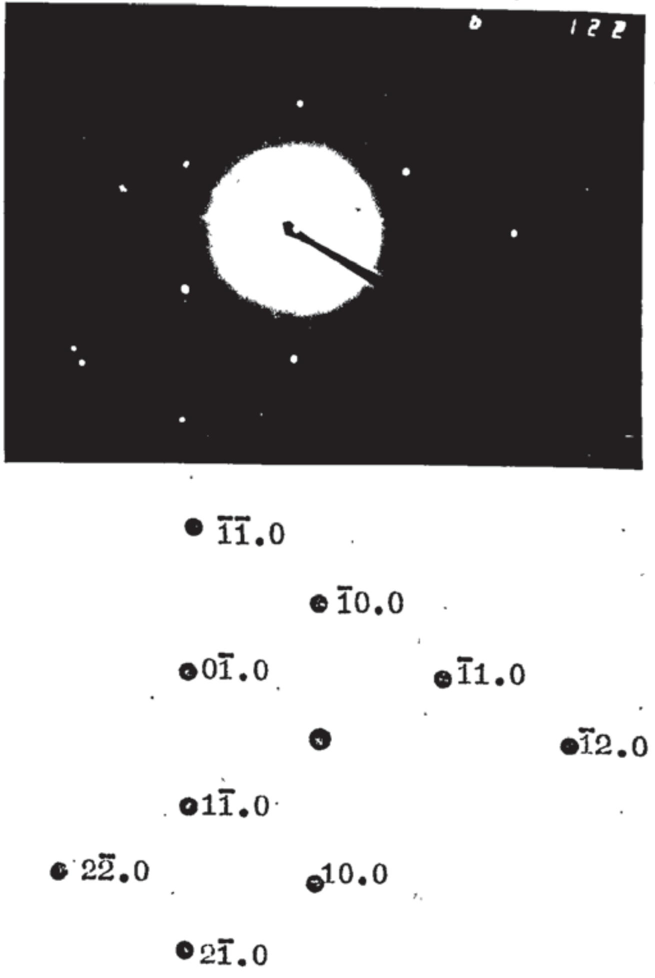

00.1

d spacings Å

Plane	Measured	Mo_2C(Ref 93)
10.0	2.595	2.600
11.0	1.48	1.501
21.0	0.98	0.983
22.0	0.75	0.750

Figure 80 Mo_2C diffraction pattern taken from a carbide needle in Figure 79.

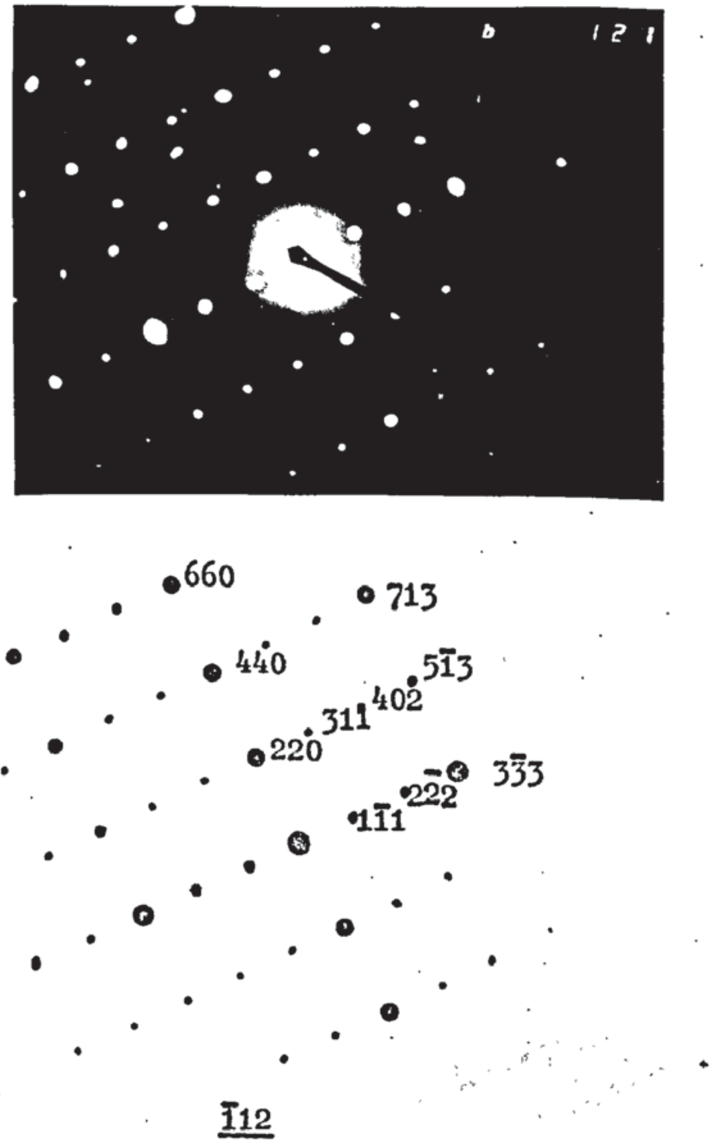

d spacings Å

Plane	Measured	$M_{23}C_6$(Ref93)
111	6.132	6.132
220	3.756	3.755
311	3.203	3.203
222	3.066	3.066
402	2.375	2.375
333	2.044	2.044
440	1.878	1.878
513	1.795	1.795
713	1.383	1.383
660	1.252	1.252

Figure 81 $M_{23}C_6$ diffraction pattern taken from a coarse carbide in Figure 79.

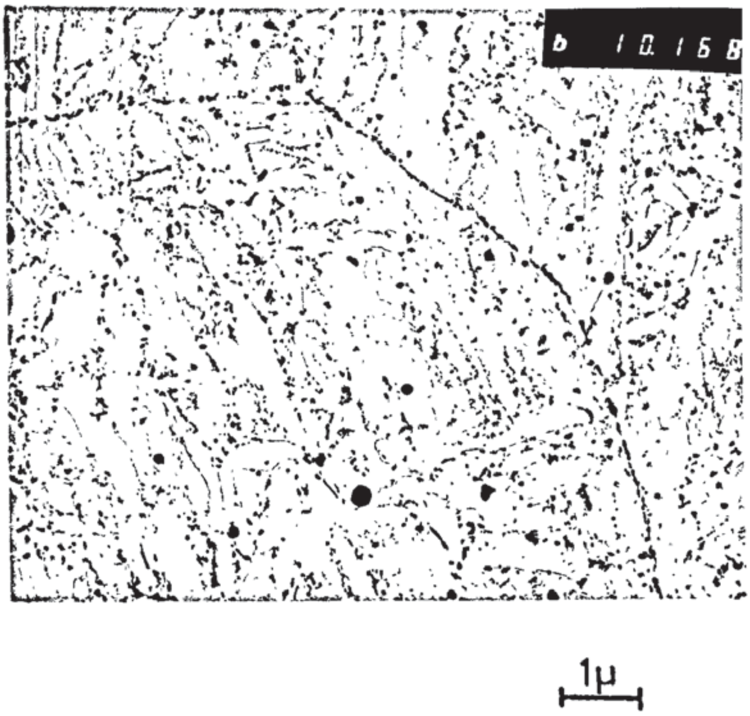

Figure 82 Carbides decorating prior austenite grain boundaries in AX140 heat treated at 550°C for 50 hours. Extraction replica.

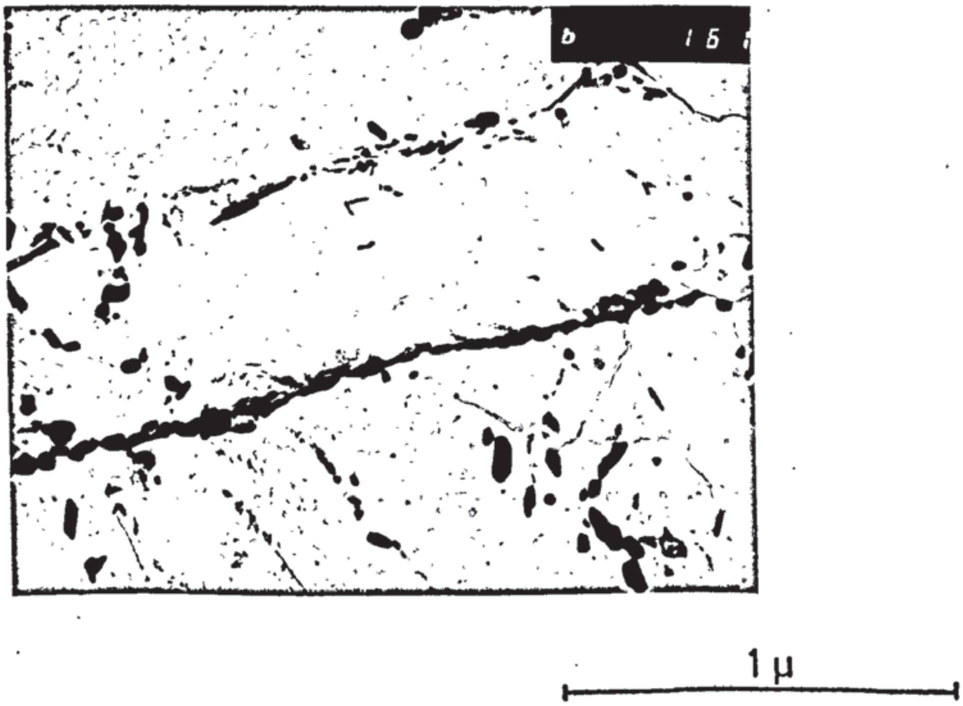

Figure 83 Heavy carbide precipitation of prior austenite grain boundary. AX140 - 550°C - 50 hours. Extraction replica.

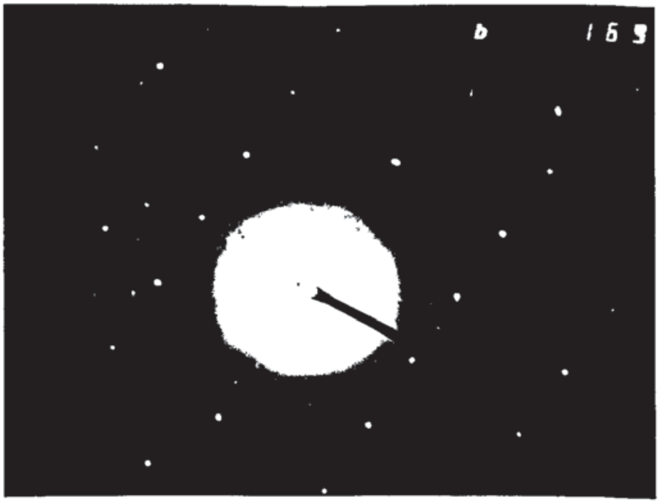

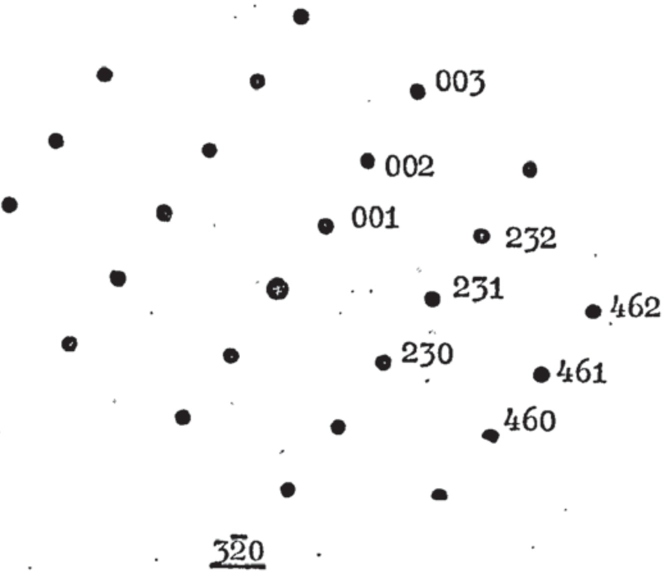

d spacings A

Plane	Measured	M_7C_3 (Ref 93)
001	4.497	4.506
230	2.770	2.777
231	2.344	2.364
002	2.248	2.253
232	1.736	1.750
460	1.385	1.389
461	1.319	1.327
462	1.172	1.182

Figure 84 M_7C_3 diffraction pattern from a grain boundary carbide shown in Figure 83.

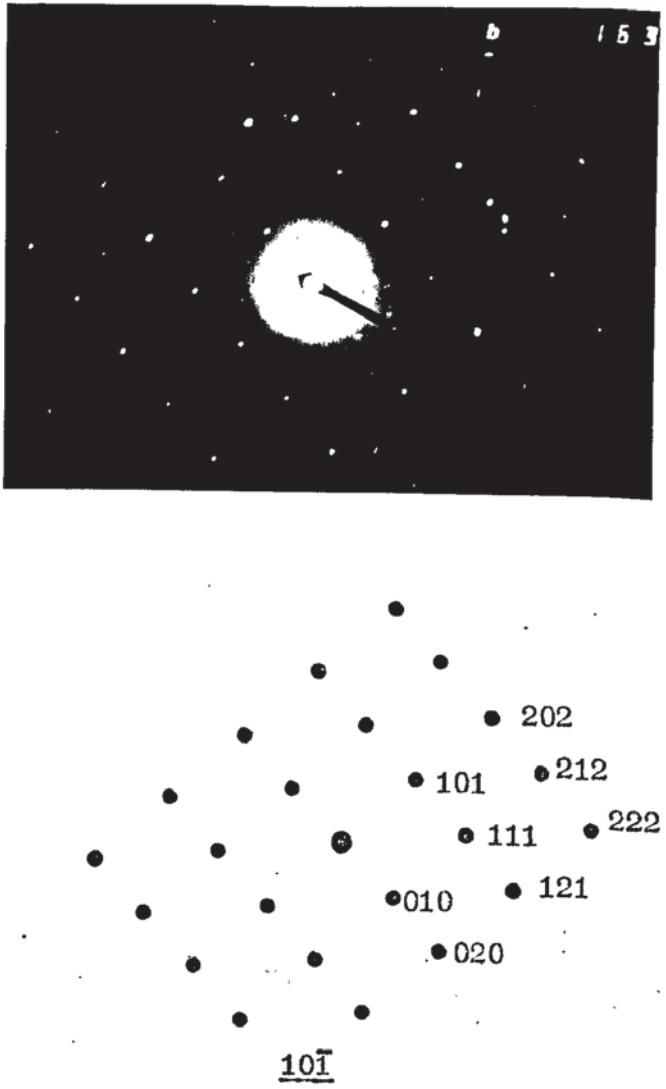

d spacings Å

Plane	Measured	Fe_3C(REF 93)
010	5.049	5.088
101	3.740	3.757
111	3.005	3.022
020	2.525	2.544
121	2.093	2.107
202	1.870	1.878
212	1.762	1.762
222	1.503	1.511

Figure 85 Fe_3C diffraction pattern from a grain boundary carbide in Figure 83.

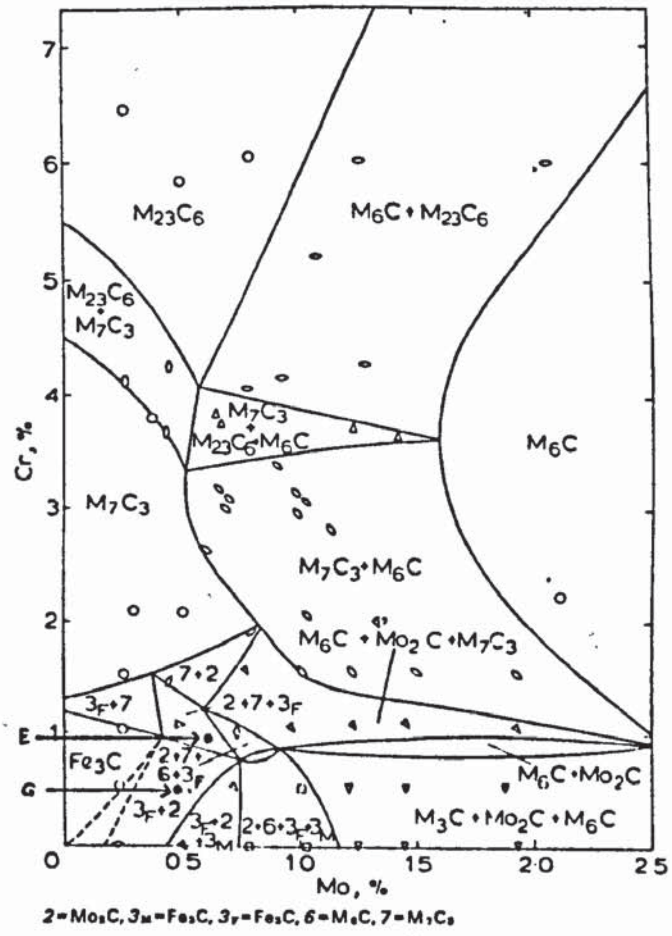

Figure 86 Carbide constitution diagram for 0.12%C, 0.5%Mn, 0.5%Si steels with varying Cr and Mo contents, heat treated at 650°C for 1000 hours (from Andrews et al., (98)). Composition of Linde 120 (G) and AX140 (E) included.

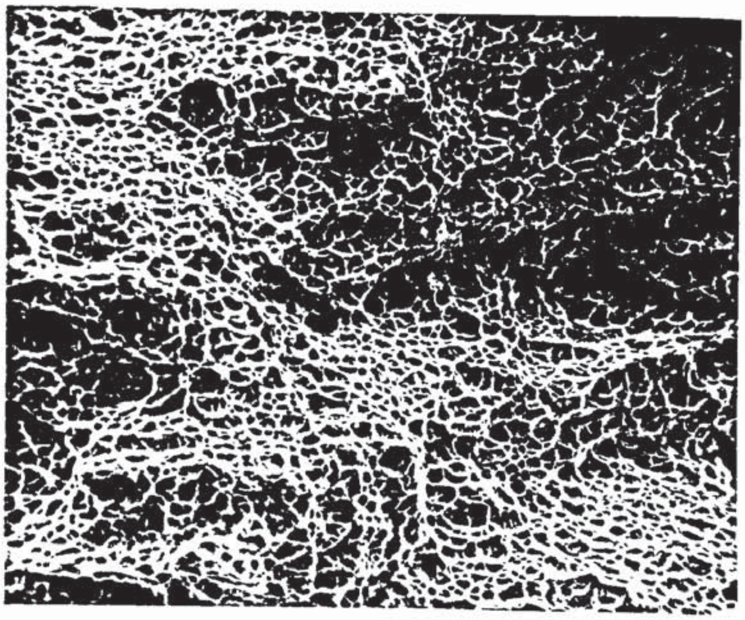

Figure 87 S.E.M. of as deposited Linde 120 showing microvoid coalescence. Specimen G1/2. X 550.

Figure 88 S.E.M. of Linde 120 heat treated at 550°C for 50 hours and fractured at -66°C. Mixed intergranular fracture and microvoid coalescence. Specimen G4/5. X 120.

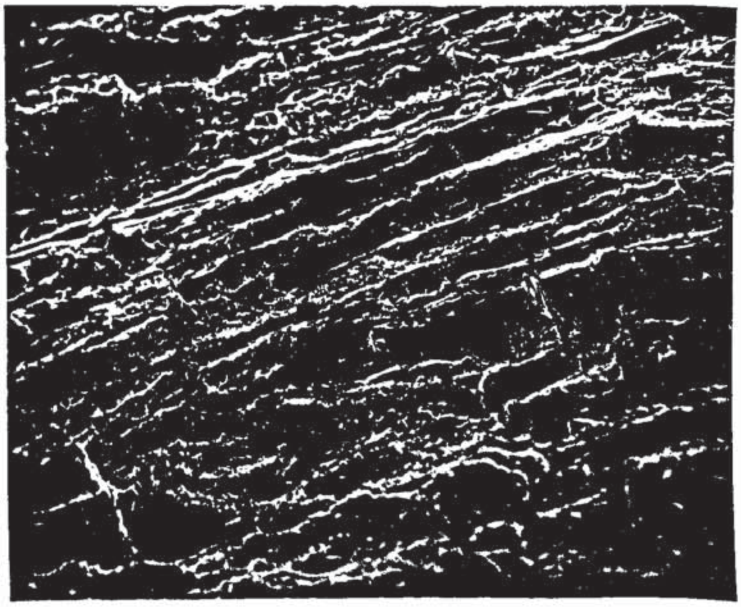

Figure 89 S.E.M. of Linde 120 heat treated at 550°C for 10 hours and cooled at 100°C/hour showing tendency toward intergranular fracture. Charpy specimen fractured at -16°C. X 130.

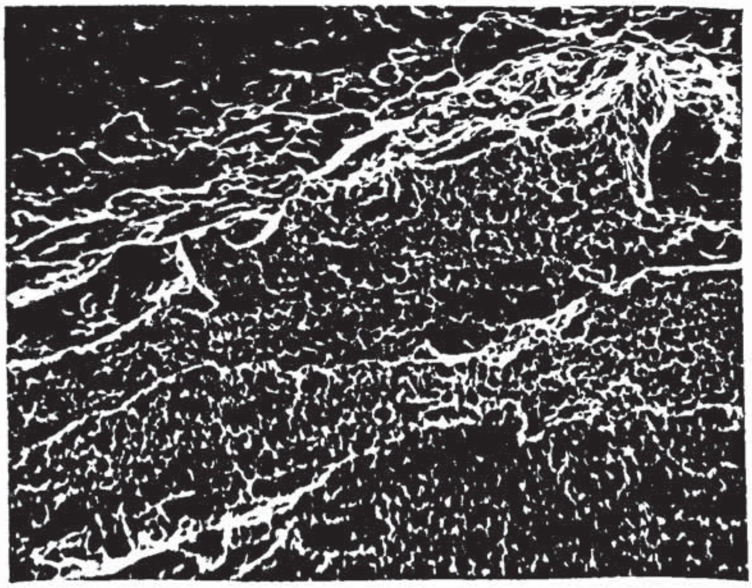

Figure 90 Close up of Figure 89 showing microvoid coalescence and cleavage (upper left). X 550.

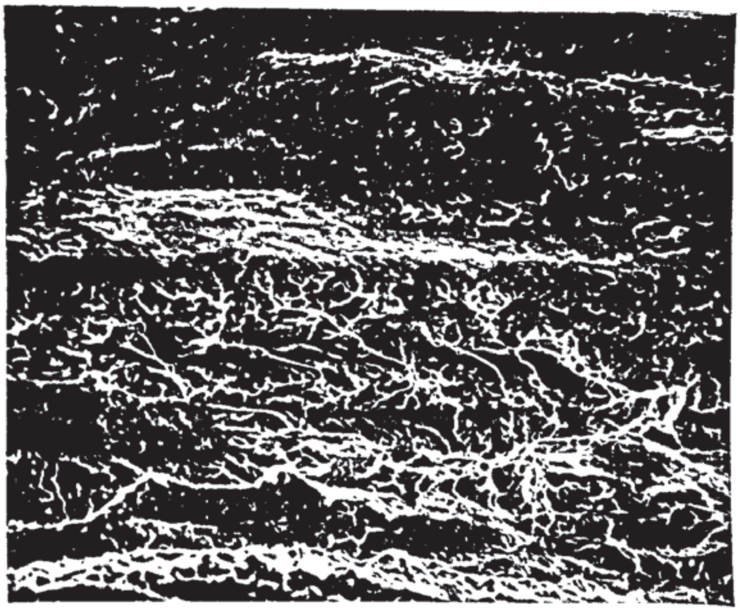

Figure 91 Close up of Figure 89 showing smooth intergranular decohesion along prior austenite grain boundaries and cleavage. X 600.

Figure 92 Same specimen as Figure 89 showing junction between columnar region, which has fractured by microvoid coalescence, cleavage and intergranular separation, and refined zone which has fractured by microvoid coalescence. X 240.

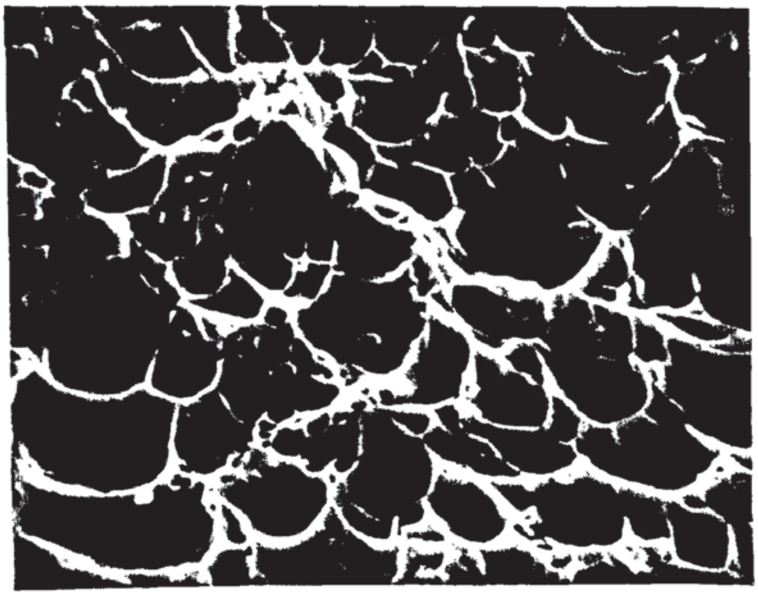

Figure 93 Detail of Figure 90. The particle in the centre was analysed by X-ray dispersive analysis and the trace is shown in Figure 94. X 6500

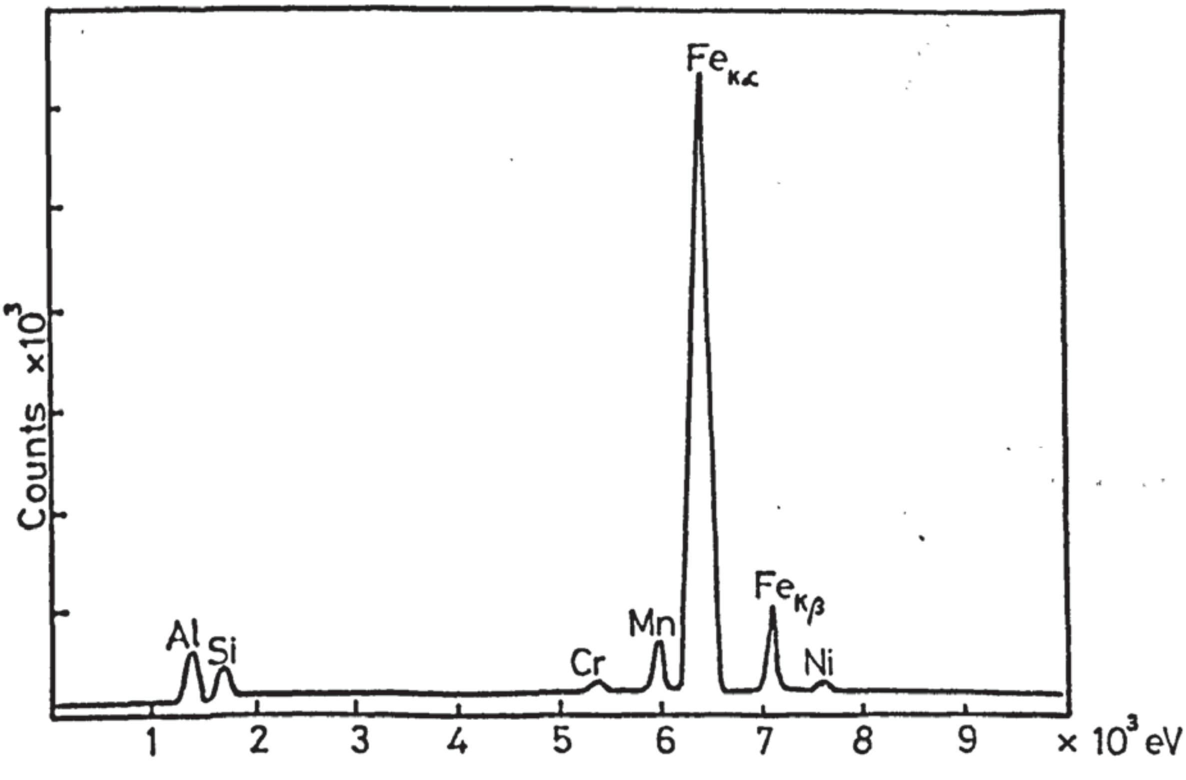

Figure 94 X-ray dispersive analysis trace of particle in Figure 93 indicating the presence of Al, Si, Mn and Fe, and showing that the particle is an inclusion.

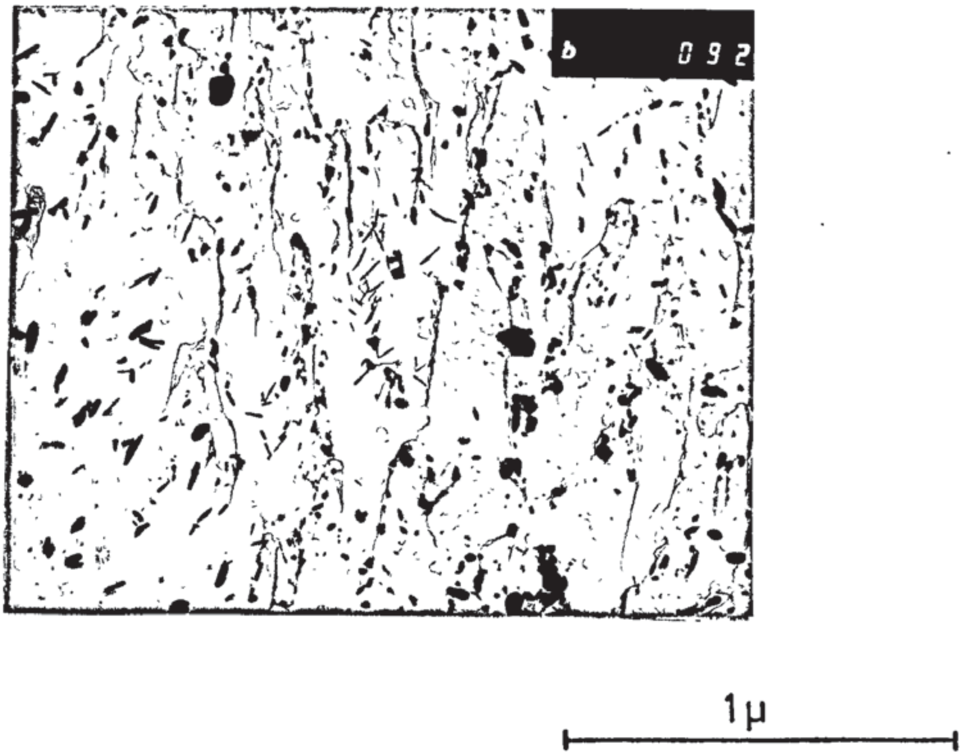

Figure 95 Carbides in Linde 120 heat treated at 650°C for 50 hours. Note concentrations of Mo_2C needles while larger rounded particles of Fe_3C are more evenly dispersed.

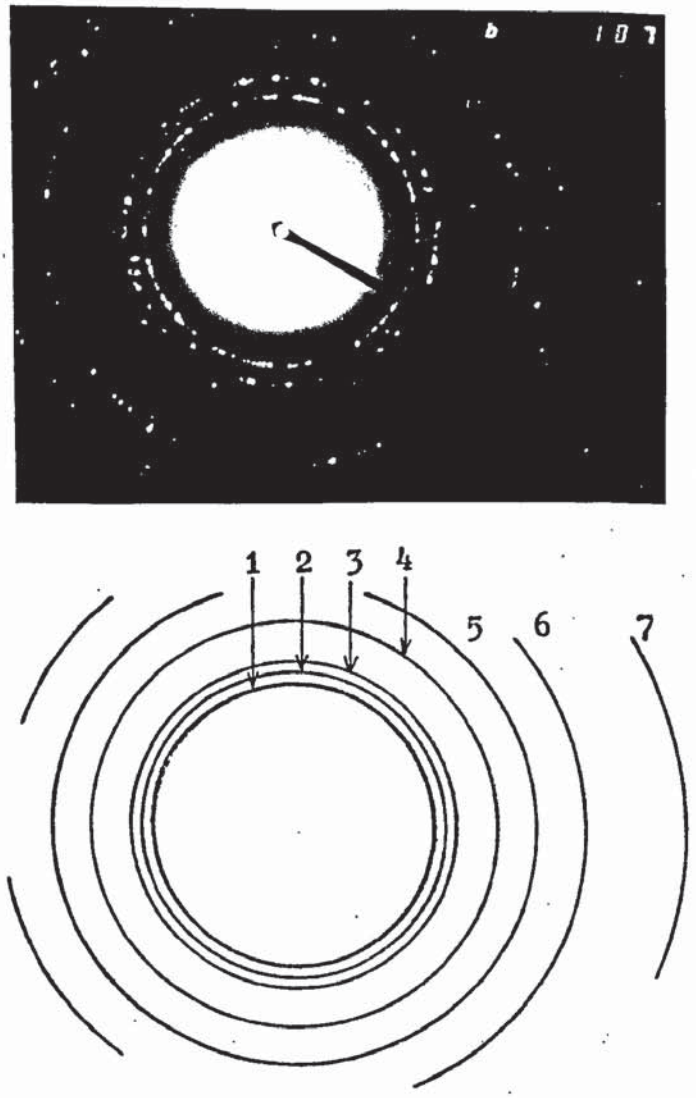

d spacings Å

Plane		Measured	Mo_2C(Ref 93)
1	01.0	2.597	2.600
2	00.2	2.359	2.362
3	01.1	2.278	2.278
4	11.0	1.485	1.510
5	02.0	1.296	1.300
6	02.1	1.250	1.253
7	00.5	0.948	0.945

Figure 96 Ring pattern of Mo_2C taken from Figure 95.

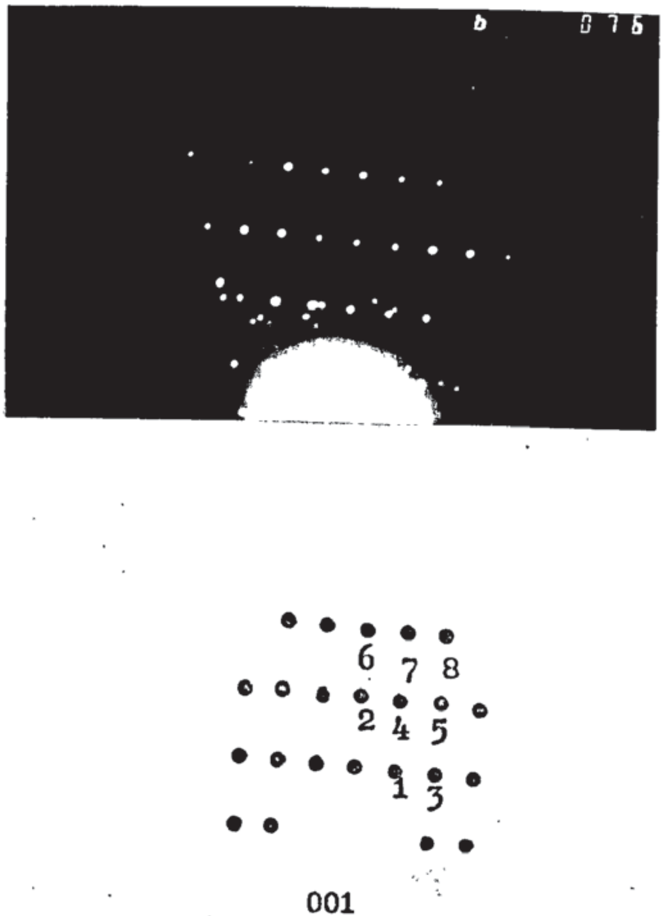

001

d spacings Å

Plane	Measured	Fe_3C(Ref 93)
1. 100	4.540	4.524
2. 020	2.548	2.544
3. 200	2.270	2.262
4. 120	2.222	2.218
5. 220	1.695	1.691
6. 040	1.274	1.272
7. 140	1.227	1.225
8. 240	1.111	1.109

Figure 97 Fe_3C diffraction pattern taken from Figure 95.

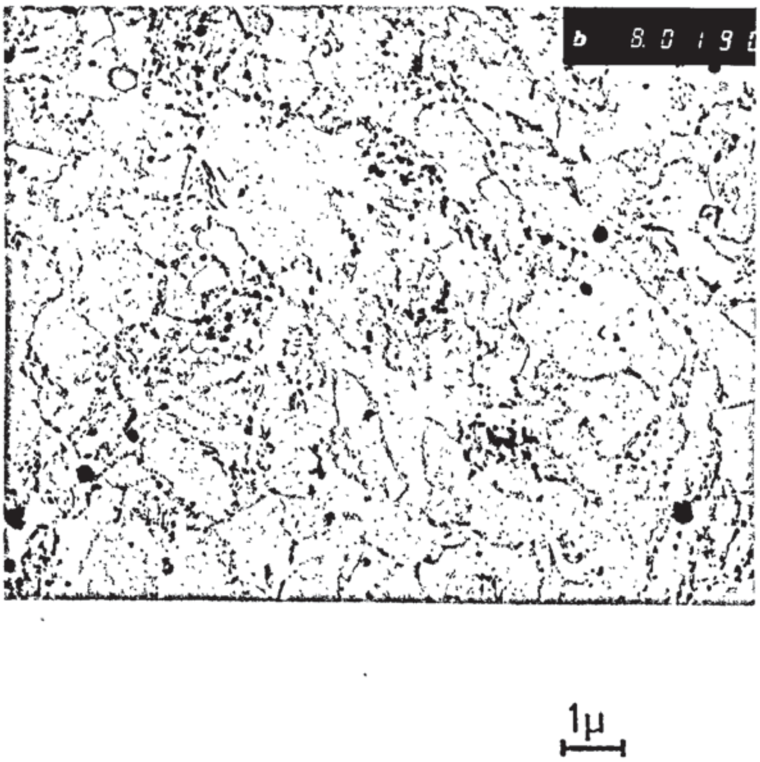

Figure 98 Carbide distribution in Linde 120 heat treated at 550°C for 50 hours.

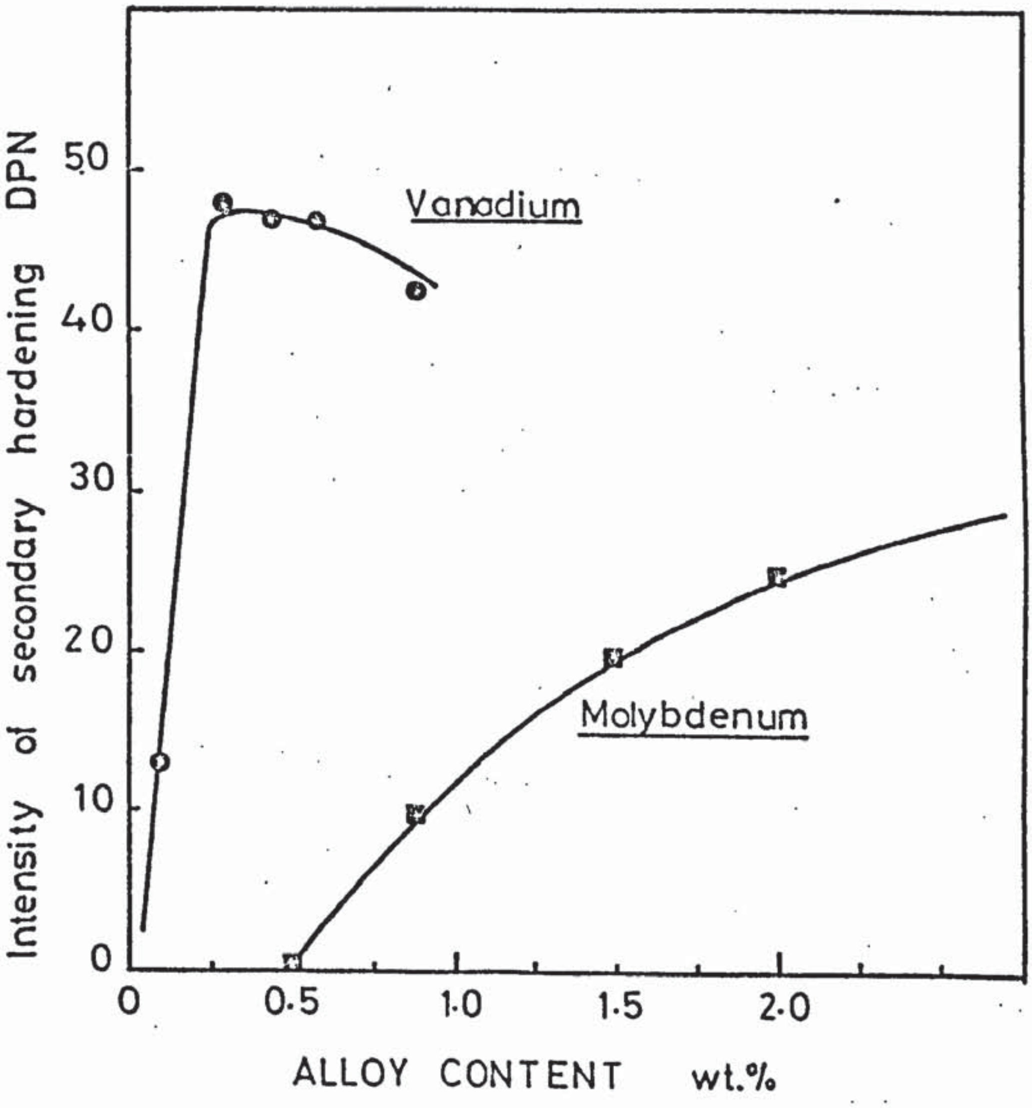

Figure 99 Intensity of secondary hardening versus alloy content for vanadium and molybdenum (after Irvine and Pickering (105)).

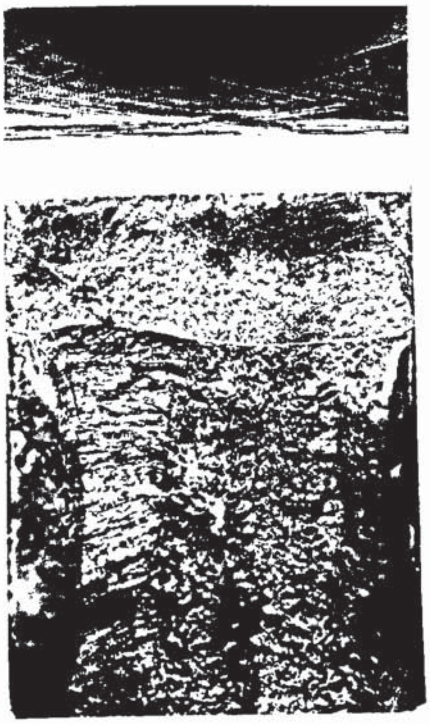

Figure 100 COD fracture surface of AX140 heat treated at 550°C for 50 hours. Note two bands of brittle intergranular fracture with more ductile region in the centre and shear lips at each surface.

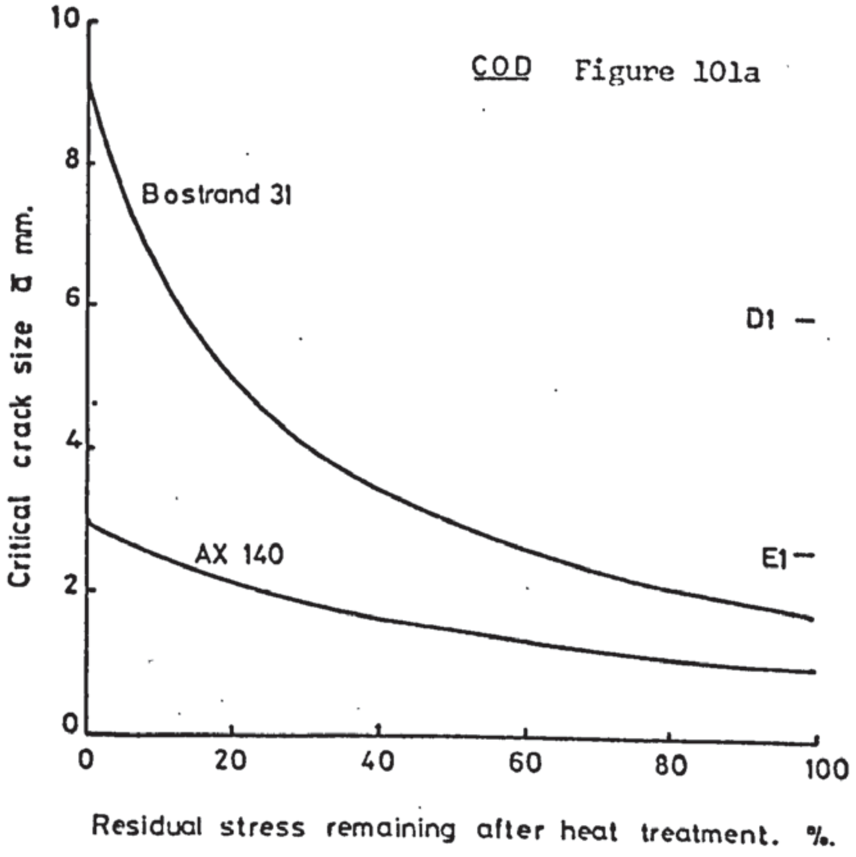

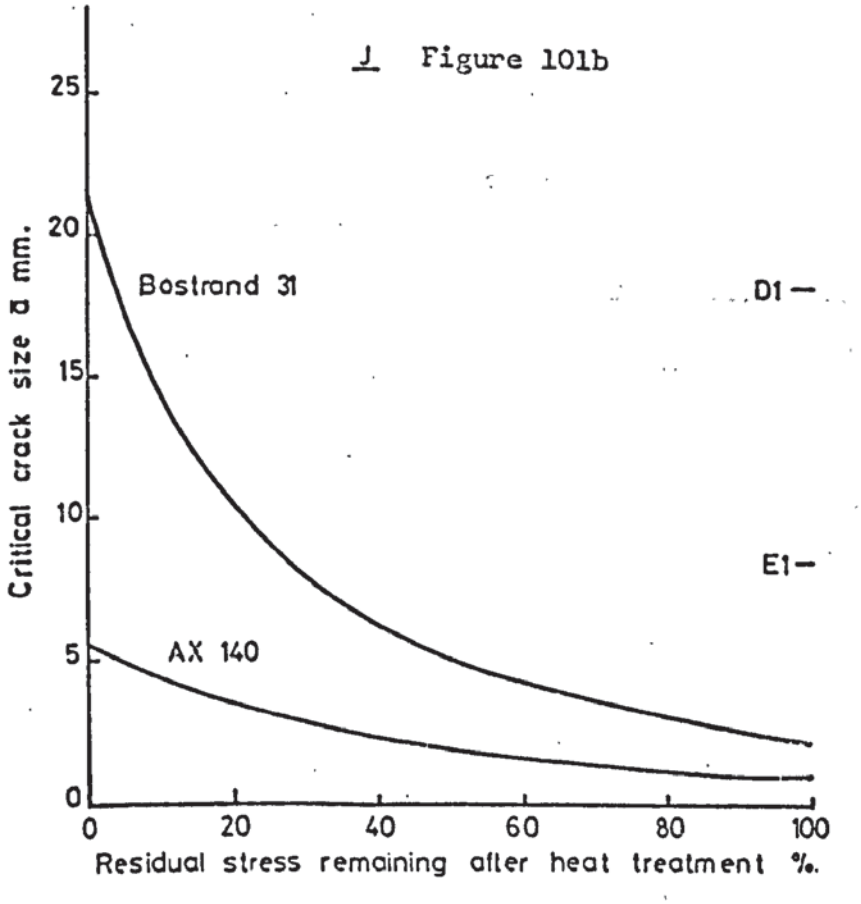

Figure 101 Critical crack length as a function of residual stress levels remaining after heat treatment for Bostrand 31 and AX140. The calculations are based on equations **iv** and **vi** in section 5.4.2. D1 and E1 are the as deposited defect tolerances of Bostrand 31 and AX140 respectively. 101a - COD design equation. 101b - J design equation.

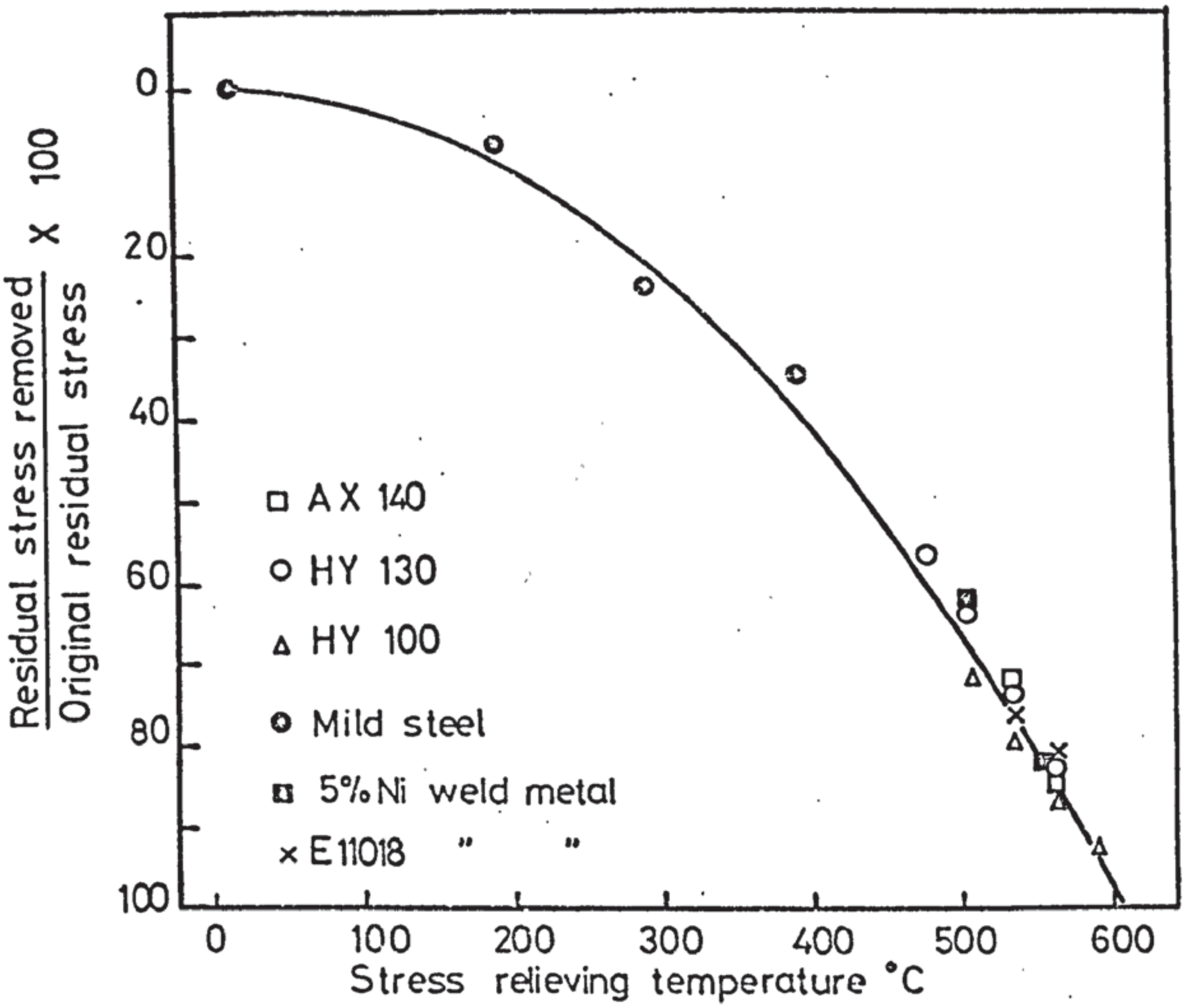

Figure 102 Residual stress levels remaining after heat treatment for 6 hours. Original residual stress assumed to be of yield strength level (after Rosenstein (21)).

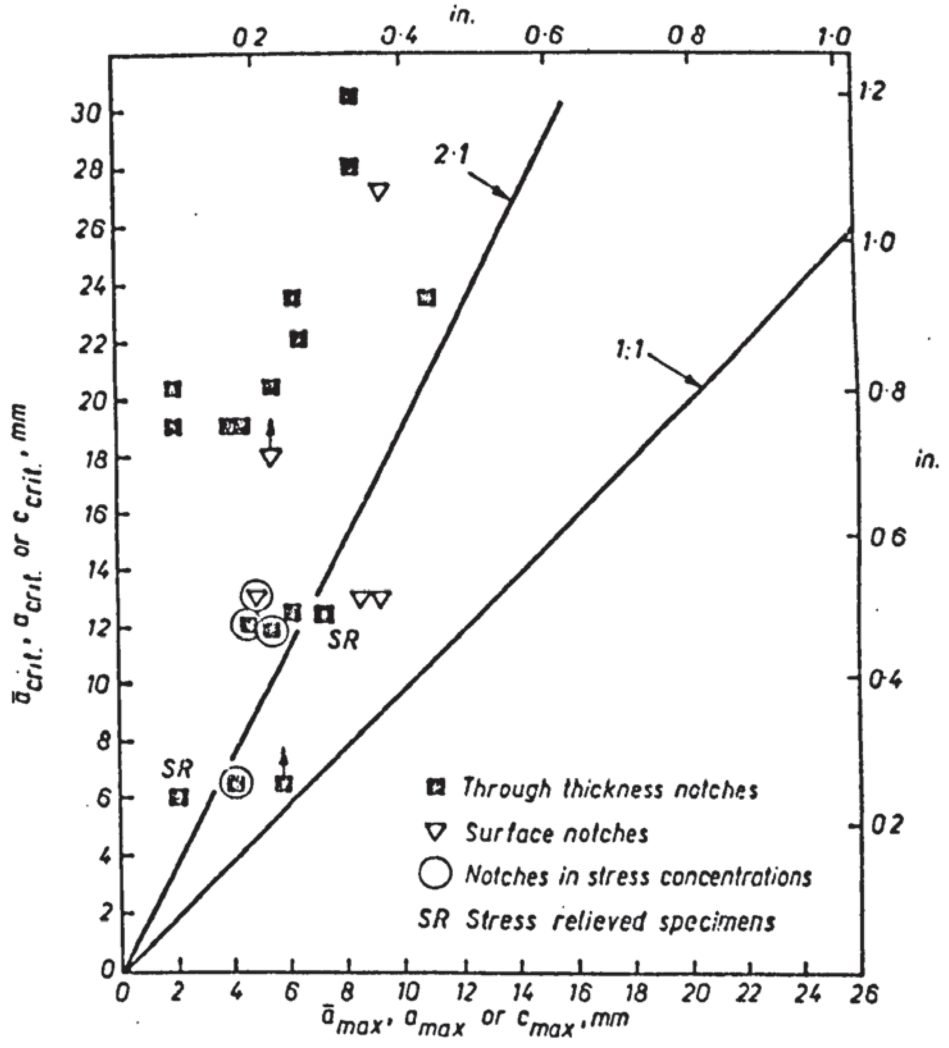

Figure 103 Comparison of critical crack sizes (from wide plate tests) and allowable crack sizes predicted by the COD design equation ($\bar{a}_{max}$), showing the design equation to be conservative (after Dawes (102)).